EXPERIMENTAL INVESTIGATION OF THE ELECTRON CAPTURE DECAY OF ^{210}At AND ^{209}At: THE LEVEL SCHEMES OF ^{210}Po AND ^{209}Po

Leslie James Jardine
(Ph. D. Thesis)

December 1971

AEC Contract No. W-7405-eng-48

DISCLAIMER

EXPERIMENTAL INVESTIGATION OF THE ELECTRON CAPTURE DECAY OF ^{210}At AND ^{209}At: THE LEVEL SCHEMES OF ^{210}Po AND ^{209}Po

Contents

EXPERIMENTAL INVESTIGATION OF THE ELECTRON CAPTURE DECAY OF ^{210}At AND ^{209}At: THE LEVEL SCHEMES OF ^{210}Po AND ^{209}Po

Leslie James Jardine

Lawrence Berkeley Laboratory
University of California
Berkeley, California 94720

December 1971

ABSTRACT

The nuclear levels of ^{210}Po and ^{209}Po populated by the electron-capture decay of ^{210}At and ^{209}At have been studied. Experimental level schemes have been constructed by using data obtained from gamma-ray singles, internal conversion electron, and gamma-gamma coincidence measurements with high resolution Ge(Li) and Si(Li) spectrometers.

For the case of ^{210}Po, present data have been used to define twenty-three levels. The multipolarity of thirty-six transitions in ^{210}Po have been determined and combined with data from recent reaction studies to assign spins and parities to the levels. All levels arising from the two-proton configuration $(h_{9/2})^2$ and from the multiplets due to the configurations $(h_{9/2}\ f_{7/2})$ and $(h_{9/2}\ i_{13/2})$, except for the lowest spin members, have been identified. The level structure is compared with two-proton shell model calculations and experimental transition probabilities for gamma decay of the $(h_{9/2}\ f_{7/2})$ and $(h_{9/2})^2$ proton multiplets are compared with predictions using several sets of shell model wave-functions. Evidence is presented which locates the 3^- collective level

in ^{210}Po at 2400 keV above the ground state. The electron-capture transition rates to odd parity levels above 2.9 MeV are discussed in terms of neutron-neutron and proton-proton particle-hole excitations of the ^{208}Pb core. A weak-coupling calculation using experimental data of neighboring isotopes in the lead region is made for the energies of the 3^- and 5^- core states of ^{210}Po.

For the case of ^{209}Po, twenty-levels have been defined by the present data. Multipolarities of thirty-one transitions in ^{209}Po have been determined and used to assign spins and parities to the levels. Five states arising from the odd neutron in ^{209}Po have been assigned by a comparison of the experimental level spectrum and the decay characteristics of levels with a shell model calculation and the levels in ^{207}Pb. A weak coupling calculation using experimental data from isotopes in the lead region to approximate residual interactions was found to explain the level structure of ^{209}Po below 2 MeV.

LIST OF FIGURES

APPENDIX B

APPENDIX C

APPENDIX E

APPENDIX F

LIST OF TABLES

APPENDIX D

APPENDIX E

APPENDIX F

APPENDIX G

I. INTRODUCTION

No single model has yet been successful in predicting nuclear structure over the whole periodic chart of the nuclides. The first model to correctly describe the shell properties and the ground-state spins of nuclei was the single-particle shell model proposed by Haxel, Jensen, and Suess[4]) and Mayer[5]). The basic assumption of the shell model was that the effect of interactions with other nucleons on a single (independent) nucleon could be approximated by an average potential generated by an "inert" core of nucleons. This independent particle description was tested by the comparison of the experimental level structure of a nucleus with one nucleon beyond a double closed shell of neutrons and protons with that predicted by the model. The same general description should be true for nuclei consisting of one less nucleon (referred to as a hole) than a double closed shell.

Nuclei with two nucleons beyond a double closed shell provide a means for examining further details of the shell model, namely residual interactions between the two nucleons. The shell model describes such a nucleus in terms of two independent particles moving in a potential generated by the double closed core of neutrons and protons. At low excitation energies the core is treated as inert with respect to the level structure. Each nucleon outside the core may be identified with a definite single-particle energy state. In a "zero-order" shell model approximation of no residual interaction between the two nucleons, all states arising from various couplings of angular momenta of a two nucleon configuration are degenerate. However, there is a residual

interaction between the two individual nucleons which removes the degeneracy and leads to a series of states which can be classified by different couplings of the angular momenta.

At higher excitation energies, the core of nucleons can have excited configurations with an angular momentum other than zero. The level structure of a double closed core nucleus gives an indication of the energy necessary to produce core excitations. For example, the experimental level scheme of ^{208}Pb has its first excited state at 2.6 MeV. Below this energy nuclei with two nucleons beyond a ^{208}Pb core might be expected to obey the shell model. Above 2.6 MeV additional core-excitations should occur with the shell model states to produce a very complex level structure. Thus a detailed examination of the level structure of a nucleus two nucleons beyond a double closed shell provides the simplest case to study the details of the residual interactions between nucleons and the validity of the inert core assumptions. If these details of the shell model are to be further investigated, the ideal nuclei to study should be those near the regions of the double closed shells.

Many details of nuclear structure have been revealed during the past five years because of improved developments in solid-state detectors and electronics. Computer analysis of data and "on line" computers have been combined to aid researchers in deciphering and collecting vast amounts of data. It is hoped that the interpretation of the data might allow a better understanding to be made of the nucleus, residual interactions, and nuclear potentials with the ultimate goal of being able to

predict the properties of any nucleus from a set of first principles. In order to achieve this goal and to determine the limitations and validity of present models, further detailed experimental information must be obtained for nuclei, in particular near double closed shells. Analysis of this data should provide information necessary to achieve the goal.

Detailed nuclear structure information has been obtained for two neutron deficient nuclei near the doubly closed shell of ^{208}Pb using the experimental programs described in this thesis. The primary goal of this study was to determine the level scheme of $^{209}_{84}Po$. The ^{209}Po nucleus is of theoretical interest due to its proximity to ^{208}Pb where one might hope to understand its low-lying level structure with a shell model. Initially we hoped to be able to identify the neutron-hole states of ^{209}Po and compare them with those previously observed in the analogous odd-neutron nucleus ^{207}Pb in order to determine the effect of the 83rd and 84th protons on such states.

An additional reward developed from the choice of the $^{209}Bi(\alpha,4n)^{209}At$ reaction for the production of sources. This required that the decay properties of ^{210}At (which was produced in sources from the competing $(\alpha,3n)$ reaction) be known. Several questions about the ^{210}At electron-capture decay scheme needed to be investigated in order to better understand the decay. Thus a reinvestigation of the ^{210}At decay was undertaken to search for finer details of the ^{210}Po level structure, in particular core-excitations. The new data combined with new reaction data on the levels of ^{210}Po and ^{208}Pb allowed a very

detailed level scheme to be constructed. As a result almost all levels due to two-proton shell model configurations and ^{208}Pb core-excitations occuring below 3.4 MeV have been identified in the ^{210}Po level structure. The identification of the neutron and proton core-excitations in the level structure has established the need for a model explicitly taking into account core-excitations.

Before proceeding with the experimental results, we shall outline the material to be presented. This thesis was written into several independent parts with the ideal of it being useful to future people entering nuclear spectroscopy. Thus there is some repetition and discussion of technical points for which the experienced spectroscopist is invited to skip. A reader should be able to read any of the five sections of interest essentially independent of the other as the referencing to other sections was kept to a minimum.

In section II a brief theoretical discussion is given of the single-particle shell model and weak coupling models as adapted to the specific examples of ^{210}Po and ^{209}Po. These models are used in our discussion and interpretation of the levels. Section III contains a detailed discussion of the experimental detection systems used in this study.

The experimental results and the interpretation of the electron-capture decay of ^{210}At are given in section IV. Results for ^{210}Po are compared with the predictions of the two-proton shell model and the weak-coupling model. Identification of two-proton shell model states and ^{208}Pb core states are made. The gamma decay transition probabilities are calculated between the low-lying even parity levels.

In section V the experimental results of the ^{209}At electron-capture decay to ^{209}Po are presented. Identification of states in ^{209}Po arising from single-neutron (particle or hole) configurations are made by a comparison of the level structure with ^{207}Pb and theoretical calculations. A weak-coupling model calculation is made for the two proton-one neutron hole configurations, and such states are identified in the ^{209}Po level structure.

Finally we have included in the Appendices a collection of useful information generated during this study but not deemed necessary to the main text. The topics included are gamma decay transition probabilities, electron-capture log ft calculations, and the data acquisition system. A compilation of gamma-ray energy calibration standards and the methods of calibrating Ge(Li) and Si(Li) spectrometers for the relative detection efficiencies of gamma-rays and conversion electrons is also given.

II. THEORETICAL BACKGROUND

Nuclei containing 2, 8, 20, 28, 50, 82, and 126 protons and/or neutrons are particularly stable and these numbers of nucleons are referred to as magic numbers or shell closures. Some abundant nuclei containing these numbers are $^{16}_{8}O$, $^{40}_{20}Ca$, $^{118}_{50}Sn$, and $^{208}_{82}Pb$. Nuclei with a doubly magic number of nucleons have a spherical shape in contrast to a deformed shape for nuclei which have a number of nucleons removed from a magic number. Successful attempts have been made to predict the shell closures and the basic assumption used to generate the closures is that a nucleon travels within a complex nucleus in a smoothly varying field of force generated by all other nucleons. The choice of a potential to represent the average potential experienced by a nucleon is determined by the nuclear force which is known to be strong but short ranged. Any form for the potential that crudely represents the general nuclear force criteria will reproduce some of the shell closures. The average potential used must be strong and nearly constant inside the nucleus and must rise rapidly near the nuclear surface since the nucleon is bound. The two simplest potentials often used are the single harmonic oscillator and the spherical potential well which are illustrated in fig. 1. The parameters in fig. 1 represent approximate values for neutrons in the lead region[1]). For example, from the relation

$$1/2\ m\omega^2\ R^2 = E = (N + 3/2)\hbar\omega \qquad (1)$$

where $R = 1.42\ A^{1/3}$ [fm], the value N = 5 (for 126 neutrons) was used. The depths of the potentials (V_o and V_o') were used in a calculation[1]).

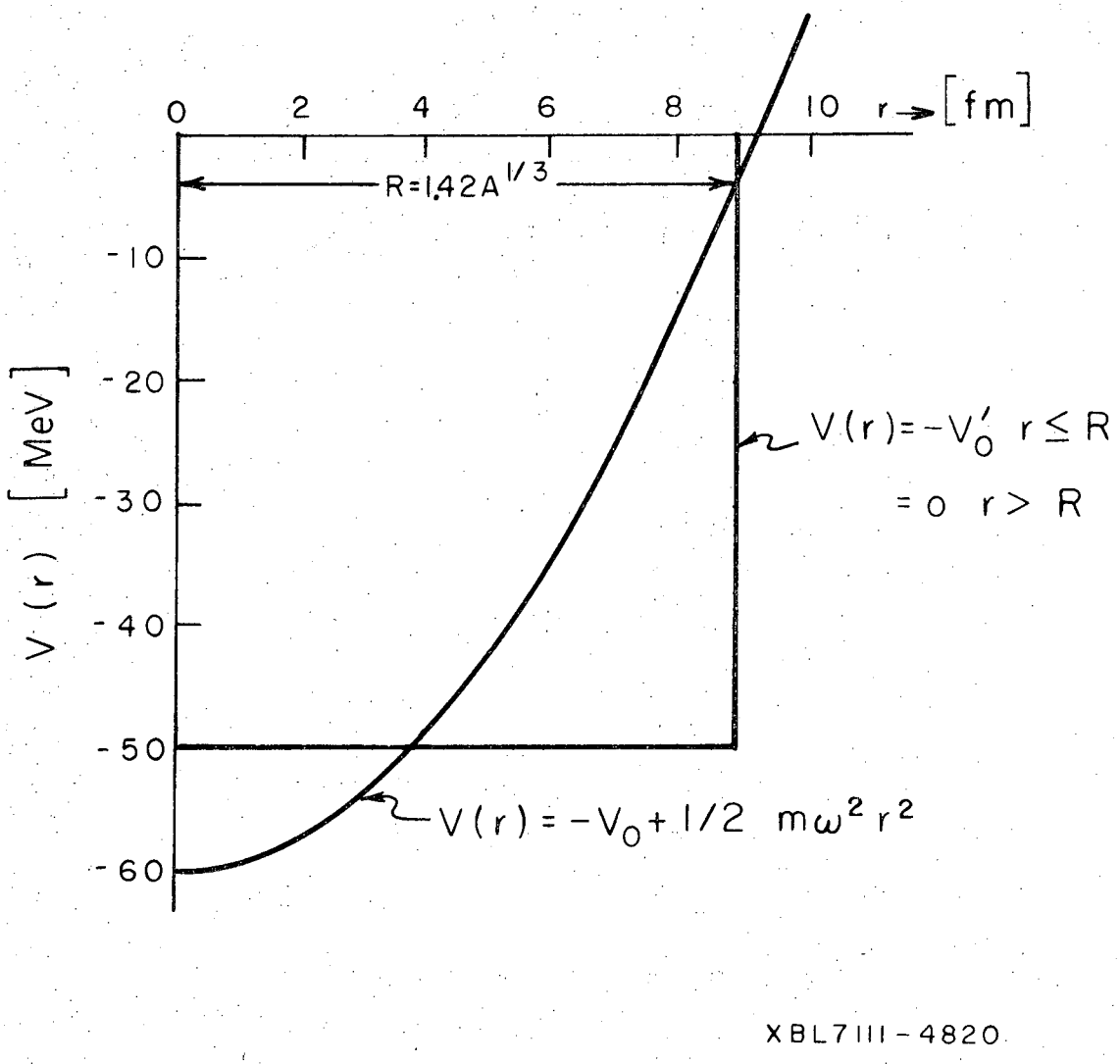

Fig. 1. The simple harmonic oscillator and spherical "square" well potentials. The parameters represent approximate values used near the 126 neutron shell[1]).

The results predicted with the single-particle model using these potentials will next be discussed followed by the introduction of the spin-orbit potential which is necessary to predict the experimentally observed shell closures.

A. Single-Particle Model

This is the simplest form of the shell model which is strictly valid only for a single nucleon (fermion) outside a doubly closed shell. The nucleon is assumed to move in an essentially undisturbed and unique orbit in a central spherically symmetric potential V(r) generated by all other nucleons composing the nucleus. The Schrödinger equation can be solved for the single-particle eigenfunctions ϕ_i and the energy eigenvalues E

$$H\phi_i = E\phi_i \tag{2}$$

where the Hamiltonian H is defined as

$$H = -\frac{\hbar^2}{2m}\vec{\nabla}^2 + V(r) \tag{3}$$

The potentials used to represent V(r) are the simple harmonic oscillator (SHO) and the spherically symmetric potential well (SPW) shown in fig. 1. The SHO potential has the analytical form

$$V(r) = -V_o + 1/2\ m\omega^2\ r^2 \tag{4}$$

and the SPW potential the form

$$V(r) = \begin{cases} -V_o' & r \leq R \\ 0 & r > R \end{cases} \tag{5}$$

where V_o, ω, and V_o' are positive constants. Both potentials have single-particle solutions (of eq. (1)) $\phi_{n\ell m}(r) \equiv |n\ell m\rangle$ which depend on the radial position r and the quantum numbers $n\ell m$ as described below.

The most frequently used potential is the SHO which leads to a set of degenerate eigenvalues given by[2,3])

$$E_{n\ell} = -V_o + \hbar\omega(N + 3/2) \tag{6}$$

where N is defined as the principle quantum number and is restricted to be integral values, including zero. For each value of N there is a series of states degenerate in energy which can be denoted by the quantum numbers n, ℓ, and m. The relation between the principle quantum number N and ℓ is[2,3])

$$N = 2(n - 1) + \ell = 0, 1, 2, \ldots \tag{7}$$

where n is defined as the radial quantum number (n - 1 is the number of nodes in the radial wavefunction portion of $\phi_{n\ell m}(r)$ for $0 < r < \infty$), and ℓ is the relative orbital angular momentum of the nucleon. The restriction that $2(n - 1) + \ell$ is zero or integral requires that ℓ is either even or odd for a given N. This leads to the fact that shells of the same principle quantum number N have orbitals of the same parity. In addition to the degeneracy in n and ℓ for a given energy, there is a $2(2\ell + 1)$ fold degeneracy (in spin and in ℓ due to its m projection) so that the

total number of degeneracies in the eigenvalues of eq. (6) is equal to $(N + 1)(N + 2)$. On the left hand side of fig. 2 are shown the energy eigenvalues of eq. (6) and the sum of the degenerate single-particle states which lead to the predicted shell closures at the (magic) occupational numbers 2, 8, 20, 40, 70, 112, and 168.

Use of the SPW potential in eq. (1) leads to eigenfunctions which have the degeneracy in the n and ℓ removed. These solutions are the spherical bessel functions $j_{\ell+1/2}(K_{n\ell})$ where the energy eigenvalues are given by the zero's of the bessel function as[3])

$$E_{n\ell} = \frac{\hbar^2}{2mR^2} K_{n\ell}^2 \qquad (8)$$

The number of zero's of the bessel function, excluding the origin, is given by n (n = 0, 1, 2, ...). The eigenvalues of eq. (8) are plotted on the right of fig. 2 in units of $\frac{\hbar^2}{2mR^2}$. The eigenvalues are still degenerate in ℓ and spin with the number of degeneracies given by $2(2\ell + 1)$. The sum of the degeneracies is also shown in fig. 2 and leads to predicted shell closures at the occupational numbers 2, 8, 20, 58, 92, and 132.

In real nuclei the true potential might be expected to be more of an average of the SHO and SPW potentials. Average energy eigenvalues and occupational numbers formed from both potentials with the n and ℓ degeneracy removed are shown in the center of fig. 2. The average predicts shell closures at 2, 8, 40, 70, 92, and 138. Except for the lightest nuclei ($A \leqslant 40$), neither of these potentials nor the average predict the

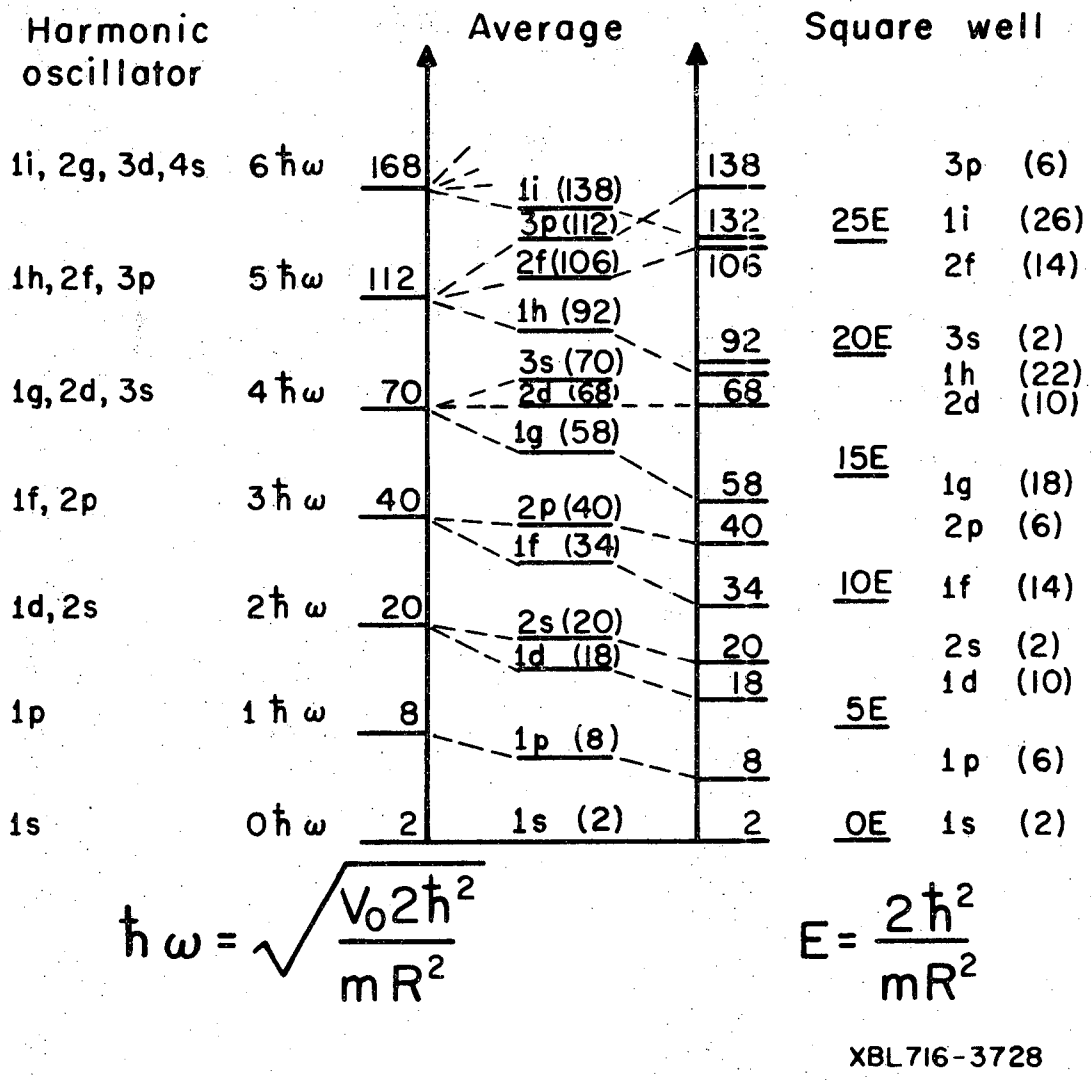

Fig. 2. Level system of the three-dimensional simple harmonic oscillator and the spherical "square" well with infinitely high walls. (This figure was taken from ref. [8].)

experimentally observed shell closures which suggests that some important detail is missing. The independent suggestions of an additional strong spin-orbit coupling term by Haxel, Jensen, and Suess[4]) and Mayer[5,6,7]) lead to the correct shell predictions. The velocity dependent spin-orbit term takes into account the interaction between the nuclear spin $\vec{s}$ and the relative angular momentum $\vec{\ell}$ for a nucleon. The form for the spin-orbit term is generally taken as[10])

$$V_{SO}(r) = -2\lambda \left(\frac{\hbar^2}{2mc}\right)^2 \frac{1}{r} \frac{dV(r)}{dr} \vec{\ell}\cdot\vec{s} \qquad (9)$$

where λ is an adjustable parameter greater than zero and is different for protons and neutrons. The inclusion of this term <u>with</u> the SHO or SPW potentials to V(r) in eq. (3) gives results different from the SHO or SPW potentials in the following qualitative way. Because of the relations

$$2\vec{\ell}\cdot\vec{s} = \vec{J}^2 - (\vec{\ell}^2 + \vec{s}^2) \quad \text{and} \quad \lambda > 0 \quad , \qquad (10)$$

states of large orbital angular momentum $\vec{\ell}$ are effected most with states of total angular momentum $\vec{J} = \vec{\ell} + \vec{s}$ more tightly bound than states of $\vec{J} = \vec{\ell} - \vec{s}$. The results[8]) of a calculation with the inclusion of spin-orbit coupling and the SPW potential are shown in fig. 3. Large angular momentum states interact strongly with the result that the states of angular momentum $\vec{J} = \vec{\ell} + \vec{s}$ are depressed (proportional to λ) in energy and the states of $\vec{J} = \vec{\ell} - \vec{s}$ are raised so that the SPW (or SHO) levels are altered. For example, the splitting of the 1g level into the $1g_{9/2}$ and $1g_{7/2}$ levels produces the magic number 50 by inclusion of 10

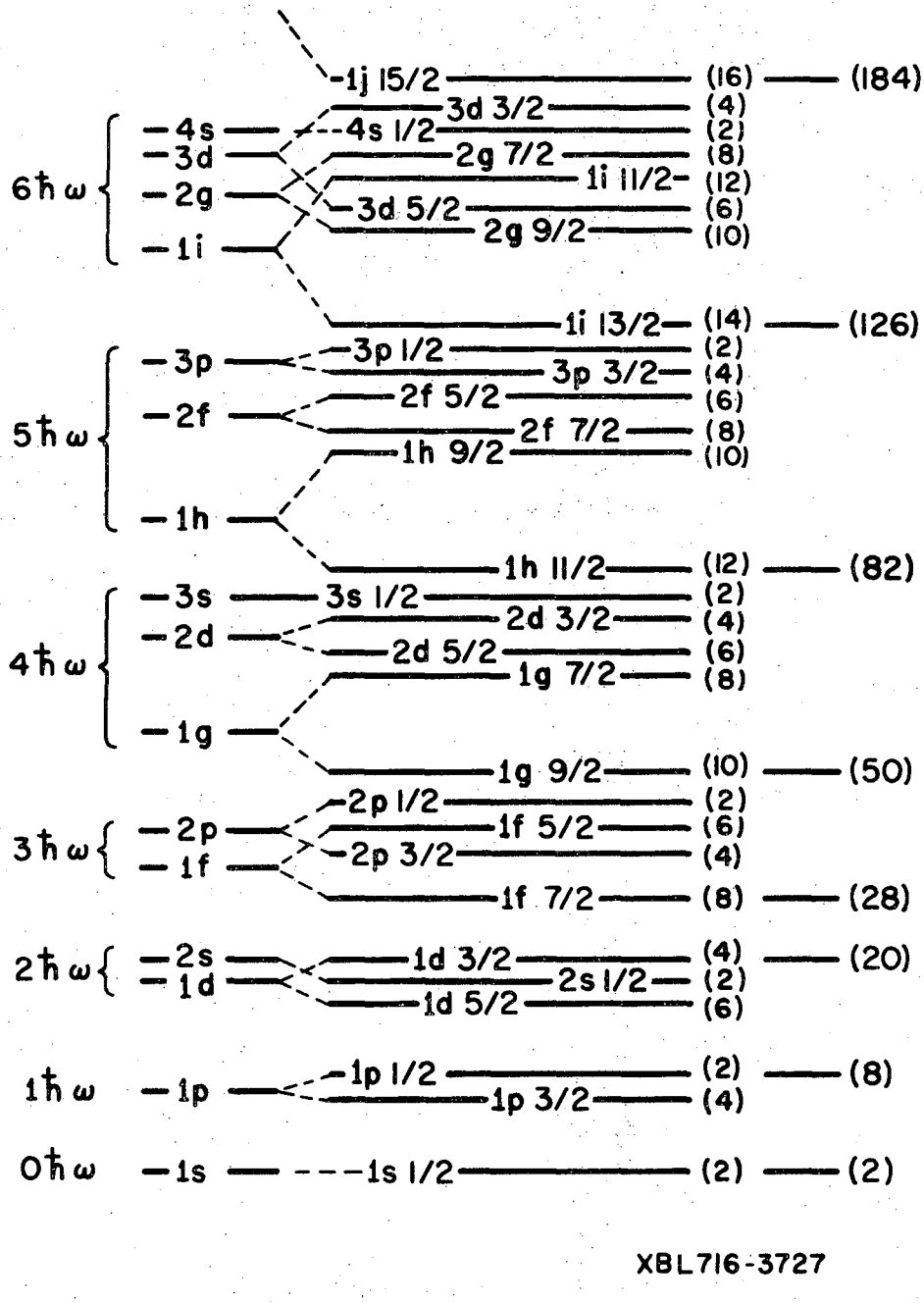

Fig. 3. Schematic diagram of the nuclear level system with spin-orbit coupling. (This figure was taken from ref. [8].)

additional states to the previous occupational number of 40 produced with either the SPW or SHO potentials. Similar splittings for other large angular momentum orbitals are responsible for producing the experimentally observed shell gaps of 28, 82, and 126, which were not produced with the SPW or SHO potentials alone.

The single-particle model with the spin-orbit term cannot correctly predict the exact ordering of orbitals for all regions of the periodic chart with one value of the parameter λ. By varying λ separately for protons and neutrons for different regions, the experimental level schemes can be reproduced. For example, the experimental[9]) single-particle levels in the lead region shown in fig. 4 can be reproduced by varying λ.

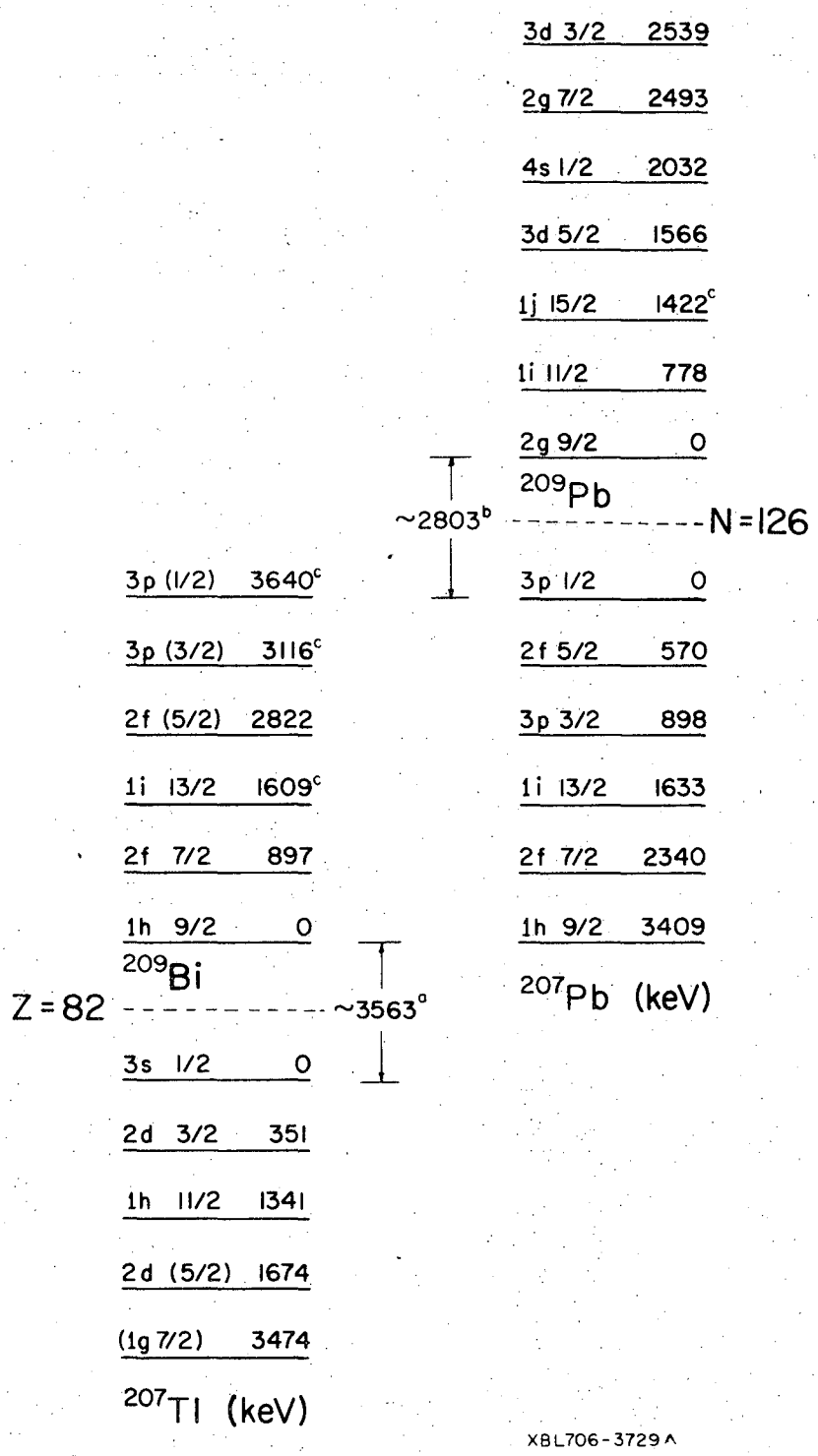

Fig. 4. Experimental[9]) single-particle states in the lead region.

(a) Gap energy of 3563 keV was estimated as the difference of the energy necessary to separate a proton from ^{207}Tl minus that required for ^{209}Bi.

(b) Gap energy of 2803 keV was estimated as the difference of the energy necessary to separate a neutron from ^{207}Pb minus that required for ^{209}Pb.

(c) The single-particle strength is believed fragmented over several levels.

B. Shell Model

The single-particle model as formulated above should be only strictly valid for nuclei with one nucleon more than a doubly closed shell. More sophisticated treatments include the description of two or more particles outside of a double closed shell. This leads to the shell model where the excited states and their spins and parities are predicted for more than a single-particle beyond a double closed shell.

The approach in a shell model calculation is to assume some form of an inert core which gives rise to a potential in which the nucleons outside this core move and interact through residual two-body interactions among themselves. To calculate energy levels, a potential with adjustable parameters representing the core and two-body interactions is selected. Implicit in the model is that the nucleons outside the core do not interact directly with the individual core nucleons. The inert core assumption may not be strictly valid but it produces a simpler model which reduces the number of degrees of freedom to a solvable problem.

The inert core assumption allows the total wavefunction of the system ψ to be written as the product of a wavefunction for the non-interacting core nucleons ψ_c and the N valence nucleons Φ. The Hamiltonian is then written as a sum of a core and a valence part,

$$\psi = \psi_c \Phi \tag{11}$$

and

$$H = H_c + H_v \tag{12}$$

These assumptions allow separation of the problem into two parts which may be solved individually. Thus in general we have eigenvalues for the core (E_c) and the valance nucleons (E_v) from the relations

$$H_c\psi_c = E_c\psi_c \tag{13}$$

and

$$H_v\Phi = E_v\Phi \tag{14}$$

To determine explicitly the meaning of the eigenvalues, we first consider the lower energy valence states where the core assumption is probably most valid. The form for the Hamiltonian describing N valance nucleons outside the inert core H_v is assumed to be further separable into two parts[2])

$$H_v = H_o + H_1 \tag{15}$$

where

$$H_o = \sum_{i=1}^{N} (T_i + V_i) \tag{16}$$

and

$$H_1 = \sum_{i<j} V_{ij} \tag{17}$$

H_o is a Hamiltonian representing the interaction of the valence nucleons with the core but not with each other. That is, H_o includes all interactions experienced by nucleons outside the selected core <u>except</u> for the

residual two-body interactions among valence nucleons. H_o is generally taken as the SHO potential where T_i is the kinetic energy of the i^{th} particle with a potential energy V_i outside the inert core. H_1 represents the sum of all <u>two-body</u> residual interactions among the valence nucleons where V_{ij} is the residual two-body interaction between the i^{th} and j^{th} valence nucleons. The assumption that only two-body forces need be considered in the residual interactions is tested in how well the predicted results agree with experimental results. The form of H_1 is generally taken from two nucleon scattering experiments[2,3] as we discuss at the end of this section.

If the simple harmonic oscillator potential (SHO) is taken for H, the well-known SHO wavefunctions are solutions for H_o [2]. Explicitly, if the nucleons outside the core are non-interacting, the solution for N nucleons can be written as a product of N single nucleon SHO wavefunctions $\phi_{\alpha_i}(i)$ (see section IIA) for the various configurations (specified by the quantum numbers $(n\ell m)$ and represented by the label α_i) as[2,3]

$$\Phi = \prod_{i=1}^{N} \phi_{\alpha_i}(i) \tag{18}$$

Thus

$$H_o\Phi = \sum_i \varepsilon_i \Phi \equiv \varepsilon\Phi \tag{19}$$

where

$$H_o = \sum_{i=1}^{N} - \frac{\hbar^2}{2m_i} \nabla^2 - V_o + 1/2\, m_i \omega^2 r^2 \qquad (20)$$

The sum of eigenvalues for <u>all</u> N nucleons outside the core in the absence of all two-body residual interactions is defined as ε. The single-particle (SHO) eigenvalues for various occupied orbitals outside the core are represented by ε_i. (The ε_i is the same as the eigenvalue $E_{n\ell}$ of eq. (8) in the single-particle model of section IIA and is numerically the mass of the i^{th} single-particle plus the core <u>minus</u> the core.) However, the wavefunction in eq. (18) is not antisymmetric as required by the Pauli exclusion principle. The properly normalized antisymmetrized orthonormal wavefunction for N valence nucleons is generally taken as a linear combination of the single nucleon SHO wavefunctions $\phi_{\alpha_i}(i)$ in the form of a Slater determinent[2])

$$\Phi = \frac{1}{\sqrt{N!}} \begin{vmatrix} \phi_{\alpha_1}(1) & \phi_{\alpha_2}(1) & \cdots & \phi_{\alpha_N}(1) \\ \phi_{\alpha_1}(2) & \phi_{\alpha_2}(2) & \cdots & \phi_{\alpha_N}(2) \\ \vdots & \vdots & & \vdots \\ \phi_{\alpha_1}(N) & \phi_{\alpha_2}(N) & \cdots & \phi_{\alpha_N}(N) \end{vmatrix} \qquad (21)$$

As an example, suppose we had two nucleons outside a core, each described by the single-particle wavefunctions $\phi_{\alpha_1}(1)$ and $\phi_{\alpha_2}(2)$, then the wavefunction Φ would be written

$$\Phi = \frac{1}{\sqrt{2}} \left[\phi_{\alpha_1}(1)\, \phi_{\alpha_2}(2) - \phi_{\alpha_1}(2)\, \phi_{\alpha_2}(1)\right] \qquad (22)$$

This is the correct normalized antisymmetrized wavefunction to be used in eq. (19).

The shell model Hamiltonian of eq. (12) and eq. (15) can be grouped and rewritten as

$$H = (H_c + H_o) + H_1 \tag{23}$$

where we have shown with eq. (11), eq. (13), and eq. (19) that

$$H\psi = (E_c + \varepsilon)\psi + H_1\psi = E\psi \tag{24}$$

This is the eigenvalue equation that can be solved by matrix diagonalization. In general Φ occuring in eq. (11) can be expanded in any complete orthonormal set of properly antisymmetrized wavefunctions. For this model, the proper choice is the complete set of Slater determinents (eq. (21)) $\{\Phi_i\}$ formed for all allowed SHO single nucleon wavefunctions ϕ_i of the configuration space outside the core. The wavefunction of eq. (11) now takes the general form[2])

$$\psi \equiv |\psi\rangle = |\psi_c\rangle \sum_i a_i |\Phi_i\rangle \tag{25}$$

Experimentally it is known that H must be rotationally invariant which implies that H is diagonal in J. The condition that H is invariant to rotations is expressed by[2,3])

$$\langle \psi_J | H | \psi_{J'} \rangle = \text{constant } \delta_{JJ'} \quad . \tag{26}$$

Rotational invariance of H is the basis of the statement that states of different J (and parity) do not interact or configuration mix. The forms of H are also restricted to be scaler or pseudo-scaler interactions[2,3]. Since H is assumed diagonal in J, the summation in eq. (25) can be truncated to include only those terms where the configurations of the N nucleons outside the core have the same spin and parity J^{π}. This allows the matrix diagonalization of eq. (24) to be performed in a smaller orbital space. However, rather than continue in a general way, a specific case will be discussed which may be generalized by the reader.

We shall proceed to outline the methods for doing a shell model calculation and discuss the techniques involved using the specific example of ^{210}Po which has two protons more than the doubly closed ^{208}Pb core. The two protons can be assumed to move in the field of the ^{208}Pb core and interact with each other through residual interactions to produce different nondegenerate nuclear states. This example involves a doubly closed core which certainly approximates the inert core model; however, a doubly closed core is not a restriction. Consideration of the single-particle states available for the protons in the lead region in fig. 4 suggests that the lower levels of ^{210}Po might be satisfactorily described by a truncated configuration space of three orbitals, namely $1h_{9/2}$, $2f_{7/2}$, and $1i_{13/2}$. This choice is determined in part by the slightly larger experimental energy gap between the $2f_{5/2}$ and the $1i_{13/2}$ orbitals than the other orbitals. However, this truncation must be tested with experimental evidence before the validity is truely known.

Thus for ^{210}Po we will assume that the two protons outside the core are allowed only in the three orbitals immediately above the Z = 82 shell. Figure 4 shows that the three allowed proton orbitals are $1h_{9/2}$, $2f_{7/2}$, and $1i_{13/2}$.

The lowest energy state (ground-state) of ^{210}Po would have both protons in the $1h_{9/2}$ orbitals coupled to 0^+ (as the ground-states of other even-even nuclei are 0^+) with the dominant ground-state configuration $\pi(h_{9/2})^2$. There are other allowed proton orbitals (and angular momentum couplings) in this two-proton model. Thus many states of different angular momentum couplings and parity (J^π) are allowed which generate the excited states. The number of states can be derived from the number of ways in which two identical particles (protons) of angular momentum $\vec{j}_1$ and $\vec{j}_2$ can be placed into three orbitals. For two identical nucleons in the same orbital, the Pauli principle excludes states of odd $\vec{J}$ couplings. (This also can be proved rigorously in the Racah algebra for a two-particle antisymmetric wavefunction[2].) The total number of ways to put two protons into the three orbitals is six with a total of 42 allowed, but different, couplings of the angular momentum $\vec{J} = \vec{j}_1 + \vec{j}_2$. These allowed configurations are enumerated in Table 1. These results can be generalized to any number of orbitals and particles although this method grows rapidly in complexity for allowed couplings.

Since the number and types of allowed two-proton states for ^{210}Po have been discussed, we consider solving eq. (24) in detail for the energy levels and wavefunctions. The procedure we will discuss is the general way in which shell model calculations are performed. We will

Table 1. The shell model orbitals and the allowed $(j_1 j_2)J$ couplings of the two protons for ^{210}Po in our three orbital space. The occupation of an orbital is represented by the symbol X.

Shell Model Proton Orbitals			Allowed Configurations
$1h_{9/2}$	$2f_{7/2}$	$1i_{13/2}$	J^π
XX			$(0,2,4,6,8)^+$
X	X		$(1,2,3,4,5,6,7,8)^+$
X		X	$(2,3,4,5,6,7,8,9,10,11)^-$
	XX		$(0,2,4,6)^+$
	X	X	$(3,4,5,6,7,8,8,10)^-$
		XX	$(0,2,4,6,8,10,12)^+$

show that since H is diagonal in $\vec{J}$ and parity is conserved, only states of the same J^π need be considered at once. After choosing a particular J^π and solving eq. (24) for the eigenfunctions and eigenvalues, the process can be repeated for a new J^π.

Suppose we first solve eq. (24) for all the $J^\pi = 0^+$ two-proton states allowed in our space for ^{210}Po. The expansion of Φ in eq. (25) reduces to three terms since only three 0^+ states from the two-proton couplings can be formed within our three orbital model (see Table 1). The three 0^+ states will produce a 3X3 matrix to be diagonalized. Explicitly we may write

$$\psi \equiv |\psi_{0^+}\rangle = |\psi_c\rangle \sum_{i=1}^{3} a_i |\Phi_{0^+}(i)\rangle \tag{27}$$

where $\Phi_{0^+}(i)$ are the three Slater determinents formed for the two protons coupled to 0^+ in the $h_{9/2}$, $f_{7/2}$ and $i_{13/2}$ orbitals

$$\begin{aligned} \Phi_{0^+}(1) &\equiv \Phi(\pi(h^2_{9/2})_{0^+}) \\ \Phi_{0^+}(2) &\equiv \Phi(\pi(f^2_{7/2})_{0^+}) \\ \Phi_{0^+}(3) &\equiv \Phi(\pi(i^2_{13/2})_{0^+}) \end{aligned} \tag{28}$$

To solve eq. (24) for the eigenvalues E and eigenfunctions ψ, we utilize our expansion of Φ in eq. (27) to generate a 3X3 matrix. Multiply

eq. (24) by each of the three Φ_i terms in the summation of eq. (27) and use the orthonormal properties $\langle \Phi_i | \Phi_j \rangle = \delta_{ij}$ and $\langle \psi_c | \psi_c \rangle = 1$ to arrive at the following set of equations.

$$\langle \psi_c | \langle \Phi_1 | H | \sum_{i=1}^{3} a_i | \Phi_i \rangle | \psi_c \rangle = E \langle \Phi_1 | \sum a_i | \Phi_i \rangle = a_1 E$$

$$\langle \psi_c | \langle \Phi_2 | H | \sum_{i=1}^{3} a_i | \Phi_i \rangle | \psi_c \rangle = a_2 E \qquad (29)$$

$$\langle \psi_c | \langle \Phi_3 | H | \sum_{i=1}^{3} a_i | \Phi_i \rangle | \psi_c \rangle = a_3 E$$

The set of equations in eq. (29) can be put into matrix form. After expanding the summations in eq. (29), we arrive at the following matrix equation

$$\begin{pmatrix} \langle \psi_c | \langle \Phi_1 | H | \Phi_1 \rangle | \psi_c \rangle - E & \langle \psi_c | \langle \Phi_1 | H | \Phi_2 \rangle | \psi_c \rangle & \langle \psi_c | \langle \Phi_1 | H | \Phi_3 \rangle | \psi_c \rangle \\ \langle \psi_c | \langle \Phi_2 | H | \Phi_1 \rangle | \psi_c \rangle & \langle \psi_c | \langle \Phi_2 | H | \Phi_2 \rangle | \psi_c \rangle - E & \langle \psi_c | \langle \Phi_2 | H | \Phi_3 \rangle | \psi_c \rangle \\ \langle \psi_c | \langle \Phi_3 | H | \Phi_1 \rangle | \psi_c \rangle & \langle \psi_c | \langle \Phi_3 | H | \Phi_2 \rangle | \psi_c \rangle & \langle \psi_c | \langle \Phi_3 | H | \Phi_3 \rangle | \psi_c \rangle - E \end{pmatrix} \begin{pmatrix} a_1 \\ a_2 \\ a_3 \end{pmatrix} = 0 \qquad (30)$$

Equation (30) can be further reduced using the definitions of H in eq. (23) and the results of operating with the various Hamiltonian operators as defined in eq. (14) and eq. (19).

$$\begin{pmatrix} \langle \Phi_1|H_1|\Phi_1\rangle + \varepsilon_1' - E & \langle \Phi_1|H_1|\Phi_2\rangle & \langle \Phi_1|H_1|\Phi_3\rangle \\ \langle \Phi_2|H_1|\Phi_1\rangle & \langle \Phi_2|H_1|\Phi_2\rangle + \varepsilon_2' - E & \langle \Phi_2|H_1|\Phi_3\rangle \\ \langle \Phi_3|H_1|\Phi_1\rangle & \langle \Phi_3|H_1|\Phi_2\rangle & \langle \Phi_3|H_1|\Phi_3\rangle + \varepsilon_3' - E \end{pmatrix} \begin{pmatrix} a_1 \\ a_2 \\ a_3 \end{pmatrix} = 0 \tag{31}$$

We have introduced a new single-particle energy ε_α' which is defined as the sum of the core energy eigenvalue E_c and the sum of the SHO single-particle eigenvalues ε for the two nucleons as defined in eq. (19). That is

$$(H_c + H_o)\psi_c\Phi_\alpha = (E_c + \varepsilon_\alpha)\psi_c\Phi_\alpha \equiv \varepsilon_\alpha' \psi_c\Phi_\alpha \tag{32}$$

where

$$\varepsilon_\alpha' \equiv \sum_{j=1}^{2} \varepsilon_{j,\alpha}' = \sum_{i=1}^{2} \varepsilon_{i,\alpha} + E_c \tag{33}$$

The values of ε_α' can be obtained from experimental data on single-particle energies. In general the individual $\varepsilon_{j,\alpha}'$ represent the energy of a single-nucleon outside the inert core in the absence of a residual interaction (i.e. $H_1 = 0$) which can in principle be estimated from an odd A nucleus composed of the same core. Specifically, in the absence of a residual interaction among the protons outside the ^{208}Pb core for ^{210}Po, the proton single-particle energies $\varepsilon_{j,\alpha}'$ may be approximated from ^{209}Bi data. The numerical value of E_c is the mass of the ^{208}Pb core, and $\varepsilon_{i,\alpha}$ the mass <u>difference</u> of the i^{th} single-particle state of

^{209}Bi and the ^{208}Pb core. The value of $\varepsilon'_{j,\alpha}$ is thus the mass of the i^{th} single-particle state of ^{209}Bi. Frequently, the mass of the ^{209}Bi ground-state is subtracted from the single-particle energies ($\varepsilon'_{j,\alpha}$) and energy differences (relative to zero) are used. For example, from the levels of ^{209}Bi (the ground-state mass subtracted) in fig. 4, we have the values $\varepsilon'_j(h_{9/2}) = 0$, $\varepsilon'_j(f_{7/2}) = 897$ and $\varepsilon'_j(i_{11/2}) = 1609$ keV. Thus the ε'_α terms in the matrix of eq. (31) may be evaluated from experimental data rather than calculated explicitly.

As an example we may write down zero-order estimates for solutions of eq. (31) for the various two-proton configurations in the absence of all residual interactions. These estimates are shown in Table 2. The states of the various two-proton configurations in Table 2 are degenerate because H_1 was assumed zero. This model would then predict five degenerate excited states at the energies shown in Table 2. (Residual interactions will remove the degeneracies and alter these zero-order estimates.)

However, since there are residual interactions, the matrix elements of H_1 must be evaluated before the final diagonalization of eq. (31) to arrive at the eigenvalues for the matrix. Before expanding on the evaluation of the residual interaction matrix elements, assume that they have been evaluated and are just numbers. This allows us to diagonalize the matrix and determine the eigenfunctions and eigenvalues for our example of the three 0^+ states. (The technique used to evaluate the H_1 matrix elements is discussed at the end of this section.)

Table 2. ^{210}Po two-proton level structure in the absence of all residual interactions as estimated from ^{209}Bi experimental data[9]) (ground-state mass subtracted).

Configuration	Unperturbed Energy $\varepsilon'_\alpha = \sum_{j=1}^{2} \varepsilon'_{j,\alpha}$ (keV)	Spins and Parity $(j_1 j_2)J^\pi$	Comments
$\pi(h_{9/2})^2$	0	$(0,2,4,6,8)^+$	ground state
$\pi(h_{9/2}\ f_{7/2})$	897	$(1,2,3,\ldots 8)^+$	1st excited state
$\pi(h_{9/2}\ i_{13/2})$	1609	$(2,3,4,\ldots 11)^-$	2nd excited state
$\pi(f_{7/2})^2$	1794	$(0,2,4,6)^+$	3rd excited state
$\pi(f_{7/2}\ i_{13/2})$	2506	$(3,4,5,\ldots 10)^-$	4th excited state
$\pi(i_{13/2})^2$	3218	$(0,2,4,\ldots 12)^+$	5th excited state

Solutions exist if the determinent of the 3X3 matrix is equal to zero. Solution of eq. (31) (with H_1 matrix elements and values of ε'_α assumed known) produces an equation which is cubic in E. The three energy eigenvalues E for the 0^+ states are the three roots of the cubic equation which can be obtained by various iterative techniques. At this stage the eigenfunctions for the eigenvalues are not yet determined. These can be obtained by picking one energy eigenvalue E at a time and using it for the value of E in each of three equations in eq. (29). This produces three equations and three unknowns (a_1, a_2, a_3) so that the amplitudes (a_i) of the wavefunctions of the expansion of $|\psi_{0^+}\rangle$ in eq. (27) may be determined. The solutions (a_1, a_2, and a_3) obtained for the lowest energy eigenvalue E represent amplitudes of the various 0^+ components of the ground state wavefunction.

$$|\psi_{0^+}\rangle = |\psi_c\rangle [a_1 \Phi(\pi(h^2_{9/2})_{0^+}) + a_2 \Phi(\pi(f^2_{7/2})_{0^+}) + a_3 \Phi(\pi(i^2_{13/2})_{0^+})] \tag{34}$$

The a_i show explicitly the amount of configuration mixing between states of a given J^π and represent the relative compositions of the wavefunction. The remaining two energy eigenvalues, when substituted into eq. (29), will yield the wavefunctions of ^{210}Po for the 2nd and 3rd 0^+ states respectively. Thus if the values of ε'_α and matrix elements of H_1 are known, the problem can be solved for the three eigenvalues and eigenfunctions. The remaining J^π states can be solved in a completely analogous fashion one at a time until the ^{210}Po problem is completely

solved. It should be noted that the degree of complexity and size of matrices involved depend upon the size of the configuration space alloted to the valence nucleons but grows very rapidly with the size.

A comparison of the theoretical eigenvalues with the experimental results provides a test of the choice of the configuration space for the valence nucleons and the choice of H_1. If the agreement between calculated and experimental eigenvalues is good, then the wavefunctions may be tested by computing quantities which depend upon the wavefunctions such as the gamma-ray decay transition probabilities or the DWBA cross sections. If the agreement is poor this may be indicative that the choice of parameters for H_1 (or the configuration space) may have been bad. The sensitivity of the results on matrix elements of H_1 may be realized by considering eq. (31). A reparameterization of H_1 may be necessary to bring the calculated results into better agreement with experimental results and the whole process repeated. If repeated attempts fail, perhaps the selected phenomenlogical representation for H_1 or the core is wrong, or the shell model is too simple a model for the nucleus being considered.

We have assumed in the above matrix diagonalizations that the two-body residual interaction matrix elements $\langle \Phi_i | H_1 | \Phi_j \rangle$ were known. Calculation of these matrix elements is the real crux of the problem in shell model calculations. Once these matrix elements are obtained, the shell model problem is essentially solved because only matrix diagonalizations remain as we have shown. Two types of formalisms used for the H_1 will be discussed.

The idea is to choose the two-body residual interaction Hamiltonian H_1 in such a way that the two-body matrix elements $\langle \Phi_i | H_1 | \Phi_j \rangle$ are calculable. The form of H_1 choosen for the residual interaction is generally deduced from experimental scattering studies of two nucleon systems[2]. The most general form for H_1 can be written as a sum of two components[2,3]

$$H_1 = H_{CT} + H_{NC} \tag{35}$$

where H_{CT} is a central potential component and H_{NC} is a tensor or non-central component. Two nucleon scattering experiments have shown that the form of the central two-body interaction potential of H_1 should be rotationally invarient (scaler or psuedo-scaler), parity invarient (scaler), charge independent (scaler in isospin), time reversal invarient, and permutation invarient[3].

H_{CT} can be written as a linear combination of the general interactions involving space and spin coordinates that involve two-body nuclear exchange forces[2,3].

$$H_{CT} = V(r)[S_W + S_M P_x + S_B P_\sigma + S_H P_x P_\sigma] \tag{36}$$

The subscripted S_i represent adjustable strengths (constants) for the various nuclear interaction potentials (i = W, M, B, H) that are called Wigner, Majorana, Bartlett, and Heisenberg potentials respectively. P_x and P_σ are <u>two-body</u> exchange operators for the space and spin coordinates respectively and V(r) is the radial dependence of the potentials. The values of the space, spin, and orbital angular momentum coordinates refer

to the relative coordinate system of the two nucleons in which the two-body force is acting. Hence $\vec{\ell}$ is the relative angular momentum of the two nucleons experiencing the residual interaction. (The wavefunction Φ used in this section has the explicit form of eq. (22) and represents two nucleons with coordinates $\vec{r}_1$ and $\vec{r}_2$, and spins $\vec{s}_1$ and $\vec{s}_2$.) The Wigner force of eq. (36) is just an ordinary r dependent force ($r \equiv |\vec{r}_1 - \vec{r}_2|$), with a variable strength S_W.

The Majorana potential in eq. (36) involves the space exchange operator P_x. For two nucleons, spatial exchange is the same as a reflection about the origin. The P_x operation involves the parity (even or oddness of the relative $\vec{\ell}$) of the states and either does, or does not, change the sign of the wavefunction depending on whether the parity of the wavefunction is odd or even[3]).

$$V(r)S_M P_x \Phi = \begin{cases} + V(r)S_M\Phi & \text{if } \ell \text{ even} \\ - V(r)S_M\Phi & \text{if } \ell \text{ odd} \end{cases} \tag{37}$$

The Bartlett potential of eq. (36) is such that for the spin exchange operator P_σ operating on a wavefunction, the following holds[3])

$$V(r)S_B P_\sigma \Phi = \begin{cases} + V(r)S_B\Phi & \text{if } \vec{S} = 1 \quad \text{(triplet)} \\ - V(r)S_B\Phi & \text{if } \vec{S} = 0 \quad \text{(singlet)} \end{cases} \tag{38}$$

where $\vec{S} = \vec{s}_1 + \vec{s}_2$. The effect of this part of the potential is to either change the sign of the wavefunction if the two nucleons are in the singlet ($\vec{S} = 0$) state or to do nothing if in the triplet state ($\vec{S} = 1$).

Finally the Heisenberg potential involves a combination of the space-spin exchange operators[3])

$$V(r)S_H P_x P_\sigma \Phi = \begin{cases} V(r)S_H\Phi & \text{if } \vec{S} = 1 \quad \ell \text{ even} \\ & \vec{S} = 0 \quad \ell \text{ odd} \\ -V(r)S_H\Phi & \text{if } \vec{S} = 0 \quad \ell \text{ even} \\ & \vec{S} = 1 \quad \ell \text{ odd} \end{cases} \tag{39}$$

Some formalisms treat the Heisenberg potential explicitly as the isospin $(\vec{\tau}\cdot\vec{\tau})$ dependence term (charge independence) of H_{CT}.

Another general formalism often used is very similar to the above and it involves the same type of linear combination as eq. (36) but introduces projection operators Π_i which are defined in terms of the exchange operators[2,3])

$$\begin{aligned} \Pi_T &= 1/2(1 + P_\sigma) \qquad i = \text{triplet } (\vec{S} = 1) \\ \Pi_S &= 1/2(1 - P_\sigma) \qquad i = \text{singlet } (\vec{S} = 0) \\ \Pi_E &= 1/2(1 + P_x) \qquad i = \text{even} \quad (\ell \text{ even}) \\ \Pi_O &= 1/2(1 - P_x) \qquad i = \text{odd} \quad (\ell \text{ odd}) \end{aligned} \tag{40}$$

These are projection operators because they either "project out" certain states or give zero upon operation on a two-nucleon wavefunction. Their behavior on a wavefunction is the following[3]):

$$\Pi_T\Phi = \begin{cases} 1\Phi & \text{if } \vec{S} = 1 \\ 0\Phi & \text{if } \vec{S} = 0 \end{cases}$$

$$\Pi_S\Phi = \begin{cases} 1\Phi & \text{if } \vec{S} = 0 \\ 0\Phi & \text{if } \vec{S} = 1 \end{cases} \qquad (41)$$

$$\Pi_E\Phi = \begin{cases} 1\Phi & \text{if } \ell \text{ even} \\ 0\Phi & \text{if } \ell \text{ odd} \end{cases}$$

$$\Pi_O\Phi = \begin{cases} 1\Phi & \text{if } \ell \text{ odd} \\ 0\Phi & \text{if } \ell \text{ even} \end{cases}$$

The convention $\Pi_{TE} \equiv \Pi_T \cdot \Pi_E = 1/4[(1 + P_\sigma)(1 + P_x)]$ is often used and is called the triplet-even (TE) projection operator. (Similarly for the triplet-odd (TO), singlet-even (SE), and single-odd (SO).) If we again let S_i represent adjustable strengths of potentials we can rewrite H_{CT} in terms of projection operators[2,3])

$$H_{CT} = V(r)[S_{TE}\Pi_{TE} + S_{TO}\Pi_{TO} + S_{SE}\Pi_{SE} + S_{SO}\Pi_{SO}] \qquad (42)$$

This form of H_{CT} is often used in the literature and has the simplification that for two identical nucleons, the triplet-even Π_{TE} and the singlet-odd Π_{SO} terms vanish. This would apply to ^{210}Po with two protons outside the ^{208}Pb core.

The forms taken for the radial dependence V(r) in eq. (36) and eq. (40) are generally either Gaussian

$$V(r) = - e^{-r^2/a^2} \qquad (43)$$

or Yukawa

$$V(r) = - Ke^{-r/a} \tag{44}$$

where K and a are adjustable parameters. Calculations using delta-function forces have also been made for V(r) and are called appropriately zero-range forces.

Two frequently used forms for the non-central part of H_1 are referred to as the tensor force and spin-orbit force. The form of the tensor force is [2,3]

$$H_{NC} = H_{CT}S_{12}$$

where

$$S_{12} = \frac{3(\vec{\sigma}_1\cdot\vec{r}_1)(\vec{\sigma}_2\cdot\vec{r}_2)}{r^2} - \vec{\sigma}_1\cdot\vec{\sigma}_2 \tag{45}$$

and H_{CT} has the form of eq. (42). The tensor force can be shown to interact only between two nucleons which are in the triplet state ($\vec{S} = 1$)[2]. The non-central Hamiltonian when the spin-orbit force is included has the form

$$H_{NC} = H_{CT}S_{12} - \gamma\,\vec{\ell}\cdot(\vec{\sigma}_1 + \vec{\sigma}_2) \tag{46}$$

where γ is an adjustable parameter. The scaler forms of H_{NC} in eq. (45) or eq. (46) insure that H_1 is rotationally invarient. Either form of H_{NC} can only interact with triplet ($\vec{S} = 1$) even or odd states and will vanish for the singlet ($\vec{S} = 0$) states.

We can now summarize and write the complete residual interaction Hamiltonian H_1 in terms of either of these two formalisms as

$$H_1 = V(r)[S_W + S_M P_x + S_B P_\sigma + S_H P_x P_\sigma] + H_{NC} \tag{47}$$

or

$$H_1 = V(r)[S_{TE}\Pi_{TE} + S_{TO}\Pi_{TO} + S_{SE}\Pi_{SE} + S_{SO}\Pi_{SO}] + H_{NC} \tag{48}$$

We have shown explicitly two phenomenlogical forms taken for H_1 in calculation of the two-body residual interaction matrix elements in eq. (31). There are other forms used for H_1, but eq. (47) and eq. (48) are two of the most common for simple shell model calculations. Once the two-body matrix elements $\langle \Phi_i | H_1 | \Phi_j \rangle$ are determined (which is not an easy task because of the complex algebra and integrations involved), the eigenvalues and eigenfunctions for a given J^π configuration can be obtained by relatively straight forward matrix diagonalization limited by the size of the space in which the calculation is done as previously discussed.

C. Weak Coupling Calculation for ^{210}Po

Consider ^{210}Po which has a ^{208}Pb core and two protons outside the core. A weak coupling model has been used to predict the energy of the 11^- state of ^{210}Po arising from the coupling of the 3^- core state with the lowest 8^+ two-proton configuration[11]. First-order energy estimates of other states in ^{210}Po arising from the weak coupling of different (^{208}Pb) core excited states with two-proton configurations can be made with the formalisms presented below. The method recouples the different angular momenta of the core and single-particle protons to deduce matrix elements representing residual interactions from experimental data rather than analytical calculations. This method may become useful for other nuclei as more detailed experimental nuclear data becomes available.

^{210}Po has a ^{208}Pb core with two interacting protons (p_1 and p_2) outside the core. It is assumed that the protons can interact weakly with the core ground state and core-excited states to produce a series of weakly coupled core-two proton states. Schematically the situation for ^{210}Po might be represented as

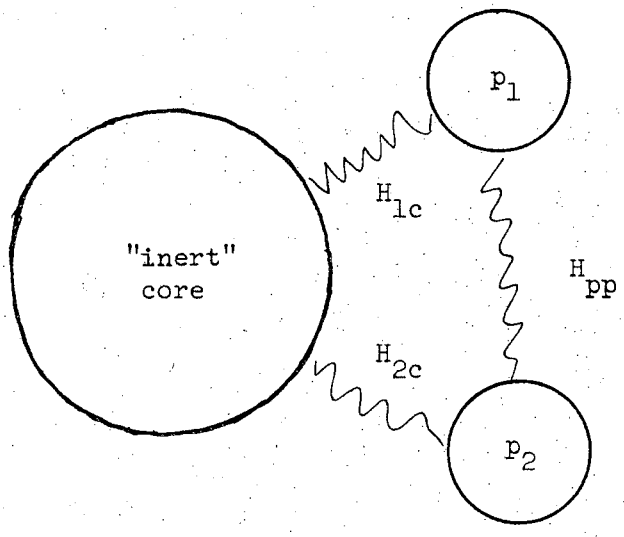

The Hamiltonians for the core and protons are represented as H_c, H_1, and H_2, respectively. The total Hamiltonian H for the ^{210}Po can be written as

$$H = H_c + (H_1 + H'_{1c}) + (H_2 + H'_{2c}) + H_{pp} \tag{49}$$

where H'_{1c} represents the proton-core interaction and H_{pp} the proton-proton interaction. We can combine H_1 and H'_{1c} and define a Hamiltonian H_{1c} which represents the proton and its interaction with the core in the absence of the proton-proton interaction. This allows us to rewrite the Hamiltonian of eq. (49) as

$$H = H_c + H_{1c} + H_{2c} + H_{pp} \tag{50}$$

The energy E_J of a state in ^{210}Po with an angular momentum $\vec{J}$ arising from the coupling of a core state with a two-proton configuration can be expressed as

$$E_J = \langle \psi | H | \psi \rangle = E_c + E_{pp} + \langle \psi | H_{1c} | \psi \rangle + \langle \psi | H_{2c} | \psi \rangle \tag{51}$$

where E_c is the energy of the ^{208}Pb core state and

$$E_{pp} = \langle \psi | H_{pp} | \psi \rangle \tag{52}$$

The energies E_c and E_{pp} can be approximated from the experimental energies as discussed later. If we assume that $H_{1c} = H_{2c}$, we may estimate the energy E_J of states in ^{210}Po from the relation

$$E_J = E_c + E_{pp} + 2 \langle \psi | H_{2c} | \psi \rangle \tag{53}$$

If there were no particle-core interaction (i.e. $H_{2c} = 0$), the zero-order energy E_J would be simply the sum of the two energies E_c and E_{pp}. However, H_{2c} is not zero and the effect of a non-zero H_{2c} will be to alter the zero-order energy estimate. Rather than calculate the matrix elements in eq. (53) with a phenomenlogical H_{2c}, residual interaction matrix elements for ^{210}Po can be approximated from a nucleus with the same core and only one single-proton outside the core in the following way.

The angular momentum of the wavefunction $|\psi\rangle$ for a state in ^{210}Po may be considered as composed of three components due to the core $\vec{J}_c$ and the two protons outside the core, $\vec{J}_1$ and $\vec{J}_2$. The wavefunction may be written explicitly as

$$|\psi\rangle = |(J_1 J_2) J_{12} J_c;\ JM\rangle \tag{54}$$

where

$$\vec{J} = (\vec{J}_1 + \vec{J}_2) + \vec{J}_c = \vec{J}_{12} + \vec{J}_c = \vec{J}_1 + (\vec{J}_2 + \vec{J}_c) = \vec{J}_1 + \vec{J}_{2c} \tag{55}$$

Use of a Racah coefficient $W(J_1 J_2 J J_c;\ J_{12} J_{2c})$ for the recoupling of three angular momenta allows the wavefunction of eq. (54) to be rewritten in terms of the product of two wavefunctions[2])

$$|(J_1 J_2) J_{12} J_c;\ JM\rangle = \sum_{J_{2c}} \sqrt{(2J_{12}+1)(2J_{2c}+1)}\, W(J_1 J_2 J J_c;\ J_{12} J_{2c})\, |J_1 (J_2 J_c) J_{2c};\ JM\rangle \tag{56}$$

where

$$|J_1(J_2J_c)J_{2c};\ JM\rangle = |J_1\rangle\,|(J_2J_c)J_{2c}\rangle \tag{57}$$

The matrix elements of H_{2c} in eq. (53) can be rewritten in terms of these wavefunctions. Using the explicit value of the wavefunction, we may write matrix elements of H_{2c} as

$$\langle\psi|H_{2c}|\psi\rangle = \sum_{J_{2c}} (2\,J_{12}+1)(2\,J_{2c}+1)$$

$$|W(J_1J_2JJ_c;\ J_{12}J_{2c})|^2\,\langle J_1(J_2J_c)J_{2c};\ JM|H_{2c}|J_1(J_2J_c)J_{2c};\ JM\rangle \tag{58}$$

To estimate the matrix elements of H_{2c} in eq. (58), consider ^{209}Bi which has a ^{208}Pb core <u>and</u> a single proton. We can write the Hamiltonian for the ^{209}Bi nucleus using the previous formalism as

$$H = H_c + H_1 + H'_{1c} = H_c + H_{1c} = H_c + H_{2c} \tag{59}$$

The energy $E_{J_{2c}}$ of excited states of ^{209}Bi will be given by

$$E_{J_{2c}} = \langle\psi(^{209}\text{Bi})|H|\psi(^{209}\text{Bi})\rangle = E_c + \langle\psi|H_{2c}|\psi\rangle \tag{60}$$

where the odd proton is coupled to various core states (including the ground state) to produce a series of states with angular momentum $\vec{J}_{2c}$. For example, the $h_{9/2}$ proton coupling to the 3^- first-excited core state

will produce a series of even parity states with angular momentum J_{2c}

$$\vec{J}^{+}_{2c} = \{ \frac{3}{2} \frac{5}{2} \frac{7}{2} \frac{9}{2} \frac{11}{2} \frac{13}{2} \frac{15}{2} \}^{+} \tag{61}$$

The wavefunction of ^{209}Bi can be written explicitly as

$$|\psi(^{209}\text{Bi})\rangle = |(J_2 J_c)J_{2c}\rangle \tag{62}$$

If the experimental data on the levels of ^{209}Bi and ^{208}Pb permit identification of the energies $E_{J_{2c}}$ and E_c, matrix elements of H_{2c} may be approximated from eq. (60) and experimental data as

$$\langle (J_2 J_c)J_{2c} | H_{2c} | (J_2 J_c)J_{2c} \rangle = E_{J_{2c}} - E_c \tag{63}$$

Hence we may now evaluate eq. (58) for ^{210}Po using experimental data from the levels of ^{209}Bi to estimate the proton-core residual interactions. Rewriting eq. (53) in terms of the above discussion and experimental energies, we produce a relation to estimate the energy of states in ^{210}Po with an angular momentum $\vec{J}$

$$E_J = E_c + E_{pp} + 2 \sum_{J_{2c}} (2 J_{12} + 1)(2 J_{2c} + 1) |W(J_1 J_2 J J_c ; J_{12} J_{2c})|^2 (E_{J_{2c}} - E_c) \tag{64}$$

Thus if experimental energies are known for nuclei of interest, eq. (64) may be simply evaluated to provide first-order weak coupling estimates of the energy of ^{210}Po configurations of spin $\vec{J} = \vec{J}_c + \vec{J}_{12}$.

As an example, consider the 11^- state of ^{210}Po formed from the coupling of the $\pi(h^2_{9/2})_{8^+}$ two-proton configuration with the 3^- core state. Equation (55) determines that the only possible proton-core couplings of $(\frac{9}{2}^- \; 3^-)J^+_{2c}$ are $13/2^+$ and $15/2^+$. The experimental ^{209}Bi energies for these J^+_{2c} configurations are[9])

$$E_{13/2^+} = 2601 \text{ keV} \quad \text{and} \quad E_{15/2^+} = 2741 \text{ keV} \tag{65}$$

where Racah coefficients are

$$W(\tfrac{9}{2}\,\tfrac{9}{2}\;11\;3;\;8\;\tfrac{13}{2}) = -0.0290 \quad \text{and} \quad W(\tfrac{9}{2}\,\tfrac{9}{2}\;11\;3;\;8\;\tfrac{15}{2}) = 0.0542 \tag{66}$$

The 8^+ level at 1556 keV in ^{210}Po and the 3^- level at 2614 keV in ^{208}Pb provide the values for E_{pp} and E_c. Thus from eq. (64) we predict the energy of the 11^- state as

$$E_{11^-} = 2614 + 1556 + 2\{17\cdot14(-.029)^2(2601 - 2614) + 17\cdot16(.0542)^2(2741 - 2614)\}$$

$$= 4368 \text{ keV} \; . \tag{67}$$

The experimental value[11]) is 4324 keV and the agreement is exceptional in this one case. The possible extension of this technique to nuclei further from the double closed shell, through use of additional recouplings (9J symbol, etc.), can be tested as more detailed experimental information become available. In section IVH, we apply this technique to our experimental results for ^{210}Po.

D. Weak Coupling Calculation for ^{209}Po

The weak coupling model has been used successfully in the description of some states in the bismuth isotopes. We shall extend the weak coupling model to predict the level structure of ^{209}Po. We assume that ^{209}Po can be described as an inert ^{208}Pb core with two-protons and one neutron-hole. Residual interactions between the neutron-hole and the protons and interactions between two-protons will be considered explicitly. We assume ^{208}Bi to be composed of a ^{208}Pb core plus an interacting proton and neutron-hole. The level structure of ^{208}Bi and ^{209}Po should include the effects of the particle-hole interaction H_{ph} and we will use data on the levels of ^{208}Bi to approximate this interaction in ^{209}Po. We shall regard ^{210}Po as represented by a ^{208}Pb core plus two protons. The level structure of ^{210}Po will include the effects of the proton-proton interaction H_{pp} and we will use data on the levels of ^{210}Po to approximate this interaction in ^{209}Po. Core excitations will be ignored.

Schematically the situation for ^{209}Po might be represented as:

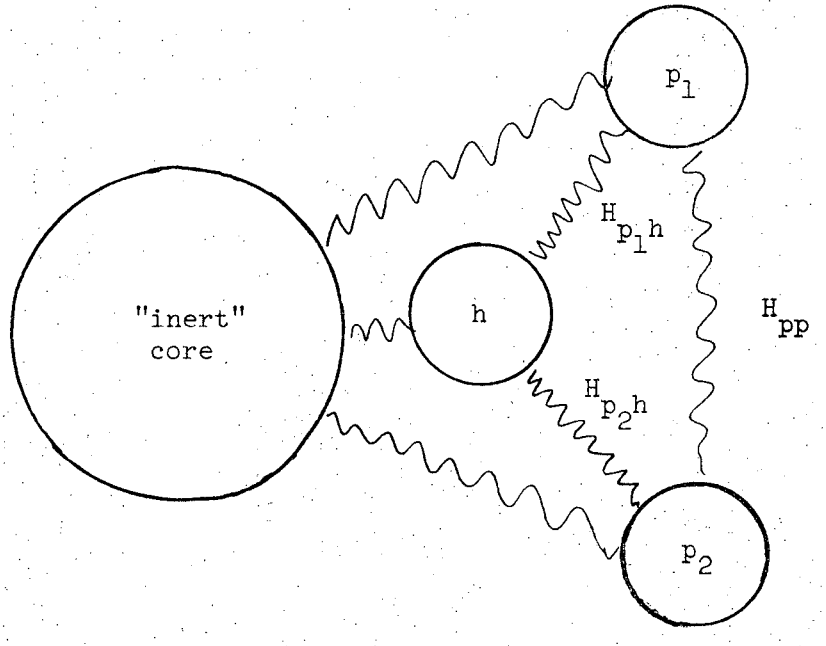

The Hamiltonians for the core, particles (protons) and hole (neutron) are defined as H_c, H_p, and H_h respectively. We can write the total Hamiltonian H for ^{209}Po as

$$H(^{209}\text{Po}) = H_c + H_{p_1} + H_{p_2} + H_h + H_{pp} + H_{p_1h} + H_{p_2h} \tag{68}$$

Matrix elements of the above Hamiltonian with the wavefunction describing ^{209}Po give the total energy or mass of the system. For ^{209}Po, the two protons are assigned angular momenta of $\vec{j}_1$ and $\vec{j}_2$ and the angular momentum of the neutron-hole is assigned $\vec{j}_h$. These three angular momenta can be vector coupled in different orders to produce the same final angular momentum $\vec{I}$ for a given state. The wavefunction for ^{209}Po may be written

$$\psi(^{209}\text{Po}) = |(j_1 j_2)J,\ j_h;\ IM\rangle \tag{69}$$

where

$$\vec{I} = \vec{J} + \vec{j}_h$$

This order of coupling the proton angular momenta ($\vec{j}_1$ and $\vec{j}_2$) first to some intermediate angular momentum $\vec{J}$, and then the coupling of $\vec{J}$ with the hole ($\vec{j}_h$) to give $\vec{I}$ can be rewritten in a different coupling order. First the proton and hole angular momenta ($\vec{j}_2$ and $\vec{j}_h$) can be coupled to $\vec{J}$ and then $\vec{J}$ to the remaining proton angular momentum ($\vec{j}_1$) to $\vec{I}$ with use of a Racah coefficient as[2]).

$$|(j_1 j_2)J,\ j_h;\ IM\rangle = \sum_{J'} \sqrt{(2J+1)(2J'+1)}\ W(j_1 j_2 I j_h;\ JJ')\,|j_1,\ (j_2 j_h)J';\ IM\rangle \tag{70}$$

where

$$\vec{I} = \vec{J}' + \vec{j}_1 = \vec{J} + \vec{j}_h \tag{71}$$

We define the following Hamiltonians

$$\begin{aligned} H(^{210}\mathrm{Po}) &= H_c + H_{p_1} + H_{p_2} + H_{pp} \\ H(^{207}\mathrm{Pb}) &= H_c + H_h \\ H(^{208}\mathrm{Pb}) &= H_c \\ H(^{209}\mathrm{Bi}) &= H_c + H_p \\ H(^{208}\mathrm{Bi}) &= H_c + H_h + H_p + H_{ph} \end{aligned} \tag{72}$$

Matrix elements of these Hamiltonians are approximated by the experimental mass $M^J(^A\mathrm{X})$ of the element X (mass number A) and are defined as:

$$\langle \psi(^{210}\mathrm{Po})|H(^{210}\mathrm{Po})|\psi(^{210}\mathrm{Po})\rangle = M^J(^{210}\mathrm{Po})$$

$$\langle \psi(^{207}\mathrm{Pb})|H(^{207}\mathrm{Pb})|\psi(^{207}\mathrm{Pb})\rangle = M^J(^{207}\mathrm{Pb})$$

$$\langle \psi(^{208}\mathrm{Pb})|H(^{208}\mathrm{Pb})|\psi(^{208}\mathrm{Pb})\rangle = M^J(^{208}\mathrm{Pb})$$

$$\langle \psi(^{209}\mathrm{Bi}) | H(^{209}\mathrm{Bi}) | \psi(^{209}\mathrm{Bi}) \rangle = M^{J}(^{209}\mathrm{Bi})$$

$$\langle \psi(^{208}\mathrm{Bi}) | H(^{208}\mathrm{Bi}) | \psi(^{208}\mathrm{Bi}) \rangle = M^{J}(^{208}\mathrm{Bi}) \qquad (73)$$

For example, $M^{J}(^{210}\mathrm{Po})$ represents the total mass of the nucleus in the state of angular momentum $\vec{J}$. The energy of the first excited state would be the difference between the mass of the first excited state and the ground-state mass.

To estimate $^{209}\mathrm{Po}$ level energies (which include the ground-state mass), we must compute the following matrix element for the Hamiltonian of eq. (68).

$$M^{J}(^{209}\mathrm{Po}) = \langle \psi(^{209}\mathrm{Po}) | H(^{209}\mathrm{Po}) | \psi(^{209}\mathrm{Po}) \rangle \qquad (74)$$

To simplify the problem, we assume first that there are no particle-hole and particle-particle interactions so that eq. (68) can be reduced to several terms which may be evaluated from the experimental masses of $^{207}\mathrm{Pb}$, $^{209}\mathrm{Bi}$, and $^{208}\mathrm{Pb}$. The matrix elements of the Hamiltonian of the proton may be evaluated as

$$\langle \psi | H_p | \psi \rangle = \langle \psi | H_c + H_p - H_c | \psi \rangle = M^{j_p}(^{209}\mathrm{Bi}) - M^{0^+}(^{208}\mathrm{Pb}) \qquad (75)$$

where H_c is for the $^{208}\mathrm{Pb}$ core. We have used the fact that for no interactions (as assumed above) and no particle-core interactions the wavefunction (the properly antisymmetrized form is assumed) of eq. (66) can be written as

$$|\psi\rangle = |\psi\rangle_{core}|\psi\rangle_{p}|\psi\rangle_{p}|\psi\rangle_{h} \tag{76}$$

Similarly for the matrix element of the neutron-hole, we find

$$\langle\psi|H_h|\psi\rangle = M^{j_h}(^{207}Pb) - M^{0^+}(^{208}Pb) \tag{77}$$

Using the results of eq. (75), eq. (77) and the assumed wavefunction of eq. (76), matrix elements of $H(^{209}Po)$ (eq. (74)) can be evaluated in terms of masses as

$$M^I(^{209}Po) = \langle\psi|H_c + H_{p_1} + H_{p_2} + H_h|\psi\rangle$$

$$= M^{j_{p_1}}(^{209}Bi) + M^{j_{p_2}}(^{209}Bi) + M^{j_h}(^{207}Pb) - 2\,M^{0^+}(^{208}Pb) \tag{78}$$

(The form of eq. (78) estimates the mass of ^{209}Po assuming that $H_{ph} = H_{pp} = 0$.)

Now assume that H_{pp} is not zero but that H_{ph} is zero. This changes the wavefunction of eq. (76) to the form

$$|\psi\rangle = |(j_1 j_2)J\rangle_{pp}|\psi\rangle_{core}|\psi\rangle_{h} \equiv |\psi(^{210}Po)\rangle|\psi\rangle_{core}|\psi\rangle_{h} \quad . \tag{79}$$

We can now evaluate the mass of ^{209}Po (assuming that $H_{ph} = 0$ but $H_{pp} \neq 0$) from the experimental masses of ^{210}Po as

$$M^{I}(^{209}\mathrm{Po}) = \langle \psi | H_c + H_{p_1} + H_{p_2} + H_{pp} + H_h | \psi \rangle$$

$$= M^{J}(^{210}\mathrm{Po}) + M^{j_h}(^{207}\mathrm{Pb}) - M^{0^+}(^{208}\mathrm{Pb}) \quad . \qquad (80)$$

Equation (80) is a valid estimate of the predicted masses of ^{209}Po assuming that H_{ph} is zero and H_{pp} is represented by ^{210}Po experimental masses or energies and with the coupling $(j_1 j_2)J$.

Finally we allow H_{ph} to be non-zero to arrive at our estimate with "all" residual interactions. Our wavefunction of eq. (79) changes to the form given in eq. (69) or eq. (70). We can evaluate the matrix elements of H_{ph} using the wavefunctions of eq. (70) realizing that

$$|j_1, (j_2 j_h)J'; IM\rangle \equiv |j_1\rangle_{p_1} |\psi^{J'}(^{208}\mathrm{Bi})\rangle_{p_2 h} |\psi\rangle_{\mathrm{core}} \quad . \qquad (81)$$

Using the Hamiltonian $H(^{208}\mathrm{Bi})$ of eq. (72), we define a quantity ΔM^{J}_{ph} for the particle-hole interaction by evaluating $M^{J}(^{208}\mathrm{Bi})$ as

$$M^{J}(^{208}\mathrm{Bi}) = \langle \psi(^{208}\mathrm{Bi}) | H_c + H_p + H_h + H_{ph} | \psi(^{208}\mathrm{Bi}) \rangle$$

$$= M^{0^+}(^{208}\mathrm{Pb}) + M^{j_p}(^{209}\mathrm{Bi}) - M^{0^+}(^{208}\mathrm{Pb}) + M^{j_h}(^{207}\mathrm{Pb}) - M^{0^+}(^{208}\mathrm{Pb})$$

$$+ \langle \psi | H_{ph} | \psi \rangle \qquad (82)$$

Rewriting eq. (82) the H_{ph} particle-hole matrix elements can be evaluated in terms of experimental masses defined as

$$\Delta M^J_{ph} \equiv \langle \psi(^{208}\mathrm{Bi}) | H_{ph} | \psi(^{208}\mathrm{Bi}) \rangle = M^J(^{208}\mathrm{Bi}) + M^{0^+}(^{208}\mathrm{Pb}) - M^{j_p}(^{209}\mathrm{Bi}) - M^{j_h}(^{207}\mathrm{Pb}$$

(83)

To summarize we rewrite the final expression for the mass of ^{209}Po in terms of the above equations.

$$M^I(^{209}\mathrm{Po}) \equiv \langle \psi | H(^{209}\mathrm{Po}) | \psi \rangle = \langle \psi | H_c + H_{p_1} + H_{p_2} + H_h + H_{p_1 h} + H_{p_2 h} + H_{pp} | \psi \rangle$$

(84)

Using eq. (80) we can rewrite eq. (84) in terms of the particle-hole interaction matrix elements

$$M^I(^{209}\mathrm{Po}) = M^J(^{210}\mathrm{Po}) + M^{j_h}(^{207}\mathrm{Pb}) - M^{0^+}(^{208}\mathrm{Pb}) + \langle \psi | H_{p_1 h} + H_{p_2 h} | \psi \rangle \quad .$$

(85)

Using eq. (70) for the definition of $|\psi\rangle$ and eq. (83) for ΔM^J_{ph}, we can rewrite eq. (85) explicitly as

$$\begin{aligned} M^I(^{209}\mathrm{Po}) = {} & M^J(^{210}\mathrm{Po}) + M^{j_h}(^{207}\mathrm{Pb}) - M^{0^+}(^{208}\mathrm{Pb}) \\ & + \sum_{J'} (2J+1)(2J'+1) \left| W(j_2 j_1 I j_h ; JJ') \right|^2 \Delta M^{J'}_{j_{p_1} j_h} \\ & + \sum_{J''} (2J+1)(2J''+1) \left| W(j_1 j_2 I j_h ; JJ'') \right|^2 \Delta M^{J''}_{j_{p_2} j_h} \end{aligned} \qquad (86)$$

where

$$\vec{I} = \vec{J} + \vec{j}_h, \ \vec{J}' = \vec{j}_p + \vec{j}_h, \text{ and } \vec{J} = \vec{j}_{p_1} + \vec{j}_{p_2} \quad . \tag{87}$$

Explicitly the meaning of the coupling order of the angular momenta in $\Delta M^{J'}_{j_p j_h}$ is

$$\Delta M^{J'}_{j_p j_h} = M^{(j_p j_h)J'}(^{208}\text{Bi}) + M^{0^+}(^{208}\text{Pb}) - M^{j_p}(^{209}\text{Bi}) - M^{j_h}(^{207}\text{Pb}) \quad . \tag{88}$$

Thus eq. (86) and eq. (88) can be used to estimate the level energies of ^{209}Po based on experimental masses of adjacent nuclei for which experimental information is available. This method should apply if our assumption is valid that the proton-proton interaction of ^{210}Po and the neutron hole-proton interaction of ^{208}Bi are the same as for ^{209}Po. We apply this method in section VH to our experimental results.

III. DETECTION SYSTEMS

The general characteristics of the experimental equipment used in our studies are described. More details are given in Appendices C, D, E, and F.

A. Gamma-Ray Singles Measurements

The detectors used during the course of this study were of several different sizes and characteristics. A planar (7.5-cm^2 × 1.3 cm active volume) Ge(Li) detector with a resolution of 1.4 keV (FWHM) at 122 keV was used for study of gamma-rays in the energy range of 60-500 keV. A true coaxial Ge(Li) detector of 35-cm^3 (active volume) with a resolution of 1.7 keV (FWHM) at 122 keV and 2.4 keV (FWHM) at 1332 keV was used for study of the entire energy region of 60-3000 keV. For investigation of the low energy region, a planar Si(Li) detector with dimensions of 0.785-cm^2 × 0.5 mm was used. This detector exhibited a resolution of 0.8 keV (FWHM) at 60 keV. All of these detectors were fabricated at this laboratory. For some measurements, including the gamma-gamma coincidence measurements, a true coaxial 40-cm^3 (active volume) Ge(Li) detector obtained commerically was also used. This detector has a resolution of 1.8 keV (FWHM) at 122 keV and 2.6 keV (FWHM) at 1332 keV.

The detectors were used with standard high-count rate electronics[13,14]) coupled to a successive (binary) approximation 4096-channel analogue-to-digital converter (ADC) designed at this laboratory[15]). A PDP-7 computer system[16,17,18]) was used as an "on-line" analyzer for all spectral measurements. The details of the electronics and the data acquisition

system are discussed in Appendix C as well as in the above references. All data collected were stored on magnetic tape for later analysis by computer. Input rates into the detectors were normally kept at 4000-8000 counts/sec to maintain maximum resolution.

Energy calibration of the γ-ray spectrometers were made by using a series of standard sources with reference to the energy data compiled[19]) in Appendix D. Relative photopeak efficiencies of the Ge(Li) detectors were determined with an estimated error of ±4% over the energy range 100-2700 keV using the isotopes and methods[20]) described in Appendix E. Relative efficiency calibration curves for two detectors are also shown in Appendix E.

B. Gamma-Gamma Coincidence Measurements

Three parameters (E1, E2, Δt) (see section IVD2) gamma-gamma coincidence measurements were carried out using the two coaxial Ge(Li) detectors described above coupled to the PDP-7 multiparameter data acquisition system described in refs. [16,17,18]). The two detectors were at a 90° geometry with a graded shield of lead, cadmium, and copper between them to minimize detector-to-detector scattering. Leading edge timing using two 100 MHz fast discriminators and a standard start-stop time to amplitude converter (TAC) was employed to extract timing information. A logrithmic TAC compensation unit described by Jaklevic et al.[21]) was used to correct the timing distribution for the variation in pulse rise-times with energy. The width (FWHM) of the prompt time distribution observed experimentally was approximately 40 nsec FWHM. Input rates into the detectors were maintained at 10000-17000 counts/sec. The particular coincidence electronics used is discussed in detail in Appendix C.

C. Internal Conversion Electron Measurements

The 5 mm-Si(Li) electron spectrometer system and methods used for measuring the relative internal conversion electrons in the decay of astatine are described in detail in Appendix F. This system gave a resolution of 2.2 keV (FWHM) for the K-conversion electron line of the 1063-keV transition in the decay of ^{207}Bi and permitted observation of well-defined electron lines at energies up to about 1600 keV. The relative efficiency calibration of this spectrometer was measured to ±8% over the range of 100-1200 keV. The energy calibration of conversion electron spectra of astatine sources was made by using the strongest K-conversion lines as internal standards based on our measured gamma-ray energies and the electron binding energies of polonium[22]). The preparation of electron sources is described in section IVC. The input count-rates into the detector were maintained at 2000-7000 counts/sec by a combination of source strengths and source-to-detector distances.

IV. THE ELECTRON-CAPTURE DECAY OF ^{210}At TO LEVELS IN ^{210}Po

A. Introduction

The electron-capture decay of ^{210}At (8.3h) to ^{210}Po provides a means of populating levels of ^{210}Po. A tentative ground state spin and parity assignment of 5^+ for ^{210}At has been made in a preliminary report of the ^{209}Bi(α,3n)^{210}At reaction[23]. Based on known experimental single-particle states in the lead region, the odd-odd nucleus ^{210}At is expected to have a ground state configurations of $(\pi(h_{9/2}^3\, s_{1/2}^2)\nu(g^0\, p_{1/2}^{-1}))_{5^+,4^+}$ and the ground state configuration of the even-even nucleus ^{210}Po should be $(\pi(h_{9/2}^2\, s_{1/2}^2)\nu(g_{9/2}^0\, s_{1/2}^2))_{0^+}$. States in ^{210}Po with spins 4, 5, and 6 should be populated directly in the electron-capture decay and states of spin 0-3 and 7-8 can be populated through the gamma decay of higher-lying levels. Direct decay of ^{210}At to the ^{210}Po ground state or any excited state with a closed ^{208}Pb core would require the transition $\pi(h_{9/2}) \xrightarrow{EC} \nu(p_{1/2})$. This transition requires a change of four units in the orbital angular momentum ($\Delta\ell = 4$) which is highly hindered. Hence the population of any pure two proton shell model states of spin 4, 5, and 6 requires a similar transition since the N = 126 shell must be filled as a result of the electron-capture decay to such states. One might expect to observe relatively high values of log ft to the pure two proton states of spins 4, 5, and 6.

However, previous studies[24,25,26,27] of the electron-capture decay observed low values of log ft for the transitions to the more energetic (> 2.9 MeV) odd parity levels which were inconsistent with the two proton model. It was pointed out[25,27] that this might be indicative

of admixture from neutron excitation of the ^{208}Pb core. A number of experimental studies[9]) have now established the odd parity characteristics of the low-lying levels in ^{208}Pb ($\geq$ 3 MeV) which arise from excitations of neutrons and protons out of this core. The mixing of such core states with those arising from the two proton configurations $(h_{9/2}\ i_{13/2})_{J^-}$ and $(f_{7/2}\ i_{13/2})_{J^-}$ of ^{210}Po should occur with the result that the electron-capture decay could proceed to the neutron and proton particle-hole (^{208}Pb core) components of such states via relatively unhindered transitions.

Previous experimental data[24,25,26,27]) on the electron-capture decay was limited in several aspects and was insufficient to identify levels involving particle-hole configurations. The lack of coincidence measurements placed some uncertainty on the inclusion of several levels in the decay scheme which involved reasonably intense gamma-rays. Of even greater importance no evidence for levels of spins other than 4, 5, or 6 was obtained.

For these reasons a detailed reinvestigation of the electron-capture decay of ^{210}At has been performed. In addition to a number of new, very weak transitions, we have measured the multipolarities of 36 of the stronger transitions. The results of multiparameter γ-γ coincidence measurements have been used with the recent data from direct reaction studies[28,29,30]) to define twenty-three levels in ^{210}Po. The level scheme is compared with shell model calculations[25,31,32,33]) using various residual interactions. Evidence is presented for a 3^- collective level at 2400 keV, and more detailed information on the higher-lying

odd-parity states has been obtained. The latter are discussed in terms of the proton and neutron particle-hole components giving rise to unhindered β-decay transitions. The transition probabilities in the gamma decay of the lower-lying even parity levels are compared with those obtained from recent theoretical calculations.

B. Previous Studies

The first study of the decay of ^{210}At by Hoff[34]) reported conversion-electron spectra, gamma-ray spectra, and alpha spectra. (^{210}At has a low intensity alpha branching decay of 0.18±0.02%[34,35]).) Mihelich, Schardt, and Segre'[24]) published the first detailed study of conversion electrons and gamma-rays emitted in the ^{210}At decay. Approximately 99% of the electron-capture decay was found to populate two odd parity levels at about 3 MeV. In 1958 Hoff and Hollander[25]) reported on the ^{210}At decay and there were some discrepancies with the earlier work of Mihelich et al.[24]). Of importance to this study was an 83.5 keV transition observed in the conversion electron spectra[24,25,36]). This transition, as well as many other weaker transitions observed in the conversion electron spectra, was not included in the decay scheme reported by either group. In 1963, Schima, Funk, and Mihelich[26]) revealed the possibility of a higher-lying level (3680 keV) which was populated by a relatively unhindered electron-capture transition. The first detailed study using solid-state detectors for conversion electrons and gamma-rays was reported in 1968 by Prussin and Hollander[27]). Because of their improved resolution they were able to observe many additional weak gamma-ray transitions over previous studies and a more complex decay scheme was proposed. A summary of the work finished before this study began is shown in the level scheme[24]) of fig. 5. Prussin and Hollander were able to place many of the previously observed weak transition into their scheme by associating the unassigned conversion electron lines to newly observed gamma-rays.

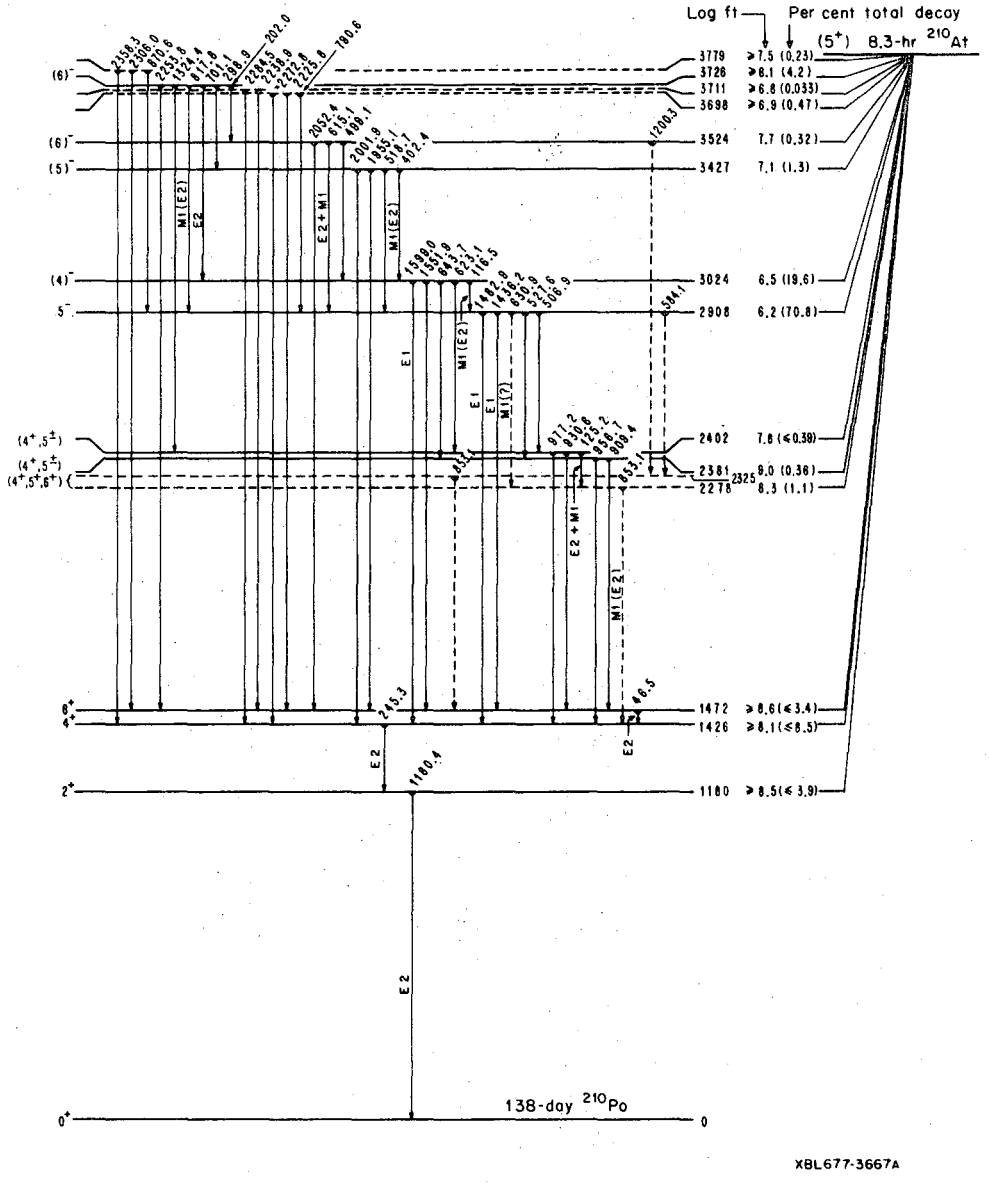

Fig. 5. Decay scheme of ^{210}At summarizing the previous studies[24,25,26,27]. This is the level scheme proposed by Prussin and Hollander[27].

Several important questions remained to be answered regarding the possible ^{210}Po core states and missing states of spins 0-3 and 7-8 which should be populated in the gamma decay of higher-lying levels. Also the spin assignments to the levels needed clarification. Because of more efficient higher resolution Si(Li) and Ge(Li) detectors for high energy conversion electrons and gamma rays, a reinvestigation was made in an attempt to answer these questions as well as to search for other levels arising from the two proton configurations $(h_{9/2}\ f_{7/2})$ and $(h_{9/2}\ i_{13/2})$. Also to establish the ^{209}At decay scheme, a reinvestigation of the ^{210}At decay was necessary since mixed sources of ^{210}At and ^{209}At were used (see section VC).

During the course of this work the results from ^{209}Bi$(\alpha,t)^{210}$Po and ^{209}Bi$(^3$He$,d)^{210}$Po reaction studies on the levels of ^{210}Po were reported[28,29]. These studies gave further information on the levels involving the proton configurations $\pi(h_{9/2}\ \ell_j)_{J^\pi}$ and is discussed in detail in section E. Also the ^{208}Pb$(\alpha,2n)^{210}$Po reaction was reinvestigated by Bergström *et al.*[30,37]. Other higher spin states of ^{210}Po were established[30] through these in-beam studies and are discussed later with reference to our proposed decay scheme in section E.

C. Source Preparation

The astatine samples used in this study were produced by the $^{209}Bi(\alpha,3n)^{210}At$ reaction at bombarding energies of 36.5-39 MeV in the Berkeley 88-inch cyclotron. (See section VC for the cross-section of this reaction.)

The bismuth metal targets were prepared by vacuum evaporation of analytical grade bismuth metal onto 10-mil aluminum backing foils. Target thicknesses varied from 17-85 mg/cm^2 and the targets were mounted in standard aluminum water-cooled target holders with one-inch beam colliminators. The backing plates served as the seal and "o-ring" contact for the water cooling of the targets during bombardment. To minimize target overheating and possible volatilization of astatine, beam currents were maintained at 5-12 μamps/hr. No loss of astatine was observed with these beam currents. (However, one run at a beam intensity of 15 μamps/hr produced a visible burn spot on the target.)

For separation of the astatine[36,38,39]) from the target, the bismuth was scraped from the aluminum backing with a razor blade and placed into a quartz crucible for heating, volatization and collection of astatine on a cooled aluminum collection foil. Platinum foils were initially used but were abandoned when found to have a higher retention (than necessary) for the astatine. A photograph (thru a 6-inch lead glass window) and a schematic diagram of the collection apparatus are shown in figs. 6 and 7 respectively. The cold-finger was maintained at dry-ice temperature with Freon-11 circulated by a mechanical pump. (In later experiments, iced-water was used satisfactorily as the coolant.)

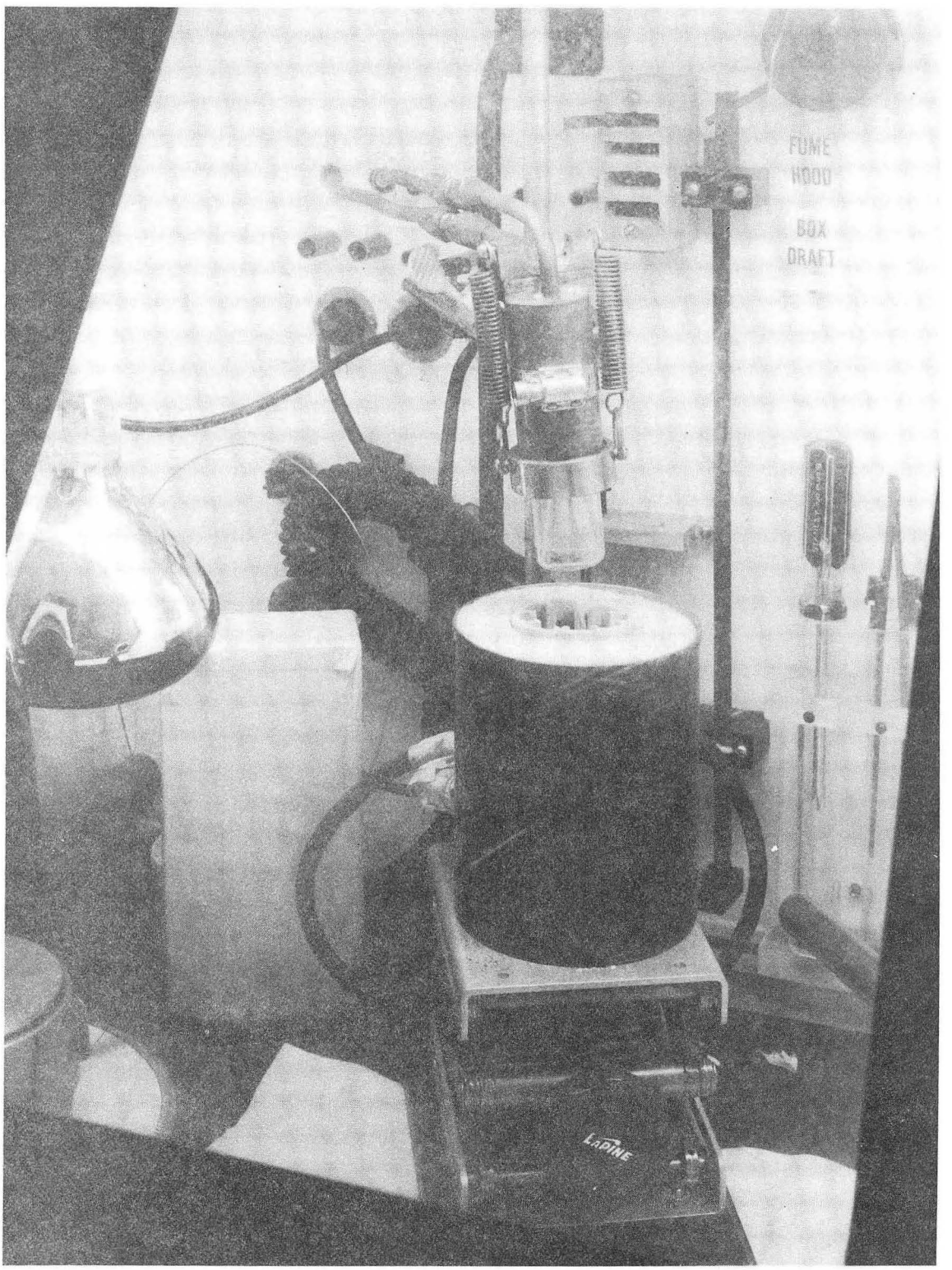

XBB 719-4243

Fig. 6. The astatine collection apparatus as photographed through a six-inch lead glass window.

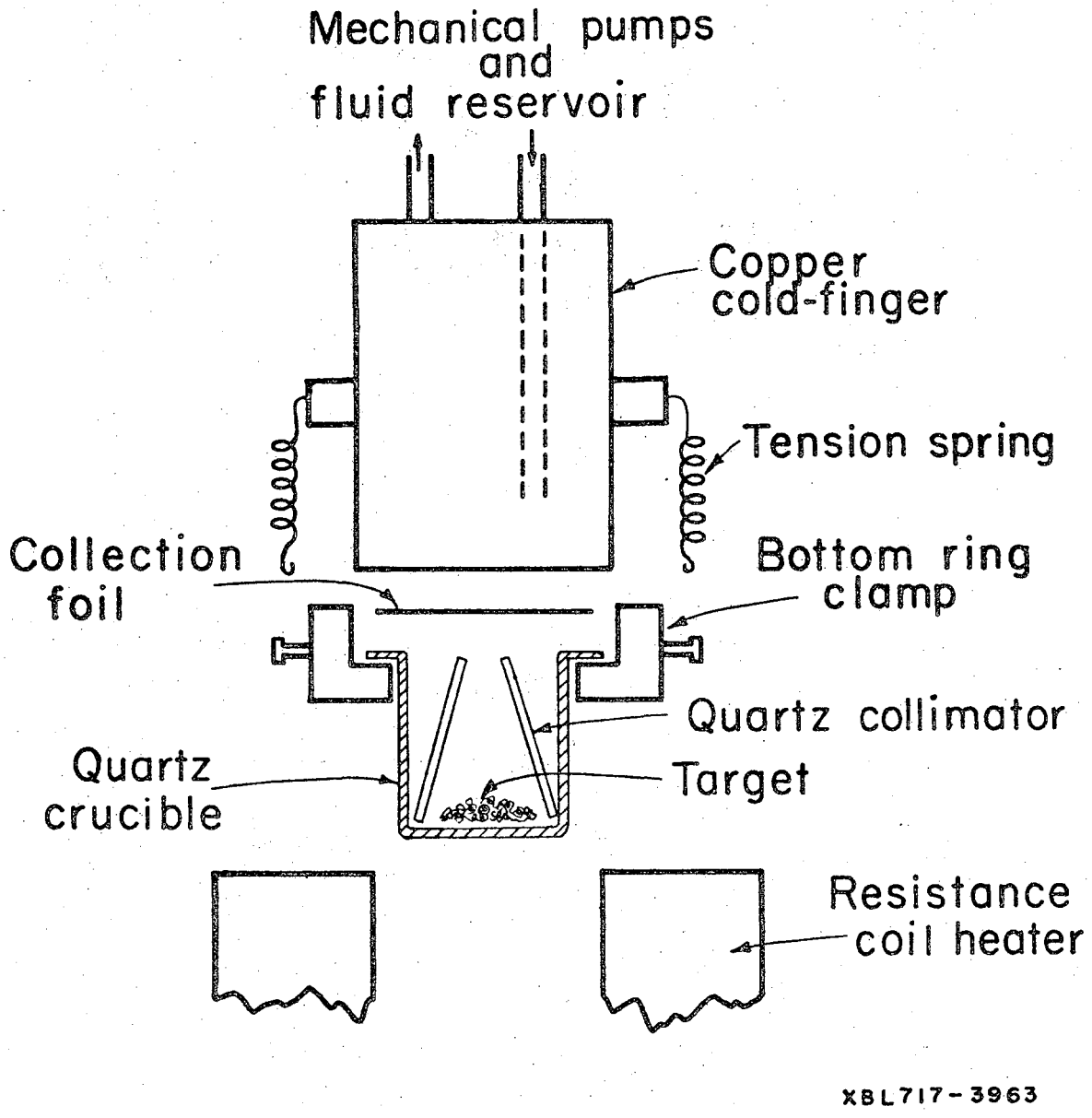

Fig. 7. Schematic diagram of the astatine collection apparatus.

The crucible and foil were held in contact by means of two tension springs. The crucible was heated with a resistance furnace which was raised and lowered by means of a lab jack. Heating of fresh targets at 320°C for approximately five minutes generally allowed about 1-20 mcuries of activity to be collected.

Sources for gamma-ray analysis were prepared by removing the activity from the collection foil with a solution 3N in HNO_3 or distilled water. For some runs a KI carrier was added. A portion of the activity was then placed into a double sealed glass or plastic vial for counting. Electron sources were made by evaporation of the acid solution or a simple aqueous solution of activity onto aluminum-coated mylar ($\sim$ 1 mg/cm^2) or gold-coated mylar ($\sim$ 0.25 mg/cm^2) stretched on ring mounts designed for the Si(Li) spectrometer. Electron sources were then covered with an aluminum coating by flash evaporation of aluminum to prevent possible volatilization of the activity in the electron detector vacuum system. The estimated thickness of the aluminum layer was $\sim$ 12 μg/cm^2.

D. Experimental Results

1. Gamma-Ray Singles Spectra

Sources of ^{210}At in less than 0.5 cc of solution were placed in small plastic bottles or cones to minimize gamma-ray attenuation while still maintaining containment of the astatine for counting. Data were generally collected over a 24 hour period in order to obtain sufficient statistics. A gamma-ray singles spectrum of ^{210}At in the energy range of 100-2500 keV taken with the 40-cm^3 (active volume) true coaxial detector is shown in fig. 8. (No higher energy gamma-ray radiations were observed.) Figure 9 shows the gamma-ray spectrum in the energy range of ~ 16-130 keV taken on the 5 mm Si(Li) detector. The presence of the highly converted 46.6 keV E2 gamma-ray (α_{total} = 272) is barely observable above the compton background. Except for the x-rays from electron-capture and internal conversion, no other major gamma-rays were observable below 100 keV.

Gamma-ray energies and intensities were obtained from photopeak area analysis of all spectra with the computer code SAMPO[40,41]. Photopeak shapes were approximated with gaussians joined to exponential tails by the code. Energy errors included the fitting errors and the error in the calibration energies. Relative intensity errors included errors from peak fitting and error in the relative photopeak efficiency determinations. Table 3 shows the results for gamma-ray energies and intensities. Below 500 keV where transition multipolarities were known or measured, the total transition intensity is also shown. The theoretical conversion coefficients of Hager and Seltzer[42,43] were used to derive these results.

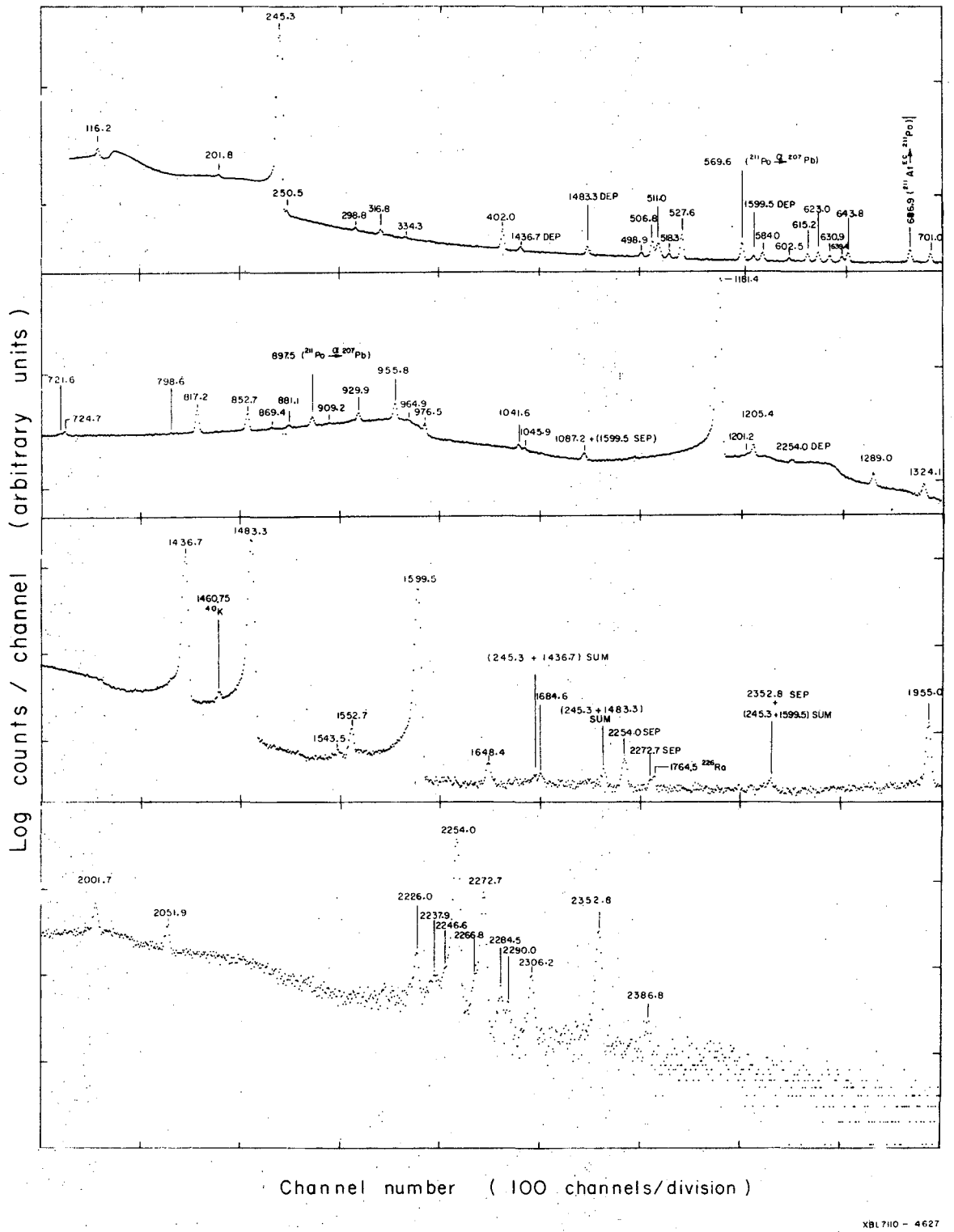

Fig. 8. Spectrum of ^{210}At gamma-rays in the energy range of 100-2500 keV taken with a coaxial Ge(Li) spectrometer.

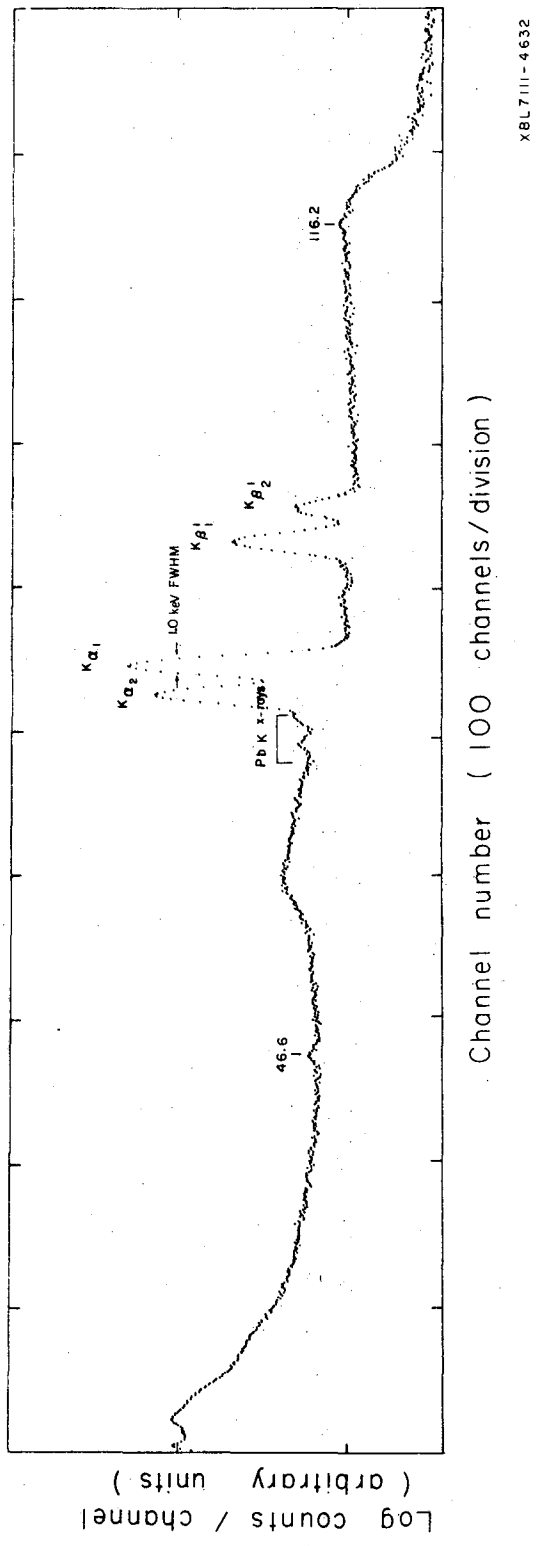

Fig. 9. Spectrum of ^{210}At gamma-rays in the energy range of 16-130 keV taken with a Si(Li) spectrometer.

Table 3. Gamma-rays observed from decay of ^{210}At.

Gamma-Ray Energy (keV)	Absolute[a] Gamma-Ray Intensity (percent of ^{210}At decays)	Absolute Transition Intensities[b] (percent of ^{210}At decays)
46.6 (2)		(34.5 (15))[i]
77.2[c]		(≈ .15)[h]
83.45[c]		(≳ 0.60 (3))[i]
92.1[c]		(≈ 0.01)[h]
112.2[c]		(≈ .27)[h]
116.2 (1)	.65 (6)	5.6 (5)
201.8 (2)	.15 (2)	.39 (4)
245.3 (1)	80.0 (40)	99.0 (50)
250.5 (2)	.21 (4)	.39 (6)
298.8 (2)	.11 (2)	.17 (2)
316.8 (2)	.17 (1)	.24 (7)
334.3 (2)[e]	.05 (1)	.07 (2)
402.0 (2)	.78 (2)	.97 (4)
498.9 (2)	.15 (1)	.17 (1)
506.8 (2)	.69 (2)	
518.3 (2)	.15 (1)	
527.6 (1)	1.15 (4)	
584.0 (2)	.34 (2)	
602.5 (2)	.12 (2)	
615.3 (2)	.36 (2)	

(continued)

Table 3. (continued)

Gamma-Ray Energy (keV)	Absolute[a] Gamma-Ray Intensity (percent of ^{210}At decays)
623.0 (2)	.43 (2)
630.9 (2)	.31 (2)
639.4 (2)	.26 (2)
643.8 (2)	.46 (2)
701.0 (2)	.47 (2)
721.6 (3)	.10 (4)
724.7 (2)	.21 (3)
798.6 (3)	.06 (2)
817.2 (2)	1.72 (5)
852.7 (2)	1.39 (5)
869.4 (2)	.13 (2)
881.1 (2)	.22 (2)
909.2 (3)	.09 (3)
929.9 (2)	.76 (3)
955.8 (1)	1.81 (6)
(960.1)[f]	(< 0.04)[f]
964.9 (2)	.16 (4)
976.5 (2)	.81 (4)
1041.6 (2)	.30 (4)
1045.9 (3)	.16 (3)

(continued)

Table 3. (continued)

Gamma-Ray Energy (keV)	Absolute[a] Gamma-Ray Intensity (percent of ^{210}At decays)
1087.2 (3)	.22 (3)[d]
1181.4 (1)	100.0 (25)
1201.2 (2)	.16 (2)
1205.4 (2)	.80 (3)
1289.0 (2)	.52 (2)
1324.1 (2)	.47 (2)
1436.7 (1)	29.2 (13)
1483.3 (1)	46.8 (20)
1543.5 (3)	.03 (1)
1552.7 (2)	.17 (1)
1599.5 (1)	13.5 (6)
1648.4 (2)	.072 (8)
1684.6 (5)	.026 (4)
1955.0 (2)	.41 (2)
2001.7 (2)	.11 (1)
2051.9 (3)	.071 (3)
2226.0 (3)	.046 (3)

(continued)

Table 3. (continued)

Gamma-Ray Energy (keV)	Absolute[a] Gamma-Ray Intensity (percent of ^{210}At decays)
2237.9 (5)	.018 (2)
2246.6[g] (5)	.026 (4)
2254.0 (2)	1.53 (5)
2266.8[e] (3)	.029 (5)
2272.7 (3)	.35 (1)
2284.5 (3)	.019 (2)
2290.0 (3)	.012 (3)
2306.2 (3)	.037 (2)
2352.8 (2)	.14 (1)
2386.8 (3)	.008 (2)

[a]Absolute intensity values were derived by normalizing results to the intensity of the 1181.4 keV transition, which is known from the level scheme to be 100.0(25)%.

[b]Transition intensities (< 500 keV) were derived from measured gamma-ray intensities by correcting for internal conversion by using the theoretical values of Hager and Seltzer[42,43].

[c]These transitions were obtained by assignment of conversion electrons reported by Hoff and Hollander[25].

[d]This intensity was obtained by correcting for contribution from the single escape peak of the 1599.5 keV gamma-ray.

[e]Assigned to ^{210}At decay but unplaced in present level scheme.

[f]This transition was not observed in the singles spectrum due to the intense compton background but was observed in the coincidence spectra of the 639.4 keV transition. The intensity limit was extracted from the coincidence spectra.

(continued)

Table 3 (continued)

[g] Assignment to ^{210}At decay is uncertain.

[h] The intensity was estimated from the relative electron intensities reported by Hoff and Hollander[25]).

[i] The intensity was estimated from an intensity balance of the decay scheme.

In addition to previously reported transitions, we have been able to observe fourteen new transitions of very low intensity. Our present data are in good agreement with those reported previously with the exception of two discrepancies worthy of note. The transition at 790.6±0.7 keV reported by Prussin and Hollander[27]) as belonging to the decay of ^{210}At is now known to arise from the decay of ^{209}At (E = 790.2±0.1 keV (see section V)). Secondly, our gamma-ray data and conversion electron data (see section IVD3) give inconclusive evidence for the 125.2 keV transition originally reported by Hoff and Hollander[25]). Finally, we note the presence of a slight systematic error in the energies reported by Prussin and Hollander. In the range 700-1200 keV, their data tend to be higher than those reported here by 0.5-0.7 keV.

2. Gamma-Gamma Coincidence Spectra

Three parameter (E1, E2, ΔT) gamma-ray coincidence data were collected with the large volume detectors and were stored digitally and serially on magnetic tape. E1 and E2 were the energies of two coincident events from each of the two detectors and ΔT the time difference between the two events. (The gamma-ray signal from one detector (E1) was used to start the time-to-amplitude converter (TAC) and the signal from the second detector (E2) was used to stop the TAC. The TAC output produced the third parameter ΔT proportional to the time difference between the two events E1 and E2. See Appendix C for a more detailed discussion of the multiparameter experiment.) The experiment was performed over a thirty-hour period in which $2.9 \cdot 10^7$ events were stored.

The tapes of data were later analyzed on LBL-CDC 6600 computer system for coincidence relations using a modified version of the code MSORT originally written by D. F. Lebeck of LBL. The code allows the setting of windows (or gates) on two of the three stored parameters (E1, E2, ΔT) so that in a scan of the three parameter data tapes, the third parameter can be sorted out and a coincidence spectrum obtained. This technique has the advantage that all coincidence events (including random events) can be stored and the gates set leisurely on the computer. This removes the requirement of doing many separate coincidence experiments with one set of gates at a time, in order to achieve the same results.

The code MSORT approximates the correction for random and compton coincidence events in the following way. With references to fig. 10, the random events are removed by subtracting a number of events in the random time spectrum (d) from the total number of valid events in the time gate (c) of the total recorded TAC spectrum. The net result should be the correct number of time events satisfying the proper (prompt) time coincidence. Similarly, the energy spectrum must be corrected for coincidences due to compton scattered events of higher energy gamma's which fall in the selected energy gate. This is done by subtracting a number of events immediately above the photopeak of the set energy gate (b) from the total number of events in the energy gate (a). The result should be only the coincident photopeak energy events. In both subtractions for the random and compton coincident events, the width of the gates (number of channels) was such that a = b and c = d. This method of sorting multiparameter coincidence tapes was also discussed by Bernthal[18]).

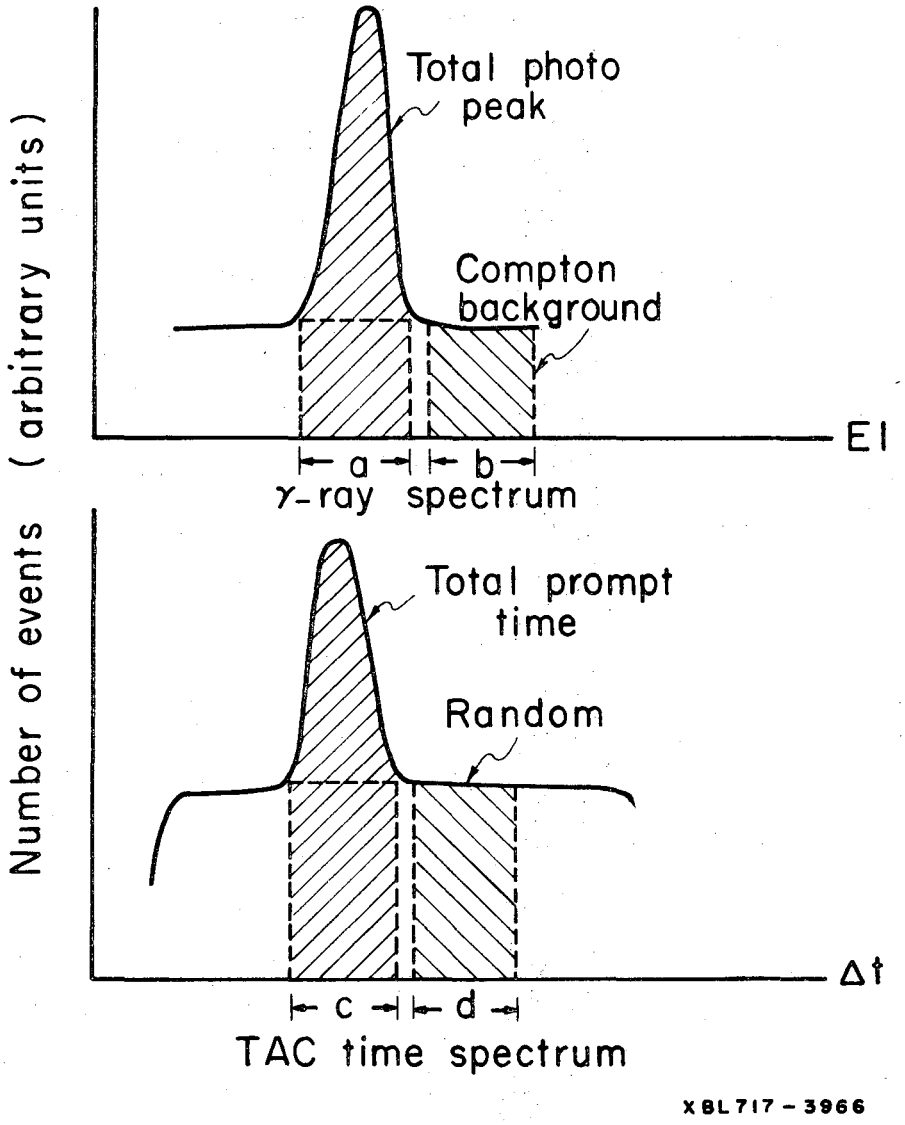

Fig. 10. Schematic diagram of coincidence gates (or windows) set for the γ-γ coincidence computer sorting of the data tapes. The upper figure represents gates set on the gamma-ray spectra to correct for compton events and the lower figure those for the TAC spectrum to correct for random coincidence events.

A sort of the data tapes was first made to establish the gross spectra for each of the three parameters (E1, E2, ΔT) stored on the tapes. This was done by leaving two of three gates open and scanning the tapes for all events of the third parameter. The results were three spectra containing the total number of events stored on the tapes for each parameter. The spectra of fig. 11 and fig. 12 represent the gross coincidence "singles" gamma spectra (E1 and E2) stored on the tapes with the only requirement that gamma pairs must have occured within the time range of the TAC in order to have been recorded and hence appear in figs. 11 and 12. Figure 13 shows the gross total time distribution (40 nsec FWHM) for all coincidences recorded. Ideally if only prompt and random energy events were stored, fig. 13 would be a gaussian (prompt) superimposed on a flat background of random coincidences. The deviation from this is due primarily to the delayed states populated in the ^{210}At decay. The plot is semilogrithmic so that the slope of the timing tail, if the random background and prompt gaussian components were subtracted, is a measure of the half-life of the states populated. Another effect which causes deviations from the gaussian shape is due to the leading edge timing. This effect and the compensation unit employed to minimize the tailing effect has been discussed in detail by Jaklevic et al.[21]).

In order to sort the coincidence events, energy gates (E2) and the compton background subtraction gates were set on the spectrum of fig. 12. Simultaneously, the TAC spectrum of fig. 13 had gates set for the prompt and random events as shown in fig. 13. The energy gates (E2)

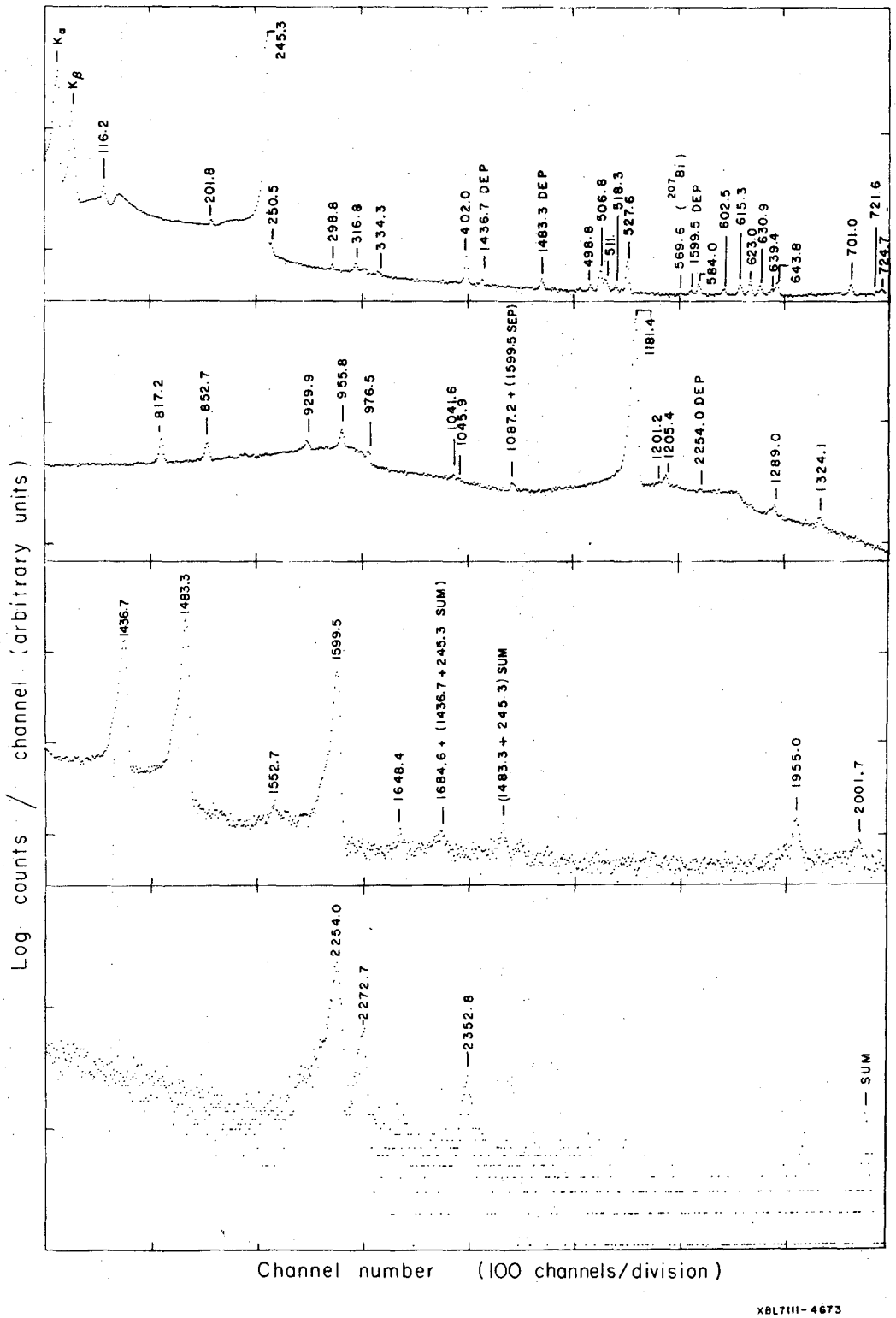

Fig. 11. "Gross" γ-γ coincidence spectrum for the 40-cm^3 (active volume) coaxial Ge(Li) detector.

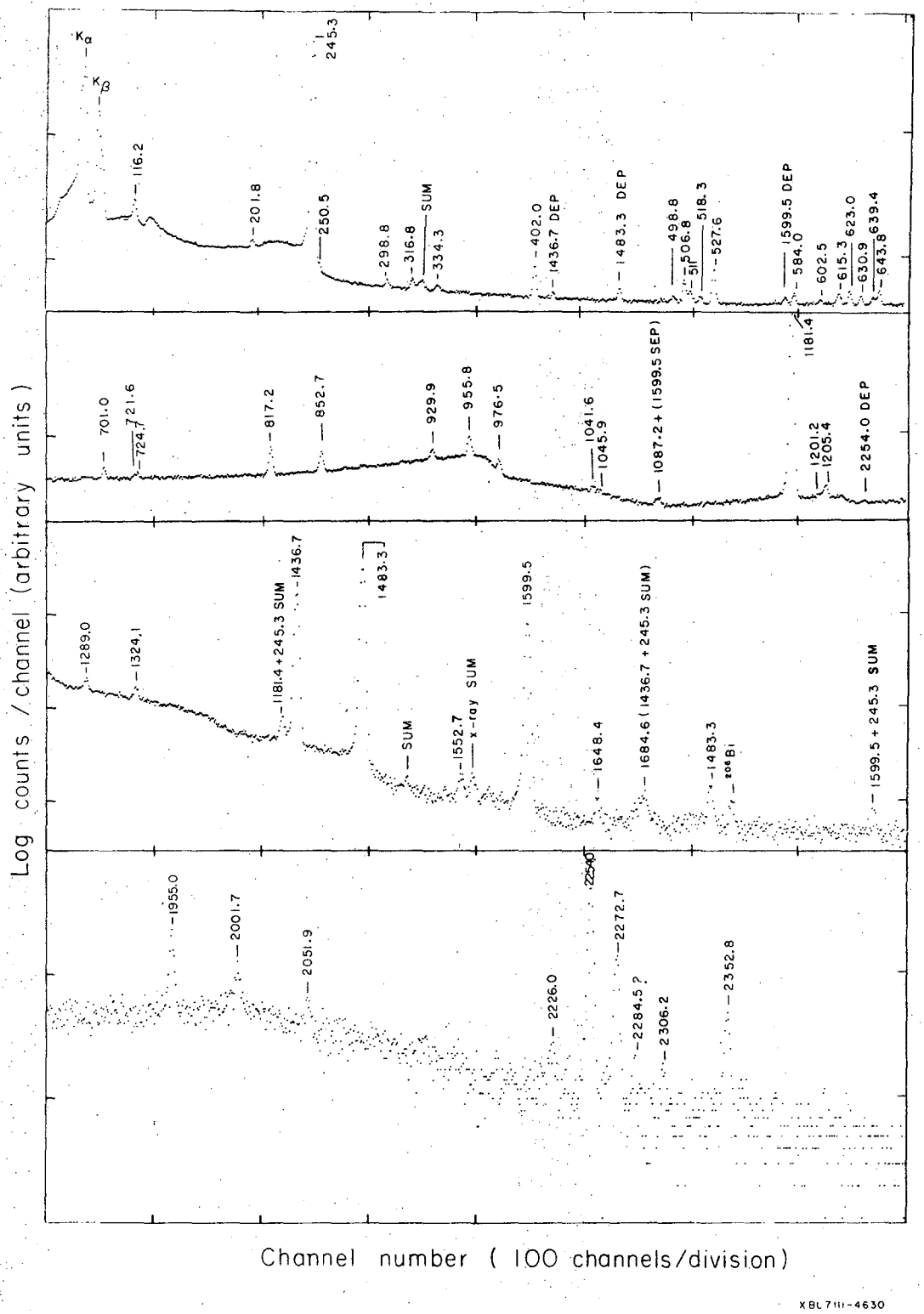

Fig. 12. "Gross" γ-γ coincidence spectrum for the 35-cm^3 (active volume) coaxial Ge(Li) detector.

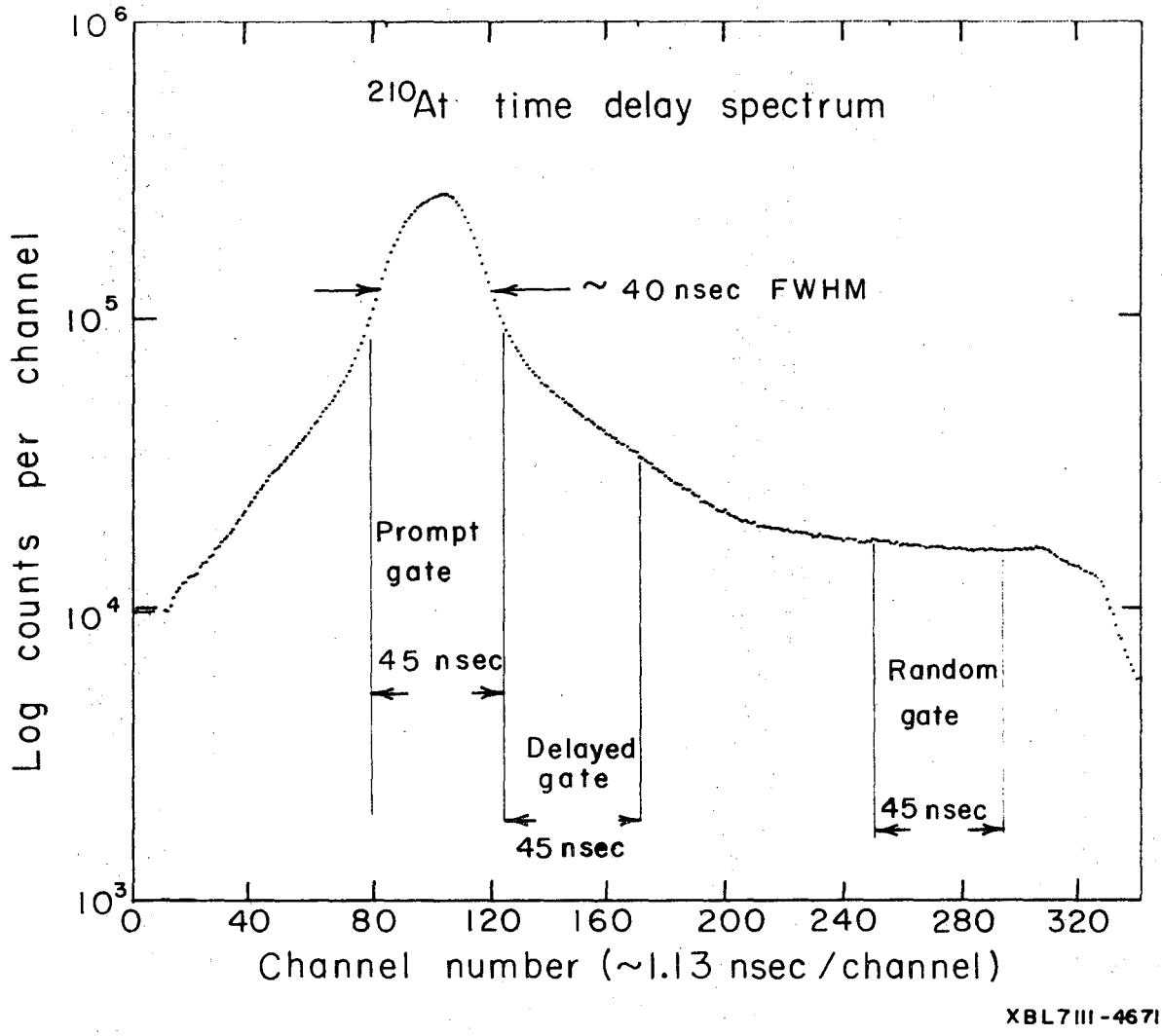

Fig. 13. "Gross" time distribution for the ^{210}At γ-γ coincidence data. The 45 nsec gates were used to obtain the coincidence events shown in figs. 14-34.

used in fig. 12 are shown in Table 4. A scan of the tapes with these gates yielded prompt coincidence spectra (E1) from fig. 11. The results of these prompt sorts are shown in figs. 14-31 and are portions from the spectrum of fig. 11 satisfying the two set gates (E2 and Δt). Several delayed coincidence sorts were tried and a sampling of those sorts is displayed in figs. 32-34. These results are discussed in connection with the construction of the ^{210}At decay scheme in section E.

Table 4. Peak and compton background gates used. With reference to the gamma-ray spectrum of fig. 12, these gates were set. The time distribution gates were set as shown in fig. 13. The coincidence events from the spectrum of fig. 11, with these gates, returned by MSORT are shown in figs. 14-34.

Energy keV	Peak gate channels		background gate channels	
116.2	169	175	190	196
≈ 125	183	189	190	196
201.8	279	286	287	293
245.3	330	342	349	361
250.5	343	348	349	354
298.8	406	412	413	419
316.8	427	435	460	468
334.3	451	459	460	468
402.0	542	549	550	557
498.8	671	679	719	727
506.8	680	688	719	727
518.3	696	704	719	727
527.6	709	717	719	727
584.0	785	791	793	799
602.5	809	816	874	881
615.3	826	834	874	882
623.0	837	844	874	881
630.9	847	854	874	881
639.4	857	864	874	881
643.8	865	872	874	881

(continued)

Table 4 (continued)

Energy keV	Peak gate channels		background gate channels	
701.0	941	948	950	957
721.6	968	973	981	986
724.7	974	979	981	986
817.1	1096	1104	1106	1114
852.7	1142	1151	1153	1162
869.3	1165	1171	1172	1178
881.1	1182	1190	1192	1200
909.2	1218	1225	1226	1233
929.9	1245	1254	1255	1264
955.8	1280	1288	1289	1297
964.9	1302	1305	1306	1309
976.5	1309	1315	1316	1322
1041.6	1395	1401	1409	1415
1045.9	1402	1408	1409	1415
$\leqslant$ 1087.2	1452	1458	1468	1474
$\geqslant$ 1087.2	1459	1465	1468	1474
1181.4	1579	1590	1591	1602
1201.5	1605	1612	1621	1628
1205.4	1613	1620	1613	1620
1289.0	1723	1731	1732	1740
1324.1	1769	1779	1780	1790

(continued)

Table 4 (continued)

Energy keV	Peak gate channels		background gate channels	
1436.7	1919	1928	1933	1942
1483.3	1978	1992	1993	2007
1543.5	2072	2082	2106	2116
1552.7	2083	2093	2106	2116
1599.5	2130	2145	2148	2163
1648.4	2199	2206	2207	2214
1954.9	2601	2612	2613	2626
2238.9	2956	2965	3003	3012
2246.6	2970	2979	3003	3012
2254.0	2992	3001	3003	3012
2272.7	3016	3026	3050	3060
2352.8	3118	3131	3146	3159

We show in pages 84-104 the complete set of γ-γ coincidence spectra (figs. 14-34) from the decay of ^{210}At. Due to incomplete background subtractions, the more intense high energy transitions of 1436.7, 1483.3, and 1599.5 keV sometimes occur where they would not if the subtraction were complete. This is also due in part to the low background in the 1500 keV region so that 10-30 counts has the appearance of a real photopeak. These peaks are appropriately marked in the figures. The reader may continue at page 105 without a loss of content.

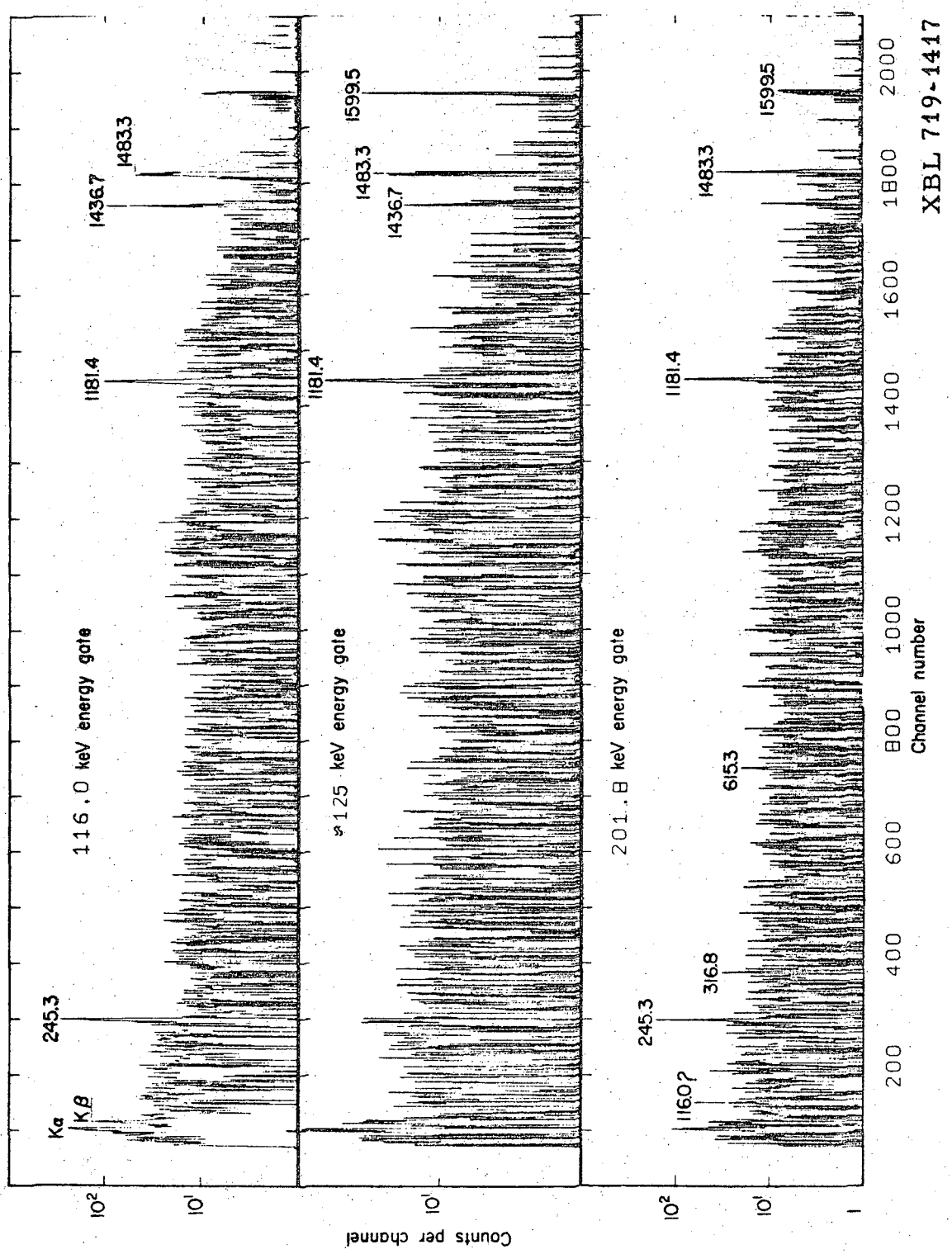

Fig. 14. Gamma-ray spectra in prompt coincidence with E_γ = 116.0 keV (top), $E_\gamma \approx 125$ keV (middle) and E_γ = 201.8 keV (bottom).

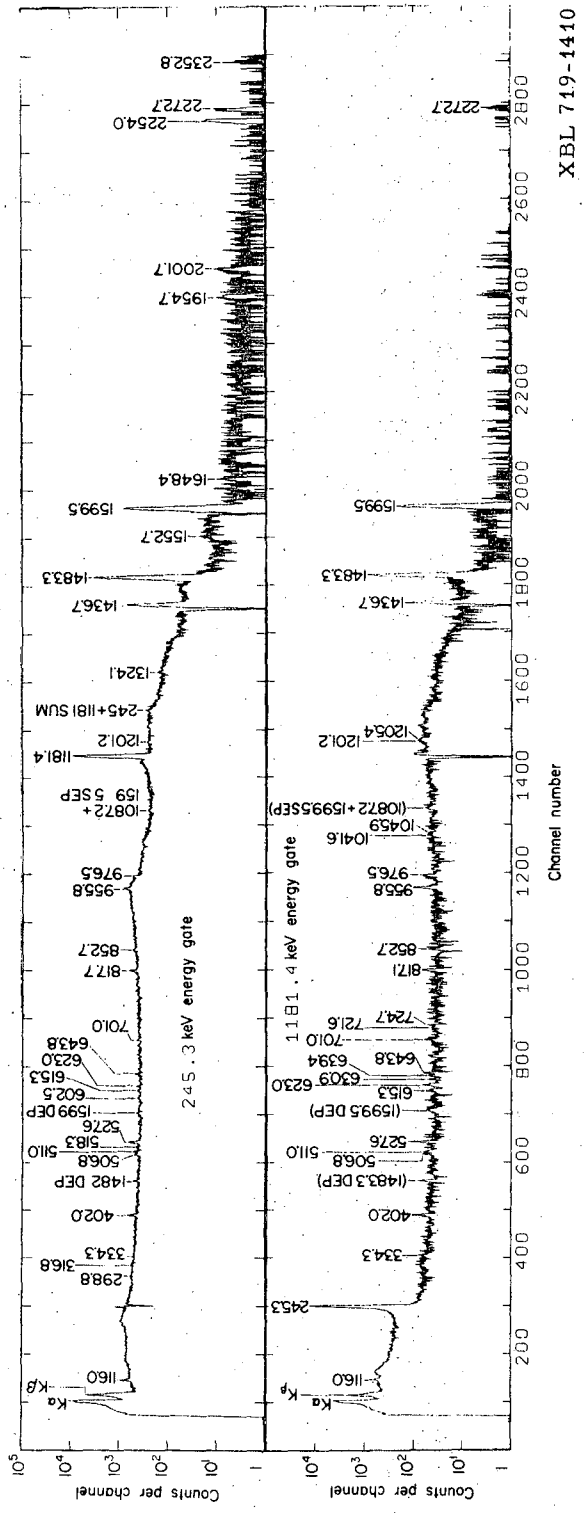

Fig. 15. Gamma-ray spectra in prompt coincidence with E_γ = 245.3 keV (top) and E_γ = 1181.4 keV (bottom).

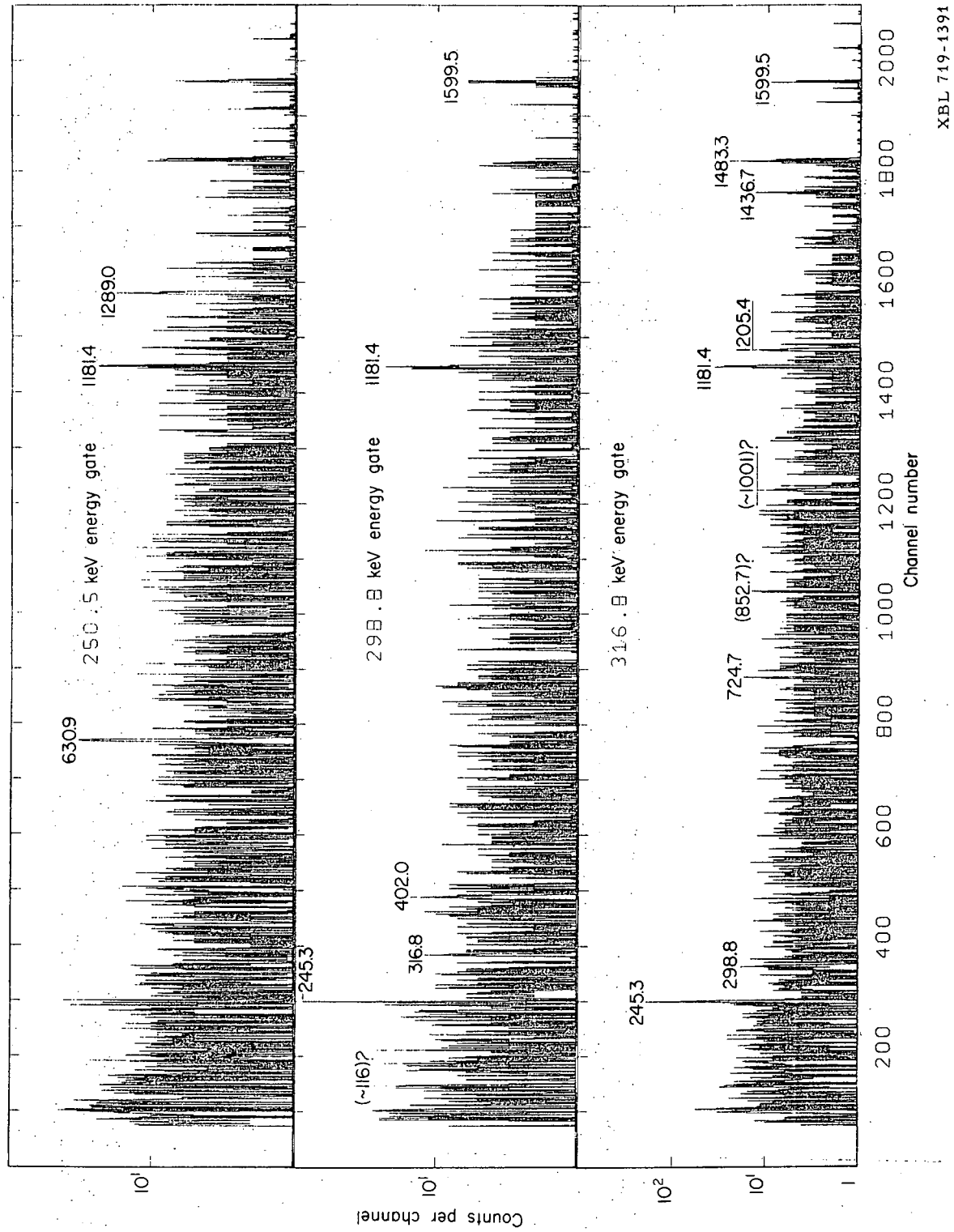

Fig. 16. Gamma-ray spectra in prompt coincidence with E_γ = 250.5 keV (top), E_γ = 298.8 keV (middle) and E_γ = 316.8 keV (bottom).

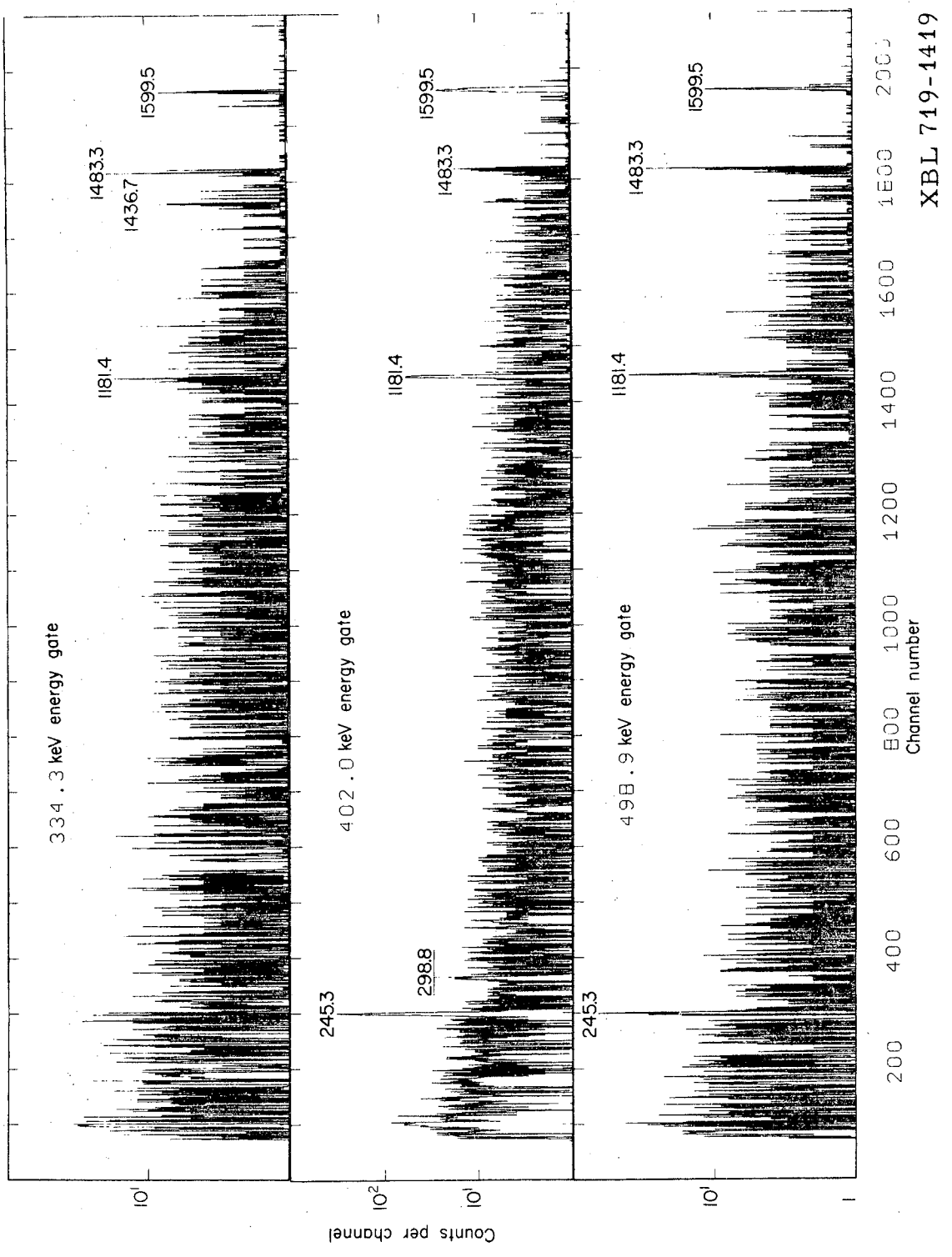

Fig. 17. Gamma-ray spectra in prompt coincidence with E_γ = 334.3 keV (top), E_γ = 402.0 keV (middle) and E_γ = 498.9 keV (bottom).

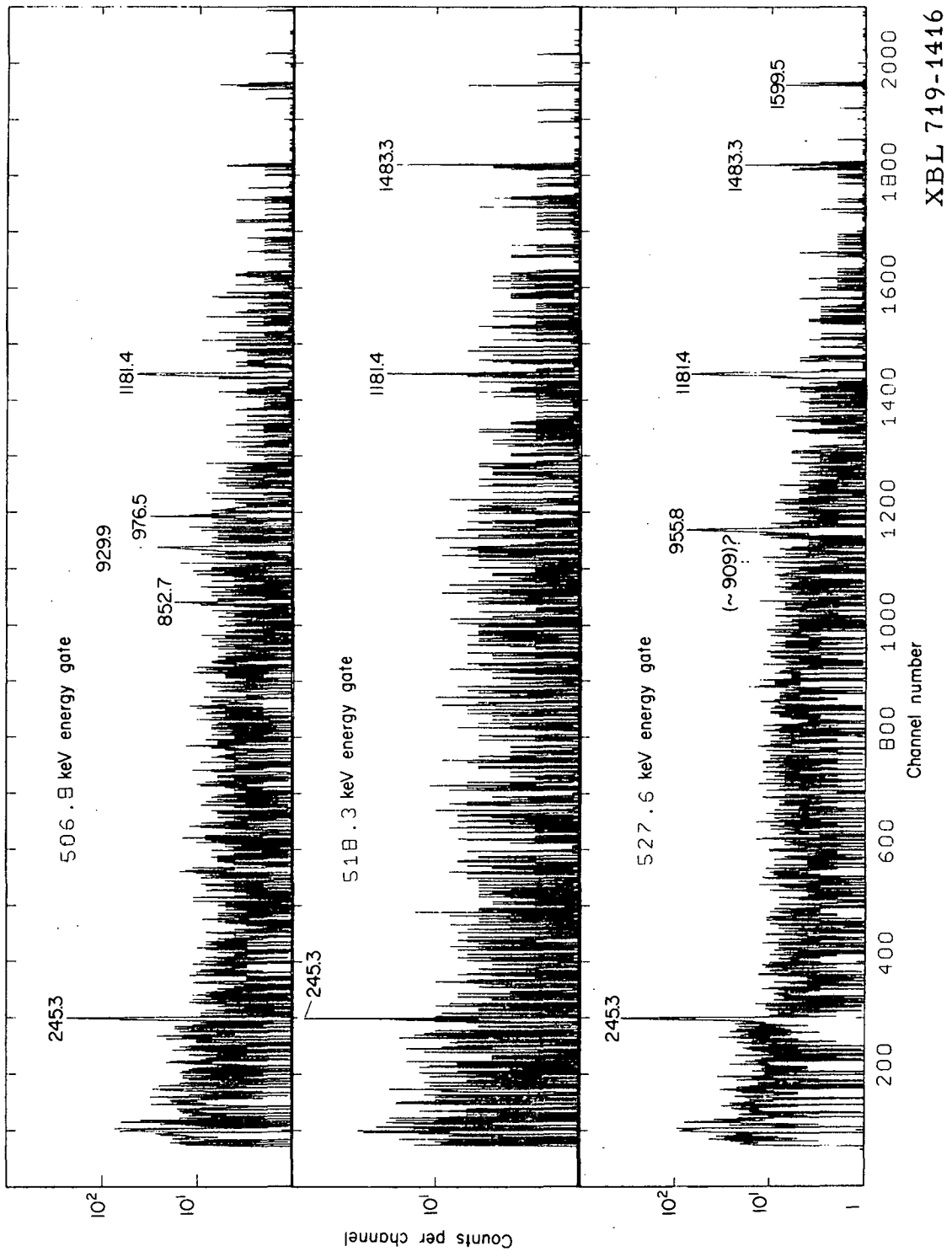

Fig. 18. Gamma-ray spectra in prompt coincidence with E_γ = 506.8 keV (top), E_γ = 518.3 keV (middle) and E_γ = 527.6 keV (bottom).

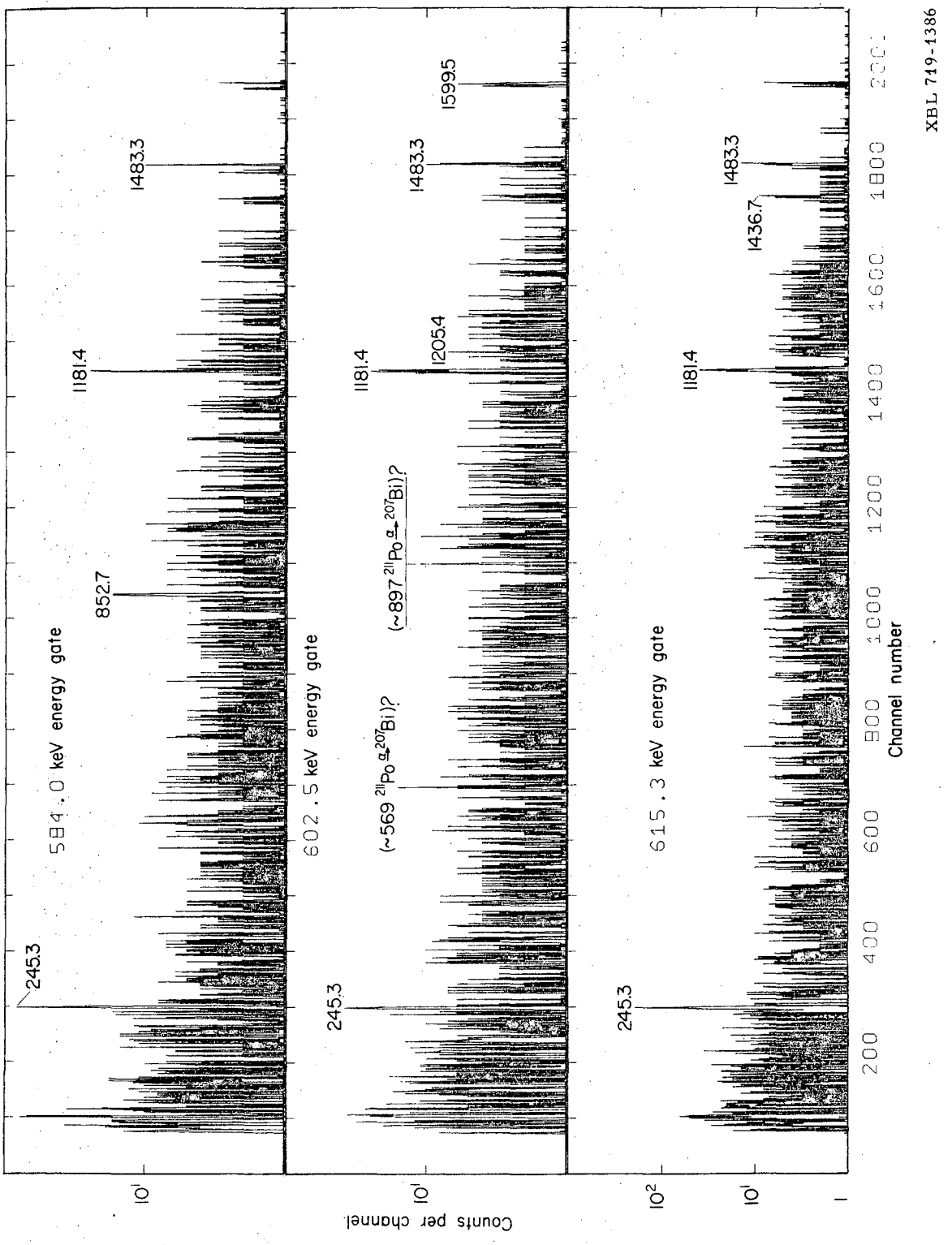

Fig. 19. Gamma-ray spectra in prompt coincidence with E_γ = 584.0 keV (top), E_γ = 602.5 keV (middle) and E_γ = 615.3 keV (bottom).

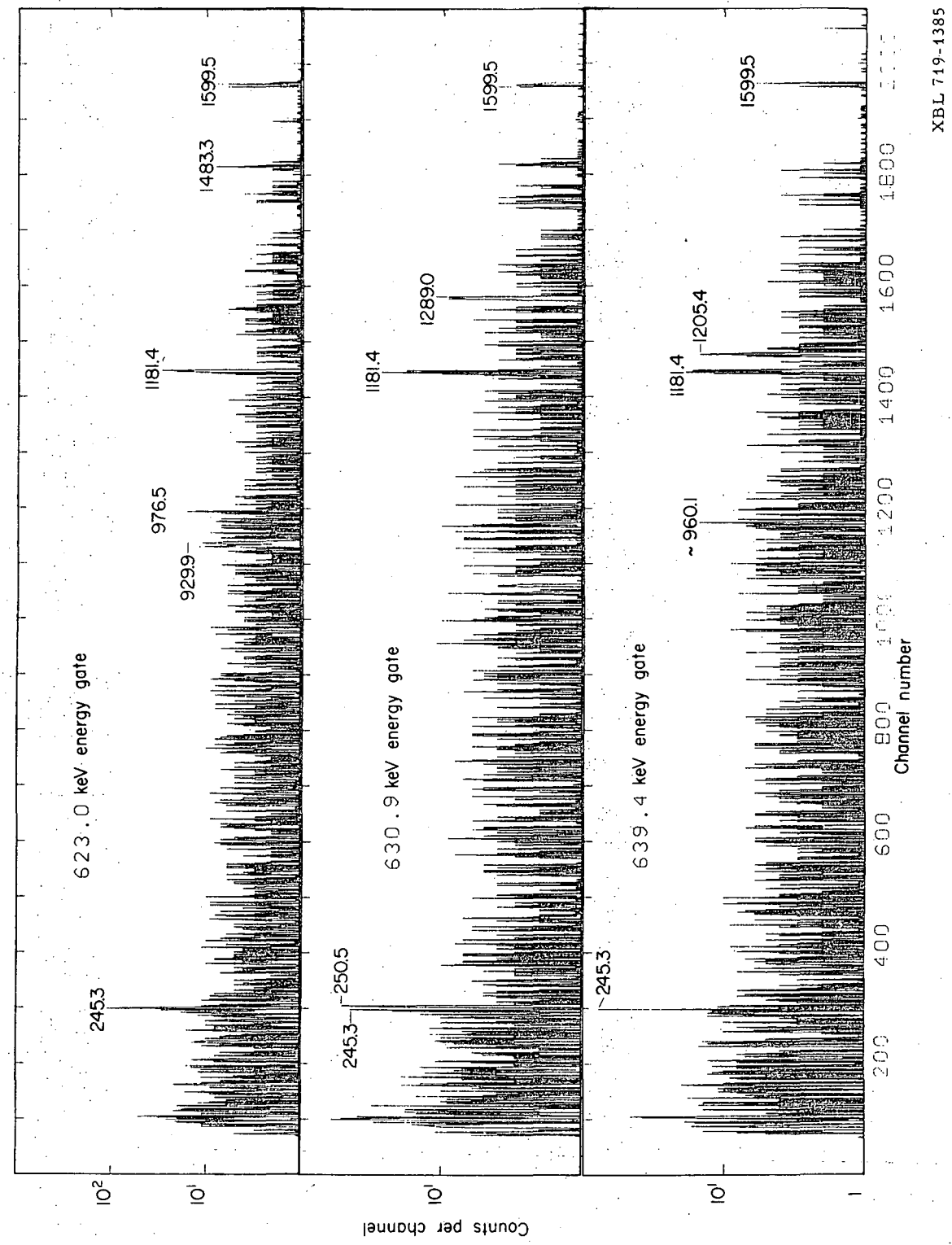

Fig. 20. Gamma-ray spectra in prompt coincidence with E_γ = 623.0 keV (top), E_γ = 630.9 keV (middle) and E_γ = 639.4 keV (bottom).

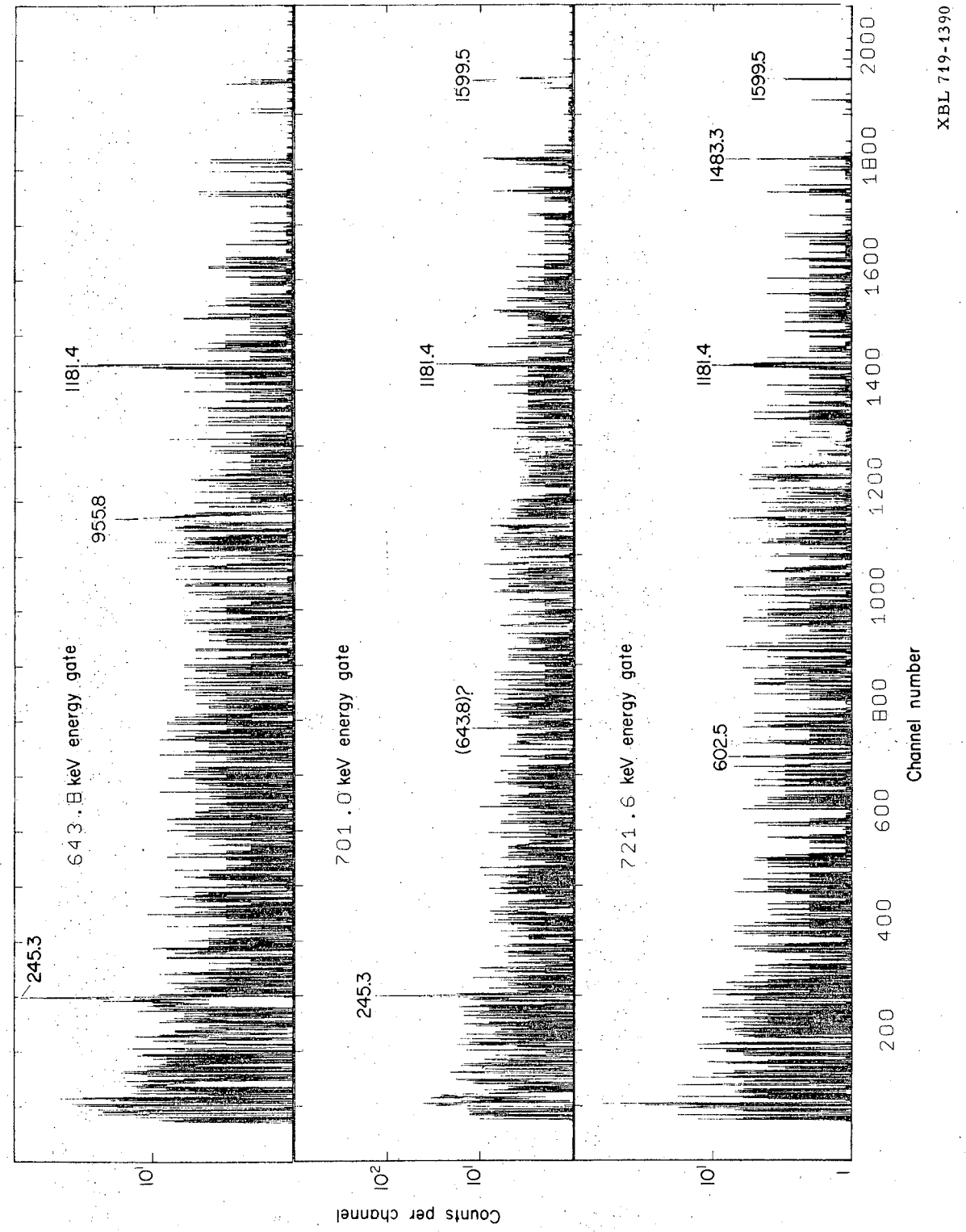

Fig. 21. Gamma-ray spectra in prompt coincidence with E_γ = 643.8 keV (top), E_γ = 701.0 keV (middle) and E_γ = 721.6 keV (bottom).

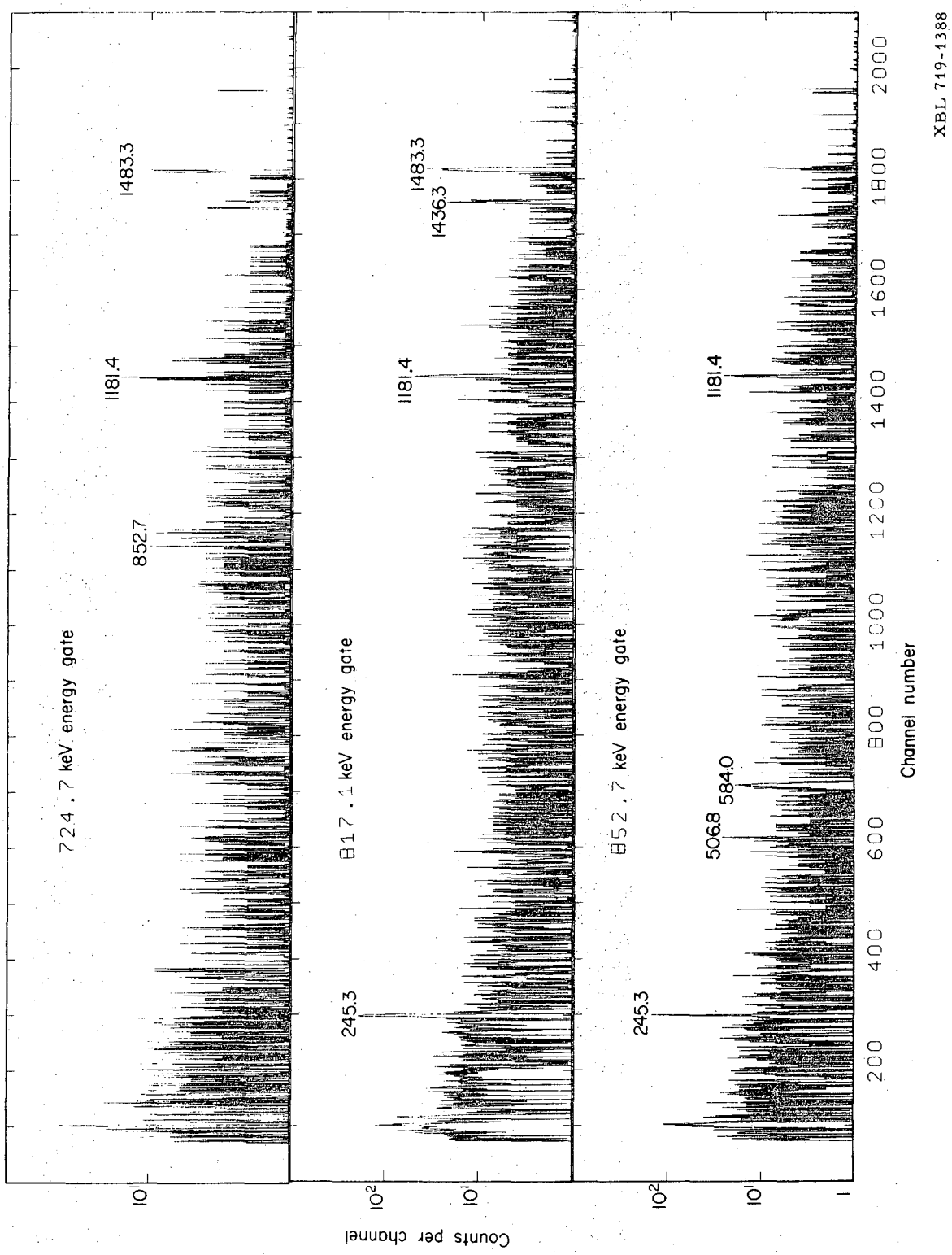

Fig. 22. Gamma-ray spectra in prompt coincidence with E_γ = 724.7 keV (top), E_γ = 817.1 keV (middle) and E_γ = 852.7 keV (bottom).

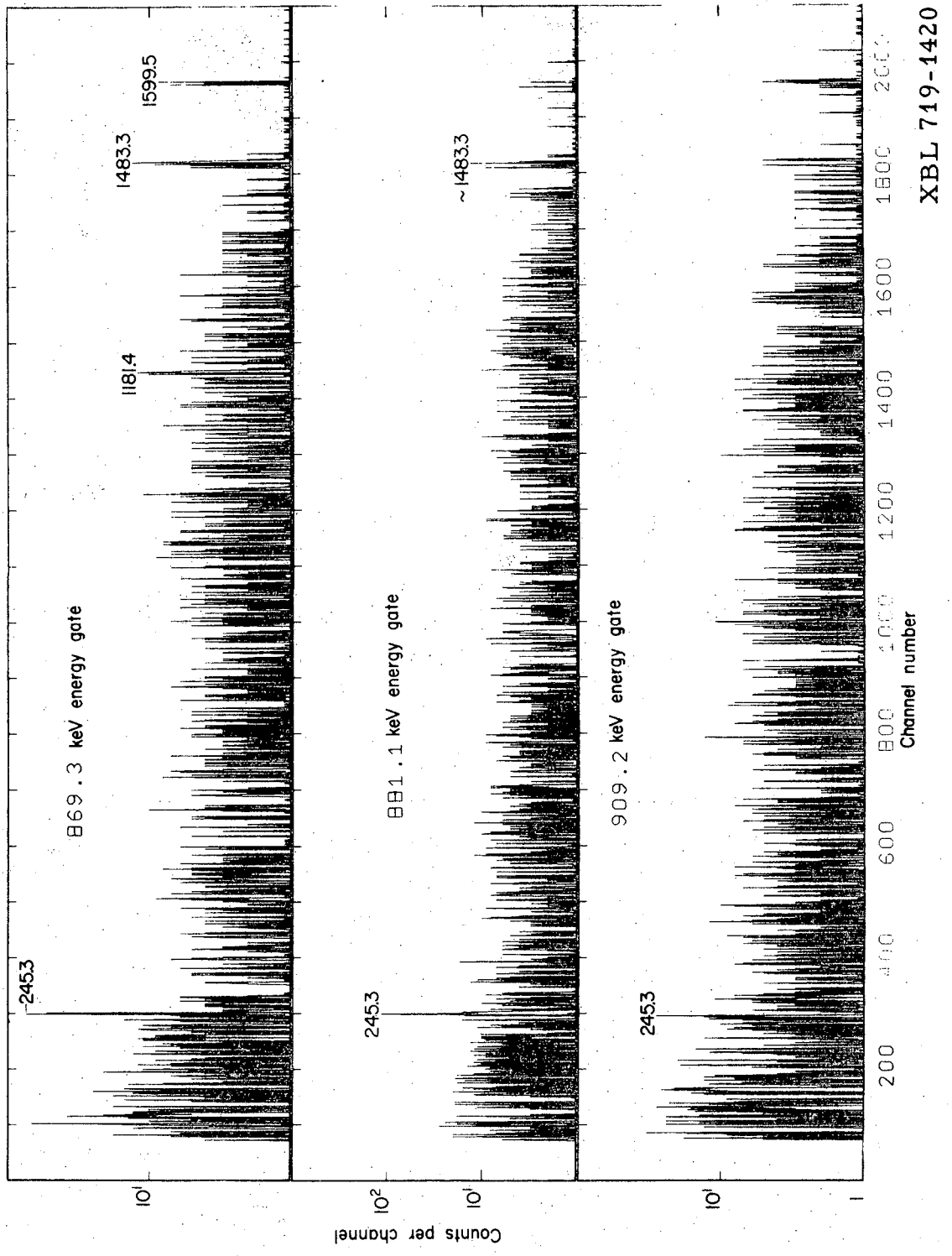

Fig. 23. Gamma-ray spectra in prompt coincidence with E_γ = 869.3 keV (top), E_γ = 881.1 keV (middle) and E_γ = 909.2 keV (bottom).

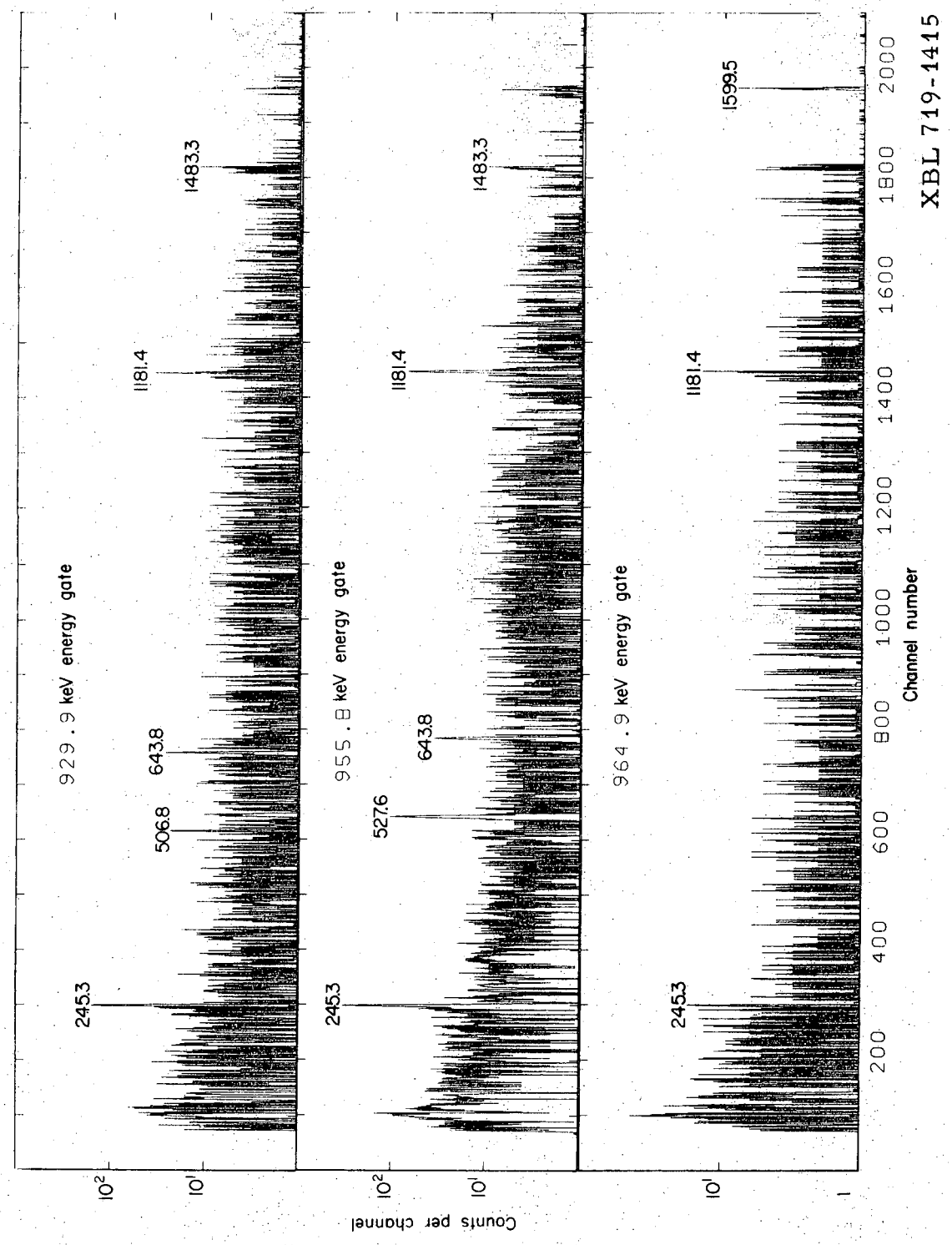

Fig. 24. Gamma-ray spectra in prompt coincidence with E_γ = 929.9 keV (top), E_γ = 955.8 keV (middle) and E_γ = 964.9 keV (bottom).

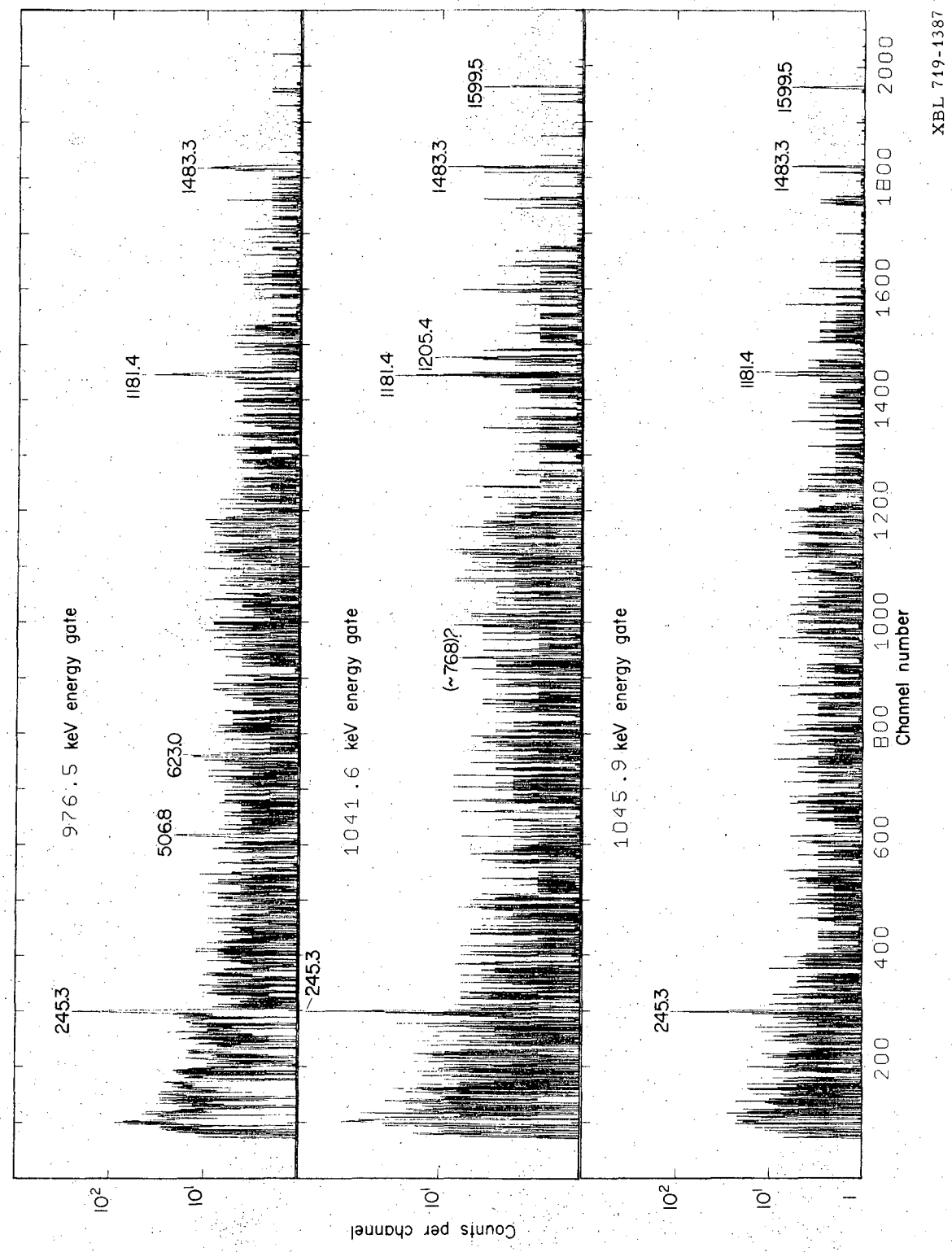

Fig. 25. Gamma-ray spectra in prompt coincidence with E_γ = 976.5 keV (top), E_γ = 1041.6 keV (middle) and E_γ = 1045.9 keV (bottom).

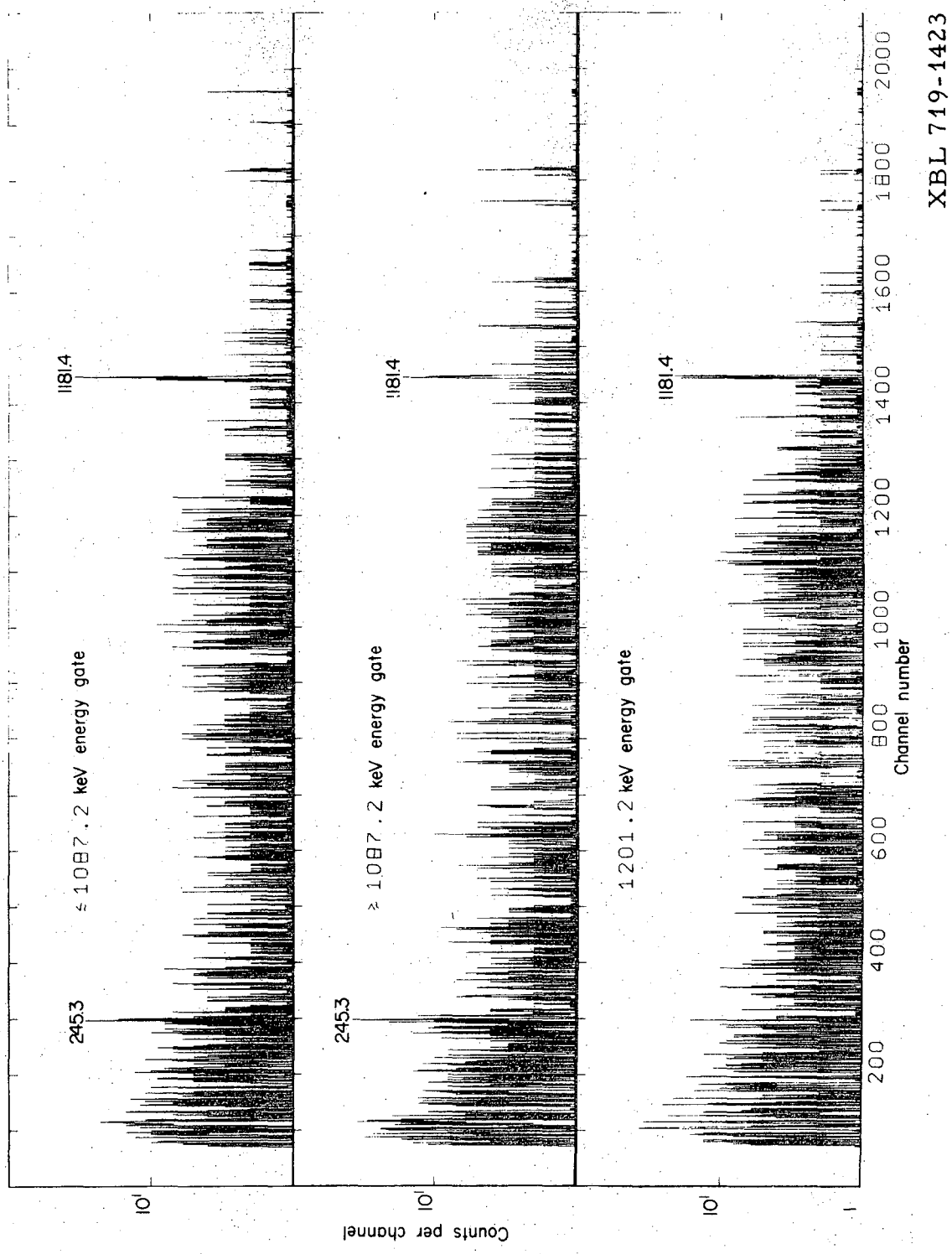

Fig. 26. Gamma-ray spectra in prompt coincidence with $E_\gamma \leq 1087.2$ keV (top), $E_\gamma \geq 1087.2$ keV (middle) and $E_\gamma = 1201.2$ keV (bottom).

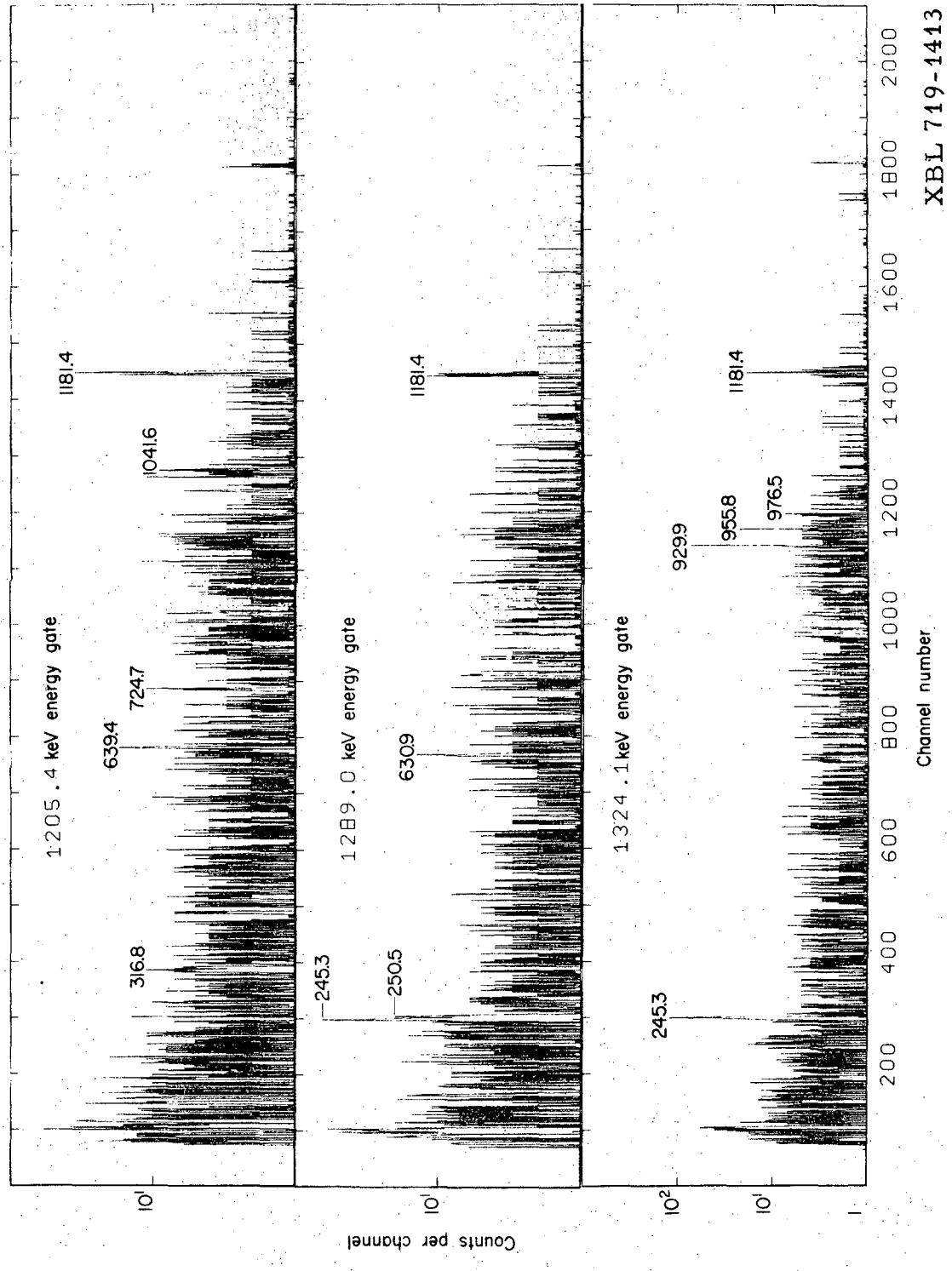

Fig. 27. Gamma-ray spectra in prompt coincidence with E_γ = 1205.4 keV (top), E_γ = 1289.0 keV (middle) and E_γ = 1324.1 keV (bottom).

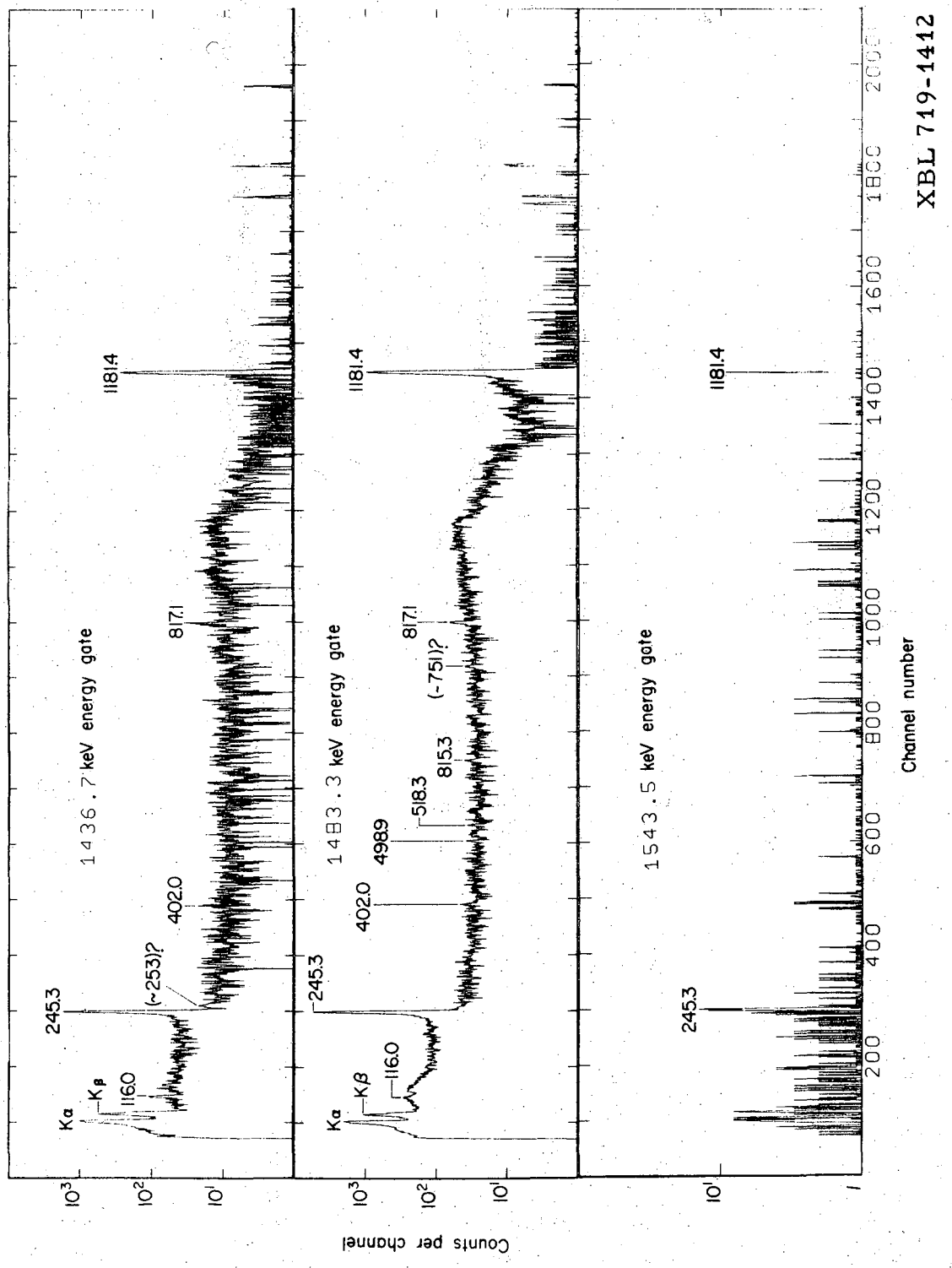

Fig. 28. Gamma-ray spectra in prompt coincidence with E_γ = 1436.7 keV (top), E_γ = 1483.3 keV (middle) and E_γ = 1543.5 keV (bottom).

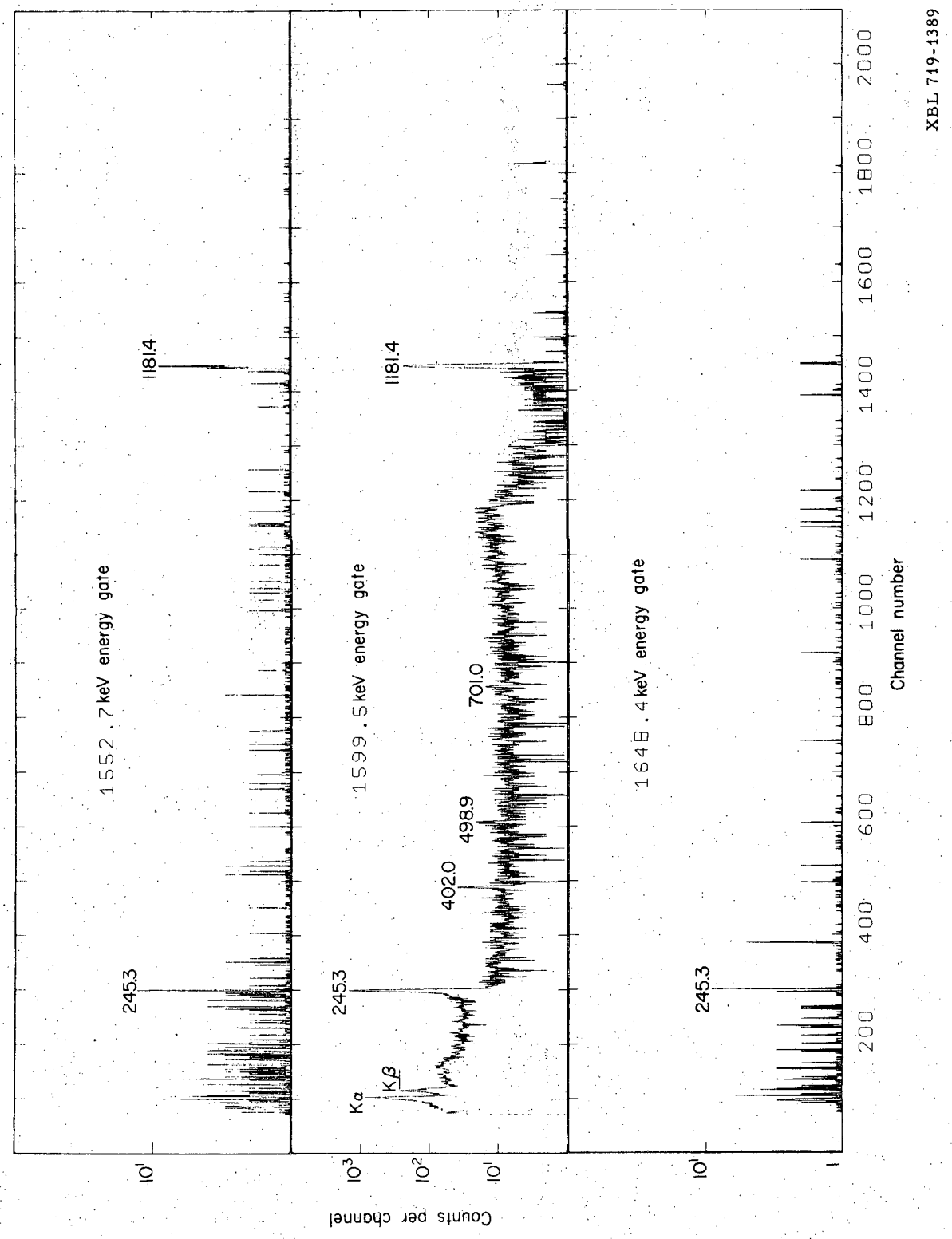

Fig. 29. Gamma-ray spectra in prompt coincidence with E_γ = 1552.7 keV (top), E_γ = 1599.5 keV (middle) and E_γ = 1648.4 keV (bottom).

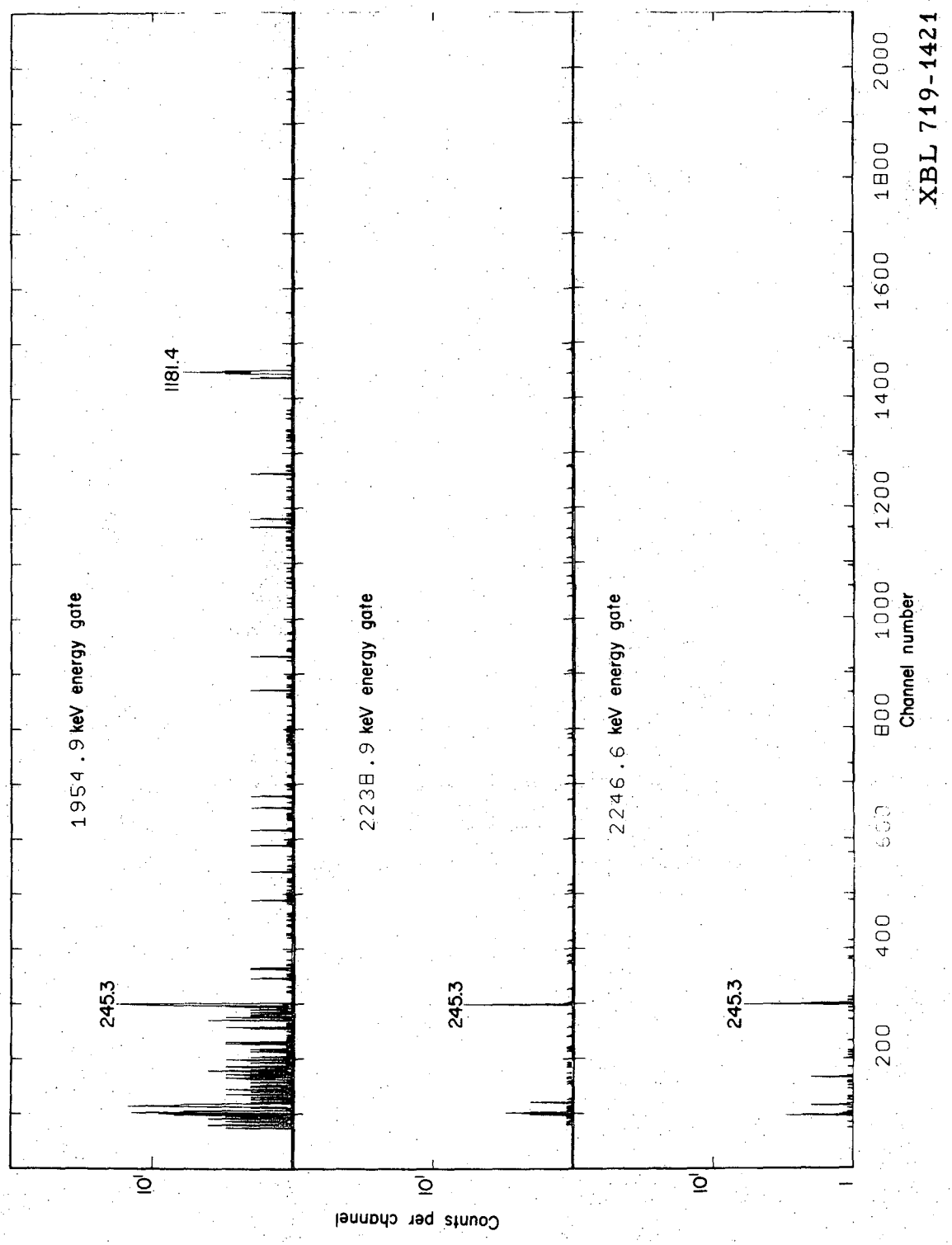

Fig. 30. Gamma-ray spectra in prompt coincidence with E_γ = 1954.9 keV (top), E_γ = 2237.9 keV (middle) and E_γ = 2246.6 keV (bottom). (Note that middle spectrum should read: 2237.9 keV energy gate.)

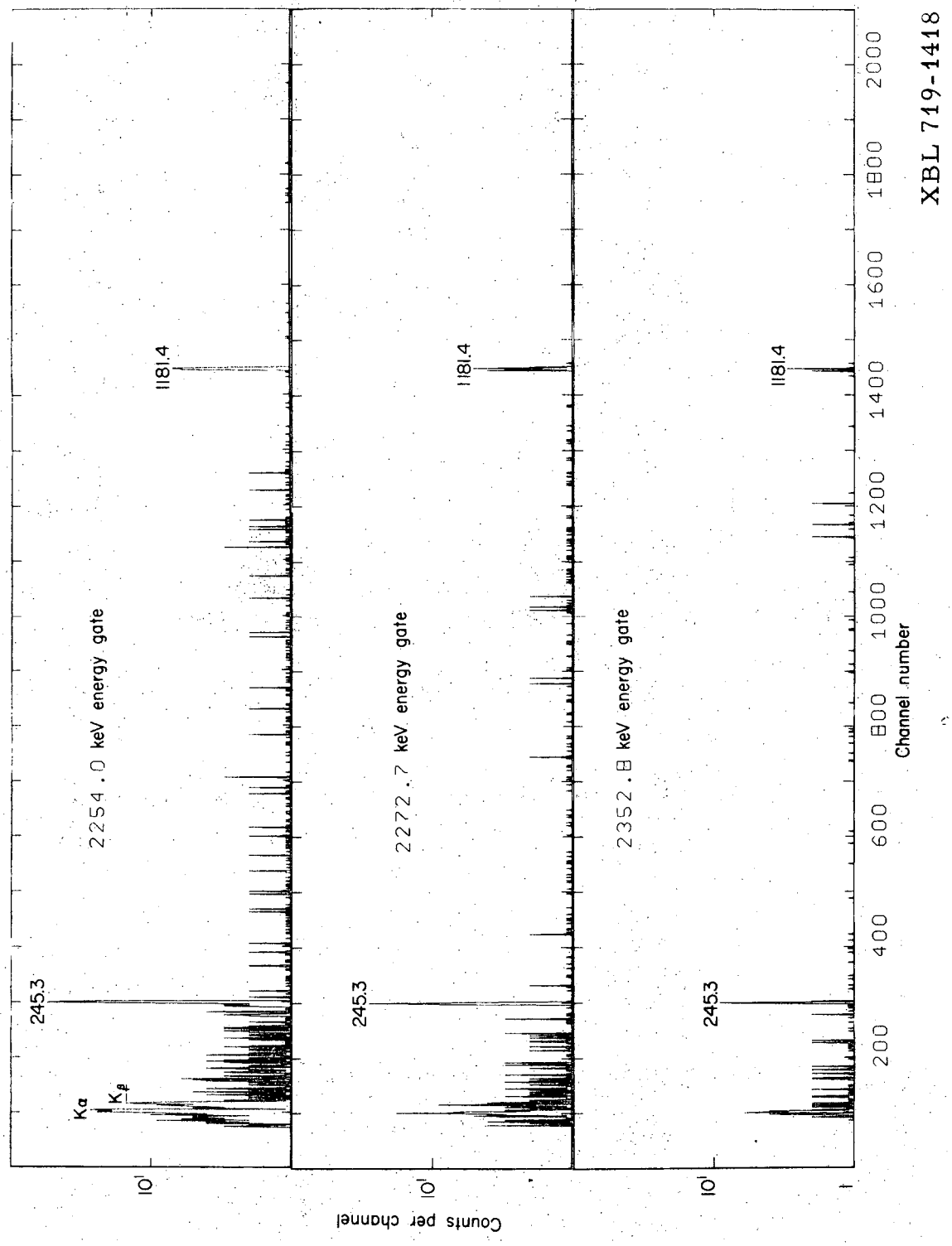

Fig. 31. Gamma-ray spectra in prompt coincidence with E_γ = 2254.0 keV (top), E_γ = 2272.7 keV (middle) and E_γ = 2352.8 keV (bottom).

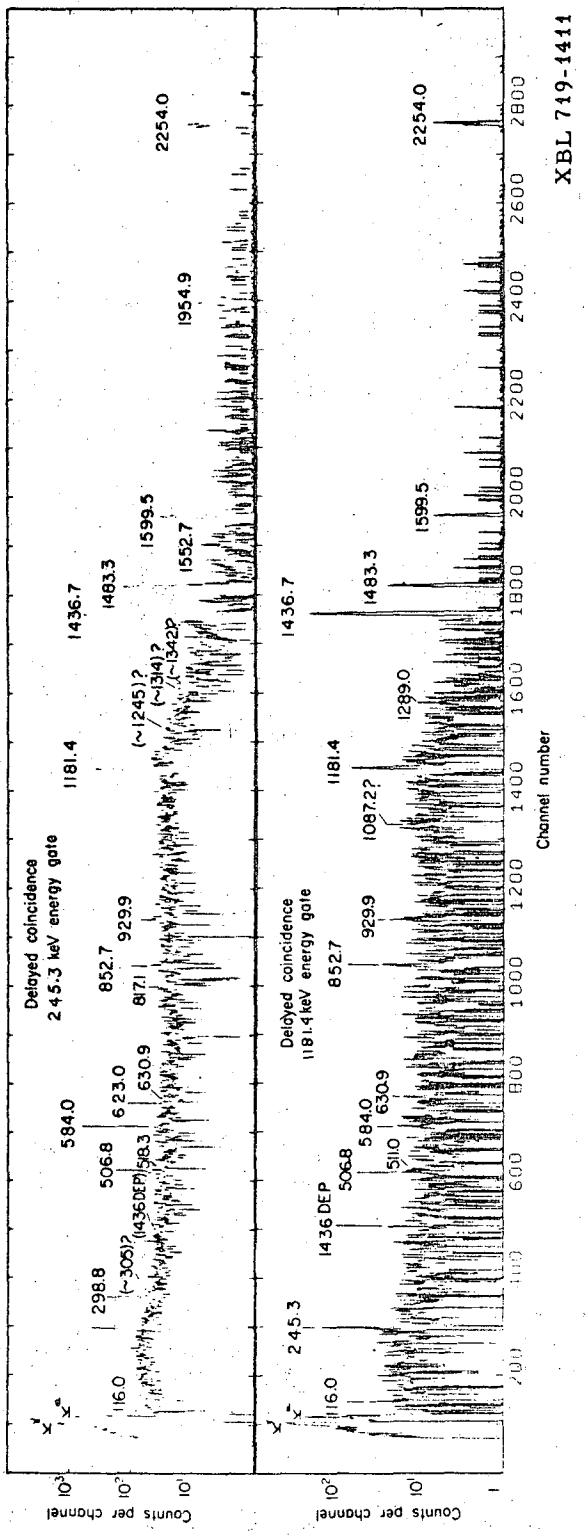

Fig. 32. Gamma-ray spectra in delayed coincidence with E_γ = 245.3 keV (top) and E_γ = 1181.4 keV (bottom).

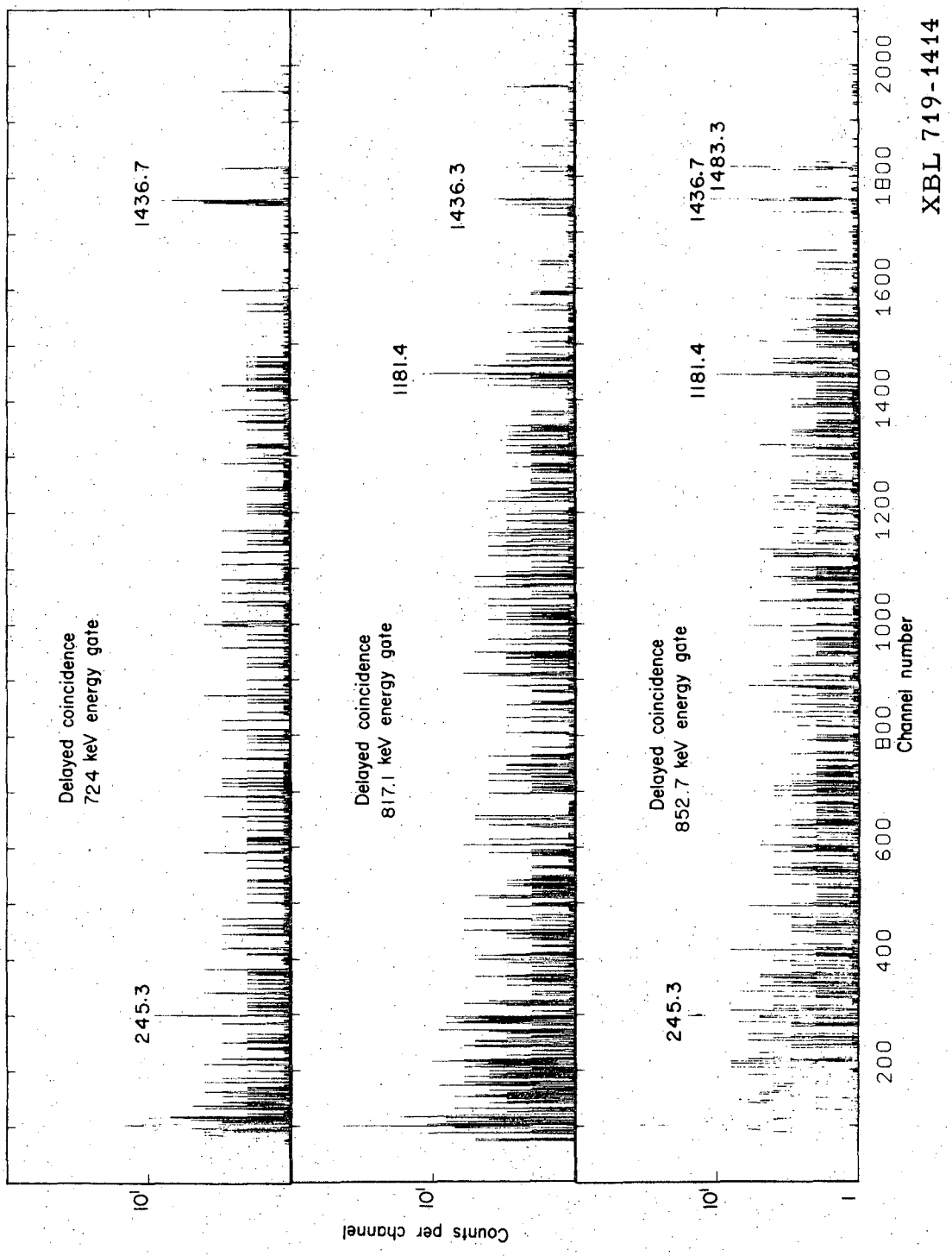

Fig. 33. Gamma-ray spectra in delayed coincidence with E_γ = 724 keV (top), E_γ = 817.1 keV (middle) and E_γ = 852.7 keV (bottom).

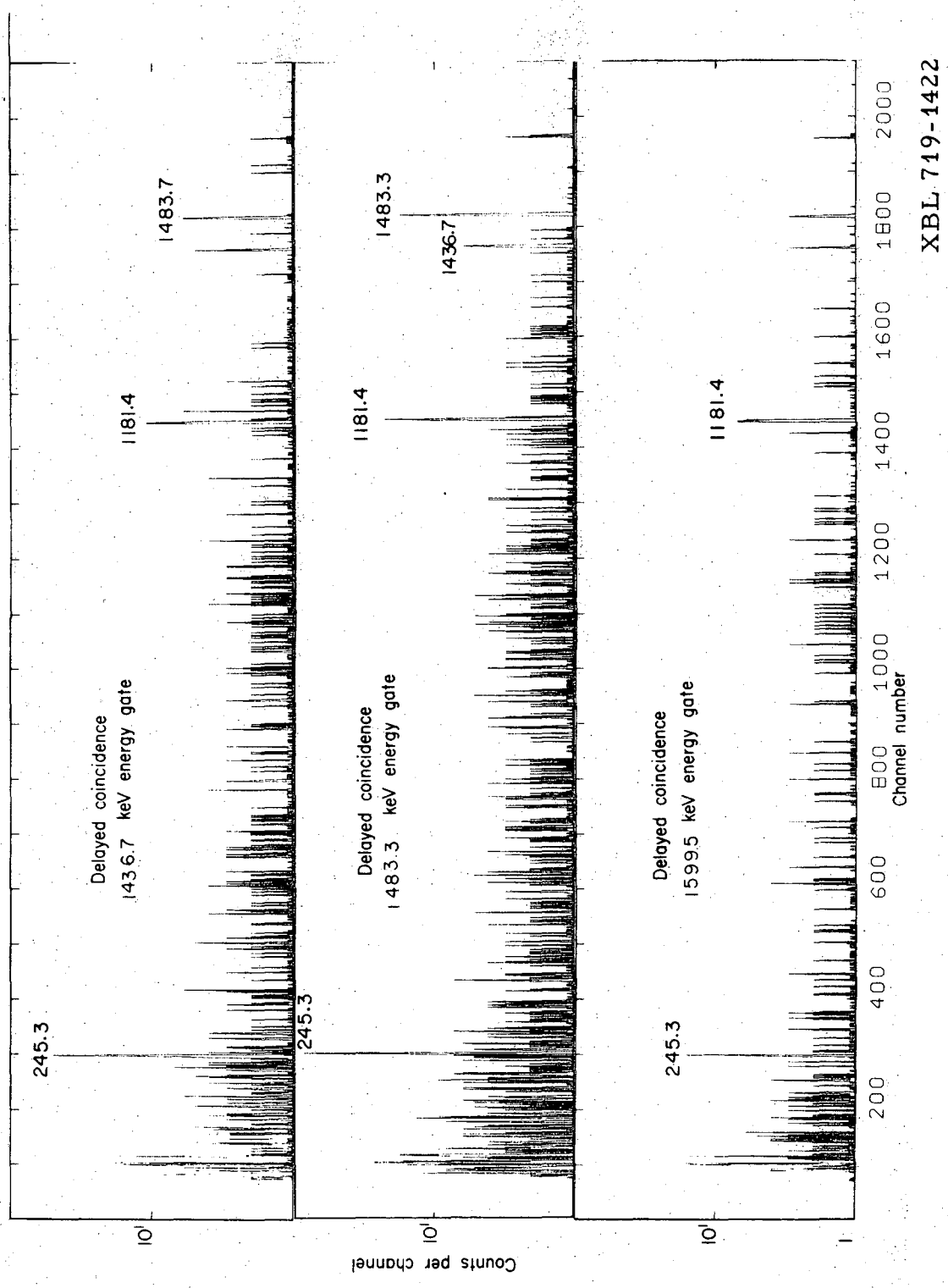

Fig. 34. Gamma-ray spectra in delayed coincidence with E_γ = 1436.7 keV (top), E_γ = 1483.3 keV (middle) and E_γ = 1599.5 keV (bottom).

3. Internal Conversion Electron Spectra

Internal conversion electron spectra taken with the 5-mm Si(Li) detector are shown in figs. 35 and 36. Figure 35 shows an electron spectrum in the energy region of 16-350 keV. The conversion electron spectrum in the energy region of 60-1600 keV are shown in fig. 36. The peak areas were determined with the computer code SAMPO[40,41]. We have used these data along with the gamma-ray intensities reported here to determine K, L, and M conversion coefficients relative to the K-conversion coefficient for the 1181 keV ($2^+ \rightarrow 0^+$) ground-state transition (pure E2) and these are given in Table 5 along with multipolarity assignments deduced by comparison with the theoretical values of Hager and Seltzer[42,43]. (This method of obtaining relative conversion coefficients is referred to as the normalized peak-to-gamma peak (NPG) method and is explained in detail in Appendix F.) The K-conversion coefficients are also shown in fig. 37 with the theoretical curves constructed from the data of ref. [42]. A number of the results are worthy of some comment in the light of previously reported data.

125-keV transition: As mentioned in section IVD2, no gamma-ray at this energy has been observed and the present data can only limit the intensity of such a transition to $I_\gamma \leq 0.32$. This limit is four times greater than the limit set by Prussin and Hollander[27]. Our limit is greater because of the lack of compton suppressed data. However, we can not rule out the existence of this transition because our conversion electron data is inconclusive. While the resolution of our electron data is poor compared to that inherent in the magnetic spectrographic results

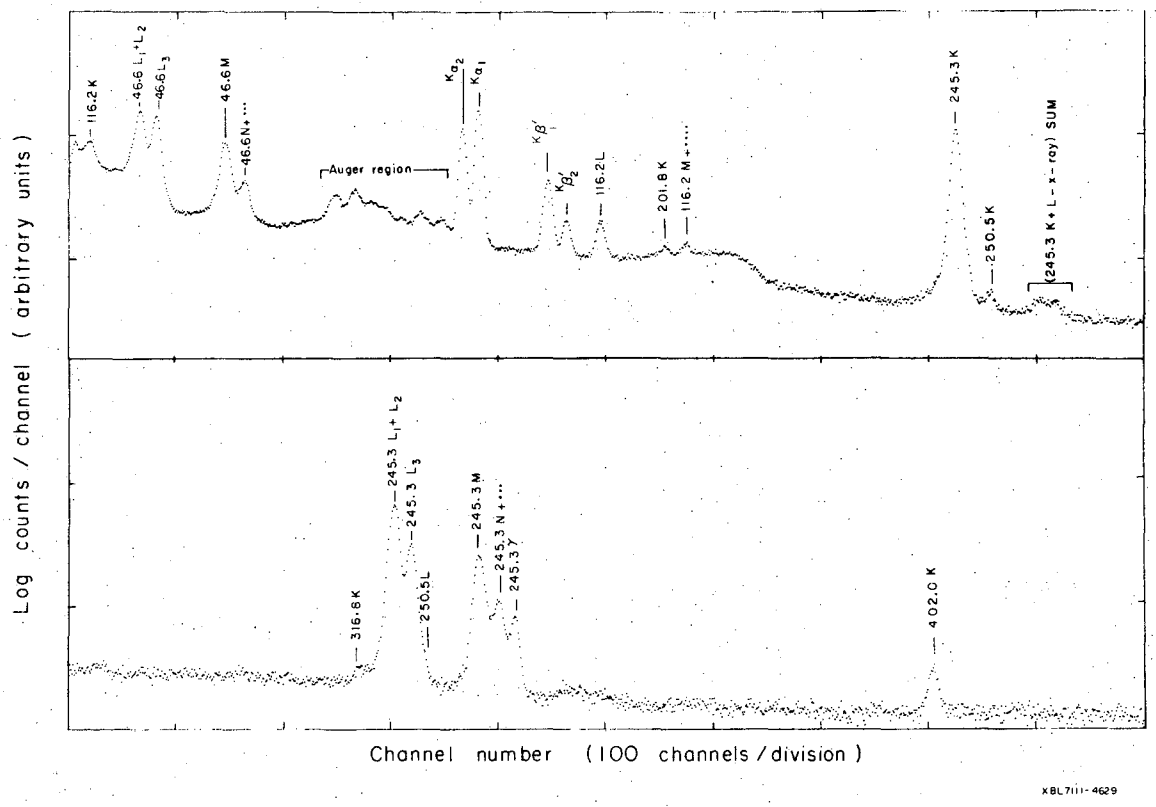

Fig. 35. Conversion-electron spectrum of ^{210}At in the energy range of 16-350 keV.

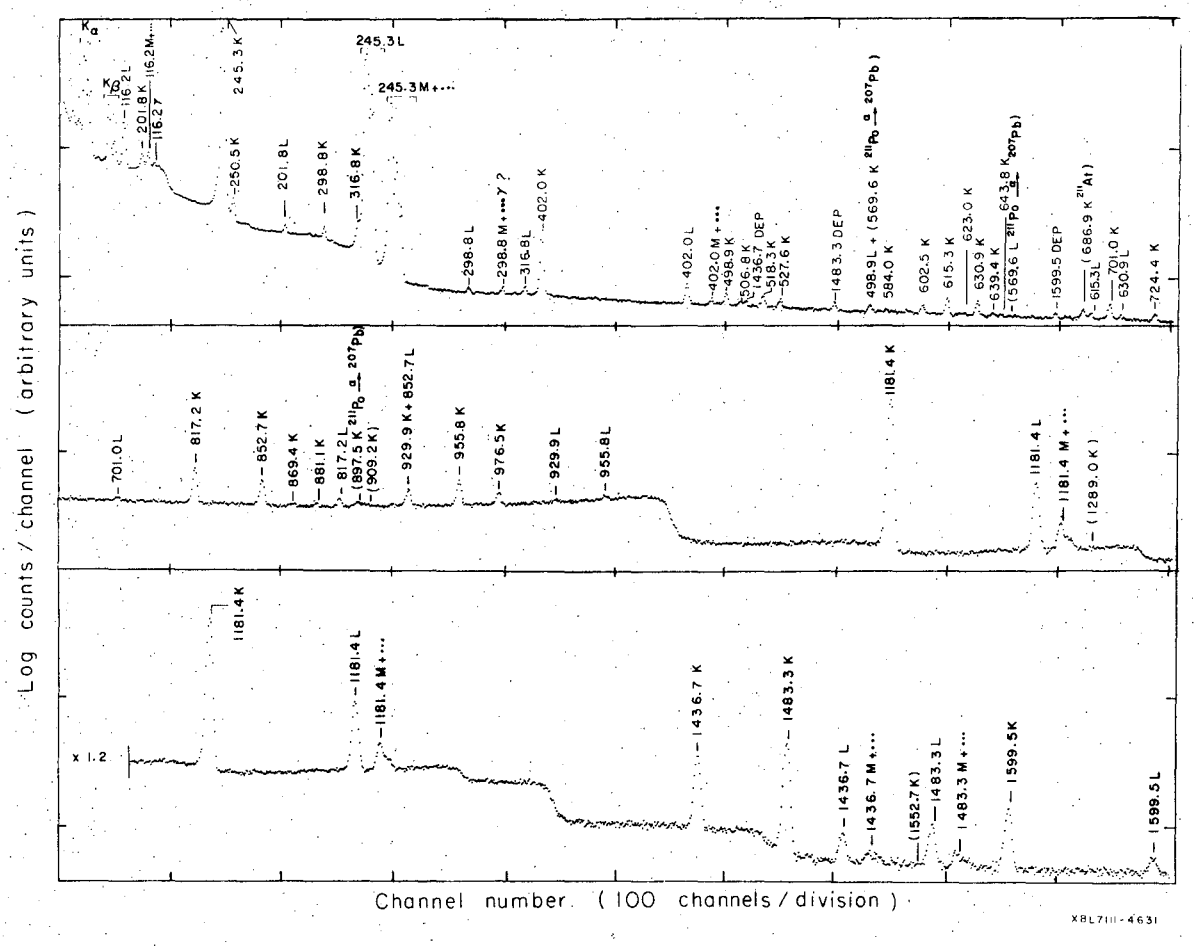

Fig. 36. Conversion-electron spectrum of ^{210}At in the energy range of 60-1600 keV.

Table 5. Experimental and theoretical internal conversion coefficients: ^{210}At.

Transition Energy keV	Experimental[c] conversion coefficient (10^{-3})	Theoretical[a] conversion coefficient			Assigned Multipolarity
		E1(10^{-3})	E2(10^{-3})	M1(10^{-3})	
46.6	$(\alpha_{L1} + \alpha_{L2})/\alpha_{L3}$ = 1010(80)	1980	1060	132800	E2
116.2	α_L = 1220 (140)	504	2580	1100	M1
	α_M = 299 (35)	11.9	687	259	
201.8	α_K = 1240 (110)	65.3	165	1290	
	α_L = 220 (22)	11.9	221	227	M1
	α_M = 50 (10)	2.8	58.2	53.5	
245.3	α_K = 110 (13)	41	107	747	
	α_L = 102 (18)	7.28	98.6	131	E2
	$(\alpha_{L1} + \alpha_{L2})/\alpha_{L3}$ = 2320(240)	6600	2500	160000	
250.5	α_K = 700 (140)	39	102	705	M1
298.8	α_K = 440 (44)	26	68.2	434	M1
	α_L = 81 (9)	4.5	45.4	76.1	
316.8	α_K = 314 (65)	22.7	59.8	370	M1(+E2)
	α_L = 62 (8)	3.91	36.4	64.8	

(continued)

Table 5 (continued)

Transition Energy keV	Experimental[c] conversion coefficient (10^{-3})	Theoretical[a] conversion coefficient			Assigned Multipolarity
		E1(10^{-3})	E2(10^{-3})	M1(10^{-3})	
402.0	α_K = 212 (15)	13.4	35.4	195	
	α_L = 37 (4)	2.26	15.5	33.9	M1
	α_M = 9.6 (10)	0.0527	0.395	7.97	
498.9	α_K = 110 (10)	8.52	22.4	109	M1
506.8	α_K = 9.2 (1.2)	8.25	21.7	105	E1
518.3	α_K = 107 (11)	7.88	20.7	99.0	M1
527.6	α_K = 8.3 (8)	7.60	20.0	94.4	E1
584.0	α_K = 7.0 (11)	6.20	16.3	72.3	E1
602.5	α_K = 80 (12)	5.83	15.3	66.6	M1
615.3	α_K = 59 (5)	5.59	14.7	63.0	M1
623.0	α_K = 6.4 (11)	5.46	14.3	61.0	E1

(continued)

Table 5 (continued)

Transition Energy keV	Experimental[c] conversion coefficient (10^{-3})	Theoretical[a] conversion coefficient			Assigned Multipolarity
		E1(10^{-3})	E2(10^{-3})	M1(10^{-3})	
630.9	α_K = 57 (5)	5.32	14.0	59.1	M1
	α_L = 12.5 (16)	0.903	4.10	10.8	
639.4	α_K = 12.5 (17)	5.19	13.6	57.0	E2
643.8	α_K = 4.7 (8)	5.12	13.5	56.0	E1
701.0	α_K = 39 (4)	4.35	11.4	44.9	M1(+ E2)
	α_L = 6.5 (11)	0.694	2.87	7.69	
724.7	α_K = 40 (4)	4.08	10.7	41.2	M1
817.2	α_K = 30 (2)	3.26	8.52	30.2	M1
	α_L = 5.5 (5)	0.514	1.93	5.13	
852.7	α_K = 24 (2)	3.01	7.87	27.0	M1
869.4	($\alpha_K \leq$ 17 (4))[b]	2.91	7.59	25.7	(M1 + E2)[b]
881.1	α_K = 18.4 (25)	2.84	7.4	24.8	M1 + E2

(continued)

Table 5 (continued)

Transition Energy keV	Experimental[c] conversion coefficient (10^{-3})	Theoretical[a] conversion coefficient			Assigned Multipolarity
		E1(10^{-3})	E2(10^{-3})	M1(10^{-3})	
909.2	(α_K < 23)[b]	2.68	6.98	22.9	(E2 ?)[b]
929.9	α_K = 20 (2)	2.57	6.69	21.6	M1
	α_L = 4.1 (5)	0.403	1.41	3.68	
955.8	α_K = 19 (2)	2.45	6.36	20.1	M1
	α_L = 3.3 (4)	0.383	1.32	3.42	
976.5	α_K = 19 (2)	2.36	6.11	19.1	M1
1181.4	α_K = 4.31 (0)[c]	1.69	4.31	11.7	pure E2
	α_L = 0.80 (7)	0.26	0.821	1.98	E2
1201.2	(α_K < 12.5)	1.64	4.19	11.2	(E2)[b]
1205.4	(α_K < 2.5)	1.63	4.16	11.1	(E1 + < 15% M2)[b]
1289.0					(E3 or E1 + < 32% M2)
1436.7	α_K = 1.13 (10)	1.21	3.03	7.12	E1
	α_L = 0.18 (2)	0.184	0.542	1.20	

(continued)

Table 5 (continued)

Transition Energy keV	Experimental[c] conversion coefficient (10^{-3})	Theoretical[a] conversion coefficient			Assigned Multipolarity
		E1(10^{-3})	E2(10^{-3})	M1(10^{-3})	
1483.3	α_K = 1.06 (10)	1.14	2.86	6.56	E1
	α_L = 0.17 (2)	0.174	0.508	1.10	
1552.7					(E1 + < 21% M2)[b]
1599.5	α_K = 0.93 (10)	1.01	2.50	5.41	E1

[a]Theoretical values were obtained by computer interpolation[43]) from the tables of Hager and Seltzer[42]).

[b]Only a limit could be set on the conversion electron intensity, as discussed in text, so that the assigned multipolarity is tentative.

[c]These (relative) conversion coefficients were measured relative to the 1181.4 keV ($2^+ \rightarrow 0^+$) transition which was assumed to be a pure E2 transition. (See Appendix F for a detailed discussion of the method.)

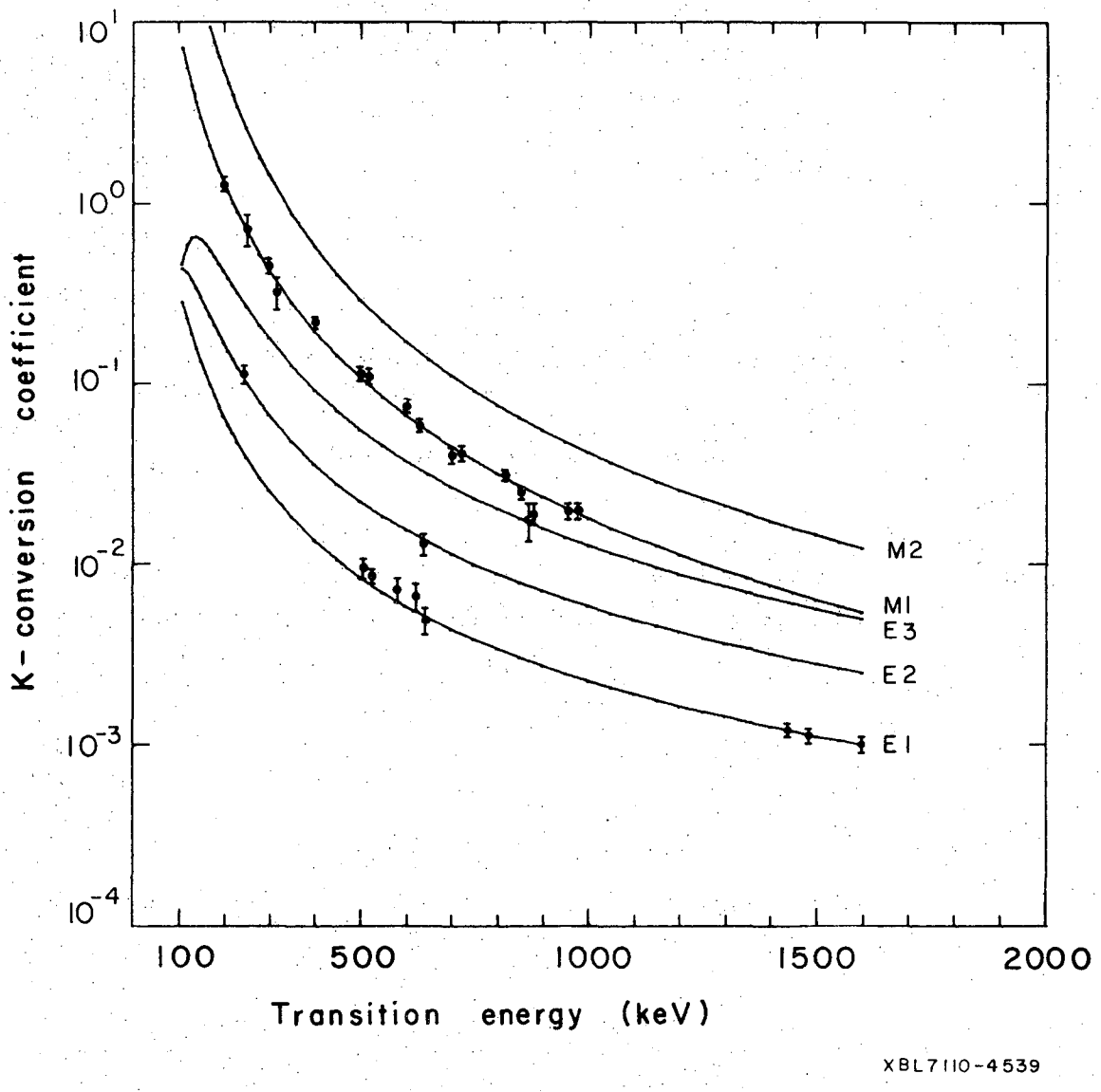

Fig. 37. Comparison of experimental K-conversion coefficients with the theoretical values of Hager and Seltzer[42]. Lines are theoretical values[42]) and points are experimental values measured relative to the 1181.4 keV E2 transition.

of Hoff and Hollander[25]), our observation of a weak γ-ray transition at 201.8±0.2 keV suggests that at least one of the L-conversion lines reported by these authors should be assigned as the K-conversion line of the new transition. Assuming this, the measured value of α_L for the 201.8 keV transition is also consistent with the multipolarity assignment of M1 obtained from the K-conversion coefficient of this transition.

83.4-keV transition: Hoff and Hollander[25]) reported the existence of weak conversion lines from ^{210}At decay which could be assigned to a transition at this energy having E2 multipolarity. Because of low intensity and poor resolution this transition was not observed in our measurements or in the previous study by Prussin and Hollander[27]). However, in the recent in-beam studies by Bergström, Fant, and Wilkström[37]), an 83.7-keV transition has been identified as the transition between the 8^+ and 6^+ members of the $(h_{9/2})^2$ ground state band in ^{210}Po. These data place the location of the 8^+ level at about 1557 keV. Recent ^{209}Bi(α,t) studies by Tickle and Bardwick (TB)[28]) and Lanford[29]) also place a level at this energy (±5 keV). With our present data, we have obtained evidence for weak population of this level following decay of ^{210}At and it is then reasonable to associate the transition reported by Hoff and Hollander with the decay of this level.

E. ^{210}At Decay Scheme

1. Introduction

To facilitate the presentation and detailed discussion of the level scheme in the next sections, a brief description of the expected levels and configurations is given. For ^{210}Po we will first assume that there is no residual interaction between the two protons outside the ^{208}Pb core in order to make some zero-order energy estimates of the expected level structure. A schematic representation of the ^{210}Po ground state and neighboring experimental[9]) single-particle states is given in fig. 38. A 0^+ ground state would be expected as is observed for all even-even nuclei (because of the large pairing energy of 0^+ states) with the configuration $(\pi(h_{9/2})^2\ \nu(p_{1/2})^2)_{0^+}$. Taking the three lowest configurations for the 83rd proton from ^{209}Bi experimental data, one can estimate the energies of a number of excited states of different spin for ^{210}Po. If there were no residual interaction between the 83rd and 84th protons of ^{210}Po, each ^{210}Po configuration would have an energy just equal to the sum of the energies of the <u>two</u> ^{209}Bi levels from which it arises. We have listed in Table 2 of section IIB the six possible degenerate ^{210}Po configurations obtained for a three orbital shell model estimate with their spins, parities and (zero-order) energies uncorrected for the proton-proton interaction. These results predicted degenerate levels at 0, 897, 1609, 1794, 2506 and 3218 keV. Because of the residual interaction, however, some of these configurations will be depressed in energy while others will remain unshifted.

In addition to these two-proton states as described above, excited states will occur in ^{210}Po due to excitation of the ^{208}Pb core. The first

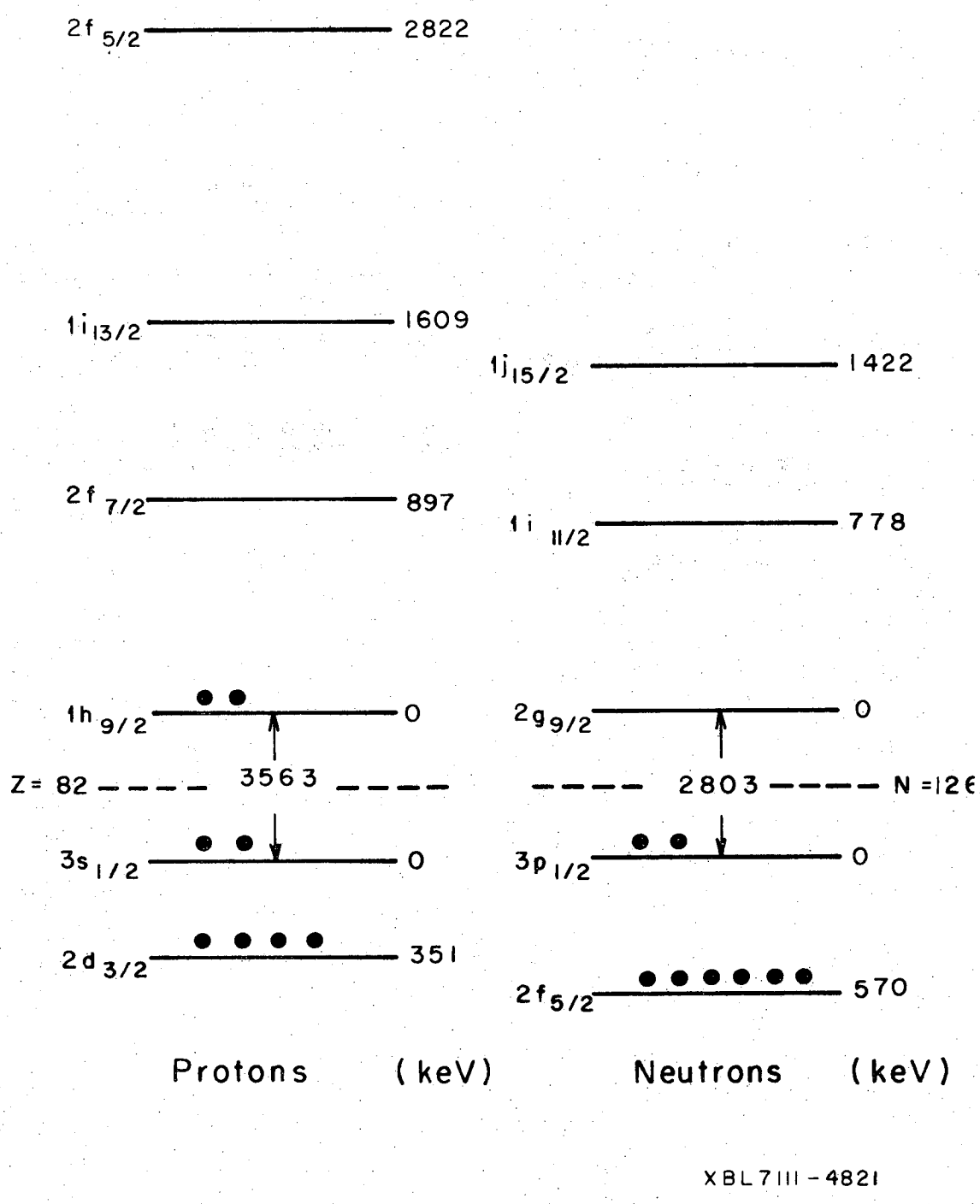

Fig. 38. Representation of the ^{210}Po ground-state and neighboring experimental[9]) single-particle states.

three levels of ^{208}Pb are at 2614 keV (3^-), 3198 keV (5^-) and 3475 (4^-). The 3^- level is a collective state due to many protons and neutrons and the 5^- and 4^- levels are primarily due to neutron excitations from breaking the N = 126 shell to produce two states of the configuration $\nu(g^1_{9/2}\ p^{-1}_{1/2})_{4^-,5^-}$. Consideration (from the schematic diagram of fig. 38) of the single-particle orbitals in this region estimates the 4^- and 5^- neutron levels as degenerate at an energy of approximately 2803 keV (plus the energy to break a pair of $(p_{1/2})^2$ neutrons). More complex excitations of ^{208}Pb are known[9] to occur in the energy range $\lesssim$ 4 MeV. These excitations should produce states which appear in the ^{210}Po level structure but we will not consider them further in this treatment.

In summary our crude calculations predict a band of even-parity states of the configuration $\pi(h_{9/2})^2$ which start with the ground state and have spins 0, 2, 4, 6, 8. Next a series of even parity states of the configuration $\pi(h_{9/2}\ f_{7/2})$ which should be approximately 900 keV above the least depressed $\pi(h_{9/2})^2$ level followed by the 3^- collective core state. Finally a series of odd-parity states due to the $\pi(h_{9/2}\ i_{13/2})$ configurations and neutron core states are predicted at approximately 3 MeV. At higher excitation two proton states and additional core excitations might be expected.

2. The Level Scheme

For the construction of the new level scheme shown in fig. 39, γ-γ coincidence measurements and, in the case of the weaker transitions, sum-difference relationships when supported by recent reaction

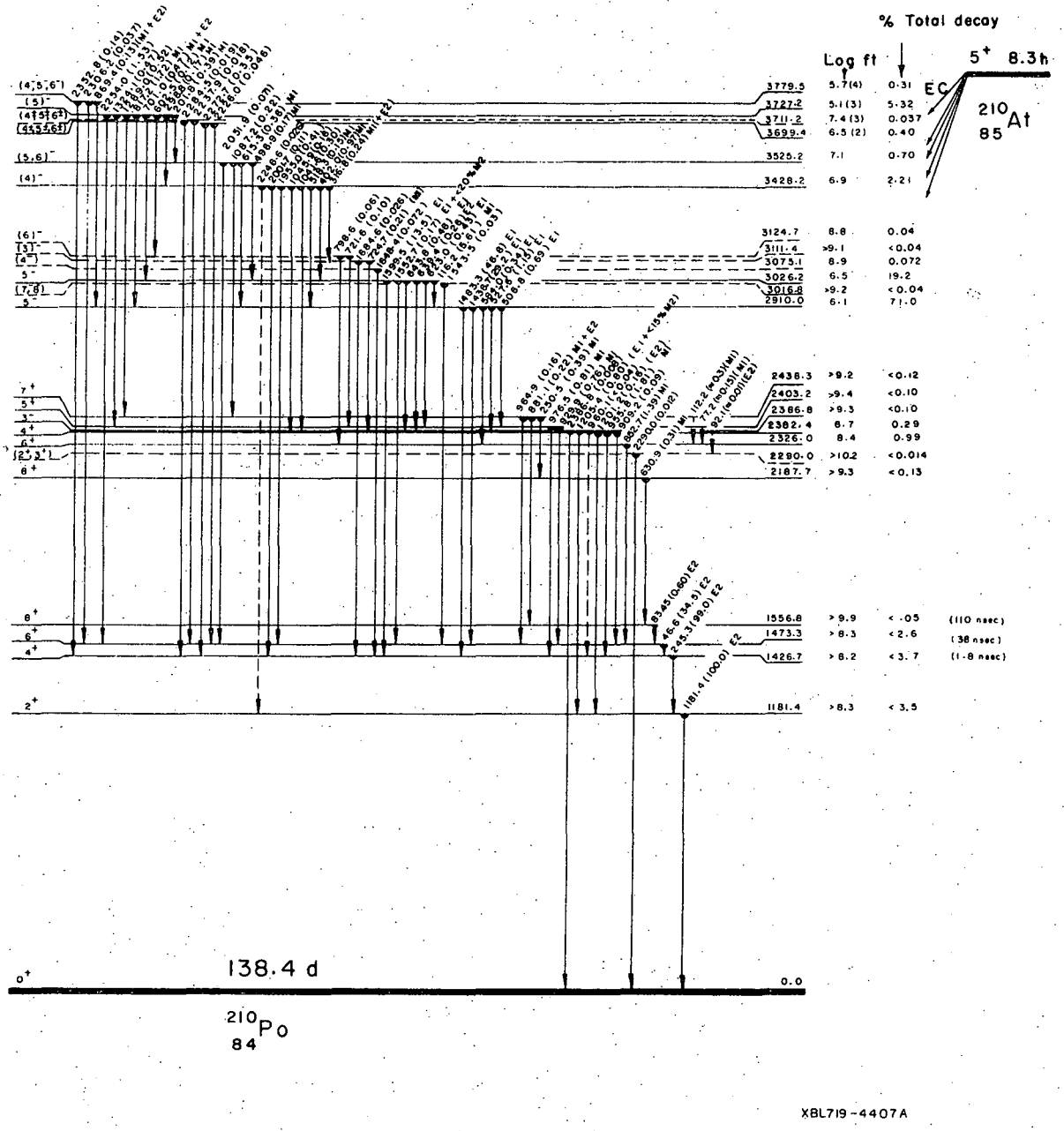

Fig. 39. Experimental decay scheme of ^{210}At. (Absolute transition intensities are shown on the level scheme.)

studies[28,29,30]) have been used. Twenty-two excited states are proposed as populated in the electron-capture decay and succeeding gamma decay. These data permit the identification of eight new levels over the previous study by Prussin and Hollander[27]). The levels shown in fig. 39 with broken lines are relatively uncertain and should be taken as only tentatively identified in this work. Spin and parity assignments are based upon previously reported data, our new conversion electron measurements, and the results of recent reaction studies[28,29,30]). Figure 40 shows the results obtained in the reaction studies plus the composite ^{210}Po level structure deduced by a comparison of the levels observed in the electron-capture decay and those populated in the reaction studies.

For convenience, the levels will be discussed in related groups which correspond to levels arising from dominant configurations based on predictions of shell model calculations[25,31,32]) and our previous discussion on the expected level structure.

a. Even Parity Levels in the Energy Range 0-1556 keV

These levels are believed to have the dominant configuration $\pi(h_{9/2})^2_{J^+}$.

1. 1181.4, 1426.7, and 1473.3 keV Levels - $2^+,4^+,6^+$

The previously measured E2 multipolarities for the 1181.4, 245.3 and 46.6 keV transitions[24,25,26,27]), the angular distribution measurements[44]) and the new reaction studies (shown in fig. 40) have established the spin and parity assignments for the 1181.4, 1426.7, and 1473.4 keV levels at 2^+, 4^+, and 6^+, respectively. Our internal conversion coefficients (Table 5) support these previous assignments.

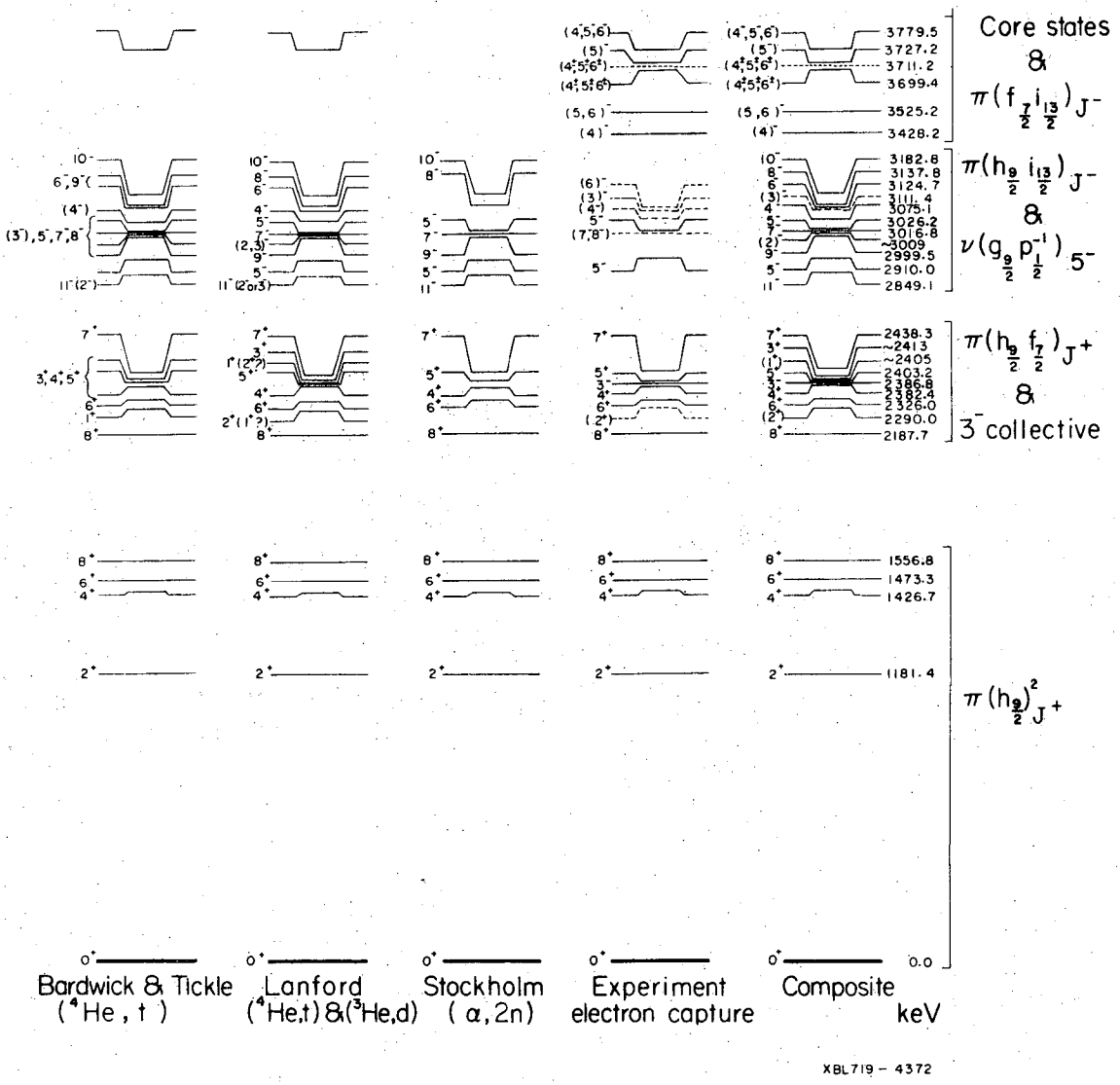

Fig. 40. Summary of available data on levels in ^{210}Po below 4 MeV. The spin and parity assignments given in the composite level diagram have been deduced by a comparison of the data from reaction studies and the electron-capture decay of ^{210}At. (Note that the spin and parity of the level at 3727.2 (in composite level diagram) should read $(5)^-$ not (5^-).)

2. 1556.8 keV Level - 8^+

The energy of this level was first inferred by Yamazaki and Ewan[45,46]) and has been established in the $^{209}Bi(\alpha,t)$, $^{209}Bi(^3He,d)$ and $^{208}Pb(\alpha,2n)$ reaction studies (fig. 40) of Tickle and Bardwick (TB)[28]), Lanford[29]) and Bergström et al.[30]). The preliminary report by Bergström et al.[30]) gives the energy of the $8^+ \rightarrow 6^+$ transition as 83.5 keV. While we have not been able to resolve the L-shell conversion electron lines from this transition due to the intense Auger electron lines in the conversion electron spectrum, the high resolution magnetic spectrographic results of Hoff and Hollander[25]) clearly indicated the presence of such a line of E2 multipolarity in the decay of ^{210}At. By assigning this transition as the $8^+ \rightarrow 6^+$, we have been able to observe the weak feeding of the 8^+ level from the 8^+ and 7^+ levels at 2187.7 and 2338.3 keV, respectively. Our coincidence data on the 630.9, 250.5, and 1289.0 keV cascade and energy sum data are consistent with the population of this level.

All levels of the $\pi(h_{9/2})^2_{J^+}$ configurations are believed identified as described above. The 4^+, 6^+ and 8^+ levels have measurable half-lives in the nanosecond range (due to the low energy E2 transitions[37,44,45,46,47])). The half-life of the 6^+ level was remeasured by a delayed coincidence measurement of the 1436.7-245.3 keV gamma-ray cascade as 40±6 nsec in agreement with the value 38±5 nsec reported by Funk et al.[44]). Shown in fig. 41 (with the appropriate random background subtractions performed) are the time (TAC) spectra for the 1436.7-245.3 keV (delayed) and 1483.3-245.3 keV (prompt) gamma-ray cascades obtained from our three parameter coincidence data in section IVD2. The shape of the 1483.3-245.3 keV cascade time spectrum was

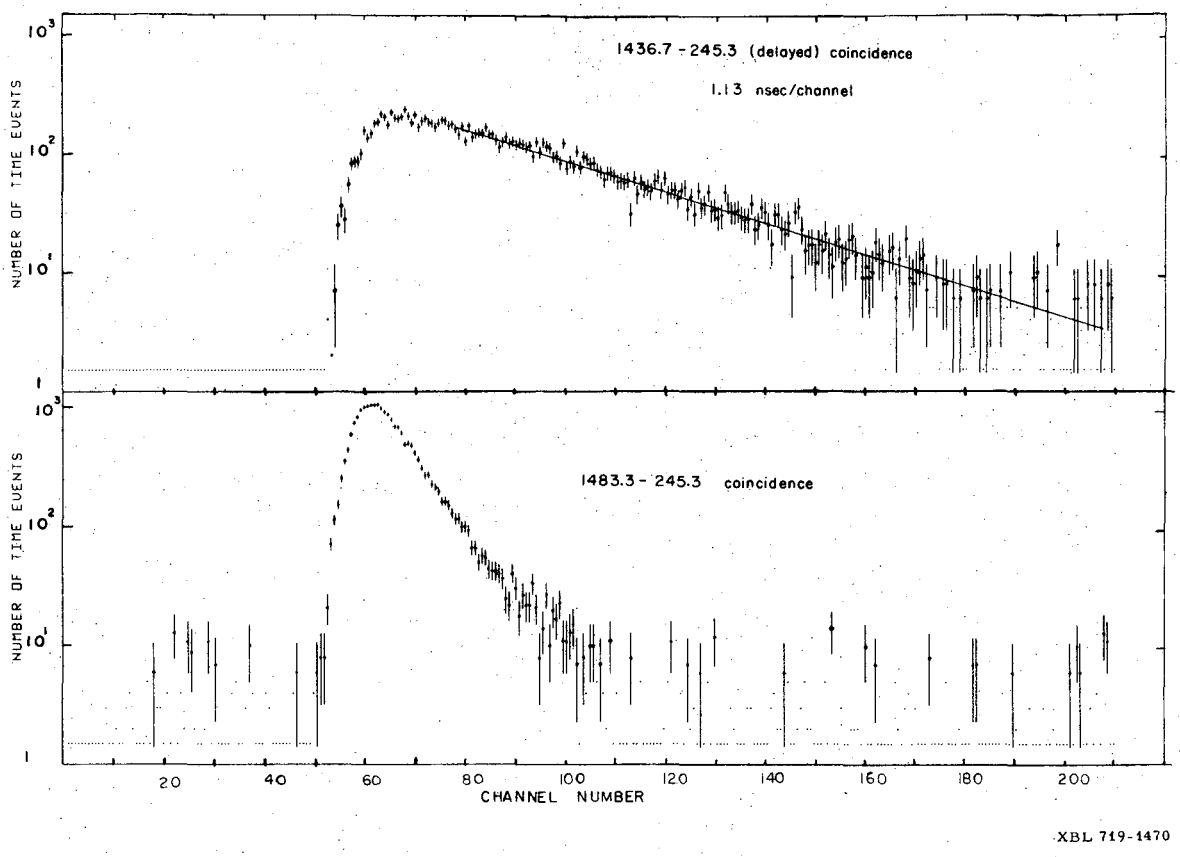

Fig. 41. Time distribution curves for the 1436.7-245.3 and 1483.3-245.3 keV gamma-ray cascades. Stop pulses (with a fixed delay) for the pulse-height circuitry were supplied by the 245.3 keV photopeak and start pulses by the 1436.7 and 1483.3 keV photopeaks.

used for the prompt component shape subtracted for the 1436.3-245.3 keV cascade time spectrum to extract the half-life of the 6^+ level as 40±6 nsec. The half-life of the 8^+ level could not be measured by this technique because the population in the electron-capture decay was too weak (~ 0.6% of the decays). However, it has been measured as 110±10 nsec by in-beam techniques[37,47].

b. Even Parity Levels in the Energy Range 2187-2438 keV

These levels are believed to have the dominant configuration $\pi(h_{9/2}\ f_{7/2})_{J^+}$.

1. 2382.4 and 2403.2 keV Levels - $5^+,4^+$

These levels were established by Prussin and Hollander[27]) and we have been able to observe several new weak transitions involving these levels. The spin and parity of the 4^+ level at 2382.4 keV is established in our work through the 527.6 keV E1 transition from the 5^- level at 2910.0 keV and by the 1201.2 (M1 + E2) and 955.8 keV (M1) transitions which connect this level to the 2^+ and 4^+ levels at 1181.4 and 1426.7 keV. This assignment is consistent with the results of the reaction studies shown in fig. 40. The spin and parity of the 5^+ level at 2403.2 keV is established by the 976.5 and 929.9 keV M1 transitions to the 4^+ and 6^+ levels at 1426.7 and 1473.3 keV and this assignment is also consistent with the reaction studies.

2. 2326.0 keV Level - 6^+

The data obtained in ref. [27]) established a tentative level at either 2278 or 2325 keV which decayed via the 852.7 keV transition to either the 4^+ or 6^+ levels at 1426.7 or 1473.3 keV. Our γ-γ coincidence data show that the 852.7 keV transition is in delayed coincidence with

the 245.3 and 1181.4 keV transitions. This result along with the apparent absence of a transition at 125.2 keV (Section IVD3) indicates the existence of a level at 2326.0 keV.

A level at this energy has also been observed in the reaction studies (fig. 40), and a spin and parity 6^+ is indicated from these data. The measured M1 multipolarity of the 852.7 keV and the E1 multipolarity of the 584.0 keV transition from the 5^- level at 2910.0 keV are consistent with the 6^+ assignment. The 584.0 and 852.7 keV transitions are also in prompt coincidence.

We note here, evidence for the existence of a transition of 77.2 keV which connects the 5^+ level at 2403.2 keV to the 6^+ level at 2326.0 keV. By re-examination of the original ^{210}At magnetic conversion electron spectrographic plate taken by Hoff and Hollander[25]) in the Auger region, it was noted that the 60.2 keV ($K - L_{II}L_{II}$) line seemed too intense by a factor of about 1.7 compared to the same Auger line in the spectrum of ^{211}At. No other electron lines were observed which could be associated with this line indicating that this line might correspond to an L_1 conversion line of a weak 77.2 keV M1 transition. (In section J we discuss how these lower energy $\pi(h_{9/2}\ f_{7/2})_{J_i^+} \rightarrow \pi(h_{9/2}\ f_{7/2})_{J_f^+}$ transitions might favorably compete.)

3. <u>2187.7 and 2438.3 keV Levels - $8^+,7^+$</u>

The levels at 2187.7 and 2438.3 keV have been observed in reaction studies[28,29,30]) and spin and parity assignments of 8^+ and 7^+ have been made, respectively. These assignments are consistent with our measured M1 multipolarities for the 630.9, 881.1, 250.5 keV transitions involving

these levels. Since these levels are only populated weakly through radioactive decay, our data remain insufficient to clearly define the spins, but are consistent with the 8^+ and 7^+ assignments from reaction studies.

We again note a possible transition of 112.3 keV from the 7^+ level 2438.3 keV to the 6^+ level at 2326.0 keV. Hoff and Hollander[25]) reported an unassigned electron line at 85.27 keV which might be the L_1 conversion line of such an M1 transition.

4. 2290.0 Tentative Level-(2^+)

This level is tentatively defined on the basis of the (α,t) studies[28,29]) which suggest a level with a spin and parity of 1^+ or 2^+ in this region (2285 ± 5 keV) and by our 2290.0 keV transition to the ground state of ^{210}Po and by decay of the 4^+ level at 2382.4 keV. The latter transition (92.0 keV) was identified by Hoff and Hollander[25]) as a probable E2 transition. If our identification is correct and corresponds to the same level observed in the reaction studies[28,29]) a spin of 2 (or 3) seems most likely for this level. The $(2^+) \rightarrow 2^+$ transition to the 1181.4 keV level was too weak to be observed in our spectra so that this must remain a tentative level.

c. Odd Parity Level at 2386.8 keV

The odd parity of this level was established from the 639.4 keV E2 transition from the 5^- level at 3026.2 keV. Figure 42 shows a portion of the gamma-ray spectrum in the 640 keV region with the corresponding K-conversion electron spectra. A qualitative inspection of fig. 42 also supports the assignments of the 615.3 and 630.9 keV (as M1) and the 623.0

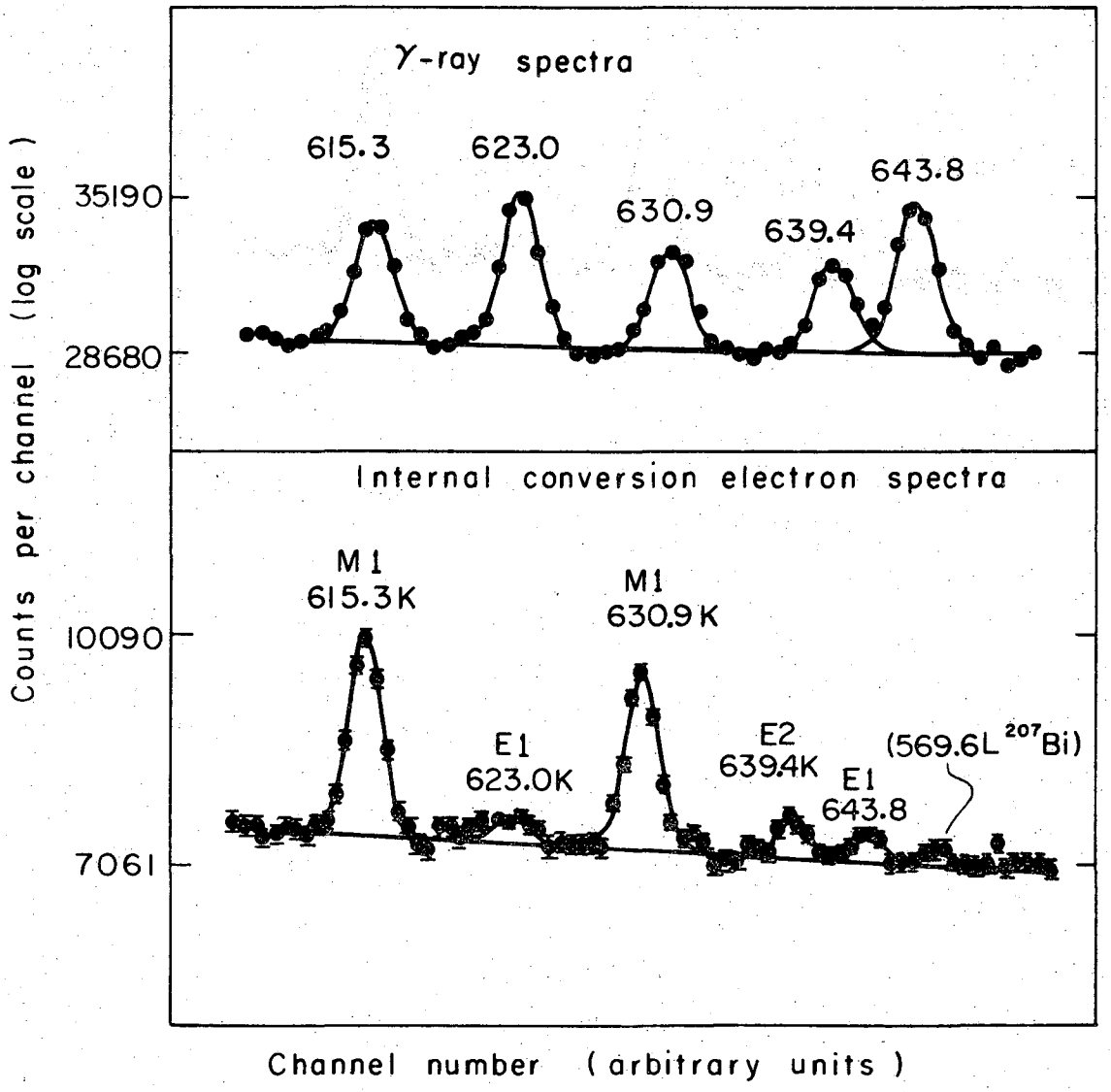

Fig. 42. Spectrum of gamma-rays (top) and conversion-electrons (bottom) from 610-650 keV transitions of ^{210}At decay.

and 643.8 keV (as E1) transitions; each pair being of the same multipolarity, but different from each other. The relative increase of the 639.4 keV K-conversion electrons relative to the 623.0 and 643.8 keV E1 transitions support the 639.4 keV E2 assignment. The L-conversion line of the 569.6 keV transition in ^{207}Pb is also present in Fig. 42. This state was populated from the alpha decay of ^{211}Po and/or the electron capture-decay of ^{207}Bi. Both isotopes are produced from the decay of ^{211}At present in the ^{210}At sources. The 569.6 keV transition (^{211}Po alpha decay) was also observed in the gamma-ray spectra (e.g. see fig. 8).

The 639.4 keV E2 transition from the 5^- level at 3026.4 keV limits the spin and parity of the 2386.8 keV level to the range of $(3\text{-}7)^-$, but the 2386.8 keV transition to the 0^+ ground state further limits the assignment to $(3,4)^-$. The 1205.4 keV gamma-ray which is in coincidence with the 639.2 keV transition to the 2^+ level at 1181.4 keV, can only be limited to E1 (+ < 15% M2) on which the assignment 3^- is favored.

The 1205.4 keV K-conversion electrons were not detectable above background in our electron spectrum of fig. 36 so that a limit had to be set on the maximum observable intensity above background. The limit was set by using the 1181.4 keV K-line as the standard line shape for various electron peak areas expected as detectable for the 1205.4 keV transition. Consideration of the energy region where the K-conversion electron peak occurs allowed a conservative limit of 1000 counts above background for the maximum non-observable peak to be set. The maximum M2 admixture from such an intensity is 15% so that the 1205.4 keV

transition was limited as E1 (+ < 15% M2). This limit favors the 3^- assignment for the 2386.8 keV level (which is probably the collective 3^- state as discussed in Section H).

d. Odd Parity Levels in the Energy Range 2849-3183 keV

These levels are believed to have the dominant configurations $\pi(h_{9/2}\, i_{13/2})_{J^-}$ and $\nu(g_{9/2}\, p^{-1}_{1/2})_{5^-}$.

1. 2910.0 and 3026.2 keV Levels-5^-

The parity of these levels has been established as odd in previous studies[24,25,26,27]) and the spin assignment of 5 to the 2910.0 keV level is also well established. The spin of the 3026.2 keV level has been established a 5 by determination of the multipolarity of the 1552.7 keV transition (to the 6^+ level at 1473.3 keV) as E1 + (< 20% M2). The 1599.5 keV E1 transition to the 4^+ level at 1426.7 keV then establishes this level as 5^-.

Shown in fig. 43 is a portion of the conversion electron spectrum in the energy region of the 1552.7 keV K-conversion lines. The proposed peak shapes (dotted lines) for the 1552.7 keV transition in fig. 43 have been calculated for transitions of either 100% M2 or 100% E1. Because of the relatively low background (~ 520 counts), a limit of 300 counts was set for the maximum unobservable electron intensity above background which limit the maximum M2 admixture as 20% for the 1552.5 keV transition.

The 5^- spin assignment for the 3026.2 keV level had been suggested by Schima *et al.*[26]) from angular distribution measurements on the 1599.5-245.3 keV gamma-ray cascade. Prussin and Hollander[27]) favored a $(4)^-$ assignment based on the large difference in the gamma-ray

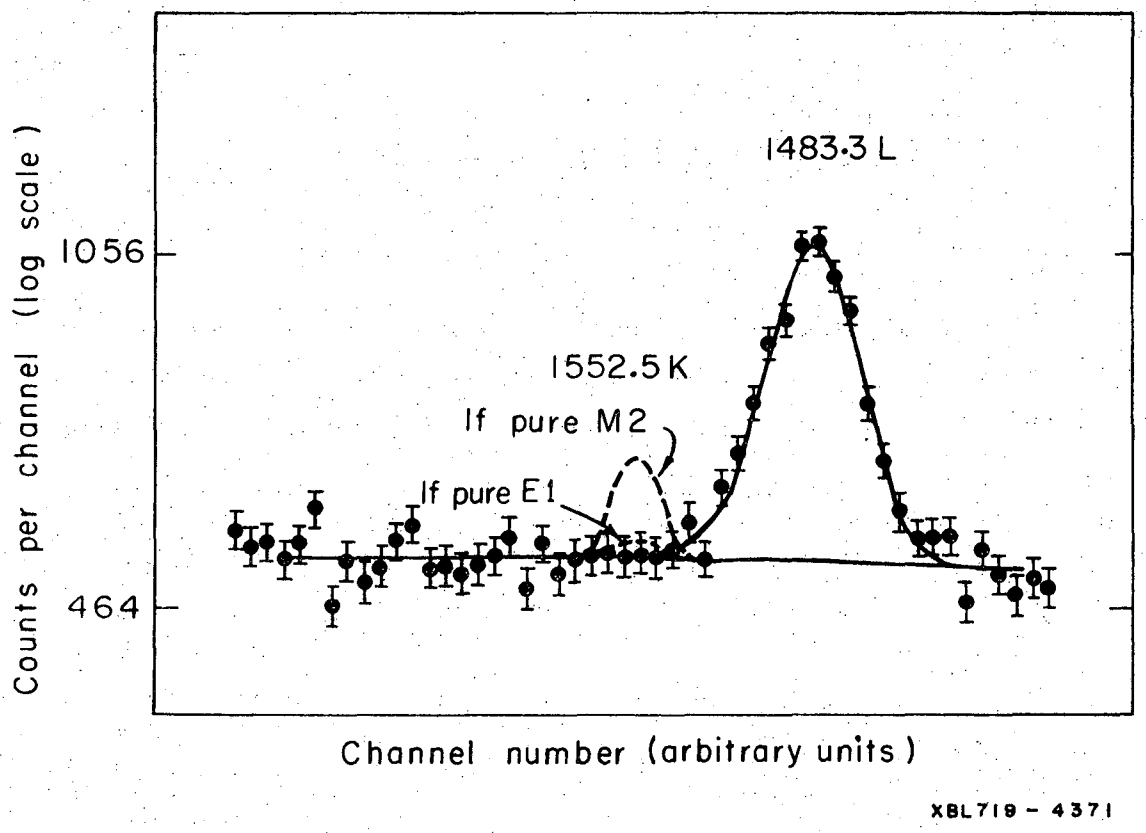

Fig. 43. Spectrum of conversion electrons in the energy range of 1440-1480 keV. The dotted lines for the 1552.5 K electron peak represent the theoretical intensities for pure M2 and E1 transitions.

branching ratio I_{1599}/I_{1552} as compared to the ratio I_{1483}/I_{1436} for the analogous decay of the 5^- level at 2910.0 keV. That this argument was weak can now be realized since the forbidden E1 transitions from these two levels must take place thru small admixtures in the wavefunctions. Any slight variations in the amplitudes that make up the initial and final states can seriously effect the gamma-ray branching ratios. Two possible mechanisms that could allow the gamma-ray transitions to take place could be for example small amplitudes of $\pi(h_{9/2}\ h_{11/2})_{J^+}$ in final states or $\pi(h_{9/2}\ i_{11/2})_{J^-}$ in the initial states. The allowed E1 transitions could then take place through the components

$$\pi(h_{9/2}\ i_{13/2})_{J^-} \xrightarrow{E1} \pi(h_{9/2}\ h_{11/2})_{J^+} \text{ or } \pi(h_{9/2}\ i_{11/2})_{J^-} \xrightarrow{E1} \pi(h_{9/2})^2_{J^+}.$$

(As will be discussed in Section I, these two 5^- levels are believed to arise from two dominant configurations $\pi(h_{9/2}\ i_{13/2})_{5^-}$ and $\nu(g_{9/2}\ p_{1/2}^{-1})_{5^-}$.)

The remaining levels in this group are tentatively identified through weak gamma-ray transitions observed in our work and we have combined these data with the preliminary results from recent reaction studies to arrive at suggested spin and parity assignments. Due to small level spacings and poor statistics, substantial differences exist between the conclusions drawn by (TB)[28]) and Lanford[29]). In the decay scheme of fig. 39 we have therefore indicated the most reasonable spin and parity assignments based upon available data and have given in fig. 40 a summary of all data available on the levels of the $\pi(h_{9/2}\ i_{13/2})$ multiplet.

2. 3075.1 keV Level-(4^-)

The level shown at 3075.1 keV may be identified with that observed in the reaction studies which have been assigned a spin and parity of 4^-. (We have only observed a single gamma-ray transition defining this level.)

3. 3124.7 keV Level-$(6)^-$

This level is established from the fact that the 602.5 and 721.6 keV transitions are in coincidence. The level at 3124.7 keV has been seen by both TB[28]) and Lanford[29]) but was not identified in the (α,2n) studies of Bergström et al.[31]). Our gamma-ray data establish the parity as odd and limit the likely spin assignment to the range 4, 5, 6. With the assumption that this level is due primarily to the two proton configuration $\pi(h_{9/2}\ i_{13/2})$, we tentatively identify this level with the 6^- level defined by Lanford. Although the original analysis ty TB[28]) was in conflict with this conclusion, a reanalysis[48]) of the data taking into account fragmentation over two 5^- states at 2910.0 and 3026.2 keV resulted in agreement with Lanford[29]).

The assumption that this level is due to the $h_{9/2}\ i_{13/2}$ configuration seems reasonable through the following arguments. First the only likely core excitation leading to levels in this energy range is the neutron configuration $\nu(g_{9/2}\ p_{1/2}^{-1})$. Secondly as discussed in section I electron-capture in ^{210}At proceeding to core-excitation in ^{210}Po should occur with much higher probabilities than those to levels of the simple two proton configuration of the 83rd and 84th protons of ^{210}Po. (Note here the low values of log ft for transitions to the 5^- levels in this region.)

4. 3016.8 keV Tentative Level-$(7^-,8^-)$

We have tentatively included a level at 3016.8 keV in agreement with the results of the reaction studies of TB[28]) and Lanford[29]). The level is defined by only a single gamma-ray transition to the 6^+ level at 1473.3 keV and thus its spin is probably limited to the range 4-8. We favor a likely assignment of 7^-, 8^- to this level.

5. 3111.4 keV Tentative Level-$(3)^-$

The remaining level in this region was established from weak coincidence data on the 316.8-724.7-1205.4 keV gamma-ray cascade (section IVD2). The level at 3111.4 keV was unresolved in the reaction studies and its decay to the 3^- level at 2386.8 keV by an M1 transition defines the parity as odd and limits spin to the range 2-4. The weak population of this level in β-decay rules out its assignment as the 4^- member of the neutron excitation $\nu(g_{9/2}\ p^{-1}_{1/2})$. The M1 decay to this level from the $(4)^-$ level at 3482.2 keV then suggests a tentative spin and parity assignment of $(3)^-$. Finally if this is the 3^- state of the $\pi(h_{9/2}\ i_{13/2})$ configuration, the possibility exists that this state may contain a small collective 3^- component from the 2386.8 keV state (section G).

In summary, levels in this energy region (2800-3400 keV) are expected to arise predominantly from the two proton configuration $\pi(h_{9/2}\ i_{13/2})_{J^-}$ and evidence from this study and previous studies[25,27]) have also established the importance of contributions from excited states of the ^{208}Pb core. In particular, the lowest energy core excitation is the neutron configuration $\nu(g_{9/2}\ p^{-1}_{1/2})_{5^-}$ (in analogy with ^{208}Pb) at approximately 3200 keV. The corresponding 4^- core configuration should

occur several hundred keV higher in energy and is consistent with our observation of two 5^- and one (4^-) states in this energy region. Of the $\pi(h_{9/2}\ i_{13/2})_{J^-}$ configurations, only the 2^- member remains unassigned since the levels of the multiplet with spins 8, 9, 10, and 11 have been identified from reaction studies. We have included these in the composite level scheme shown in fig. 40. The location of the levels with spins 10 and 11 at energies of 3183 and 2849 keV seem well defined. However, the definite assignment of spins 8 and 9 to the levels at 3138 and 3009 keV respectively is open to question as reaction data are in conflict here. Both Bardwick and Tickle[28]) and Lanford[29]) have argued for an unresolved doublet at about 2845 keV composed of the 11^- and (possibly) 2^- members of this multiplet. With our tentative assignment of the $(3)^-$ member at 3111.4 keV, it would appear that the 2^- member might belong in the quartet of states in the energy range 3000-3030 keV. While reaction studies require a greater strength at 2845 keV than can be accounted for by the 11^- level alone, this may reflect a relatively weaker strength for the lower spin members of the multiplet due to configuration mixing with the $\pi(f_{7/2}\ i_{13/2})_{J^-}$ states. The calculations of Kim and Rasmussen[32]) locate the levels of the $\pi(f_{7/2}\ i_{13/2})$ proton multiplet at about 800-1000 keV above the corresponding $\pi(h_{9/2}\ i_{13/2})$ multiplet. Configuration mixing between these two configurations would leave the 2^- and 11^- members of the $\pi(h_{9/2}\ i_{13/2})$ multiplet pure and give them an apparent greater intensity in the (α,t) or $(^3He,d)$ studies relative to the remaining levels of the $\pi(h_{9/2}\ i_{13/2})$ configuration.

e. Levels in the Energy Range 3428-3780 keV

These levels are all populated rather strongly in the decay of ^{210}At (log ft $\cong$ 5.1 - 7.1) which may indicate large core components due to both proton and neutron excitations (in anology with ^{208}Pb excited states in this region). Two proton states due to $\pi(f_{7/2}\ i_{13/2})_J$- configurations should also occur in this region but should not be populated directly in the electron-capture decay except thru core configuration admixtures. One might speculate that the states populated in the decay may be of spins 4, 5, and 6. Of the core excitations, the likely proton particle-hole states in this region would be of spins 4 and 5 and due to the $\pi(h_{9/2}\ s_{1/2}^{-1})$ configurations, in addition to neutron excitations.

1. Level at 3428.2 keV - $(4)^-$

The spin of this level is limited to $(4, 5)^-$ by observation of the 518.3 and 402.0 keV M1 transitions to the 5^- levels at 2910.0 and 3026.2 keV and by the gamma decay to the 2^+ level at 1181.4 keV. The probable assignment of $(4)^-$ has been inferred by the M1 + E2 assignment to the 316.8 keV transition from this level to the $(3)^-$ level at 3111.4 keV. As long as the latter level is limited to a spin of 2 or 3, the presence of any M1 component in the 316.8 keV transition requires both that the spin of the 3111.4 keV level be 3 and the spin of the 3428.2 keV level be 4.

2. Level at 3727.2 keV - $(5)^-$

The spin and parity of this level is defined as $(5)^-$ by the measured M1 transitions to the levels of spin 4, 5, and 6.

3. Level at 3525.2 keV-$(5,6)^-$

This spin and parity assignment to this level can be limited to $(5,6)^-$ if the 1087.2 keV transition to the 7^+ level is placed correctly. We were able to set a (crude) limit for the multipolarity of the 1087.2 keV transition as (E1 + < 50% M2) or (E3 + < 34% M2) which is not inconsistent with a $(5,6)^-$ assignment.

4. Levels at 3699.4, 3711.5, and 3779.5 keV-$(4^-,5^-,6^-)$ and $(4^\pm,5^\pm,6^\pm)$

These remaining levels can probably be limited to spins of (4,5,6) and odd parity although we have no data to rule out even parity for the levels at 3699.4 and 3711.5 keV.

F. Shell Model Comparison of Level Structure

1. Introduction

Using known experimental single-particle energies for the odd proton in ^{209}Bi and a delta function singlet force to represent the residual proton-proton interaction[49,50]), Hoff and Hollander (ref. x)[25]) calculated the two-proton level structure shown in fig. 44. (The proton-proton coulomb interaction was also included in these calculations.)

In 1959 Newby and Konopinski (ref. y)[31]) performed a much more detailed calculation on the ^{210}Po level structure but did not include contributions of neutron orbitals or collective excitations from the ^{208}Pb core. They used a gaussian singlet-even potential (Π_{SE}) with no spin-orbit term (see section IIB). They reported the level spectra shown in fig. 44 and configuration-mixed wavefunctions for the even-parity states of spin 0, 2, 4, and 6.

Kim and Rasmussen (ref. z)[32]) made another detailed (inert ^{208}Pb core) calculation for ^{210}Po with a central force and no spin-orbit coupling. They included a non-central or tensor force in their calculations but the eigenvalues were found to be relatively insensitive to the details of configuration mixing and the strength of the tensor force. The results of their calculation are shown in fig. 44.

Shown in fig. 44 with the two-proton shell model calculations of Hoff and Hollander (ref. x)[15]), Newby and Konopinski (ref. y)[21]), and Kim and Rasmussen (ref. z)[22]) are the experimental levels for ^{210}Po populated in the electron-capture decay of ^{210}At. It is interesting that both in the theoretical and experimental spectrum, groupings of levels

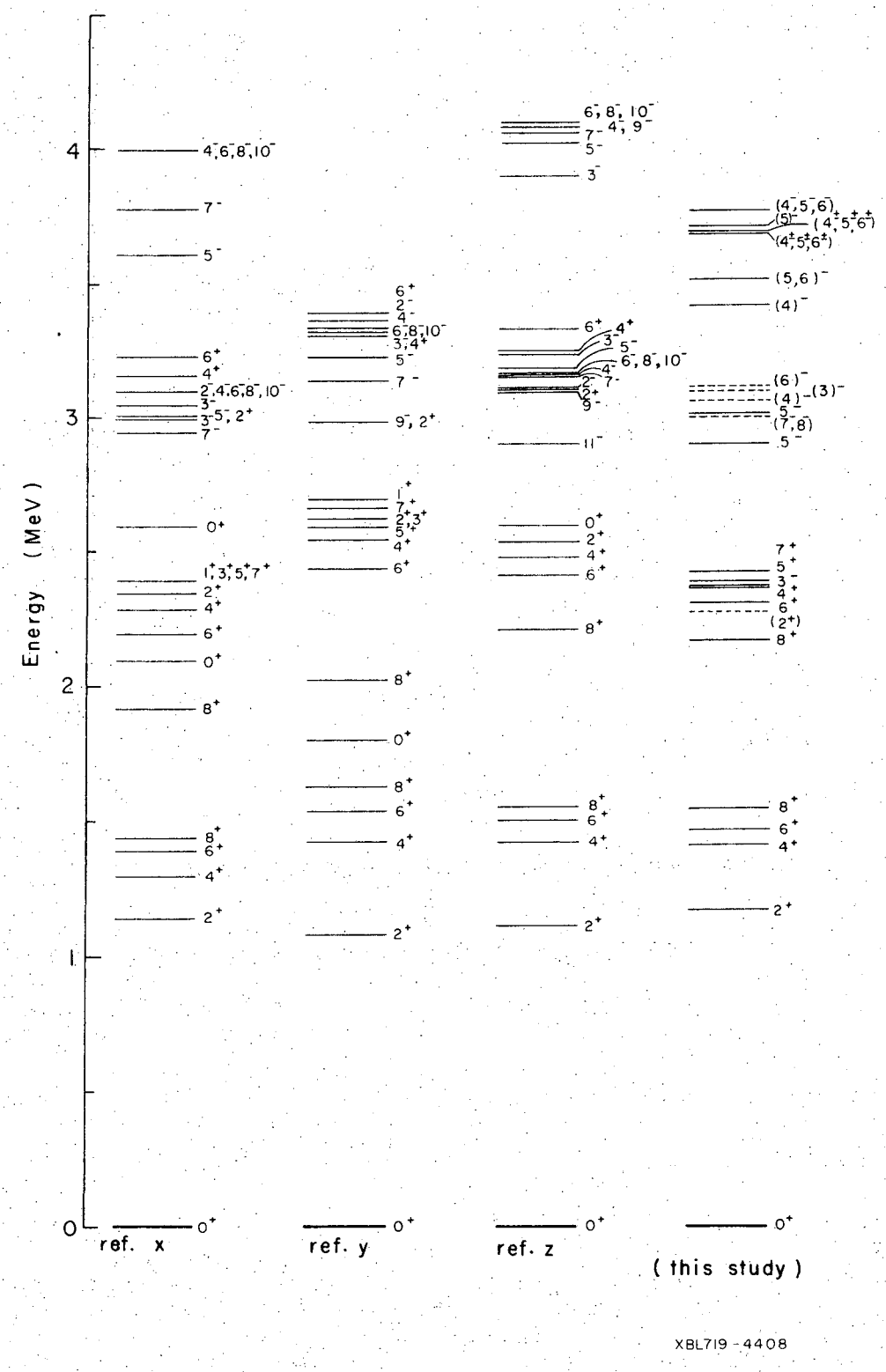

Fig. 44. Comparison of the two-proton theoretical results of Hoff and Hollander (ref. x)[25], Newby and Konopinski (ref. y)[31] and Kim and Rasmussen (ref. z)[32] with the experimental levels of ^{210}Po.

appear. This increases the confidence of making level assignments such that consistent assignments to almost all observed levels under 3.2 MeV can be made to configurations calculated from the simple two-proton model with two notable exceptions. The two exceptions are odd parity levels of spins 3 and 5 at 2386 and 2910 keV which have been identified as predominantly the collective and neutron $\nu(g_{9/2}\ p^{-1}_{1/2})$ core states of ^{208}Pb. These are discussed in detail in sections G and I.

2. Even Parity Levels in the Energy Range 0-1556 keV

All calculations clearly predict a ground-state band of levels due to the coupling of the 83rd and 84th protons in the $\pi(h_{9/2})^2$ configuration and they are in reasonably good agreement with the observed energies of the low-lying excited states (0^+, 2^+, 4^+, 6^+, and 8^+). The effect of the residual interaction (within the band) to depress the low spin members more than the high spin members is evident in all calculations. The $\sim$ 1500 keV depression of the 0^+ state relative to the 8^+ state is due to the large pairing energy associated for two identical nucleons in the same orbital.

3. Even Parity Levels in the Energy Range 2187-2438 keV

These even parity levels, with the exception of that of spin 0, are due to the $\pi(h_{9/2}\ f_{7/2})$ configuration which all calculations predict in this energy region. (The 0^+ state is due to the $\pi(f_{7/2})^2$ configuration.) The $\pi(f_{7/2})^2$ configurations are expected to be very weakly populated (if at all) in the decay of ^{210}At and not observable in our study. The exception of the odd parity level at 2386 keV is discussed in section G.

4. Odd Parity Levels in the Energy Range 3016-3125 keV

The next grouping of levels (at 3 MeV) in the experimental spectrum are of odd parity and of the dominant two proton configuration $\pi(h_{9/2}\ i_{13/2})$. The theoretical calculations predict a group of odd parity levels of spins 2-11 due to these configurations. The occurance of two 5^- levels in the 3 MeV region is explained in detail in Section I as due to configuration mixing of the neutron core $\nu(g_{9/2}\ p^{-1}_{1/2})_{5^-}$ and the two proton $\pi(h_{9/2}\ i_{13/2})_{5^-}$ states to produce two 5^- levels.

5. Higher Energy Excited States (> 3.2 MeV)

At higher energies the two proton theoretical level spectra become less clear but odd parity states of the type $\pi(f_{7/2}\ i_{13/2})$ occur within the energy range that the electron capture decay can populate. However, since core states (similar to ^{208}Pb) have been observed and identified in the lower energy spectrum, core states due to proton and/or neutrons excitations are expected to produce a complex series of states above 3 MeV. Configuration mixing of core states and two-proton states seems very likely. This point is discussed further in section I.

G. Odd Parity Level at 2386.8 keV

We have identified the 2386.8 keV level in ^{210}Po as a 3^- state. Our previous shell model discussion of ^{210}Po levels (section F) did not predict any odd parity states this low in energy which argues against the state arising from a simple two proton configuration. Shown in fig. 45 is a plot of the experimental collective levels[51,52,53] for nuclei in the lead region which makes the collective assignment seem reasonable. Further the 3^- level is not populated directly in the electron capture decay (log ft > 9.3) but is populated by gamma-ray decay from higher-lying states. Inspection of fig. 45 shows that in the even-even lead isotopes ($N \leqslant 126$ neutrons) the 3^- state occurs at a relatively constant energy of 2600 keV. ^{207}Pb shows that the coupling of the $\nu(p_{1/2}^{-1})$ neutron-hole to the 3^- collective state is weak and two such states occur in the 2600 keV energy region. For the odd-even Tl isotopes, the coupling of the $\pi(s_{1/2}^{-1})$ proton hole to the 3^- core state is again weak and produces a series of states at approximately 2600 keV. Weak coupling is also apparent for the odd proton couplings with the 3^- state of ^{209}Bi. For the case of ^{210}Pb and ^{210}Po with two particles more than the ^{208}Pb core, the 3^- states seem to be depressed significantly.

In ^{210}Pb, two 3^- states, the lowest depressed ~ 800 keV from 2600 keV, have been experimentally observed from ^{210}Pb (p,p') and ^{210}Pb (t,t') studies by Ellegaard et al.[54]). The collective strength of the lower 3^- level at 1869 keV was found to be approximately 2/3 that of the collective strength in ^{208}Pb with the upper 3^- level at 2828 keV having the remaining 1/3 strength. The fragmentation of the 3^- strength

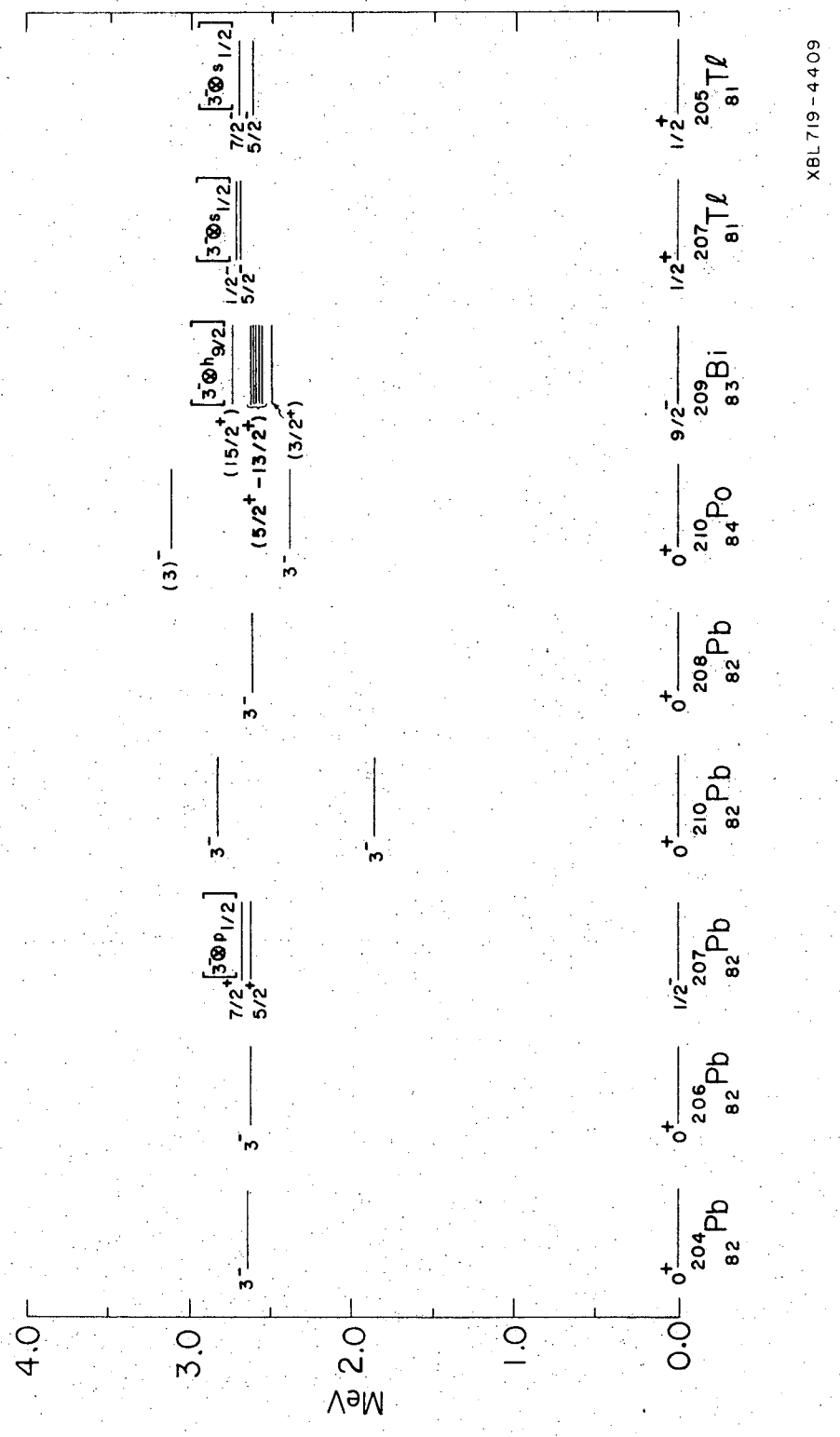

Fig. 45. Experimentally known[9]) collective states in the lead region.

has been interpreted with a particle-vibrational coupling model[54,55]) in terms of the configuration mixing of the $\nu(g_{9/2}\ j_{15/2})_{3^-}$ state with the collective 3^- state. A similar situation exists for ^{210}Po for the mixing of the two-proton configuration $\pi(h_{9/2}\ i_{13/2})_{3^-}$ (which has been tentatively identified at 3111.4 keV) with the collective 3^- core state at 2386.8 keV. The results of Hamamoto's calculation[55,56]) for the interaction matrix elements show this point.

$$\langle 0,\ (g_{9/2}\ j_{15/2})_{3^-} | H_{\text{coupling}} | 3^-_{\text{collective}} \rangle = 666 \text{ keV (for } ^{210}\text{Pb)}$$

$$\langle 0,\ (h_{9/2}\ i_{13/2})_{3^-} | H_{\text{coupling}} | 3^-_{\text{collective}} \rangle = 163 \text{ keV (for } ^{210}\text{Po)}$$

However, the interaction between the 3^- core state and the 3^- two-proton state is not as strong for ^{210}Po as the interaction for the two-neutron state of ^{210}Pb. This is because the interaction Hamiltonian H_{coupling} is stronger[57]) for single particle-matrix elements between single-particle states with $\vec{J} = \vec{\ell} + \vec{s}$ (e.g. $g_{9/2}$, $j_{15/2}$, $i_{13/2}$) and the 3^- collective states than with $\vec{J} = \vec{\ell} - \vec{s}$ (e.g. $h_{9/2}$).

These results might qualitatively explain the 200 keV depression (from 2600 keV) of the 3^- core state in ^{210}Po while the depression ($\sim$ 800 keV) for ^{210}Pb is greater. The results of Hamamoto's calculations[55,56]) for the eigenvalues of the 3^- states are shown in Table 6. This allows us to conclude that the 3^- level at 2386.8 keV in ^{210}Po is approximately the full strength collective 3^- core state.

Table 6. Results of the 3^- collective core and single-particle coupling calculation for ^{210}Pb and ^{210}Po by Hamamoto[52,53].

Isotope	Spin-parity	Level Energy	
	J^π	Experiment keV	Theory keV
^{210}Pb	3^-	1869	2110
	3^-	2828	3310
^{210}Po	3^-	2386.8	2520
	$(3)^-$	(3111.4)	2880

H. Weak Coupling Calculation to Predict the Energies of the 3^- and 5^- Core States

The energies of levels due to core states of ^{210}Po are expected to be shifted from those observed in ^{208}Pb by the 83rd and 84th protons. Using experimental data on ^{209}Bi to represent the proton-core interaction and the experimental data of ^{210}Po to represent the proton-proton interaction, we have estimated the energies of the core states for the 3^- and 5^- collective excitations (3^- coupled to 0^+ and 2^+, respectively) and the $\nu(g_{9/2}\, p_{1/2}^{-1})_{5^-}$ neutron excitation of ^{210}Po. The formalation of the calculation has been presented in detail in section IIC.

The energy of the core states were estimated from the following equation

$$E \approx E_{J_c} + E_{J_{12}} + \sum_{J_{2c}} (2J_{12}+1)(2J_{2c}+1)\left|W(J_1 J_2 J J_c;\, J_{12}\, J_{2c})\right|^2 (E_{J_{2c}} - E_J) \tag{89}$$

The energies of the 3^- and 5^- core states E_{J_c} were taken as the experimental[9]) energies observed in ^{208}Pb. The term $E_{J_{12}}$ was taken as zero since our calculation assumes the weak coupling of the 3^- and 5^- core states to the 0^+ and 2^+ states in ^{210}Po. The values $E_{J_{2c}}$ used for the various ^{209}Bi proton-core configurations are shown in Table 7.

The 3^- collective state (coupled to the 0^+ ground state) is predicted from Eq. 89 to be at 2630 keV which is consistent with other observed 3^- states in the lead region (see section G). However, the experimental value is 2386.8 keV which is significantly depressed. The

Table 7. Spin and energy assignments[9]) used for ^{209}Bi 3^- and 5^- core states coupled weakly to the $1h_{9/2}$ proton.

Spin and Parity J^+_{2c}	Energy E_{J_c} (keV)	Probable Configuration
$3/2^+$	2492	
$9/2^+$	2563	
$7/2^+$	2582	
$11/2^+$	2599	$[(^{208}\text{Pb}\ 3^-) \otimes 1h_{9/2}]_{J^+_{2c}}$
$13/2^+$	2601	
$5/2^+$	2616	
$15/2^+$	2741	
$13/2^+$	2987	
$3/2^+$	3038	
$5/2^+$	3091	
$11/2^+ + 19/2^+$	3135	$[(^{208}\text{Pb}\ 5^-) \otimes 1h_{9/2}]_{J^+_{2c}}$
$17/2^+ + 7/2^+ (+ 1/2^+)$	3154	
$15/2^+$	3170	
$9/2^+$	3212	

250 keV depression may be indicative of particle-vibrational coupling[63,65] as discussed in section G (i.e. configuration mixing between the two-proton configuration $\pi(h_{9/2}\ i_{13/2})_{3^-}$ and the collective 3^- state).

The energy of the neutron core state $\nu(g_{9/2}\ p_{1/2}^{-1})_{5^-}$ is calculated as 3058 keV which is within 150 keV of the 5^- member of the $\pi(h_{9/2}\ i_{13/2})$ configuration calculated by Hoff and Hollander[25], Newby and Konopinski[31], and Kim and Rasumssen[32]. Configuration mixing of the two 5^- states at nearly the same energy is expected. The result is that <u>two</u> configuration admixed 5^- states should occur in the 3 MeV region. Experimentally two 5^- states are observed at energies of 2910.0 and 3026.2 keV. We have been able to determine (from analysis of the β-decay) the following experimental wavefunctions for each of these 5^- states by assuming that the levels are composed of <u>only</u> these two components (see section I for the calculation).

$$\psi_{5^-}(2910) \cong 0.534\,|\pi(h_{9/2}\ i_{13/2})\rangle_{5^-} + 0.846\,|\nu(g_{9/2}\ p_{1/2}^{-1})\rangle_{5^-} \qquad (90)$$

$$\psi_{5^-}(3026) \cong 0.846\,|\pi(h_{9/2}\ i_{13/2})\rangle_{5^-} \mp 0.534\,|\nu(g_{9/2}\ p_{1/2}^{-1})\rangle_{5^-} \qquad (91)$$

These experimental wavefunctions show that configuration mixing does take place with the lower 5^- state at 2910.0 keV having the dominant core component. This is consistent with our weak coupling calculation.

The energy of the 3^- core state coupled to the 2^+ state at 1181.4 keV was also computed with eq. (89). The energy of this 5^- state is predicted as 3822 keV. This level occurs at an energy where other 5^-

states [$(\pi(h_{9/2}\ s_{1/2}^{-1})$, $\nu(g_{9/2}\ f_{5/2}^{-1})$, $\pi(f_{7/2}\ i_{13/2})$] are believed to exist so that a simple description may no longer be possible. Perhaps coulomb excitation of a ^{210}Po target would reveal such states as well as the collective 3^- state.

I. Electron-Capture Decay Rates and Particle-Hole Core Excitation in ^{210}Po

1. Introduction

The log ft values for electron-capture transitions to levels in ^{210}Po below 3400 keV have been obtained with the expanded nomogram of Moszkowski[22,58]. For higher-lying levels log ft values have been obtained by using the method discussed by Konopinski and Rose[59] for allowed transitions (see Appendix B for the method). The K-to-total electron-capture ratios were taken from the graphs given in the Table of Isotopes[22]. The Q-value for the electron-capture decay was taken as Q_{EC} = 3877±26 keV[60] and electron-capture branching ratios were obtained from our γ-ray intensity data corrected for internal conversion.

In their early paper Newby and Konopinski[31] discussed the importance of particle-hole core excitations in the level spectrum of ^{210}Po. Experimental evidence for such effects was first pointed out by Hoff and Hollander[25] through analysis of the electron-capture decay rates of ^{210}At to the odd-parity levels in ^{210}Po above 3 MeV. Specifically, they pointed out that the decay of ^{210}At (assumed ground-state configuration $(\pi(h_{9/2}^3)\ \nu(p_{1/2}^{-1}))_{5^+}$ to levels of the two proton configurations $\pi(h_{9/2})^2$, $\pi(h_{9/2}\ f_{7/2})$ or $\pi(h_{9/2}\ i_{13/2})$ should all be highly forbidden due to the large change in orbital angular momentum required for conversion of an $h_{9/2}$ proton into a $p_{1/2}$ neutron. Experimentally, highly-hindered electron-capture transitions are evident for the allowed decay to all even-parity levels below 2.9 MeV. Above this energy, however, unhindered transitions of the first-forbidden type to the odd-parity levels at

2910 and 3026 keV were observed and were attributed to contributions in these states from neutron excitation of the ^{208}Pb core.

Recently a fairly complete picture of core-excited states in ^{208}Pb has been obtained in the energy range below about 4.1 MeV through numerous reaction studies. The observed levels[53]) are shown to the left in fig. 46 and their dominant configurations[61]) are given in Table 8. The lowest levels due to core excitation (3198 and 3475 keV) are the predominantly two components of the neutron excitation $\nu(g_{9/2}\ p^{-1}_{1/2})_{5^-,4^-}$ respectively. Although a number of the levels in the energy range 3700-4100 keV have unknown parentage, at least four levels arise predominantly from the neutron excitation $\nu(g_{9/2}\ f^{-1}_{5/2})_{J^-}$ and the proton excitation $\pi(h_{9/2}\ s^{-1}_{1/2})_{J^-}$. Configuration mixing between components of these excitations is evident from the wavefunctions for these states calculated by True et al.[61]).

In the case of ^{210}Po these core excitations occur in the vicinity of the odd-parity levels arising from the two-proton configurations $\pi(h_{9/2}\ i_{13/2})_{J^-}$ and $\pi(f_{7/2}\ i_{13/2})_{J^-}$ as is evident from the level spectra calculated by Hoff and Hollander[25]) and Kim and Rasmussen[32]) (fig. 44, section F). Although the effect of the additional 83rd and 84th protons on the zero-order energies of the particle-hole core excitations is unknown, energy shifts should be small and strong configuration mixing between these states and those arising from the two-proton configurations is expected. As a result although electron-capture decay of ^{210}At to the two-proton components of levels in ^{210}Po should be highly-hindered, decay to odd parity levels which contain components of

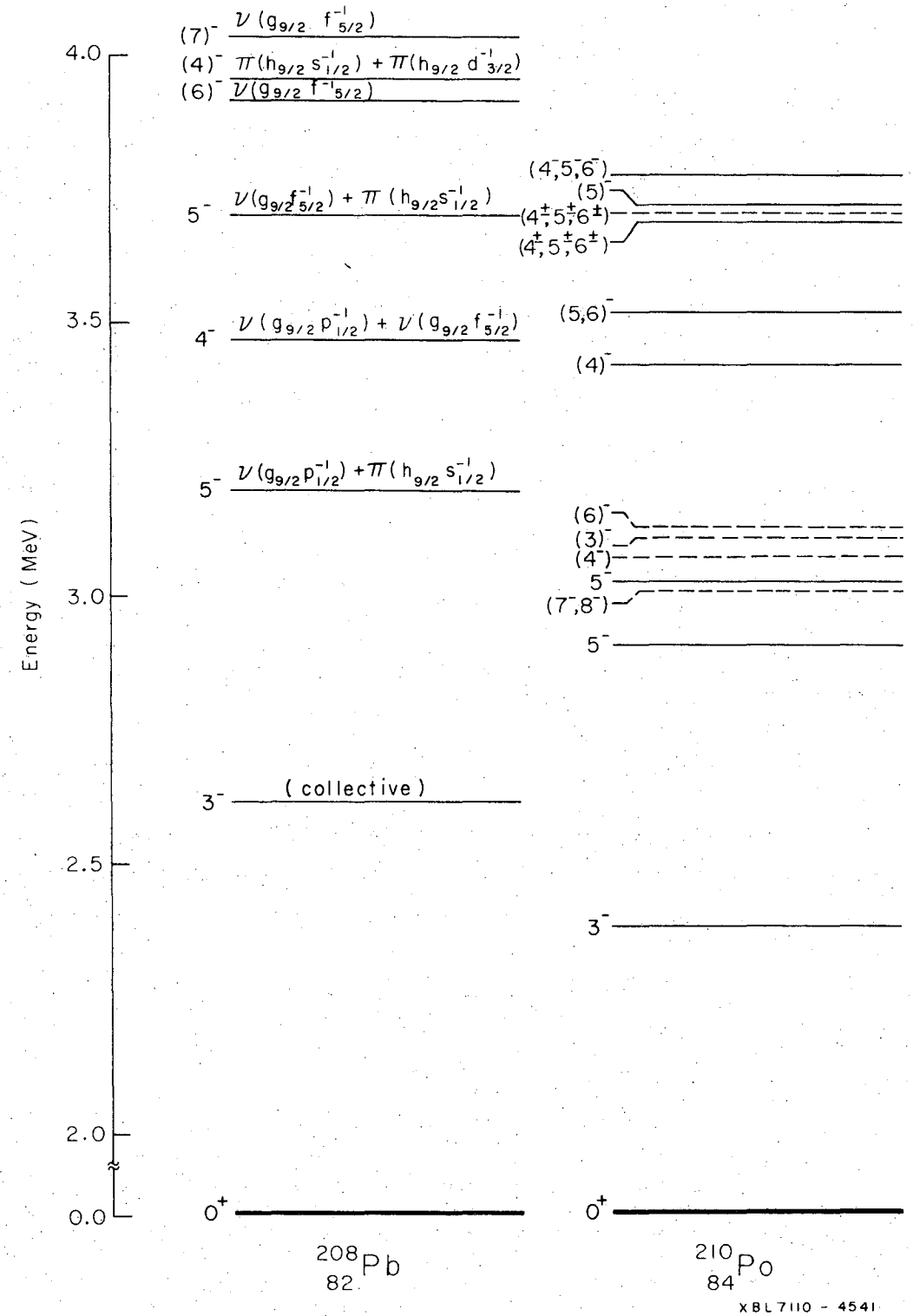

Fig. 46. Comparison of the experimental odd-parity levels of ^{208}Pb and ^{210}Po. The configurations shown for the ^{208}Pb levels represent the two largest components in each state as calculated by True, Ma, and Pinkston[61]).

Table 8. Dominant configurations of ^{208}Pb odd parity levels below 4.1 MeV as calculated by True, Ma, and Pinkston[61]).

Energy[a] (MeV)	Spin J	Configurations[b]
2.487	3	(collective)
3.350	5	$-0.92\ \nu(g_{9/2}p_{1/2}^{-1}) + 0.20\ \pi(h_{9/2}s_{1/2}^{-1})$
3.509	4	$-0.94\ \nu(g_{9/2}p_{1/2}^{-1}) + 0.25\ \nu(g_{9/2}f_{5/2}^{-1}) + 0.23\ \nu(g_{9/2}p_{3/2}^{-1})$
3.680	5	$-0.57\ \nu(g_{9/2}f_{5/2}^{-1}) + 0.52\ \pi(h_{9/2}s_{1/2}^{-1}) + 0.36\ \nu(i_{11/2}p_{1/2}^{-1}) + 0.29\ \pi(g_{9/2}p_{1/2}^{-1})$
3.982	6	$0.98\ \nu(g_{9/2}f_{5/2}^{-1})$
4.066	4	$-0.87\ \pi(h_{9/2}s_{1/2}^{-1}) - 0.47\ \pi(h_{9/2}d_{3/2}^{-1})$
4.047	7	$-.99\ \nu(g_{9/2}f_{5/2}^{-1})$

[a] Energies were those calculated in ref. [61]).

[b] Only those configurations with amplitudes (a_i) greater than 0.2 are listed.

the neutron particle-hole excitation $\nu(g_{9/2}\ p_{1/2}^{-1})$ and/or the proton particle-hole excitation $\pi(h_{9/2}^{3}\ s_{1/2}^{-1})$ will be relatively unhindered. In the first case, unhindered 1st forbidden decay is due to conversion of an $1h_{9/2}$ proton into a $2g_{9/2}$ neutron. For the proton excitation, decay of a $3s_{1/2}$ core proton in ^{210}At to a $3p_{1/2}$ neutron is similarly unhindered. From the experimental and theoretical data available, we can conclude that unhindered β-decay to odd-parity levels in ^{210}Po is due primarily to components in these states arising from excitation of the ^{208}Pb core, and that the β-decay transition probabilities to levels in ^{210}Po above about 3 MeV should be a measure of the total amplitudes in these states of the neutron wavefunction $|\nu(g_{9/2}\ p_{1/2}^{-1})>$ and the proton wavefunction $|\pi(h_{9/2}^{3}\ s_{1/2}^{-1})>$. This is of particular importance to the characterization of the more highly excited levels in ^{210}Po, since the complimentary information on amplitudes of two proton components is derived from the reaction data of (α,t) and $(^{3}He,d)$ studies.

2. Electron-Capture Decay to Levels at 2910.0 and 3026.2 keV

Both of these levels are populated by relatively unhindered electron-capture transitions, and they are identified with the two states arising from configuration mixing of the first two-proton 5^- state in ^{210}Po (predominantly $\pi(h_{9/2}\ i_{13/2})_{5^-}$) and the first 5^- level in ^{208}Pb (the two-proton wavefunction undoubtedly contains a small component of the configuration $\pi(f_{7/2}\ i_{13/2})_{5^-}$, but this does not affect the following argument). The wavefunction for the first 5^- state in ^{208}Pb has been calculated by True, Ma and Pinkston (TMP)[61] as

$$\psi_{5^-}(3198) = -0.923|\nu(g_{9/2}\, p_{1/2}^{-1})> + 0.200|\pi(h_{9/2}\, s_{1/2}^{-1})>$$

$$+ 0.147|\nu(i_{11/2}\, p_{1/2}^{-1})> + 0.144|\pi(h_{9/2}\, d_{3/2}^{-1})> \qquad (92)$$

$$- 0.122|\pi(f_{7/2}\, d_{3/2}^{-1})> + 0.0199|\nu(g_{9/2}\, f_{5/2}^{-1})>$$

and the amplitudes of the two principle components are in agreement with the experimental data of McClatchie, Glashausser, and Hendrie[62]) and Bardwick and Tickle[63]). With the assumption that the ground state wavefunction of ^{210}At is $|\pi(h_{9/2}^3)\ \nu(p_{1/2}^{-1})>_{5^+}$, the electron-capture decay to the two 5^- levels will be dominated by amplitudes of the first and second components of the above wavefunction that contribute to these states.

As an estimate of the relative amplitudes of core and two proton components in these states we follow the analysis of first-forbidden β-decay given by Damgaard and Winther[64]), and Damgaard, Broglia and Riedel[65]). Their analysis has shown that in the region around ^{208}Pb, the values of ft for β^- transitions of this type between single-particle or single-hole states can be estimated to a good approximation by the relation

$$ft = \frac{Dg_v^2}{4\pi[B(\lambda = 0) + B(\lambda = 1)]} \qquad (93)$$

where D = 6250 sec and the B(λ) are given (in units of g_v^2) as

$$B(\lambda) = \frac{1}{2J_i + 1}\ |<J_f\|O(\lambda)\|J_i>|^2 \qquad (94)$$

In particular, the decay of ^{208}Tl to the first two 5^- levels in ^{208}Pb was shown to be dominated by the components in these states of the core excitations $\nu(g_{9/2}\, p_{1/2}^{-1})$ and $\pi(h_{9/2}\, s_{1/2}^{-1})$. While the analysis has been carried out only for β^- decay, it is reasonable to expect that the same formulation is applicable for examination of <u>relative</u> ft values in the electron-capture transitions involving the same particle configurations.

In the present case we have made the simplifying assumptions that the wavefunction for the ground-state of ^{210}At can be written as $|\pi(h_{9/2}^3)\ \nu(p_{1/2}^{-1})>_{5^+}$ and that the wavefunctions for the two 5^- levels in ^{210}Po can be approximated by the two component vectors

$$\psi_{5^-}(2910) = a_1|\pi(h_{9/2}\ i_{13/2})>_{5^-} + b_1|\nu(g_{9/2}\ p_{1/2}^{-1})>_{5^-} \qquad (95)$$

$$\psi_{5^-}(3026) = a_2|\pi(h_{9/2}\ i_{13/2})>_{5^-} + b_2|\nu(g_{9/2}\ p_{1/2}^{-1})>_{5^-} \qquad (96)$$

If we choose the phases so that the a's are positive, then $b_1 = \pm(1 - a_1^2)^{1/2}$, $a_2 = |b_1|$ and $|b_2| = a_1$. We can then rewrite our second wavefunction of eq. (96) up to a phase δ as

$$\psi_{5^-}(3026) = |b_1|\ |\pi(h_{9/2}\ i_{13/2})>_{5^-} + a_1\delta|\nu(g_{9/2}\ p_{1/2}^{-1})>_{5^-} \qquad (97)$$

It is further assumed that the full strength of the two proton and neutron core excitation components are accounted for in these states. With the final assumption that decay via the highly ℓ-forbidden transition $\pi(h_{9/2}) \xrightarrow{EC} \nu(p_{1/2})$ can be neglected, the ratio $(ft)_{2910}/(ft)_{3026}$ gives

$$\frac{(ft)_{2910}}{(ft)_{3026}} = \frac{a_1^2}{1 - a_1^2} = \frac{a_1^2}{|b_1|^2} = \frac{a_1^2}{|a_2|^2} \tag{98}$$

Using our measured ft values in the decay for these two levels we find

$$\frac{a_1^2}{|b_2|^2} = \frac{6.1}{6.5} = \frac{1}{2.51} = 0.40 \tag{99}$$

Thus we may construct the experimental two component wavefunction (up to phase δ) for the two 5^- levels. Using our arbitrary phase convention $b_1 = \pm(1 - a_1^2)^{1/2}$), the two-component vectors become

$$\psi_{5^-}(2910) \approx 0.534|\pi(h_{9/2}\, i_{13/2})>_{5^-} + 0.846|\nu(g_{9/2}\, p_{1/2}^{-1})>_{5^-} \tag{100}$$

$$\psi_{5^-}(3026) \approx 0.846|\pi(h_{9/2}\, i_{13/2})>_{5^-} + 0.534|\nu(g_{9/2}\, p_{1/2}^{-1})>_{5^-} \tag{101}$$

These results can be compared directly to the relative two-proton ampltiudes obtained from the $^{209}Bi(\alpha,t)$ and $^{209}Bi(^3He,d)$ reaction studies of TB[28]) and Lanford[29]). In both studies the 5^- level at 2910 keV was excited and well resolved from members of the $\pi(h_{9/2}\, i_{13/2})$ multiplet. Since the 11^- member of this multiplet is expected to arise only from this two-proton configuration, the ratios $I_{5^-}(2910)/I_{11^-}(2945)$, corrected for the $(2J + 1)$ dependence of the reaction cross sections, directly yield experimental values for the amplitude a_1^2. By assuming that the remainder of the two proton strength is located in the level at 3026

keV, the ratios of the two proton components in these states are estimated from these data as

$$\left(\frac{|a_1|^2}{|a_2|^2}\right)_{(TB)^{28,48}} = 0.41 \qquad (102)$$

and

$$\left(\frac{|a_1|^2}{|a_2|^2}\right)_{(\text{Lanford})^{29}} = 0.82\pm0.20 \qquad (103)$$

The agreement between these values and that derived from analysis of the electron-capture transition rates (eq. (99)) is good, in spite of the many simplifying assumptions required in the calculations, and is suggestive of the correct interpretation of the character of these levels. Unfortunately the lack of experimental data and the complexity of the wavefunctions for other odd-parity states involving core excitations precludes extension of this analysis at present. The fact that only the two lowest energy core excitations are expected to contribute significantly to unhindered β-decay does however permit the qualitative discussions given in the following paragraphs.

3. Electron-Capture Decay to Levels at 3075.1 and 3428.2 keV

The experimental results of Bondorf, von Brentano, and Richard[66] have indicated that the wavefunction for the first 4^- level in ^{208}Pb (at 3475 keV) can be written

$$\psi_{4^-}(3475) = (0.96\pm0.02)|\nu(g_{9/2}\ p_{1/2}^{-1})\rangle$$

$$- (0.26\pm0.03)|\nu(g_{9/2}\ p_{3/2}^{-1})\rangle + (0.07\pm0.16)|\nu(g_{9/2}\ f_{5/2}^{-1})\rangle \quad (104)$$

which is in good agreement with the calculated wavefunction of TMP[61]). The extent to which this configuration mixes with the 4^- level arising from the $\pi(h_{9/2}\ i_{13/2})$ configuration should be reduced relative to that observed in the 5^- levels because of the larger difference in zeroth order energies of these states. Unhindered electron-capture decay is then expected only to the relatively pure core state and it is reasonable to associate this state with the $(4)^-$ level at 3428.2 keV (log ft = 6.9). Decay to the $(4)^-$ level at 3075.1 keV is highly hindered (log ft = 8.9). While no quantitative estimates can be made, the reaction studies indicate that the greater part of the strength of the $\pi(h_{9/2}\ i_{13/2})_{4^-}$ configuration is located in the latter level since the other member of this pair was apparently not excited to a measurable extent.

4. Electron-Capture Decay to Levels at 3525.2, 3699.4, 3711.2, 3727.2, and 3779.5 keV

The electron-capture decay to these levels is also relatively unhindered which reflect strong admixtures of particle-hole core components in the wavefunction of these states. Of the possible core components that are expected here, the most probable admixture that can give rise to these fast transitions is the proton excitation $\pi(h_{9/2}\ s_{1/2})_{4^-,5^-}$ in addition to the neutron excitation discussed above. The decay of the $3s_{1/2}$ proton in ^{210}At to the $3p_{1/2}$ neutron in

^{210}Po might be expected to occur with a somewhat greater absolute rate than for the similar decay of a $1h_{9/2}$ proton into a $2g_{9/2}$ neutron because of better overlap of the wavefunctions of the initial and final states. Thus the low log ft values assigned to transitions to the two highest energy levels of this group may be due to strong admixtures of this proton core excitation. The inverse of these decay processes, observed in the decay of ^{208}Tl to the core states of ^{208}Pb, proceed with similar (but somewhat lower) log ft.

J. Gamma-Ray Transition Rates Between the Even Parity Levels

The data available from reaction studies and β-decay of ^{210}At now give a fairly detailed picture of the lower-lying levels in ^{210}Po. All levels of the $\pi(h_{9/2})^2$ ground state multiplet are well characterized and except for the low spin members of the $\pi(h_{9/2}\ f_{7/2})$ multiplet, the major transitions in the decay of these levels are now known. Comparison of the shell model level sequence calculated by Hoff and Hollander[25], Newby and Konopinski[31] and Kim and Rasmussen[32] with the experimental spectrum (section F, fig. 42) indicates general agreement with energies and level spacing. With the decay properties of these levels known, the experimental data may serve as a strong guide to future calculations. In particular the M1 branching ratios in decay of the odd spin members of the $\pi(h_{9/2}\ f_{7/2})$ band to the low-lying even parity levels may serve as a sensitive test of the $\pi(h_{9/2}\ f_{7/2})$ admixtures in the $\pi(h_{9/2})^2$ band since M1 transitions to the major components are forbidden ($\Delta\ell = 2$).

For the purpose of testing the accuracy of ^{210}Po wavefunctions[31,32,33] shown in Table 9, we have calculated (using the formalation presented in Appendix A) the total absolute gamma-ray transition probabilities $T(\lambda)$ for decay of a number of levels of the $\pi(h_{9/2}\ f_{7/2})$ multiplet. For the effective charge which is necessary for the calculation of T(E2), we used the value of 1.5e for the proton as was discussed by Astner et al.[67]. The oscillator parameter ν for the calculation of E2 matrix elements was fixed at 0.165 from the relation $\nu = 0.98/A^{1/3}$. The gyromagnetic ratio g_j used for the T(M1) calculations was obtained from the tabulated measured magnetic moments[68,69] for the $1h_{9/2}$, $2f_{7/2}$ and $1i_{13/2}$

Table 9. This is tabulation of the eigenvalues and eigenfunctions calculated for ^{210}Po by Ma and True (MT),[33] Kim and Rasmussen (KR),[32] and Newby and Konopinski (NK).[31] The first column gives the reference, the second column the spin and parity and the third the calculated excitation energy. For each spin the remaining columns give the two proton configurations on top and the corresponding amplitudes below. For example, the amplitude of the $|1h_{9/2}2f_{5/2}\rangle$ configuration for the 2^+ level at 1057 keV of MT is .0805.

Ref.	J^π	E (keV)	Eigenfunctions							
			$\|1h_{9/2}1h_{9/2}\rangle$	$\|1h_{9/2}2f_{7/2}\rangle$	$\|1h_{9/2}2f_{5/2}\rangle$	$\|1h_{9/2}3p_{3/2}\rangle$	$\|1h_{9/2}3p_{1/2}\rangle$	$\|2f_{7/2}2f_{7/2}\rangle$	$\|2f_{7/2}2f_{5/2}\rangle$	$\|2f_{7/2}3p_{3/2}\rangle$
			$\|2f_{7/2}3p_{1/2}\rangle$	$\|11_{13/2}11_{13/2}\rangle$	$\|2f_{5/2}2f_{5/2}\rangle$	$\|2f_{5/2}3p_{3/2}\rangle$	$\|2f_{5/2}3p_{1/2}\rangle$	$\|3p_{3/2}3p_{3/2}\rangle$	$\|3p_{3/2}3p_{1/2}\rangle$	$\|3p_{1/2}3p_{1/2}\rangle$
MT	0^+	0	-.9172	...	...	...	...	-.3619	...	...
			...	.4175	-.1475	...	...	-.0608	...	-.0380
KR	0^+	0	.8845	...	...	...	...	.3032	...	...
			...	-.3544	...	...	...	...	...	...
NK	0^+	0	.9432	...	...	...	...	.1008	...	...
			...	.3167	...	...	...	...	...	...
MT	2^+	1057	.9398	-.0498	.0805	...	...	.1902	.0514	.0470
			...	-.2490	.0614	-.0135	.0234	.0152	.0199	...
KR	2^+	1233	.9890	-.0422	...	...	...	.0875	...	...
			...	-.1113	...	...	...	...	...	...
NK	2^+	1085	.9821	.0417	...	...	...	.0542	...	...
			...	.1755	...	...	...	...	...	...
MT	4^+	1455	.9905	-.0823	.0500	-.0114	.0163	.0628	.0334	.0171
			.0180	-.0546	.0166	-.0157	...	...	...	...
KR	4^+	1429	.9958	-.0523	...	...	...	.0449	...	...
			...	-.0595	...	...	...	...	...	...
NK	4^+	1430	.9927	.0690	...	...	...	.0373	...	...
			...	.0919	...	...	...	...	...	...
MT	6^+	1558	-.9937	.0987	-.0286	.0184	...	-.0248	-.0298	...
			...	-.0124	...	...	...	...	...	...
KR	6^+	1511	.9969	-.0637	...	...	...	.0257	...	...
			...	-.0392	...	...	...	...	...	...
NK	6^+	1545	.9935	.0945	...	...	...	.0250	...	...
			...	.0590	...	...	...	...	...	...
MT	8^+	1580	-.9817	.1878	...	...	...	...	...	...
			...	.0311	...	...	...	...	...	...
KR	8^+	1565	.9940	-.1056	...	...	...	...	...	...
			...	-.0283	...	...	...	...	...	...
MT	1^+	2525	...	-1.0	...	...	...	...	...	...
			...	...	...	...	...	...	...	...
KR	1^+	1900	...	1.0	...	...	...	...	...	...
			...	...	...	...	...	...	...	...
NK	1^+	2702	...	1.0	...	...	...	...	...	...
			...	...	...	...	...	...	...	...
MT	2^+	2465	-.1509	-.9360	.1151	...	...	.2452	.0398	.0640
			...	-.1364	.0413	-.0163	.0276	.0158	.0204	...
KR	2^+	2554	.0489	.9978	...	...	...	-.0325	...	...
			...	.0302	...	...	...	...	...	...
NK	2^+	2634	-.0478	.9958	...	...	...	.0773	...	...
			...	.0067	...	...	...	...	...	...
MT	3^+	2502	...	-.9995	.0283	.0000	...	...	.0000	.0089
			.0044	...	...	-.0041	.0033	...	...	...
KR	3^+	2389	...	1.0	...	...	...	...	...	...
			...	...	...	...	...	...	...	...
NK	3^+	2633	...	1.0	...	...	...	...	...	...
			...	...	...	...	...	...	...	...
MT	4^+	2406	-.1087	-.9566	.0946	-.0331	.0449	.1529	.0556	.0333
			.0340	-.1757	.0249	-.0280	...	...	...	...
KR	4^+	2490	.0552	.9977	...	...	...	-.0214	...	...
			...	.0317	...	...	...	...	...	...
NK	4^+	2557	-.0738	.9960	...	...	...	.0391	...	...
			...	.0330	...	...	...	...	...	...
MT	5^+	2522	...	-.9997	.0016	-.0189	.0125	...	...	...
			...	...	...	...	...	...	...	...
KR	5^+	2452	...	1.0	...	...	...	...	...	...
			...	...	...	...	...	...	...	...
NK	5^+	2597	...	1.0	...	...	...	...	...	...
			...	...	...	...	...	...	...	...
MT	6^+	2330	-.1013	-.9579	+.0765	-.0871	...	.0953	.0844	...
			...	-.2062	...	...	...	...	...	...
KR	6^+	2424	.0655	.9971	...	...	...	-.0152	...	...
			...	.0349	...	...	...	...	...	...
NK	6^+	2450	-.0979	.9936	...	...	...	.0390	...	...
			...	.0410	...	...	...	...	...	...
MT	7^+	2548	...	.9999	.0067	...	...	...	...	...
			...	...	...	...	...	...	...	...
KR	7^+	2461	...	1.0	...	...	...	...	...	...
			...	...	...	...	...	...	...	...
NK	7^+	2573	...	1.0	...	...	...	...	...	...
			...	...	...	...	...	...	...	...
MT	8^+	2088	-.1901	-.9745	...	...	...	...	...	...
			...	-.1189	...	...	...	...	...	...
KR	8^+	2227	.1068	.9933	...	...	...	...	...	...
			...	.0443	...	...	...	...	...	...

proton orbitals and from the Schmidt (free space) values for the $2f_{5/2}$, $3p_{3/2}$ and $3p_{1/2}$ orbitals occurring in the wavefunctions of Ma and True[33]). Table 10 shows the effective magnetic moments used to obtain g_j. The Schmidt values (used in the calculations in Appendix G) for all proton orbitals are also shown.

Listed in Table 9 are the wavefunctions of Ma and True (MT)[33]), Kim and Rasmussen (KR)[32]) and Newby and Konopinski (NK)[31]) used to calculate the absolute gamma-ray transition probabilities shown in Table 11. The experimental level energies have been used to calculate the values of $T(\lambda)$ rather than the theoretical level energies. With our rather limited data we can not state that one particular set of wavefunctions yielded calculations in better agreement with experimental data than any other. This can be seen more directly from the data given in Table 12 where we have listed experimental and theoretical E2-M1 gamma-ray mixing ratios δ^2 for several transitions. A limit of δ^2 was set when the transitions were measured as <u>pure</u> M1 ($\delta^2 = 0$). The limit corresponds to the maximum E2 admixture within our rather large error limits. Clearly, more experimental mixing ratios are needed in order to make any definite test of the wavefunctions using the transition probabilities.

The calculations also point to relatively intense low-energy intraband transitions in competition with the more energetic interband decay to the levels of the dominant $\pi(h_{9/2})^2$ configuration. This lends some support to our placement of the 77.2, 92.1 and 112.2 keV transitions in the decay scheme. (The theoretical results also predict the M1 character of the 77.2 and 112.2 keV transitions.) A similar intraband transition

Table 10. Magnetic moments used to obtain the gyromagnetic ratios.

Shell	Effective Moment Used μ	Schmidt Value μ
$1h_{9/2}$	4.08	2.6241
$2f_{7/2}$	4.41	5.79275
$1i_{13/2}$	7.9	8.79275
$2f_{5/2}$	0.862	0.8623
$3p_{3/2}$	3.793	3.79275
$3p_{1/2}$	-0.2643	-0.26425

Table 11. Calculated Transition Probabilities for M1 and E2 transitions for the $\pi(h_{9/2}, f_{7/2})$ and $\pi(h_{9/2})^2$ configurations using the wave functions of Ma and True (MT),[33] Kim and Rasmussen (KR),[32] and Newby and Konopinski (NK).[31] The single-particle estimates[22] are also tabulated in addition to the observed gamma-ray intensities.

Transition Energy (keV)	Angular[c] Momentum $J_i \rightarrow J_f$	Experimental Gamma-Ray Intensity (%)	T(λ)(sec^{-1}) Theoretical MT T(M1)10^{-8}	MT T(E2)10^{-8}	KR T(M1)10^{-8}	KR T(E2)10^{-8}	NK T(M1)10^{-8}	NK T(E2)10^{-8}	Single Particle T(λ) 10^{-8}
881.1	$7_1 \rightarrow 8_1$	0.22(2)	305.6	51.0	89.3	60.1	---	---	1.92 10^5(M1)
250.5	$7_1 \rightarrow 8_2$	0.21(4)	189.2	0.053	181.6	0.0443	---	---	4400(M1)
964.9	$7_1 \rightarrow 6_1$	0.16(4)	4.58	36.9	69.9	33.3	153.9	28.8	$2.51 \cdot 10^5$(M1)
112.2	$7_1 \rightarrow 6_2$	≈ .029[a]	11.39	$1.58 \cdot 10^{-6}$	27.0	$7.86 \cdot 10^{-5}$	26.8	$2.53 \cdot 10^{-4}$	140(M1)
929.9	$5_1 \rightarrow 6_1$	0.76(3)	378.1	4.7	102.0	3.01	224.6	1.80	$2.25 \cdot 10^5$(M1)
77.2	$5_1 \rightarrow 6_2$	≈ .026[a]	14.9	$2.63 \cdot 10^{-5}$	14.3	$2.04 \cdot 10^{-5}$	14.2	$3.14 \cdot 10^{-5}$	129(M1)
976.5	$5_1 \rightarrow 4_1$	0.81(4)	38.5	66.9	81.6	66.2	142.0	88.0	$2.60 \cdot 10^5$(M1)
630.9	$8_2 \rightarrow 8_1$	0.31(2)	654.8	21.5	208.4	16.3	---	---	70300(M1)
714.4	$8_2 \rightarrow 6_1$	(<.04)[b]	0	$1.59 \cdot 10^{-7}$	0	0.0475	---	---	$1.02 \cdot 10^5$(E2)
769.2	$6_2 \rightarrow 8_1$	(<.05)[b]	0	1.05	0	33.2	---	---	538(E2)
852.7	$6_2 \rightarrow 6_1$	1.39(5)	506.9	109.	95.3	65.5	217.7	37.6	$1.73 \cdot 10^5$(M1)
899.3	$6_2 \rightarrow 4_1$	(<.2)[b]	0	26.5	0	6.08	0	17.1	1170(E2)
1201.2	$4_2 \rightarrow 2_1$	0.16(2)	0	433	0	98.0	0	161	4990(E2)
92.1	$4_2 \rightarrow 2_2$	(~.001)[a]	0	0.025	0	.022	0	.021	
955.8	$4_2 \rightarrow 4_1$	1.81(6)	1017.	158	26.5	50.3	47.4	35.4	87300(M1)
909.2	$4_2 \rightarrow 6_1$	0.09(3)	0	46.1	0	107	0	126	1240(E2)
2290.0	$2_2 \rightarrow 0_1$	0.012(3)	0	17300	0	4400	0	6612	$1.26 \cdot 10^5$(E2)
1108.6	$2_2 \rightarrow 2_1$	---	1924.	231	1.08	1.44	1.23	2.57	$3.74 \cdot 10^5$(M1)
863.3	$2_2 \rightarrow 4_1$	---	0	75.7	0	78.0	0	99.7	957(E2)

[a] Estimated from the conversion electron line intensities in the spectrographic plates obtained by Hoff and Hollander.[25]

[b] Estimated from preliminary data taken with a compton suppressed Ge(Li) spectrometer (Ref. 70).

[c] J_i and J_f refer to the spins of the initial and final states respectively. The subscripts 1 and 2 refer to the first and second levels (increasing energy) of a given spin.

Table 12. E2-M1 Mixing Ratios (δ^2)[a]

Angular[c] Momentum $J_i \rightarrow J_f$	Transition Energy (keV)	δ^2 (experimental)[b]	Theory MT	Theory KR	Theory NK
$7_1 \rightarrow 8_2$	250.5	<0.32	0.00028	0.00024	—
$8_2 \rightarrow 8_1$	630.9	<0.19	0.0328	0.078	—
$6_2 \rightarrow 6_1$	852.7	$0.19^{+0.16}_{-0.14}$	0.215	0.687	0.173
$7_1 \rightarrow 8_1$	881.7	$0.58^{+0.47}_{-0.29}$	0.167	0.673	—
$5_1 \rightarrow 6_1$	929.9	<0.32	0.012	0.0295	0.008
$4_2 \rightarrow 4_1$	955.8	<0.29	0.155	1.898	0.746
$5_1 \rightarrow 4_1$	976.5	<0.19	1.74	0.81	0.62

[a]The mixing ratio δ^2 is defined as $\delta^2 = \frac{|< \|E2\| >|^2}{|< \|M1\| >|^2} \equiv \frac{T(E2)}{T(M1)}$.

[b]The experimental δ^2 were obtained from comparison of our K-conversion coefficients with the theoretical values of Hager and Seltzer[42]).

[c]J_i and J_f refer to the spins of the initial and final states respectively. The subscripts 1 and 2 refer to the first and second levels (increasing energy) of a given spin.

may be responsible for the weak 125.2 keV transition reported by Hoff and Hollander[25]). In general agreement between the calculated and experimental gamma-ray branching ratios in the decay of members of the $\pi(h_{9/2}\ f_{7/2})$ band is also rather inconsistent. This is seen more directly by the data given in Table 13 where we have listed the experimental and theoretical gamma-ray branching ratios. It should be noted that a second set of ^{210}Po wavefunctions calculated by MT[33]) using different force parameters gave slightly better agreement in the gamma-ray branching ratios while not significantly changing the agreement in the mixing ratios. MT[33]) are currently investigating this point. Qualitatively, however, the theoretical results do account for the low intensities of transitions not observed experimentally. For example, the transitions $6_2 \rightarrow 8_1$ (769.2 keV), $6_2 \rightarrow 4_1$ (899.3 keV), $2_2 \rightarrow 4_1$ (863.3 keV) and $2_2 \rightarrow 2_1$ (1188.6 keV) are predicted to have small intensities compared to the competing transitions observed experimentally.

All of the above calculations were repeated in Appendix G using <u>all</u> values of g_j which were obtained from the Schmidt values as shown in Table 10. The T(M1) values seemed rather sensitive to small changes in g_j. For example, a 20% change for the $f_{7/2}$ orbital changed several T(M1) by more than two orders of magnitude. This point is discussed further in Appendix G.

Finally in Table 14 we have listed the experimental and calculated absolute values of T(E2) for the $\pi(h_{9/2})^2$ configurations. The results are in agreement which supports the value of 1.5e recommended by Astner <u>et al.</u>[67]) for the effective charge of the proton in the lead region.

Table 13. Gamma-ray branching ratios for some transitions in ^{210}Po.

Transitions		Ratios[a] γ_1/γ_2		
Energy (keV)	(Experiment)[b]	Theory		
		MT	KR	NK
881.1/964.9	$1.38^{+.62}_{-.38}$	8.59	1.45	–
881.1/250.5	$1.04^{+.37}_{-.24}$	1.88	0.82	–
881.1/112.2	$(\approx(6.75)^{c}$	31.3	5.53	–
929.9/976.5	$0.94^{+.09}_{-.08}$	3.63	0.71	0.98
929.9/77.2	$(\approx(28.7)^{c}$	25.6	7.3	15.9
955.8/909.2	$20.1^{+11.2}_{-5.5}$	25.4	0.72	0.657
955.8/1201.2	$11.3^{+1.0}_{-2.2}$	2.71	0.78	0.514

[a]The γ-ray branching ratios are defined as $\gamma_1/\gamma_2 \equiv (T(M1) + T(E2))_1/(T(M1) + T(E2))_2$ from Table 11.

[b]The experimental ratios were obtained from our gamma-ray intensity data.

[c]Intensity was estimated from the conversion electron line intensities in the spectrographic plates obtained by Hoff and Hollander[25]).

Table 14. Comparison of the observed transition probabilities for the E2 transitions between the $\pi(h_{9/2})^2$ configurations with the calculated transition probabilities for the wave functions of Ma and True (MT)[33], Kim and Rasmussen (KR)[32] and Newby and Konopinski (NK)[31]. The single-particle estimates[22] are also given.

Transition Angular Momentum $J_i \rightarrow J_f$	Energy (keV)	Total Conversion Coefficient	Experimental Half Life sec	Experimental T(E2) sec^{-1} sec^{-1}	Theoretical T(E2) sec^{-1} MT	KR	NK	Single Particle
$2_1 \rightarrow 0_1$	1181.4	---	---	---	$8.3\ 10^{11}$	$6.9\ 10^{11}$	$7.4\ 10^{11}$	$4.65\ 10^{11}$
$4_1 \rightarrow 2_1$	245.3	0.239	$1.7(2)\ 10^{-9}$	$3.3(4)\ 10^{8}$	$3.5\ 10^{8}$	$3.4\ 10^{8}$	$3.4\ 10^{8}$	$1.8\ 10^{8}$
$6_1 \rightarrow 4_1$	46.6	272	$38(5)\ 10^{-9}$	$6.7(9)\ 10^{4}$	$6.1\ 10^{4}$	$5.7\ 10^{4}$	$5.9\ 10^{4}$	$4.4\ 10^{4}$
$8_1 \rightarrow 6_1$	83.5	16.2	$110(8)\ 10^{-9}$	$3.7(3)\ 10^{5}$	$4.6\ 10^{5}$	$4.1\ 10^{5}$	---	$8.1\ 10^{5}$

K. Final Remarks

The best summary of this study can be made with use of a figure. In fig. 47 we have shown the two-proton theoretical level structure of ^{210}Po calculated by Ma and True[33]) and the experimental level structure of ^{210}Po and ^{208}Pb. The two-proton model does not include core excitations and the "extra" 3^- and 5^- states in the region of $\leqslant 3.2$ MeV have been identified in sections G, H and I as due to core states. Above 3.2 MeV, the situation is not so clear. There are six states which are fed directly in the decay and these presumably have spins of 4, 5 or 6. The sum of the number of ^{208}Pb core states and the number of two-proton states of spins 4, 5, or 6 in the energy range of 3.2 - 4.3 MeV is seven. It is tempting to speculate that the experimental states which are fed in the decay have admixed configurations due to the two-proton states and core states with the electron-capture decay proceeding via the core components as discussed in section IV I.

It has been established from this study that the next generation "shell model" calculation for ^{210}Po should include configuration mixing of the two-proton configurations and core states. In order to aid such calculations several additional experiments could be performed. An angular correlation measurement of the gamma-rays from the decay of ^{210}At might determine the spin of the odd parity states at 3428 and 3727 keV. Higher resolution ^{209}Bi(^{3}He,d) reactions might be used to look for fragmentation of the $\pi(h_{9/2}\ i_{13/2})$ configurations over the $\pi(f_{7/2}\ i_{13/2})$ and/or the core configurations. In particular mixing of the $(4)^-$ states at 3075.1 and 3428.2 keV could be investigated. A ^{210}Po target might be

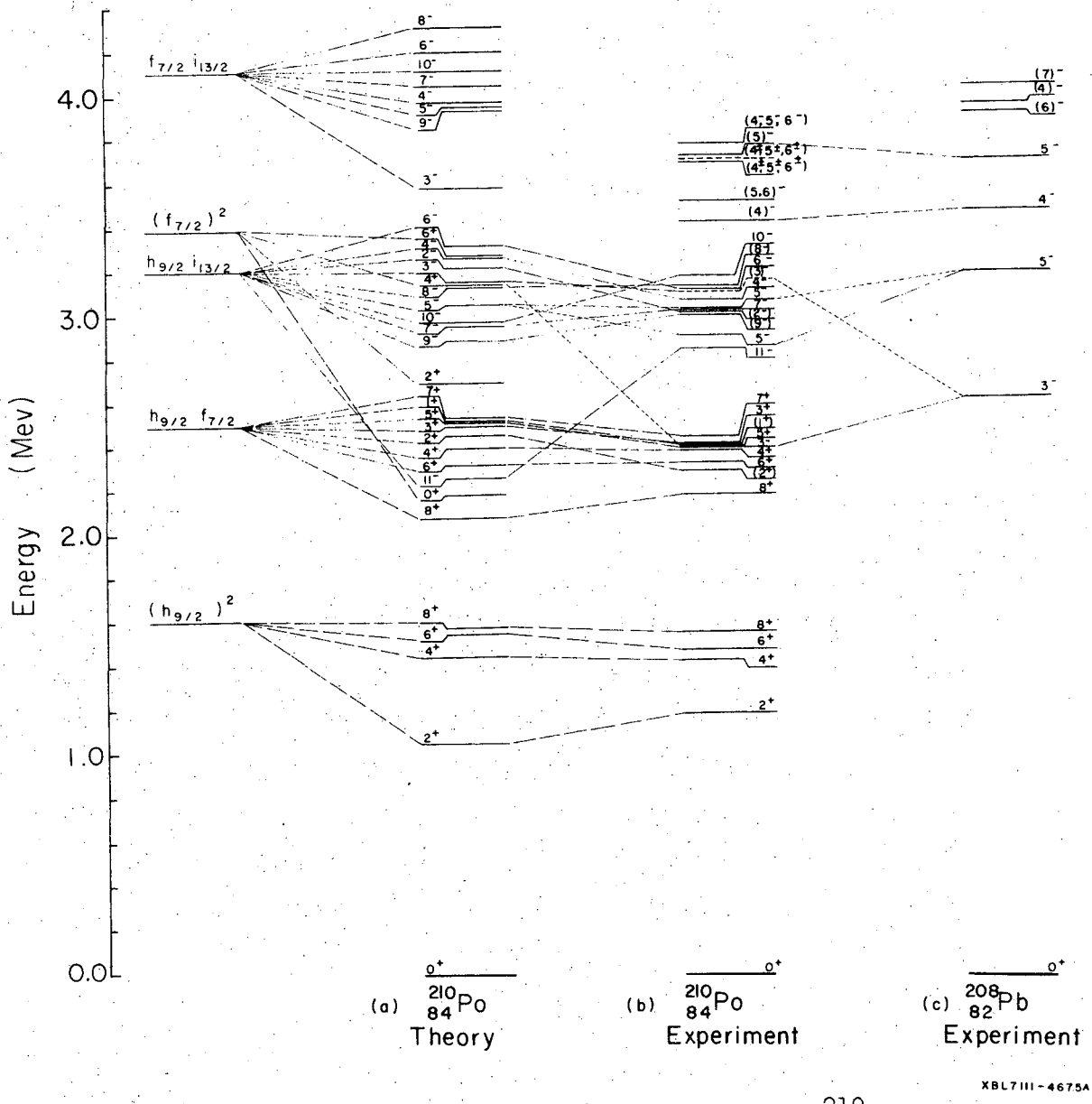

Fig. 47. Comparison of the experimental level scheme of ^{210}Po (b) with a shell model calculation[41]) (a) and with the experimental level scheme of ^{208}Pb [35]) (c). The dotted lines connect levels believed to have components due to the same configuration. The zero-order energies of the two-proton configurations in ^{210}Po are shown to the left.

used to investigate the collective states via inelastic scattering. Configuration mixing of the 3^- collective state with the $\pi(h_{9/2}\, i_{13/2})_{3^-}$ configuration also could be investigated. This experiment might explain the 3^- depression in energy from that observed in ^{208}Pb as discussed in section G. The configurations due the coupling of the 3^- core state to the 2^+ first excited state might also be observable. (The 5^- state was predicted at an energy of 3822 keV in section IVH.)

Our gamma-ray decay transition probabilities discussed in section J showed that a sensitive test may exist for the wavefunctions calculated with various potentials. One might be able to adjust the parameters of the calculation until agreement of energy levels and gamma-ray branching ratios is achieved. The transition probability calculations predicted that low energy intraband transitions can compete among the higher energy interband transitions. However, we were not able to directly observe these transitions but rather make assignments to previously reported unassigned conversion electrons[25]. Thus a high-resolution reinvestigation of low energy electron spectrum might allow other transitions to be observed and with a better intensity measurement.

It seems clear that this nucleus because of its structure can serve as a useful guide for future theoretical calculations in lead region to test phenomenological and realistic potentials representing the residual interactions.

V. THE ELECTRON-CAPTURE DECAY OF ^{209}At TO LEVELS IN ^{209}Po

A. Introduction

This nucleus is of theoretical interest because it has two protons more than a closed shell of Z = 82 and one neutron less than a closed shell of N = 126. The electron-capture decay of ^{209}At(5.5h) to ^{209}Po populates levels of ^{209}Po and hence provides a means of studying the nuclear level structure.

The ground-state spin and parity of ^{209}At has not been measured but is predicted on the basis of the shell model and experimental data[9] in the lead region to have the configuration $(\pi(h_{9/2}^3\, s_{1/2}^2)_{9^-/2}\ \nu(p_{1/2}^0\, f_{5/2}^6)_{0^+})_{9^-/2}$. The spin assignment of 9/2 gains some support from the measured[71] spin of 9/2 for the ground-state of ^{211}At. The ground-state spin of ^{209}Po has been measured[72] as 1/2 and has the probable configuration $(\pi(h_{9/2}^2\, s_{1/2}^2)_{0^+}\ \nu(p_{1/2}^{-1}\, f_{5/2}^6)_{1^-/2})_{1^-/2}$. Thus states of spin 7/2, 9/2 and 11/2 should be directly populated in the decay and states of spin 1/2-5/2 and 13/2-15/2 by the gamma decay of higher-lying levels.

Electron-capture decay transitions from the odd-even nucleus ^{209}At to the even-odd nucleus ^{209}Po should favor population of single neutron (particle or hole) states if such transitions are not hindered. Direct decay to the ground-state would involve the conversion of an $1h_{9/2}$ proton to a $3p_{1/2}$ neutron which requires a change of four units ($\Delta\ell = 4$) in the orbital angular momentum (i.e. $\pi(h_{9/2}) \xrightarrow{EC} \nu(p_{1/2})$) and should be hindered. Thus population of excited states is expected.

No previous studies of the decay have been made with high resolution Ge(Li) detectors so that a detailed investigation has been performed. In this section we report on the investigation of the transitions following the electron-capture decay of ^{209}At. The energies and intensities of 87 γ-rays between levels in ^{209}Po have been measured. The multipolarities of 27 transitions have been determined by measuring relative internal conversion coefficients. Sixty-three of the transitions have been placed into a decay scheme with the aid of γ-γ coincidence measurements defining 20 levels. The levels of ^{209}Po have been compared with a weak coupling calculation using experimental data from the levels of ^{208}Bi, ^{210}Po, ^{209}Bi and ^{207}Pb to represent the neutron hole-proton and proton-proton interactions using the formalism presented in section IID.

B. Previous Studies

^{209}At(5.5h) was first identified by Barton, Ghiorso and Perlman[73] in 1951 who reported decay by alpha emission and electron-capture. (The per cent alpha branching of ^{209}At per decay has been measured[35] as 4.1±0.5%.) The conversion electrons from the ^{209}At decay were reported in 1954 by Mihelich, Schardt, and Segre'[24] although no decay scheme was proposed. In 1956 Stoner[36] reported in detail the ^{209}At conversion electron, gamma-ray and alpha spectra. He reported intense gamma-rays at 90.8, 195, 545 and 780 keV in coincidence and proposed the decay scheme shown in fig. 48b. The ^{209}Bi(α,4n)^{209}At reaction was used by Stoner to produce intense electron sources with appreciable amounts of ^{210}At present from the competing (α,3n) reaction. An alternate method of production involving proton spallation of thorium metal to produce ^{213}Ra was used to isolate much smaller quantities of ^{209}At after an appropriate decay period. This produced low intensity sources free of ^{210}At for measurement of the gamma-ray spectra.

In 1965 Yamazaki and Matthias[74] investigated the levels of ^{209}Po with the ^{208}Pb(α,3n)^{209}Po reaction and Ge(Li) detectors. They established the spin sequence 9/2(782Q) 5/2(545Q) 1/2 for the lower levels of ^{209}Po shown in fig. 48a. Yamazaki and Matthias[74] also reported a 100 ns isomeric level at an energy similar to the 8^+ level of ^{210}Po. They suggested the possible two particle-one hole configurations $(\pi(h_{9/2}^2)_{8^+}\ \nu(p_{1/2}^{-1}))_{17^-/2,15^-/2}$ for the isomeric level.

During the course of our study, preliminary reports have been made by Alpsten, Appleqvist, and Astner[75] and Alpsten and Astner[76] on

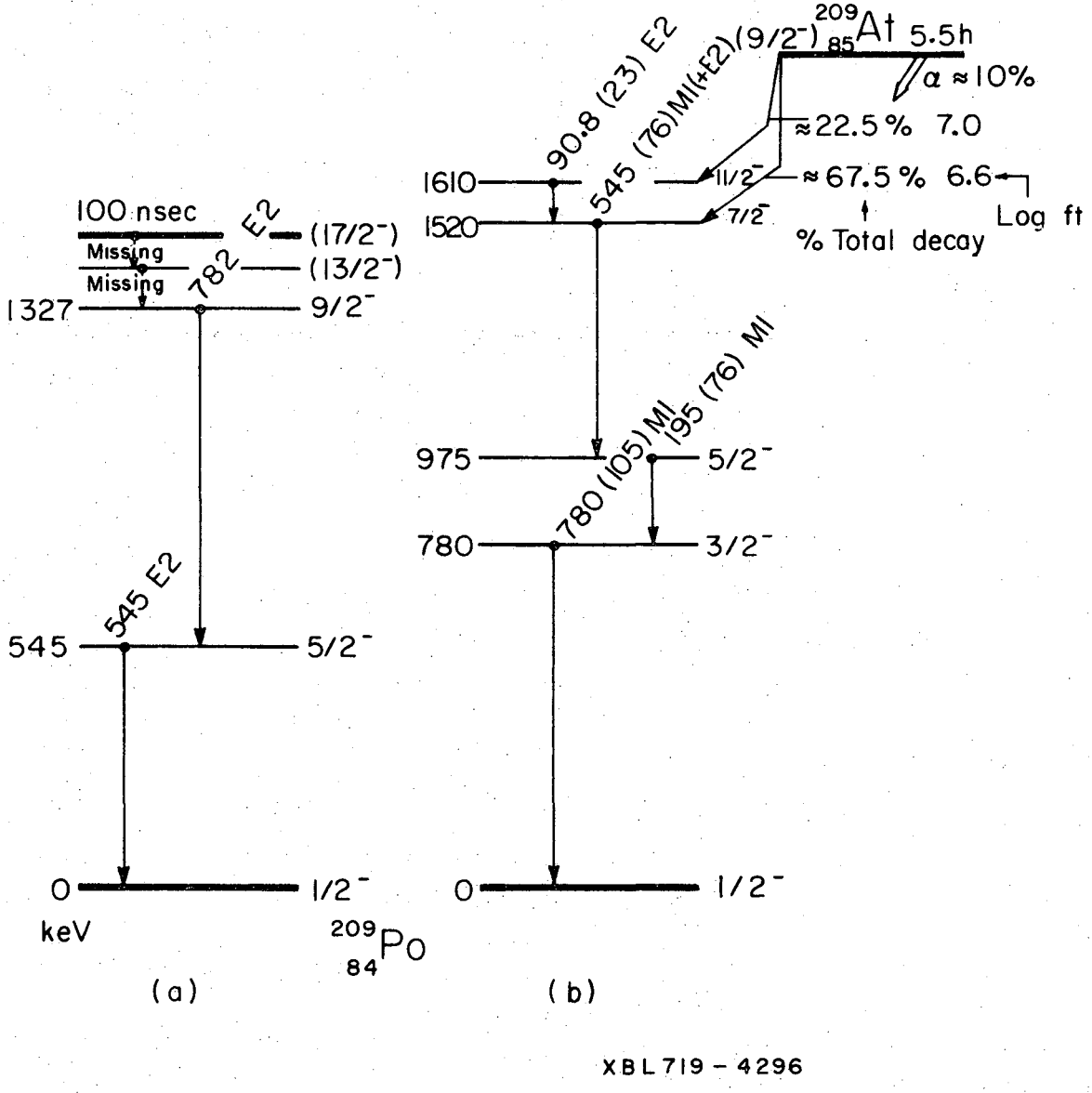

Fig. 48. Summary of previous studies of ^{209}Po level structure.
(a) Level scheme of ^{209}Po proposed by Yamazaki and Matthias[74]).
(b) Decay scheme of ^{210}At proposed by Stoner[36]).

the electron-capture decay. Bergström *et al.*[77]) issued a preliminary report on a reinvestigation of the $^{208}Pb(\alpha,3n)^{209}Po$ reaction.

C. Source Preparation

Sources used in this study were obtained by the $^{209}Bi(\alpha,4n)^{209}At$ reaction in the Berkeley 88-inch cyclotron at bombarding energies of 49-51 MeV, with bismuth metal target thicknesses of 30-59 mg/cm^2. The astatine was separated from the bismuth target by volatilization and sources were prepared as previously described[36,38,39] in section IVC. These sources contained, in addition to ^{209}At, varying amounts of ^{208}At, ^{210}At and ^{211}At from the competing $(\alpha,5n)$, $(\alpha,3n)$ and $(\alpha,2n)$ reactions, respectively, depending upon the energy of the incident alpha particles.

The $(\alpha,3n)$ and $(\alpha,2n)$ cross sections had been previously determined[78,79] in the energy region of 20-42 MeV. The $(\alpha,4n)$ and $(\alpha,5n)$ cross sections had not been studied in the energy region of 41-65 MeV. To determine the $(\alpha,4n)$ and $(\alpha,5n)$ cross sections relative to the $(\alpha,3n)$, a measurement was made of the relative gamma-ray activities of astatine isotopes produced in a series of four stacked foils with an incident beam energy of 72 MeV. Measurement of the relative gamma-ray intensities of three transitions of 1181.4, 545.0 and 686 keV and consideration of the decay schemes allowed determination of the relative atom ratios $^{210}At/^{209}At/^{208}At$ that were produced. These measurements yielded the relative production cross section ratios of three astatine isotopes at mean bombarding energies of 68, 61.7, 54.6 and 47.7 MeV. These results are shown in Table 15.

In order to qualitatively compare these gamma-ray ratios to previous cross sections measurements at lower energies (<42 MeV), an extrapolation of the $(\alpha,3n)$ reaction cross section was made and is shown

Table 15. Relative gamma-ray ratios and cross sections for various astatine isotopes produced by $^{209}Bi(^{4}He,xn)$ reactions based on measured gamma-ray transition intensities. The 1181.4, 545.0, and 686 keV γ-ray transitions in ^{210}Po, ^{209}Po, and ^{208}Po were measured (relatively) to arrive at these values after correcting for alpha-branching and appropriate decay times.

Alpha Energy[a]	Gamma-ray ratios				Relative cross section (barns)		
MeV	$^{210}At/^{210}At$	$^{209}At/^{210}At$	$^{208}At/^{210}At$	$^{209}At/^{208}At$	$\sigma(\alpha,3n)$[b]	$\sigma(\alpha,4n)$[b]	$\sigma(\alpha,5n)$[b]
68	1.0	2.9	18.95	0.15	0.07	0.226	1.32
61	1.0	3.4	24.8	0.14	0.12	0.455	2.98
54	1.0	5.45	11.7	0.465	2.0	1.21	2.34
47	1.0	4.2	0.785	5.35	5.2	2.43	0.408

[a]The error (estimated ±2.5 keV) reflects uncertainty in the target thicknesses and corrections for energy losses within the targets and aluminum backing foils[80].

[b]This cross section value is based on earlier results[78,79] at lower energy and the extrapolation procedure described in the text.

as a dotted line in fig. 49. This extrapolated shape of the (α,3n) cross section was used only to provide a normalization point for the measured relative cross section ratios of Table 15 and these results are included in fig. 49. All data points of fig. 49 in the region 45-70 MeV are results of our measurements based on this exprapolation procedure. Because of the uncertainty in the validity of this extrapolation procedure, no errors in the absolute cross section are shown. However, errors in the measured relative cross sections ratios (due to uncertainty in half-life, relative photon intensity determinations, and counting times) were estimated as ±8%. Errors shown in fig. 49 for the helium-ion energy reflect the uncertainty in the target thicknesses and corrections[80]) for energy losses within the targets and aluminum backing foils.

To identify ^{208}At, the energies and intensities of the major radiations reported by Treytl, Hyde, and Yamazaki[81]) were remeasured. We note that the ^{208}At could be minimized by bombarding below the threshold energy (~ 48 MeV) for production of detectable amounts relative to the ^{209}At. The "impurities" from ^{210}At in spectra were identified by comparison of the energies and intensities of gamma-rays and conversion electrons reported in section IV.

It should be noted that this production method limited observation of the weaker transitions following the decay of ^{209}At due to an increased background. Typically, at the end of bombardment, the largest ratio of the relative gamma-rays of (^{209}At) to (^{210}At) was approximately 4-5$\frac{1}{2}$ to 1. In order to check the relative γ-ray intensities obtained

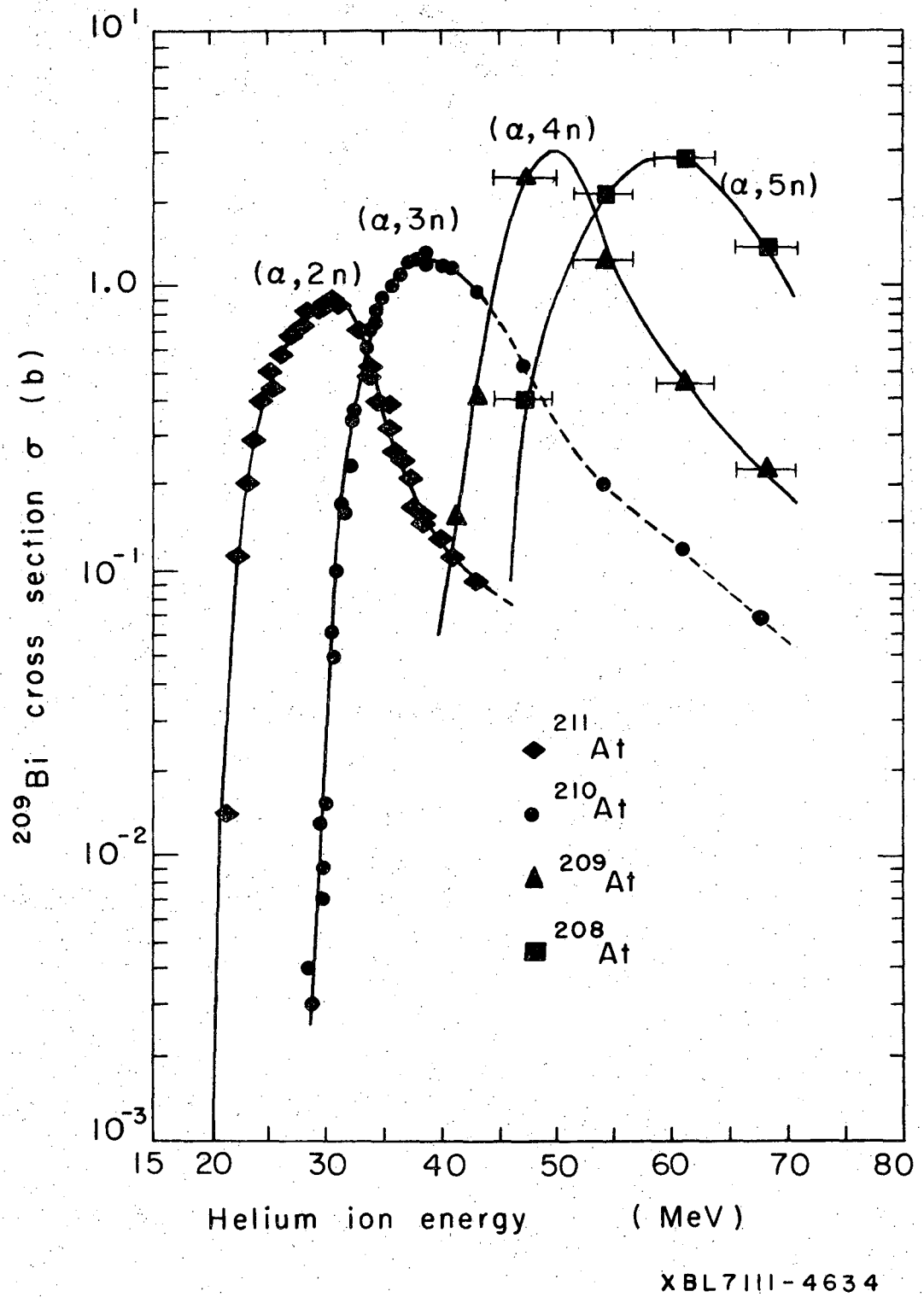

Fig. 49. Excitation functions for the reactions ^{209}Bi (α,xn) $^{213-x}$At, for x = 2, 3, 4, 5. The (α,2n) and (α,3n) results below 43 MeV are due to Ramler et al.[78]) and Kelly and Segre'[79]). The data points above 43 MeV are from this study. The vertical scale for these points is arbitrary.

from mixed sources, some data were taken with appreciable amounts of ^{208}At in the sample because of the higher $I_\gamma(^{209}\text{At})/I_\gamma(^{210}\text{At})$ ratios.

Toward the end of our study, we were fortunate to obtain a low intensity mass separated astatine source from M. C. Michel and the (virgin) Berkeley Isotope Separator in order to further check on intensity assignments with mixed astatine sources. The sample was essentially free of ^{210}At ($\leqslant 10^{-3}$% relative to ^{209}At). The portion of the 5 mm aluminum collection foil from the mass separator containing the mass 209 deposit was used directly as a source for obtaining gamma-ray and conversion electron spectra.

D. Experimental Results

1. Gamma-Ray Singles Spectra

The data for ^{209}At gamma-ray singles measurements were collected as previously described in section IIIA. Mixed sources of astatine (^{210}At, ^{209}At and ^{208}At) were used (see section IIIC) and data were collected over a period of 0.25-20 hours after end of bombardment to minimize the ^{210}At background. Figures 50 and 51 show spectra taken with the 35-cm^3 (active volume) coaxial Ge(Li) detector over the energy ranges of 100-1600 keV and 630-2760 keV respectively. Photopeaks from ^{208}At are present in the spectrum of fig. 50. A gamma-ray spectrum of the lower energy range of 16-240 keV obtained with the Si(Li) detector is shown in section VD3 in the bottom of fig. 75. This spectrum was obtained with a Teflon absorber covering the source to distinguish between gamma-rays and conversion electrons.

To investigate weak gamma-ray transitions, a mass separated ^{209}At source of low intensity was obtained and the resulting activity measured with the Ge(Li) spectrometer. The spectrum obtained is shown in fig. 52. The low intensity source coupled with the large volume of the detector produced many sum peaks. However, several new transitions were identified from this spectrum and several other transitions barely observable above the high compton background with mixed sources were confirmed. Four occured at the same energy as some intense ^{210}At transitions. Table 16 lists additional transitions observed with the mass separated source but which could not be definitely assigned to ^{209}At decay. Clearly a more intense source is needed to extract more definite information from such a spectrum.

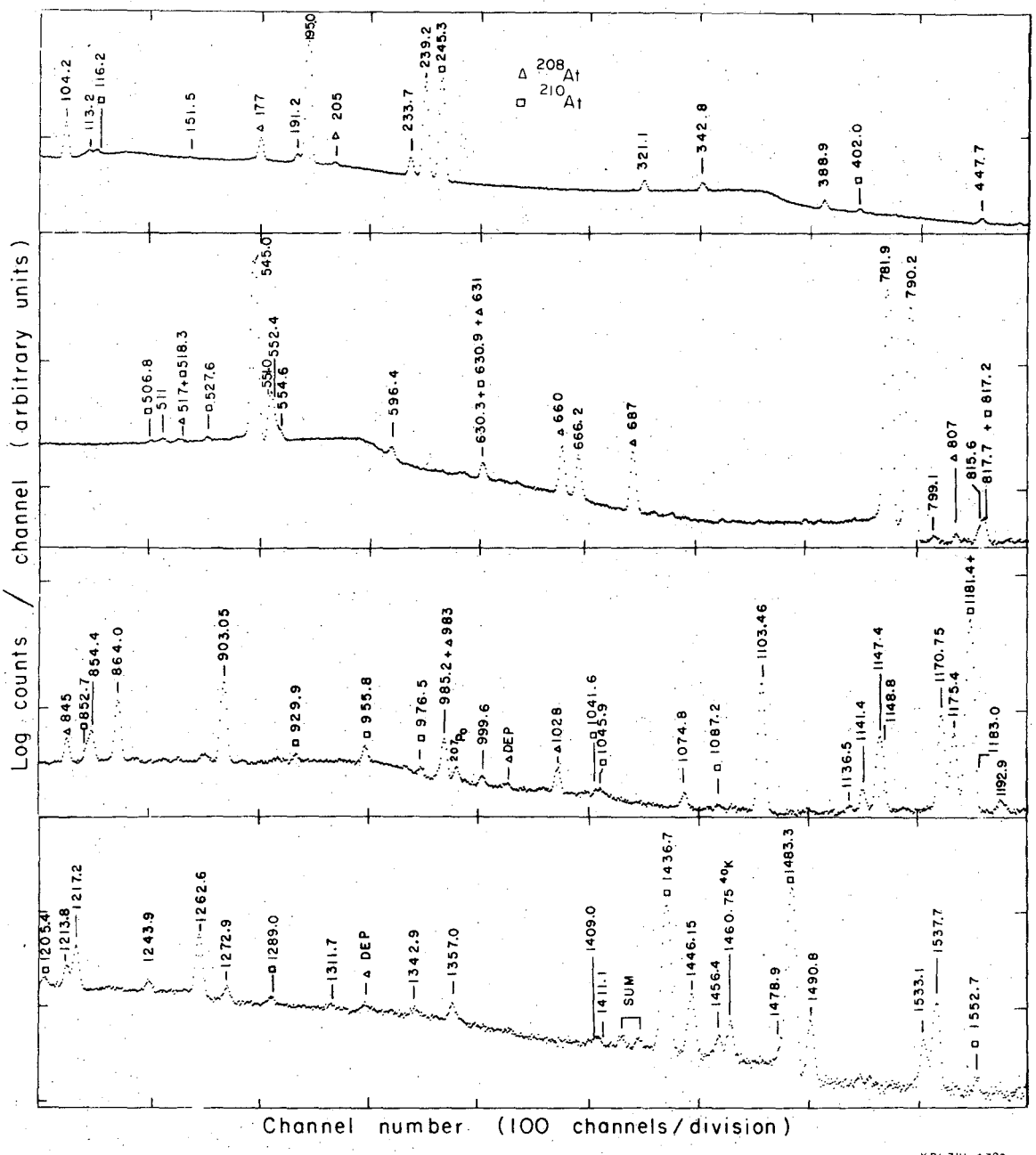

Fig. 50. Gamma-ray spectrum of a mixed source of astatine in the energy range of 100-1600 keV taken with a coaxial Ge(Li) spectrometer. Symbols are used to denote gamma-rays due to isotopes other than ^{209}At.

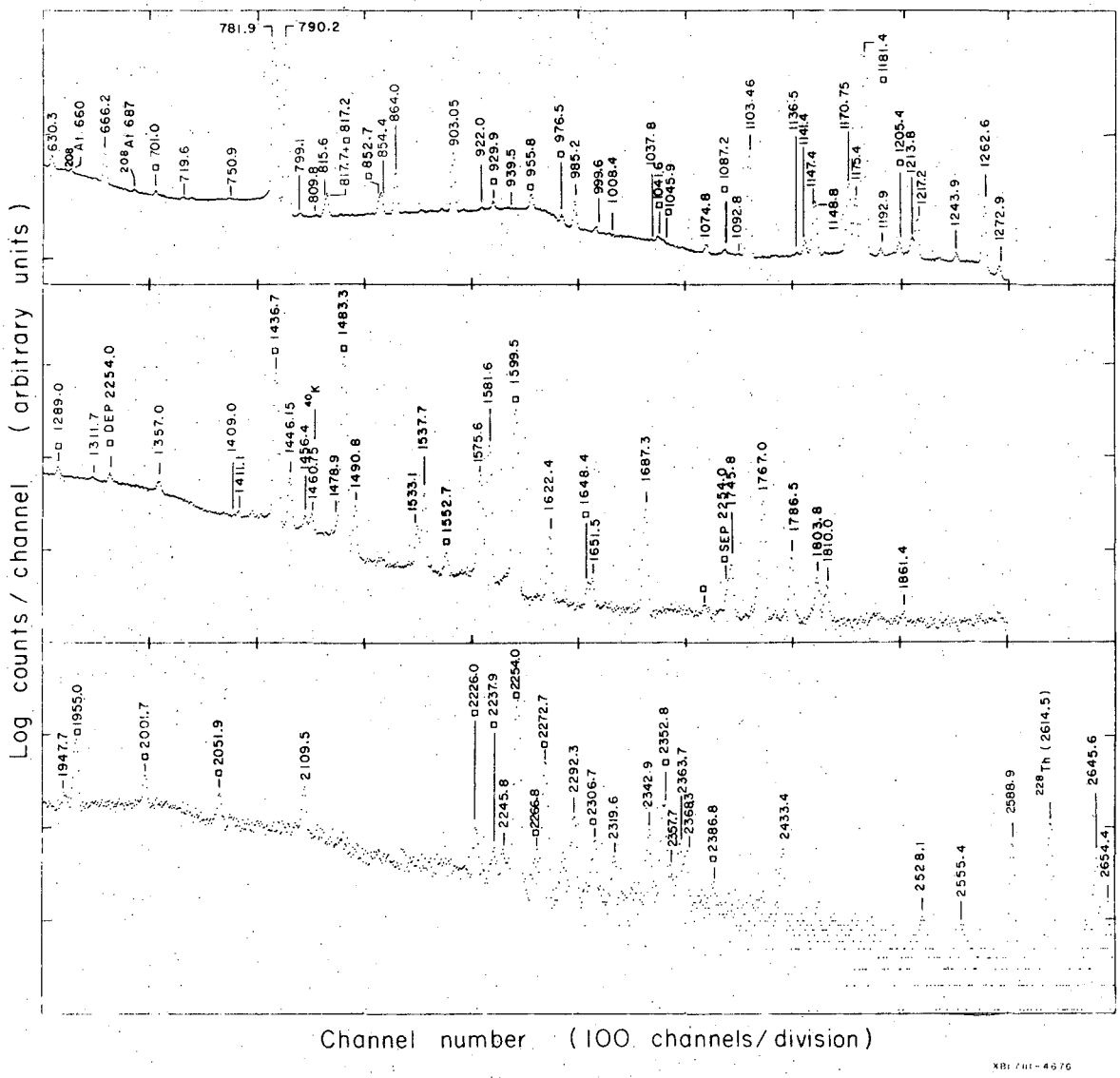

Fig. 51. Gamma-ray spectrum of a mixed source of astatine in the energy range of 630-2660 keV taken with a coaxial Ge(Li) spectrometer. The symbol □ is used to denote gamma-rays due to the decay of ^{210}At.

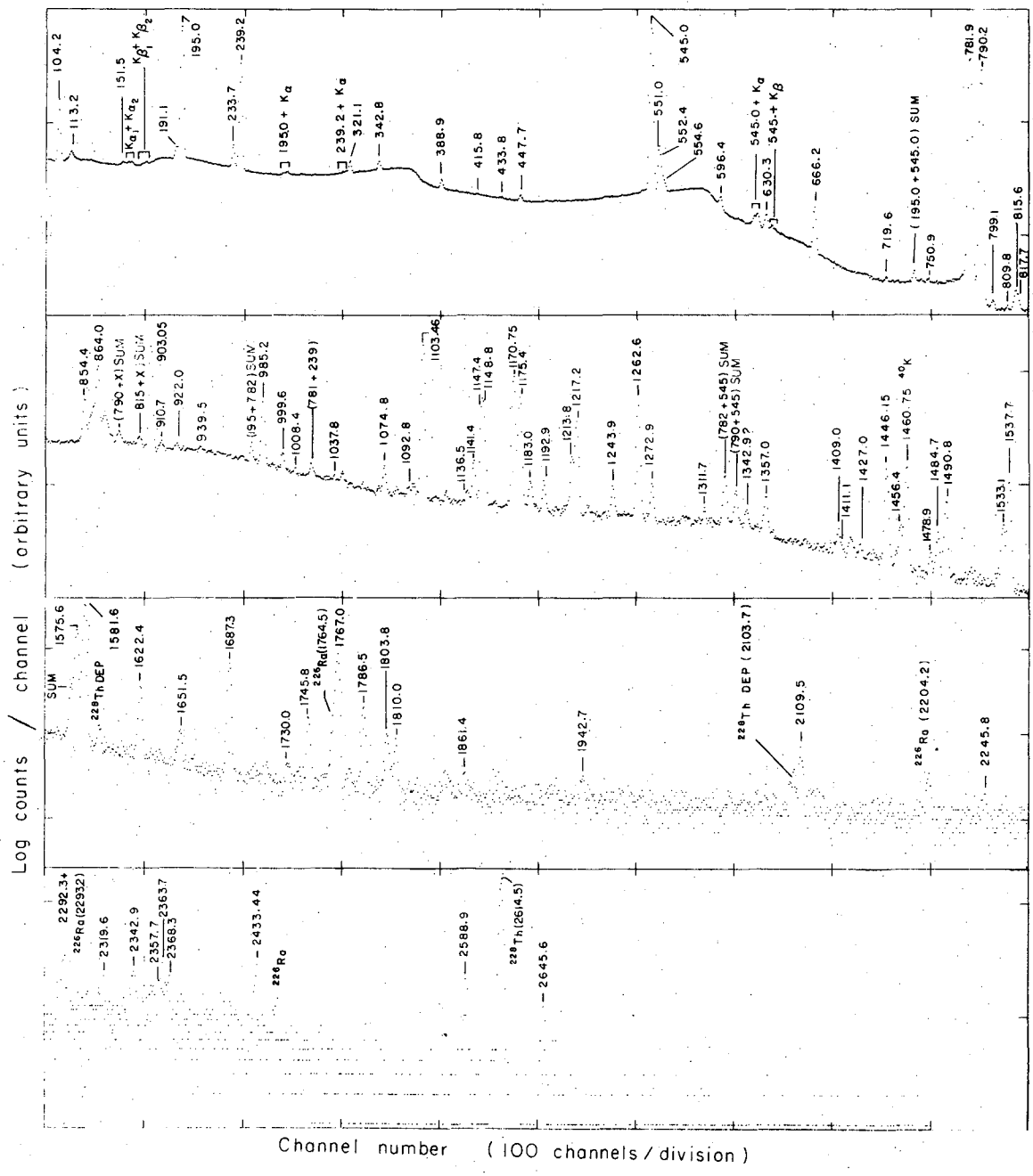

Fig. 52. Gamma-ray spectrum of a mass separated ^{209}At source in the energy range of 100-2700 keV taken with a coaxial Ge(Li) spectrometer.

Table 16. Weak transitions observed from a low intensity mass separated ^{209}At source. The assignment of these transitions to ^{209}At decay is uncertain and these are not placed in the current level scheme.

Gamma-ray Energy keV	Absolute gamma-ray intensity % of ^{209}At EC decays
515.1 (3)	.05 (2)
523.0 (3)	.04 (2)
1084.0 (4)	0.037 (5)
1112.9 (6)	0.022 (6)
1202.3 (4)	0.022 (6)
1210.2 (4)	0.047 (10)
1295.8 (4)	0.026 (6)
1299.0 (5)	0.022 (6)
1361.7 (6)	0.0092 (40)
1419.4 (4)	0.041 (9)
1421.5 (5)	0.023 (8)
1529.4 (5)	0.016 (5)
1706.1 (7)	0.013 (2)
2102.0 (4)	0.008 (3)

The energies and intensities of the γ-rays were obtained by analysis of the spectra with the computer code SAMPO[40,41]. Energy calibrations were obtained using the standard energies compiled[19] in Appendix D. The relative photopeak efficiency was determined with an IAEA calibrated intensity set and ^{180m}Hf as described in Appendix E. Uncertainties in the relative photopeak efficiency measurements are estimated to be ±5% in the energy range of 100-600 keV and ±4% in the range 500-2800 keV. In Table 17 we list the energies and absolute gamma-ray intensities per electron-capture decay of the observed photopeaks assigned to the decay of ^{209}At. The assignments were based on half-life measurements for the more intense transitions and by comparison of spectra taken with different ratios of astatine isotopes. The errors quoted include the calibration and fitting errors.

In Table 17, below 500 keV where transition multipolarities were assumed or measured, the total transition intensity is also shown. The theoretical conversion coefficients of Hager and Seltzer[42,43] were used to derive these results. The multipolarities of the 113.2 and 151.5 keV transitions were assumed to be pure E2 and the 195.0 keV transition was determined in section VD2 to be M1 + 20% E2. The 90.8 keV gamma-ray not resolvable from the K x-rays with the detectors employed so that the reported gamma-ray intensity is based on our measured relative L-conversion electron intensities and the theoretical E2 conversion coefficient (see section VD3). The multipolarity of the 104.2 keV transition could not be determined from this study and we have listed the transition intensities in Table 17 for both M1 and E2 multipolarities.

Table 17. Gamma-rays observed in the decay of ^{209}At.

Gamma-ray Energy (keV)	Absolute[a] gamma-ray intensity (% of ^{209}At EC decays)	Absolute[b] transition intensity (% of ^{209}At EC decays)
90.8 (2)	(1.69 (12))[k]	(19.8 (15))[k]
104.2 (2)	2.50 (25)	(17.9 (E2), 28.4 (M1))
113.2 (3)	0.16 (4)	(0.85)[e]
151.5 (3)	0.055 (20)	(0.13)[e]
191.1 (3)[d]	0.41 (7)	–
195.0 (1)	25.0 (1.2)	65.0 (32)[f]
233.7 (1)	1.14 (9)	2.33 (18)
239.2 (1)	14.25 (50)	15.05 (65)
321.1 (2)	0.71 (3)	0.72 (4)
342.8 (2)[d]	0.57 (3)	0.67 (5)
388.9 (2)	0.56 (3)	0.70 (5)
415.8 (6)[c]	0.06 (2)	–
433.8 (3)[c]	0.08 (2)	–
447.7 (2)	0.28 (2)	0.32 (3)

Gamma-ray Energy (keV)	Absolute[a] gamma-ray intensity (% of ^{209}At EC decays)	Gamma-ray Energy (keV)	Absolute[a] gamma-ray intensity (% of ^{209}At EC decays)
545.0 (1)	97.4 (30)	1272.9 (2)[d]	0.22 (2)
551.0 (3)	5.21 (24)	1311.7 (3)	0.056 (6)
552.4 (4)	1.36 (20)	1342.9 (3)[d,l]	0.070 (6)
554.6 (4)	0.61 (11)	1357.0 (2)	0.18 (1)

(continued)

Table 17 (continued)

Gamma-ray Energy (keV)	Absolute[a] gamma-ray intensity (% of ^{209}At EC decays)	Gamma-ray Energy (keV)	Absolute[a] gamma-ray intensity (% of ^{209}At EC decays)
596.4 (2)	0.72 (4)	1409.0 (6)[c]	0.019 (8)
630.3 (2)	0.75 (3)	1411.1 (4)[d,g]	0.057 (8)
666.2 (1)	2.01 (7)	1427.0 (3)[c]	0.030 (6)
719.6 (3)[d]	0.08 (1)	1446.15 (10)	0.56 (2)
750.9 (2)[d]	0.07 (1)	1456.4 (2)	0.12 (1)
781.9 (1)	87.0 (26)	1478.9 (3)	0.044 (4)
790.2 (1)	66.3 (20)	1484.7 (3)[c]	0.10 (1)
799.1 (2)[d]	0.11 (2)	1490.8 (2)	0.28 (2)
809.8 (3)[d,g]	0.036 (8)	1533.1 (2)[d]	0.16 (1)
815.6 (3)	0.24 (3)	1537.7 (1)	0.51 (3)
817.7 (3)[d,c]	0.18 (4)	1575.6 (2)	0.89 (4)
826.8 (3)[d,g]	0.05 (1)	1581.6 (1)	1.87 (7)
854.4 (2)	0.62 (4)	1622.4 (2)[d]	0.18 (1)
864.0 (1)	2.11 (10)	1651.5 (5)	0.043 (4)
903.05 (10)	3.87 (12)	1687.3 (2)[d]	0.40 (2)
910.7 (5)[d,g]	0.078 (11)[h]	1730.0 (4)[c]	0.013 (2)
922.0 (3)[d,g]	0.077 (10)	1745.8 (3)	0.086 (5)
939.5 (3)[c]	0.05 (1)	1767.0 (1)	0.54 (3)
985.2 (2)	0.8 (1)[h]	1786.5 (2)[d]	0.13 (1)
999.6 (2)[d]	0.17 (1)	1803.8 (2)[d]	0.056 (4)
1008.4 (4)[d,g]	0.038 (9)	1810.0 (2)[d]	0.039 (4)

(continued)

Table 17 (continued)

Gamma-ray Energy (keV)	Absolute[a] gamma-ray intensity (% of ^{209}At EC decays)	Gamma-ray Energy (keV)	Absolute[a] gamma-ray intensity (% of ^{209}At EC decays)
1037.8 (4)[d,g]	0.030 (6)	1861.4 (5)[d,j]	0.008 (2)
1074.8 (2)	0.21 (1)	1947.7 (4)[d]	0.014 (2)
1092.8 (4)[d]	0.049 (7)	2109.5 (3)	0.042 (4)
1103.46 (10)	5.5 (2)	2245.8 (6)[d]	0.007 (1)
1136.5 (3)	0.075 (10)	2292.3 (5)[d,g]	0.014 (4)[i]
1141.4 (3)	0.34 (2)	2319.6 (4)	0.007 (2)
1147.4 (3)	1.37 (10)	2342.9 (4)[d]	0.017 (5)
1148.8 (3)	0.85 (10)	2357.7 (6)	0.007 (2)
1170.75 (10)	3.1 (2)	2363.7 (4)	0.015 (2)
1175.4 (2)	2.0 (1)	2368.3 (4)[d]	0.012 (2)
1183.0 (3)[d,c]	0.16 (2)	2433.44 (20)	0.015 (2)
1192.9 (3)	0.16 (7)	2528.1 (6)	0.0025 (10)
1213.8 (2)[d]	0.46 (4)	2555.4 (4)[d]	0.002 (1)
1217.2 (2)	1.13 (8)	2588.9 (4)[d]	0.017 (3)
1243.9 (2)[d]	0.16 (2)	2645.6 (3)[d]	0.010 (3)
1262.6 (1)	2.00 (8)	2654.4 (4)	0.0021 (9)

[a]Absolute intensity per electron capture decay is based on the new level scheme.

[b]The theoretical conversion coefficients of Hager and Seltzer[42]) were used to derive these transition intensities.

[c]Assignment to ^{209}At decay is based on the observation of the transition in a low intensity ^{209}At mass separated source.

(continued)

Table 17 (continued)

[d] These transitions are unplaced in the present level scheme.

[e] The multipolarity of this transition was assumed E2.

[f] The multipolarity of this transition was assumed M1 + 20% E2 based on our measured α_K, α_L, and α_M values (see section VD3).

[g] This transition was observed very weakly in mixed ^{210}At and ^{209}At sources so that assignment to ^{209}At decay is uncertain. This was also observed in the low intensity ^{209}At mass separated source.

[h] The intensity was corrected for a ^{205}Bi component.

[i] The intensity was corrected for a ^{226}Ra component from room background.

[j] Assignment to ^{209}At decay is uncertain (^{205}Bi?).

[k] These intensities were extracted from the relative conversion electron intensities where the 90.8 keV transition was measured as 100% E2.

[l] Assignment to ^{209}At decay is uncertain.

2. Gamma-Gamma Coincidence Spectra

Three parameter gamma-gamma coincidence measurements of two mixed sources were taken with two coaxial Ge(Li) detectors operated "on line" with a PDP-7 multiparameter data acquisition system[16,17,18] (see section IIIB). The second source was obtained approximately midway through the 32-hour experiment to enhance the ratio of ^{209}At to ^{210}At. The axes of the two detectors were positioned at 90° with respect to the sources and were separated by a graded lead-cadmium-copper shield to minimize scattering between the detectors. A fast-coincidence electronic arrangement (see Appendix C) similar to that described by Jaklevic et al.[21] was used. The width of the distribution (shown in fig. 53) for the experiment was about 46 ns (FWHM). (Coincidences recorded for the population of delayed states in ^{210}At and ^{209}At are primarily responsible for the (delayed coincidence) shape of the time spectrum of fig. 53.) A total of $3.9 \cdot 10^7$ three parameter (E1, E2, ΔT) events were stored serially on magnetic tape for later sorting and analysis on the LBL CDC-6600 computer system using the methods described in section IVD2. (The sorting routine employed permitted subtraction of random events and events associated with the neighboring compton distributions from each energy gate.) The gross coincidence spectra collected for each of the coaxial detectors are shown in figs. 54 and 55. The coincidence sorting was performed by setting gates (for photopeak and compton background coincident events) on the energy spectrum of fig. 55 and the time spectrum of fig. 53. Shown in Table 18 are the gates set in the spectrum of fig. 55 for the sorting of the tapes. Approximately sixty sorts were

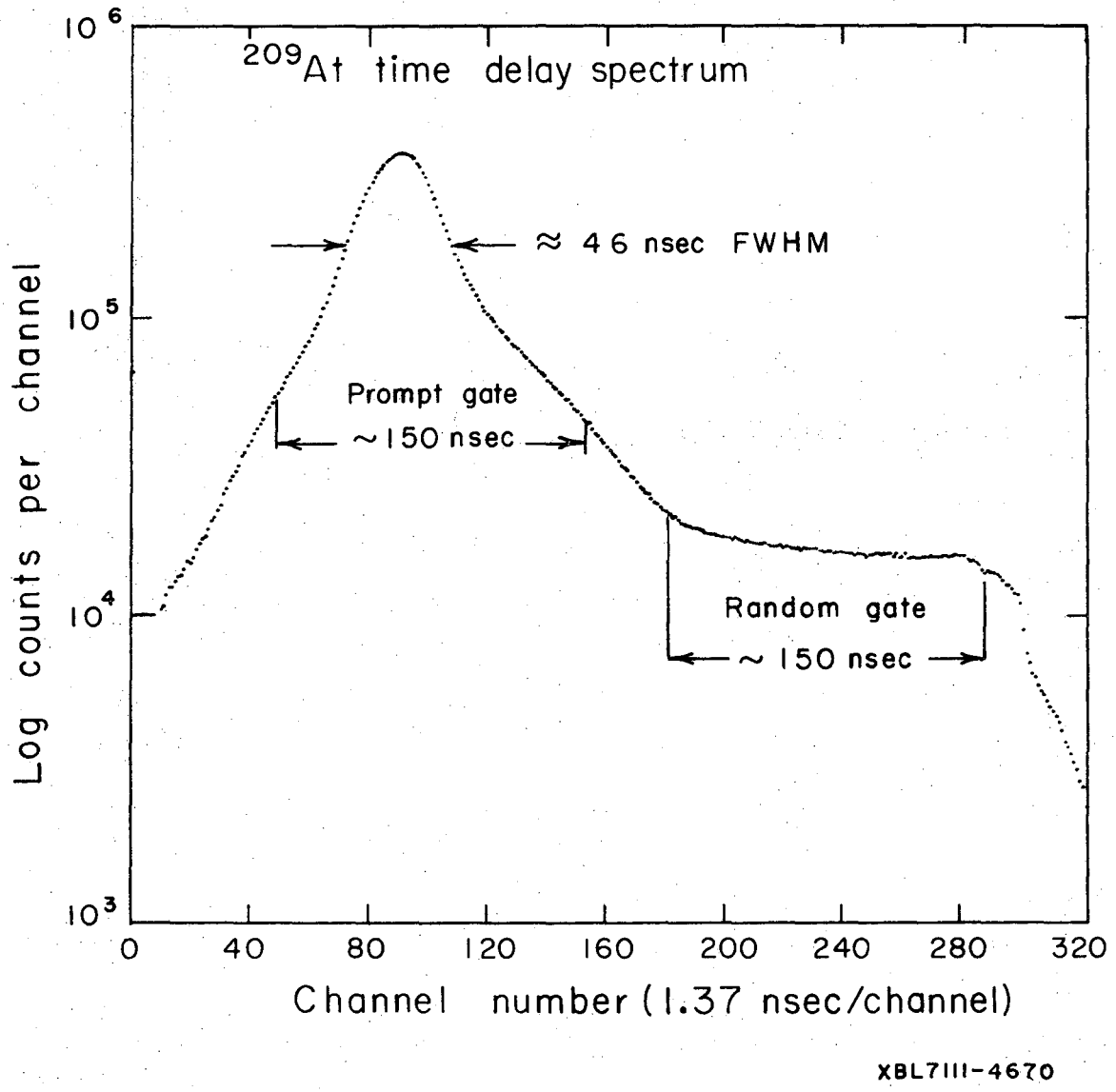

Fig. 53. "Gross" time distribution for the ^{209}At γ-γ coincidence data. The 150 nsec gates were used to obtain the coincidence events shown in figs. 56-74.

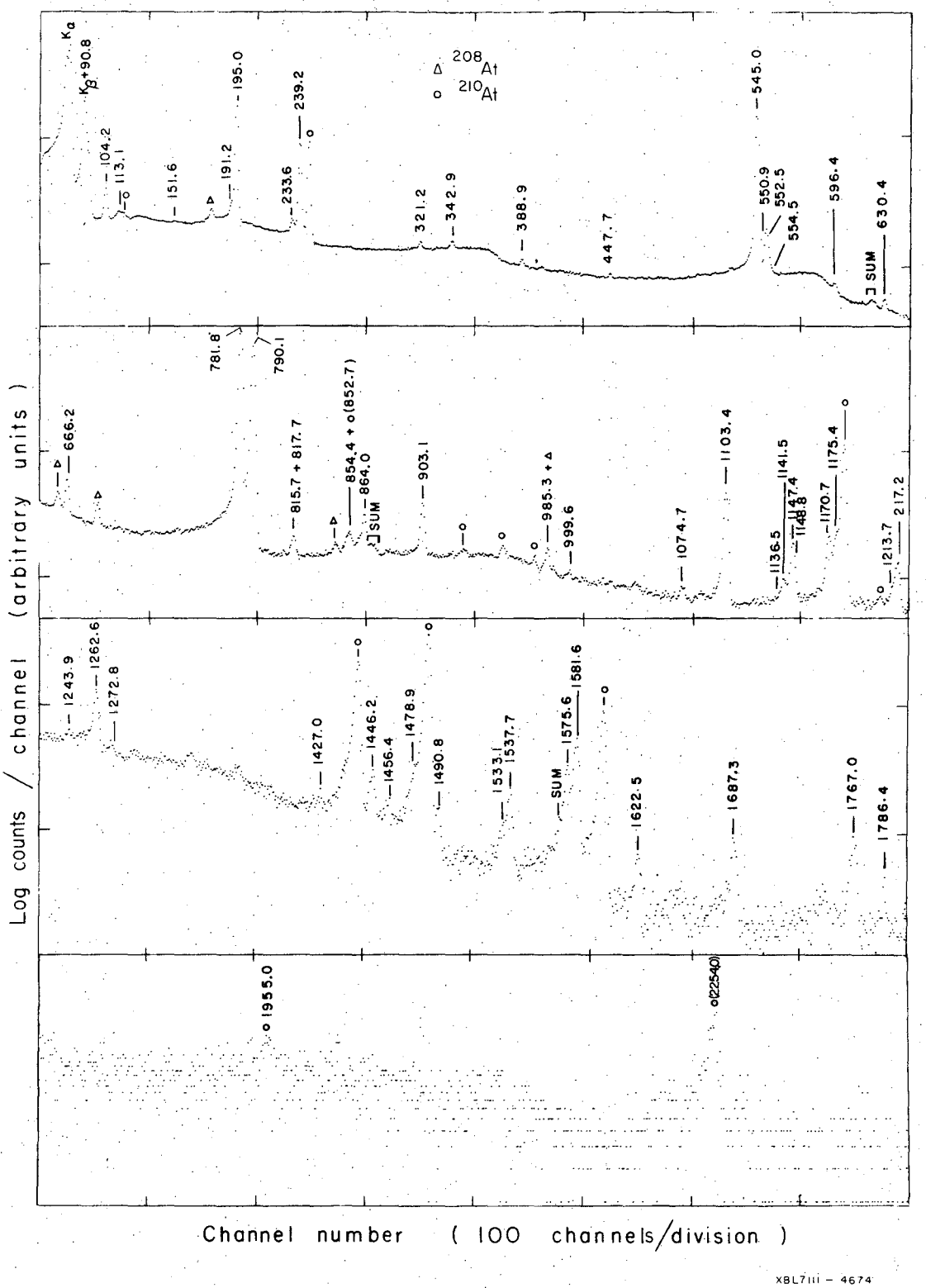

Fig. 54. "Gross" γ-γ coincidence spectrum for the 40-cm^3 (active volume) coaxial Ge(Li) detector. Symbols are used to denote gamma-rays due to isotopes other than ^{209}At.

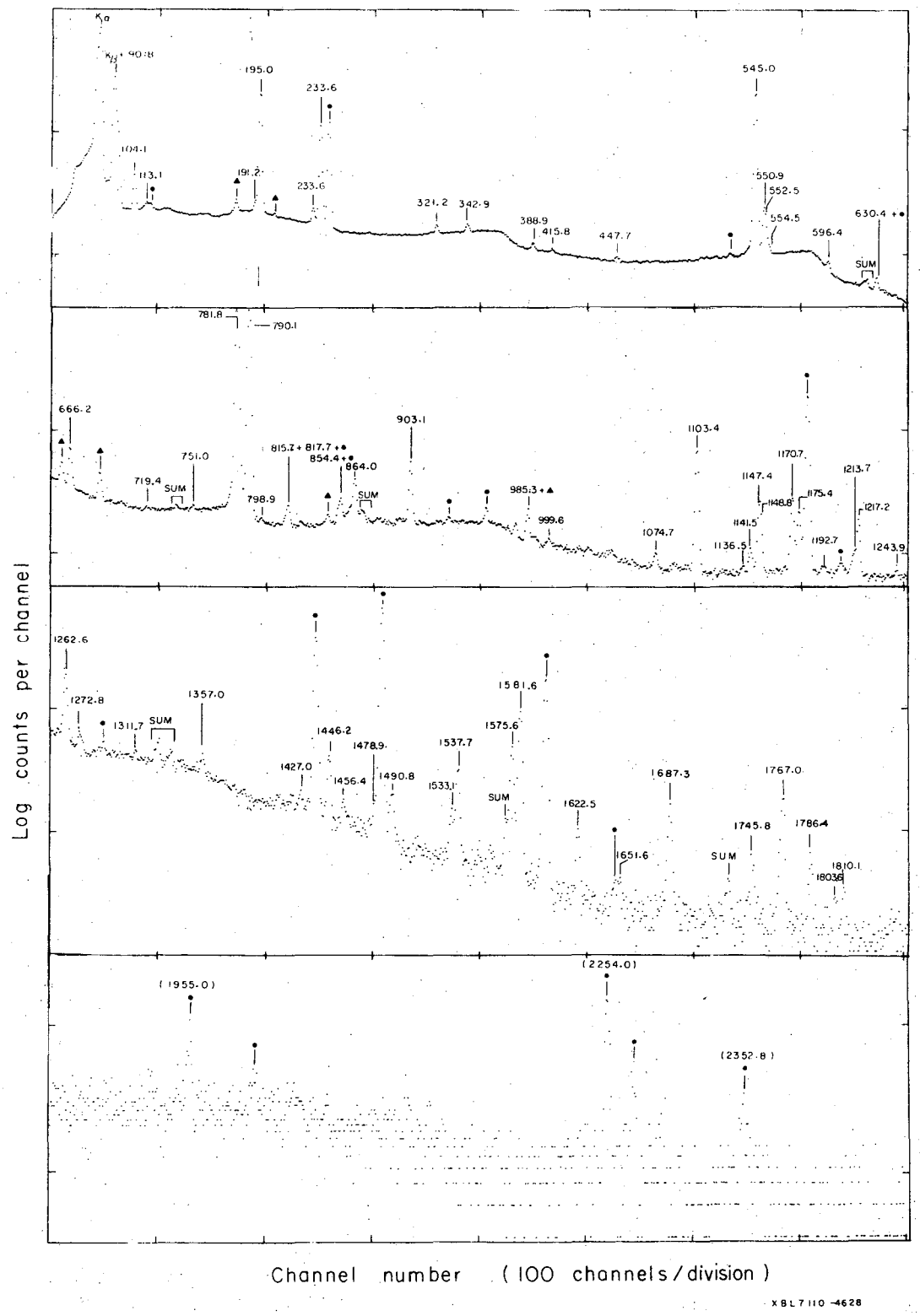

Fig. 55. "Gross" γ-γ coincidence spectrum for the 35-cm^3 (active volume) coaxial Ge(Li) detector. Symbols ▲ denote transitions due to ^{208}At and ● due to ^{210}At.

Table 18. Peak and compton background gates used. With reference to the gamma-ray spectrum of fig. 55, these gates were set. The time distribution gates were set as shown in fig. 53. The coincidence events from the spectrum of fig. 54 (with these gates) as returned by MSORT are shown in figs. 56-74.

Energy keV	Peak gate channels		Background gate channels		Energy keV	Peak gate channels		Background gate channels	
90.8	136	140	141	145	854.4	1146	1153	1177	1184
104.2	153	160	176	183	864.0	1160	1166	1177	1183
113.2	163	170	176	183	903.1	1210	1220	1221	1231
191.1	264	269	290	295	985.2	1321	1328	1349	1356
195.0	269	279	290	300	999.6	1340	1348	1349	1357
233.7	319	325	345	351	≈ 1022	1368	1376	1380	1388
239.2	325	334	345	354	1074.8	1441	1449	1450	1458
321.1	433	442	445	454	1103.5	1477	1488	1489	1500
342.8	462	471	472	481	1141.4	1530	1537	1549	1556
388.9	525	533	534	542	≈ 1148	1537	1546	1549	1558
447.7	601	613	615	627	1170.7	1566	1575	1640	1649
545.0	732	741	754	763	1175.4	1576	1582	1593	1599
551.0	740	745	760	765	1192.9	1595	1701	1643	1649
552.4	745	748	760	763	1213.8	1624	1631	1642	1649
554.6	749	755	756	762	1217.2	1631	1641	1641	1652
596.4	802	808	809	815	1262.6	1689	1700	1716	1727

(continued)

Table 18 (continued)

Energy keV	Peak gate channels		Background gate channels		Energy keV	Peak gate channels		Background gate channels	
≈ 623	834	840	854	860	1311.7	1753	1762	1763	1772
630.3	847	853	854	860	≈ 1337	1785	1795	1796	1805
666.2	895	903	904	912	1357.0	1816	1825	1826	1835
719.6	964	975	976	987	1446.1	1933	1944	1959	1970
750.9	1006	1018	1019	1031	1456.4	1946	1957	1959	1970
781.9	1046	1058	1079	1091	1490.8	1994	2004	2005	2072
790.2	1059	1071	1079	1091	1533.1	2049	2055	2066	2072
799.1	1073	1081	1119	1127	1537.7	2056	2064	2066	2074
809.8	1087	1095	1119	1127	1575.6	2106	2114	2124	2132
815.6	1095	1100	1108	1113	1581.6	2114	2123	2124	2133
817.7	1101	1106	1107	1112	1687.3	2252	2265	2266	2279
1243.9	1666	1675	1676	1685					
1272.9	1703	1714	1716	1727					
1767.0	2354	2369	2370	2385					

performed at a resolving time of about 150 ns. Prompt coincidence spectra (from the spectrum of fig. 54) are shown in figs. 56-74. Gamma-ray photopeaks of ^{210}At were not present to any "significant" degree in the sorted spectra. The ^{209}At coincidence results are discussed in connection with the construction of the decay scheme in section E.

We show in pages 199-217 the complete set of prompt γ-γ coincidence spectra (figs. 56-74) from the decay of ^{209}At. Due to incomplete background subtractions, some photopeaks due to the ^{210}At decay occur in the spectra. These peaks are denoted on figs. 56-74 by the symbol ●. The reader may continue at page 218 without a loss of content.

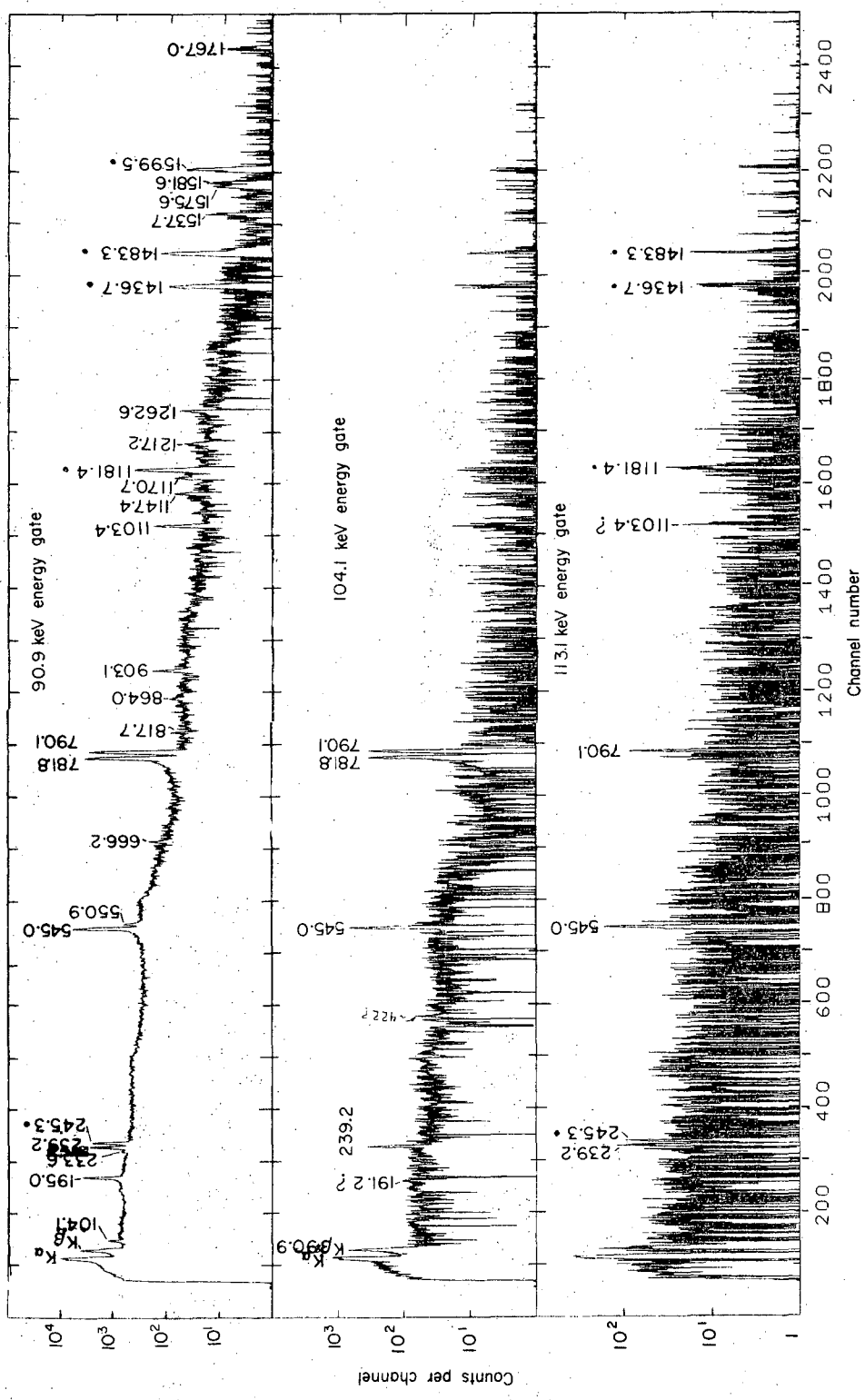

Fig. 56. Gamma-ray spectra in prompt coincidence with E_γ = 90.9 keV (top), E_γ = 104.1 keV (middle) and E_γ = 113.1 keV (bottom).

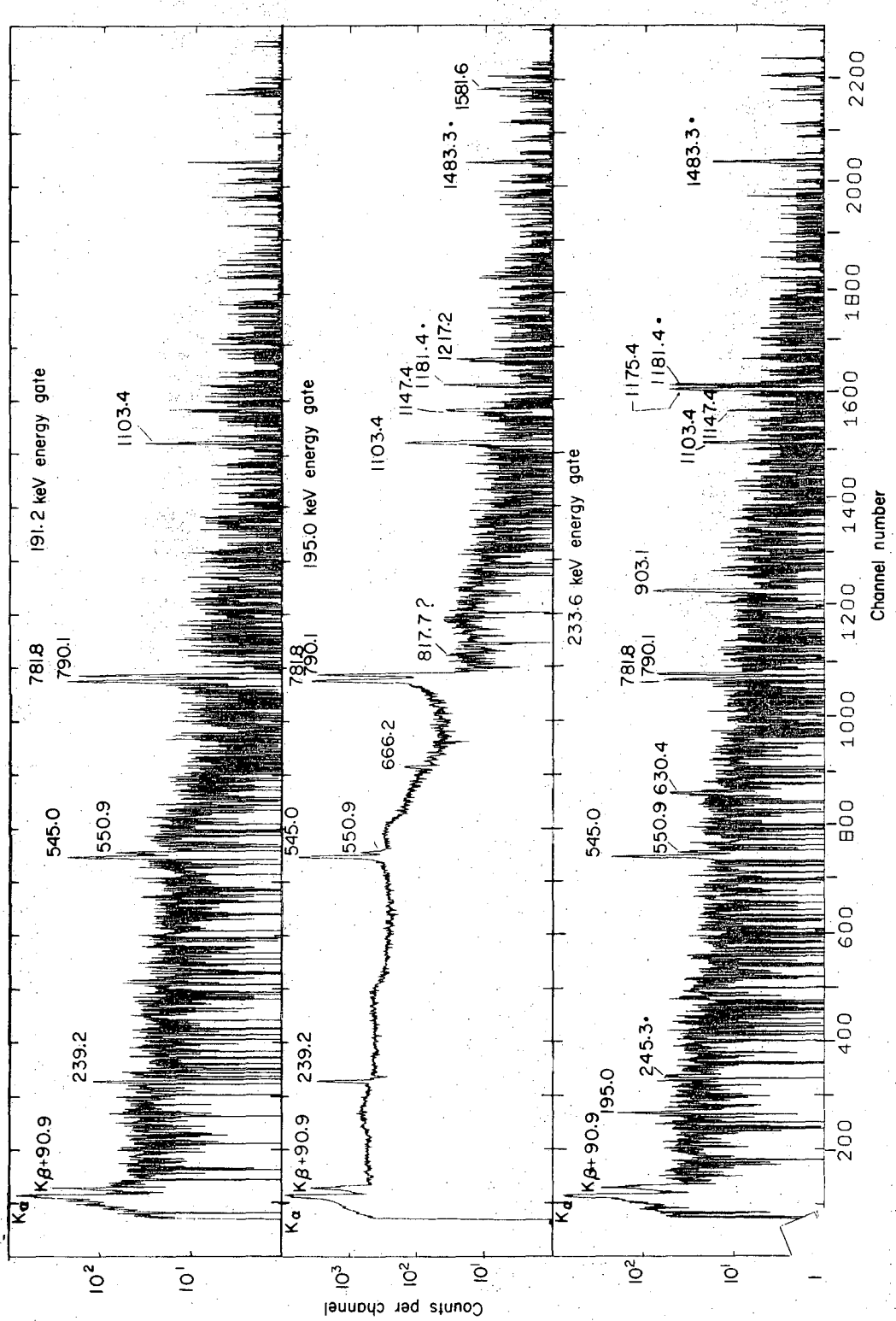

Fig. 57. Gamma-ray spectra in prompt coincidence with E_γ = 191.2 keV (top), E_γ = 195.0 keV (middle) and E_γ = 233.6 keV (bottom).

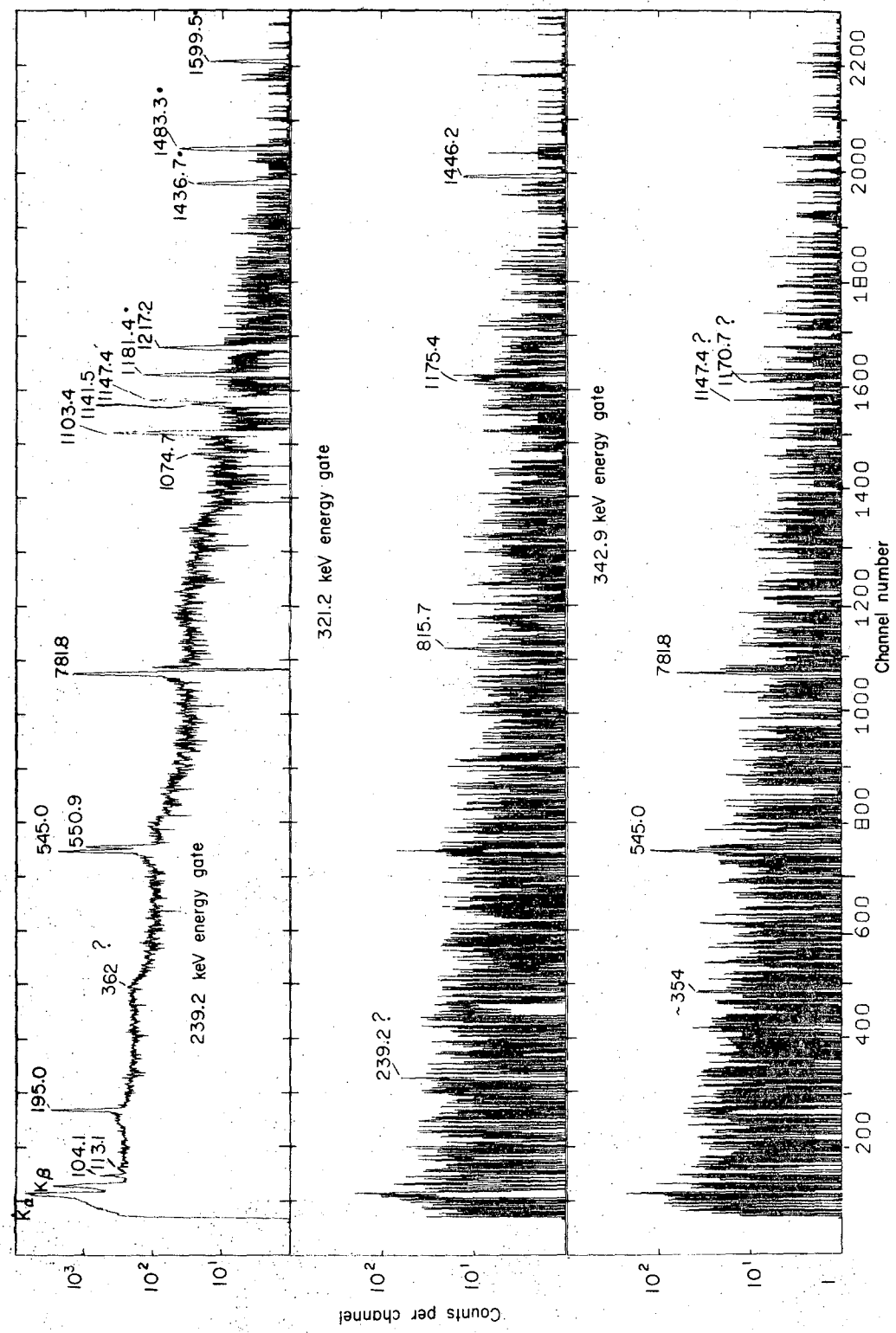

Fig. 58. Gamma-ray spectra in prompt coincidence with E_γ = 239.2 keV (top), E_γ = 321.2 keV (middle) and E_γ = 342.9 keV (bottom).

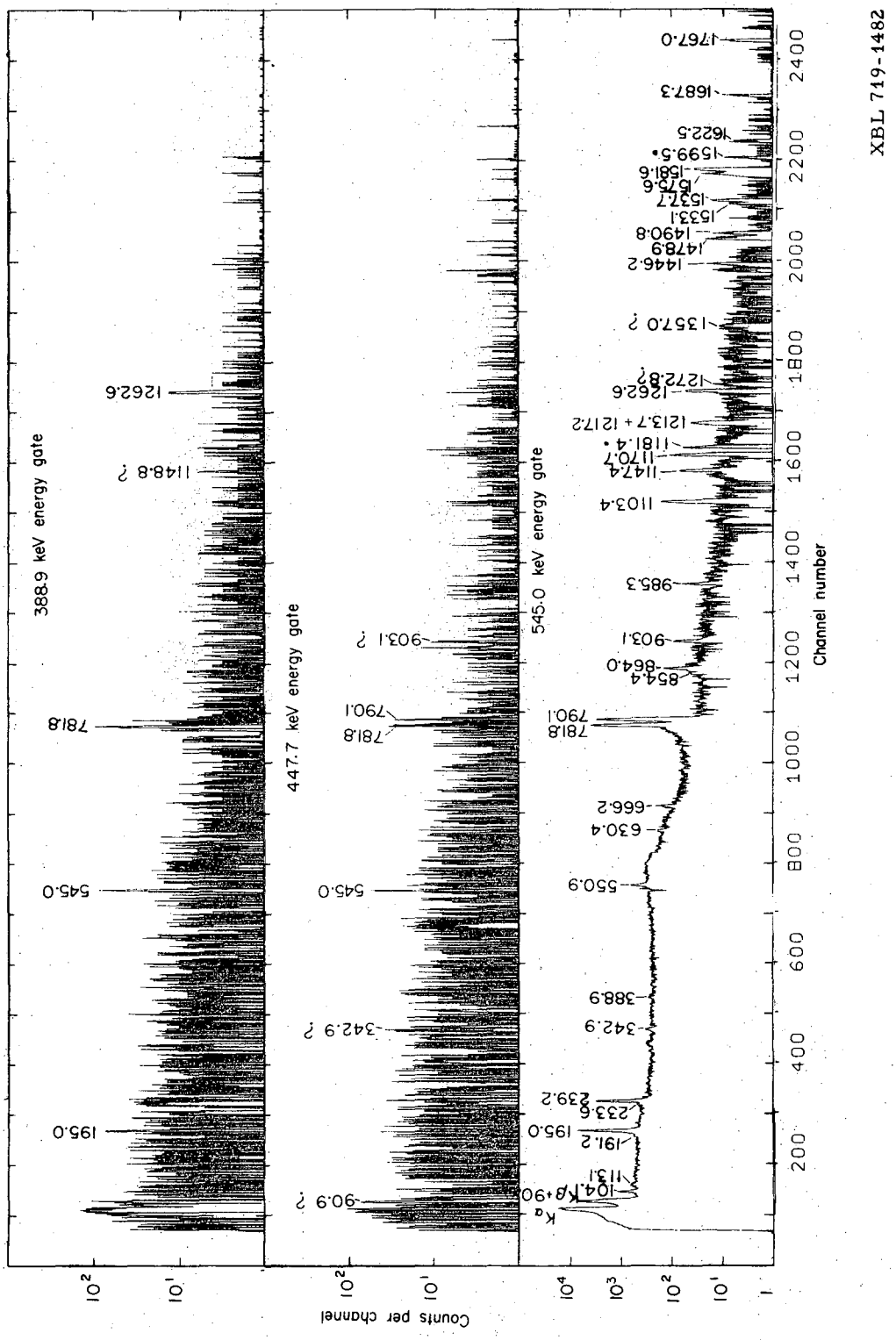

Fig. 59. Gamma-ray spectra in prompt coincidence with E_γ = 388.9 keV (top), E_γ = 447.7 keV (middle) and E_γ = 545.0 keV (bottom).

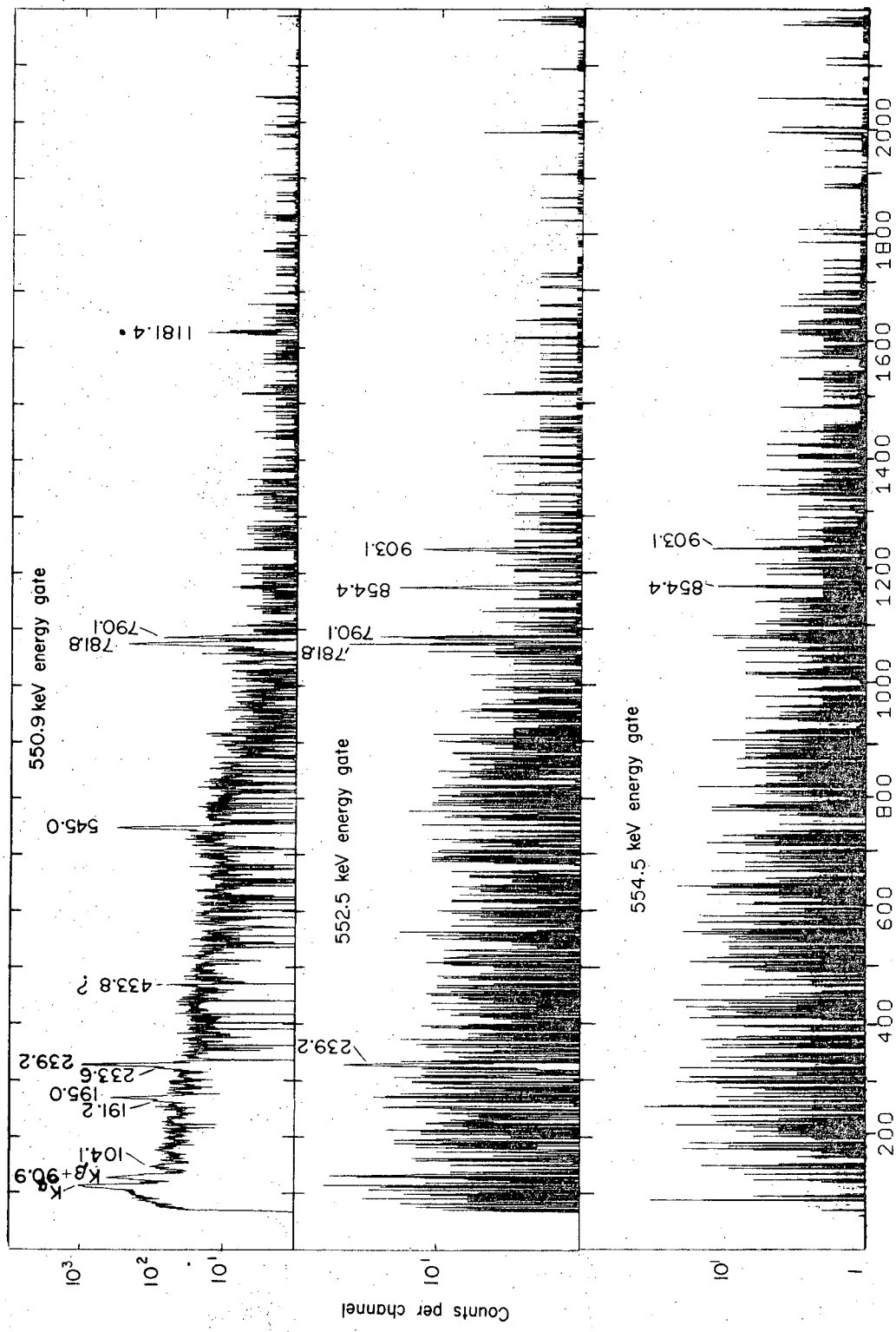

Fig. 60. Gamma-ray spectra in prompt coincidence with E_γ = 550.9 keV (top), E_γ = 552.5 keV (middle) and E_γ = 554.5 keV (bottom).

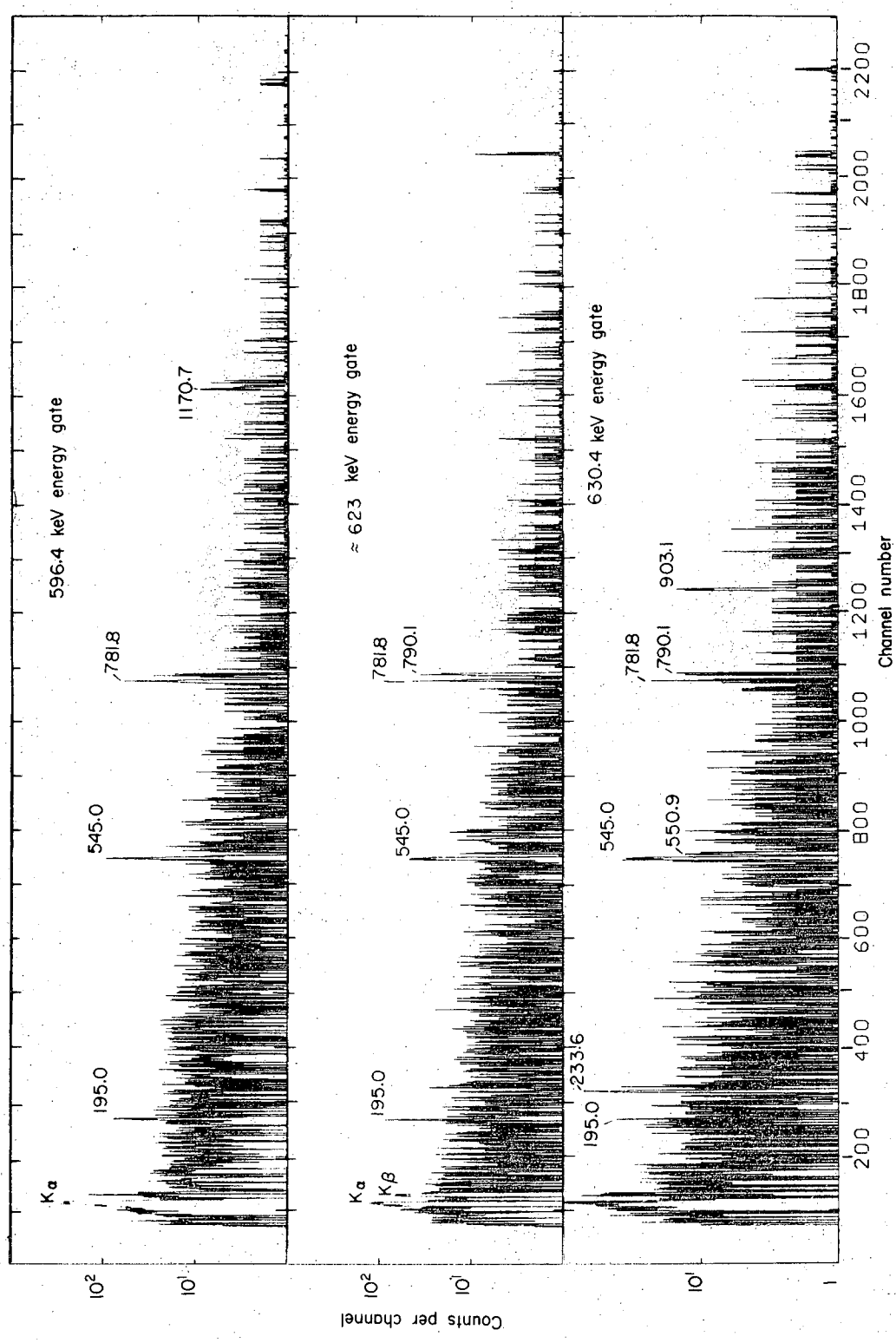

Fig. 61. Gamma-ray spectra in prompt coincidence with E_γ = 596.4 keV (top), $E_\gamma \approx$ 623 keV (middle) and E_γ = 630.4 keV (bottom).

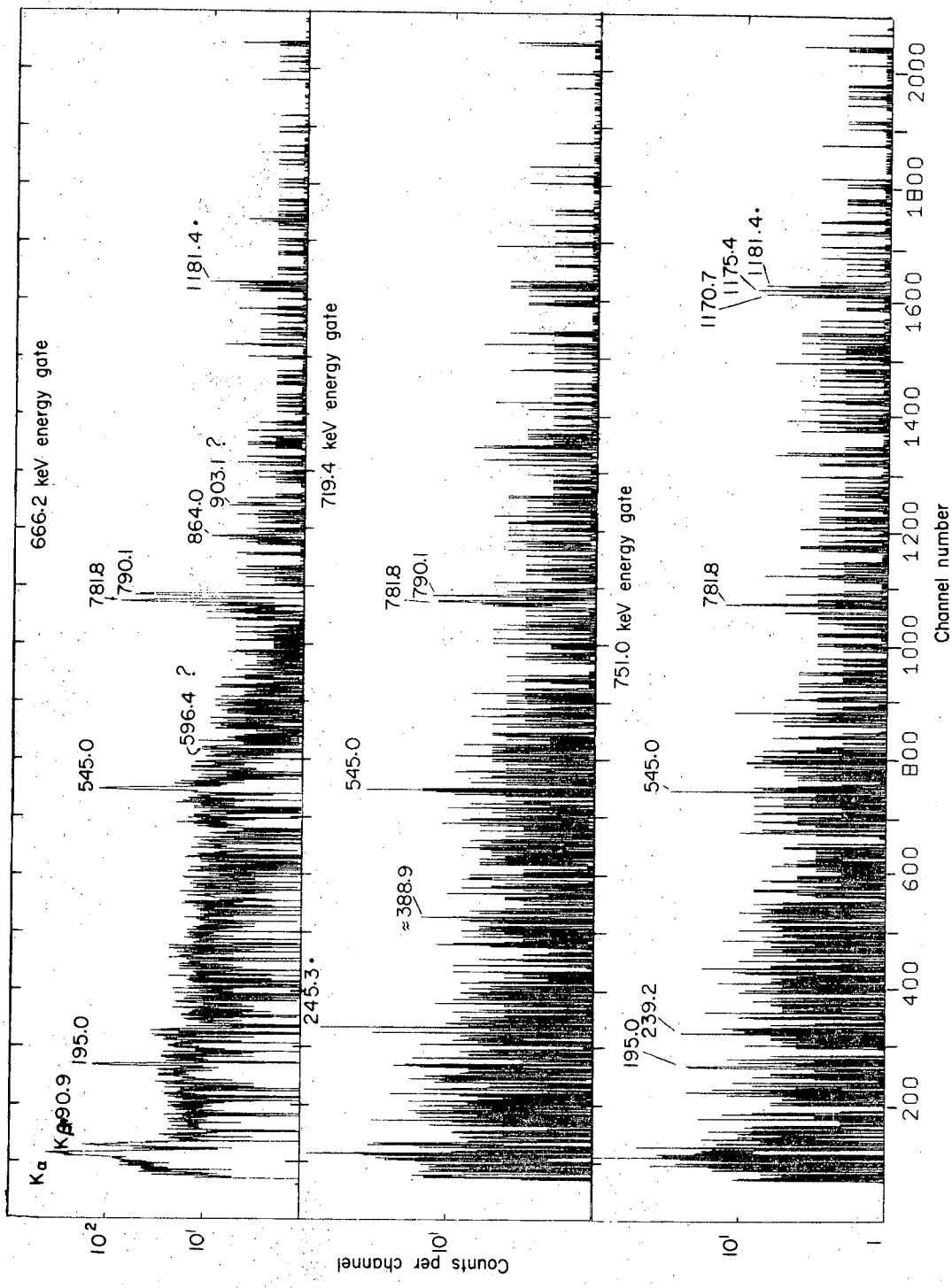

Fig. 62. Gamma-ray spectra in prompt coincidence with E_γ = 666.2 keV (top), E_γ = 719.4 keV (middle) and E_γ = 751.0 keV (bottom).

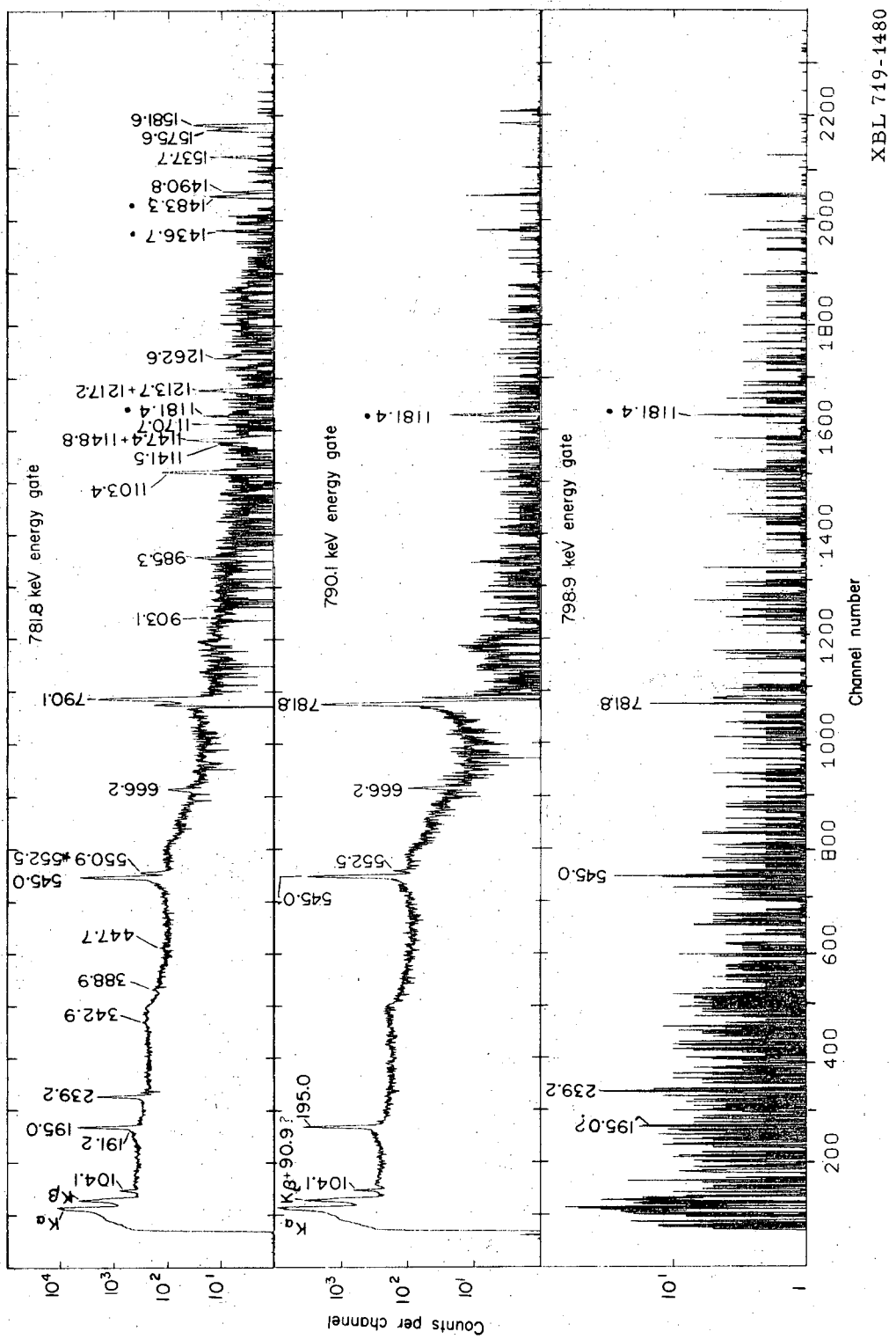

Fig. 63. Gamma-ray spectra in prompt coincidence with E_γ = 781.8 keV (top), E_γ = 790.1 keV (middle) and E_γ = 798.9 keV (bottom).

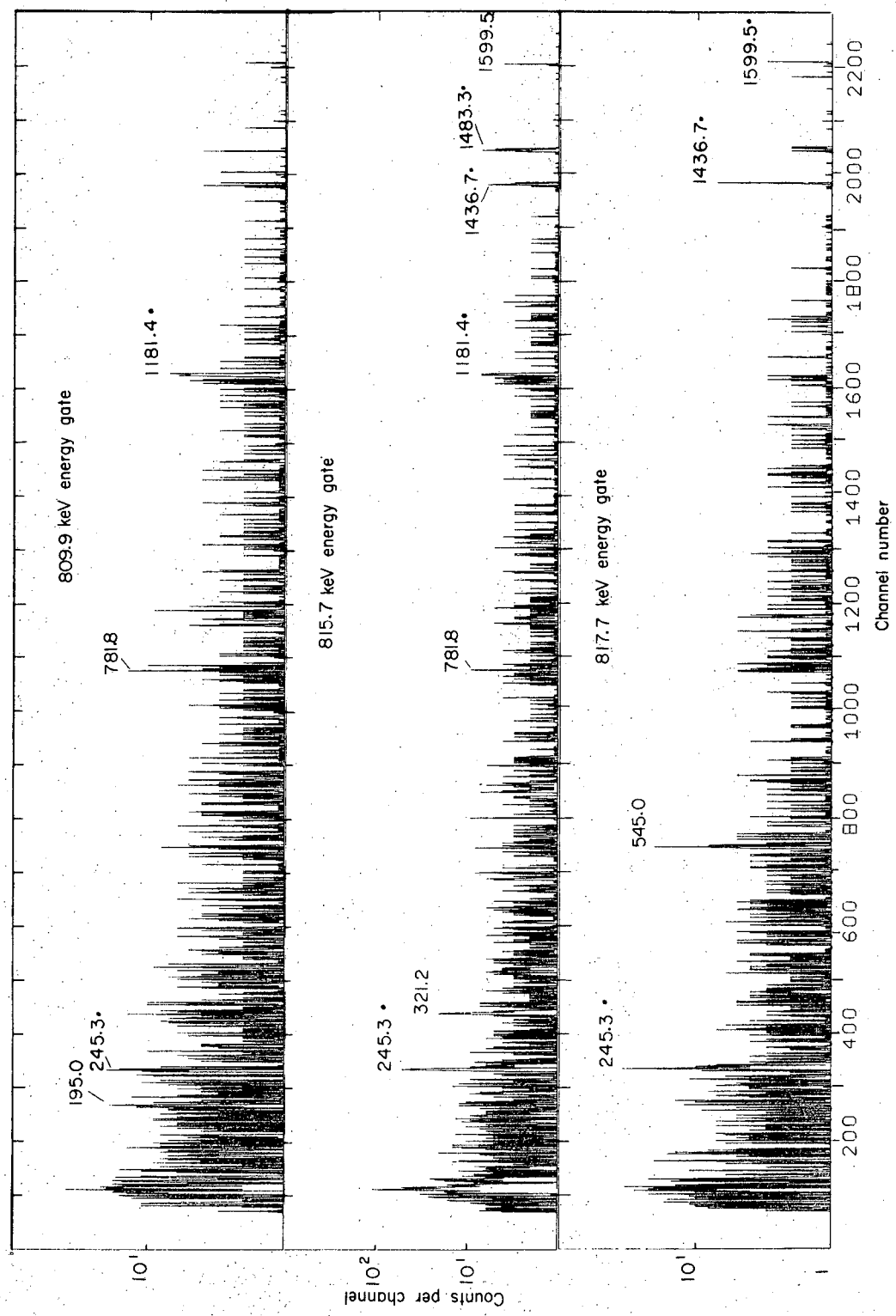

Fig. 64. Gamma-ray spectra in prompt coincidence with E_γ = 809.9 keV (top), E_γ = 815.7 keV (middle) and E_γ = 817.7 keV (bottom).

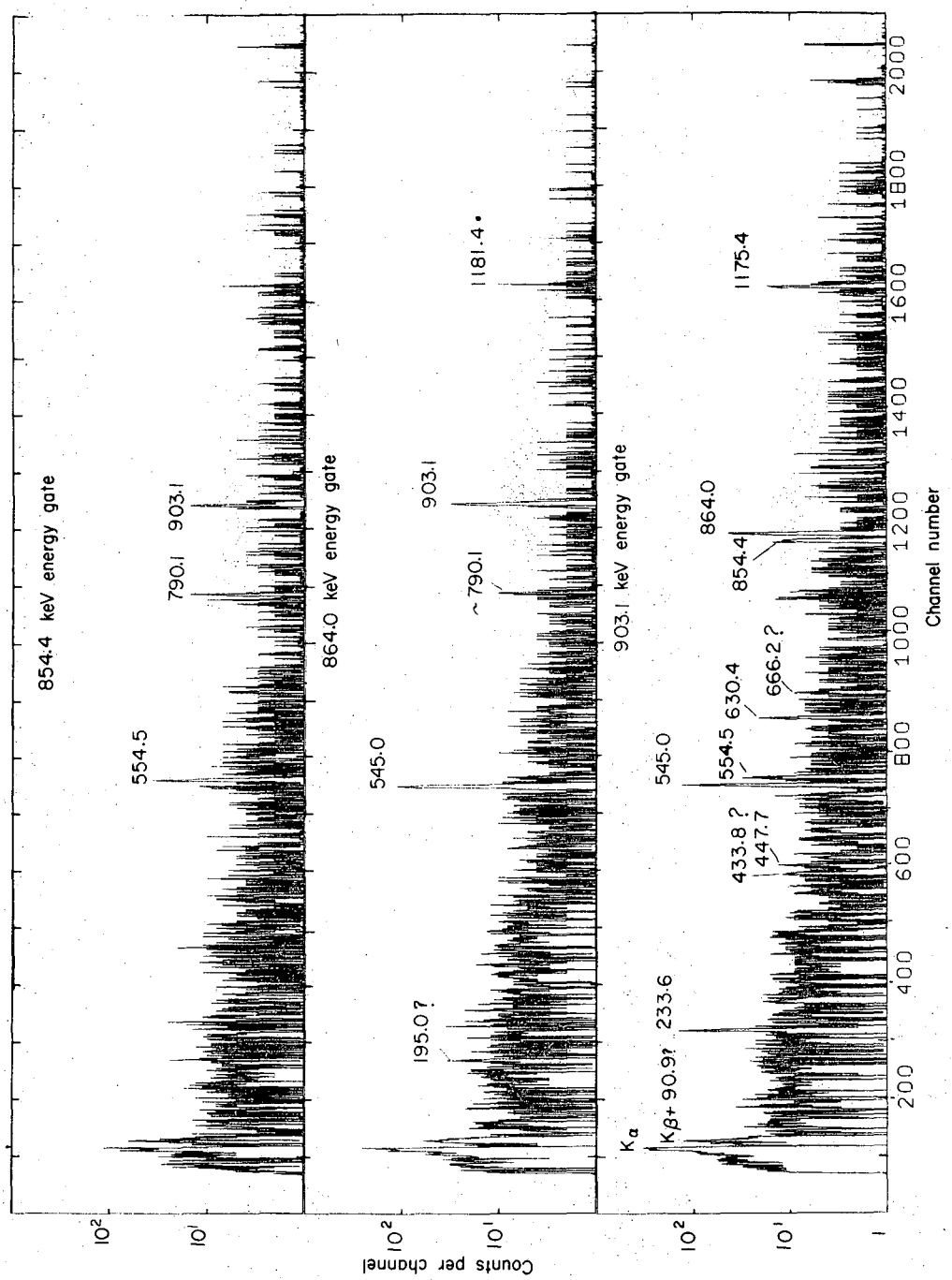

Fig. 65. Gamma-ray spectra in prompt coincidence with E_γ = 854.4 keV (top), E_γ = 864.0 keV (middle) and E_γ = 903.1 keV (bottom).

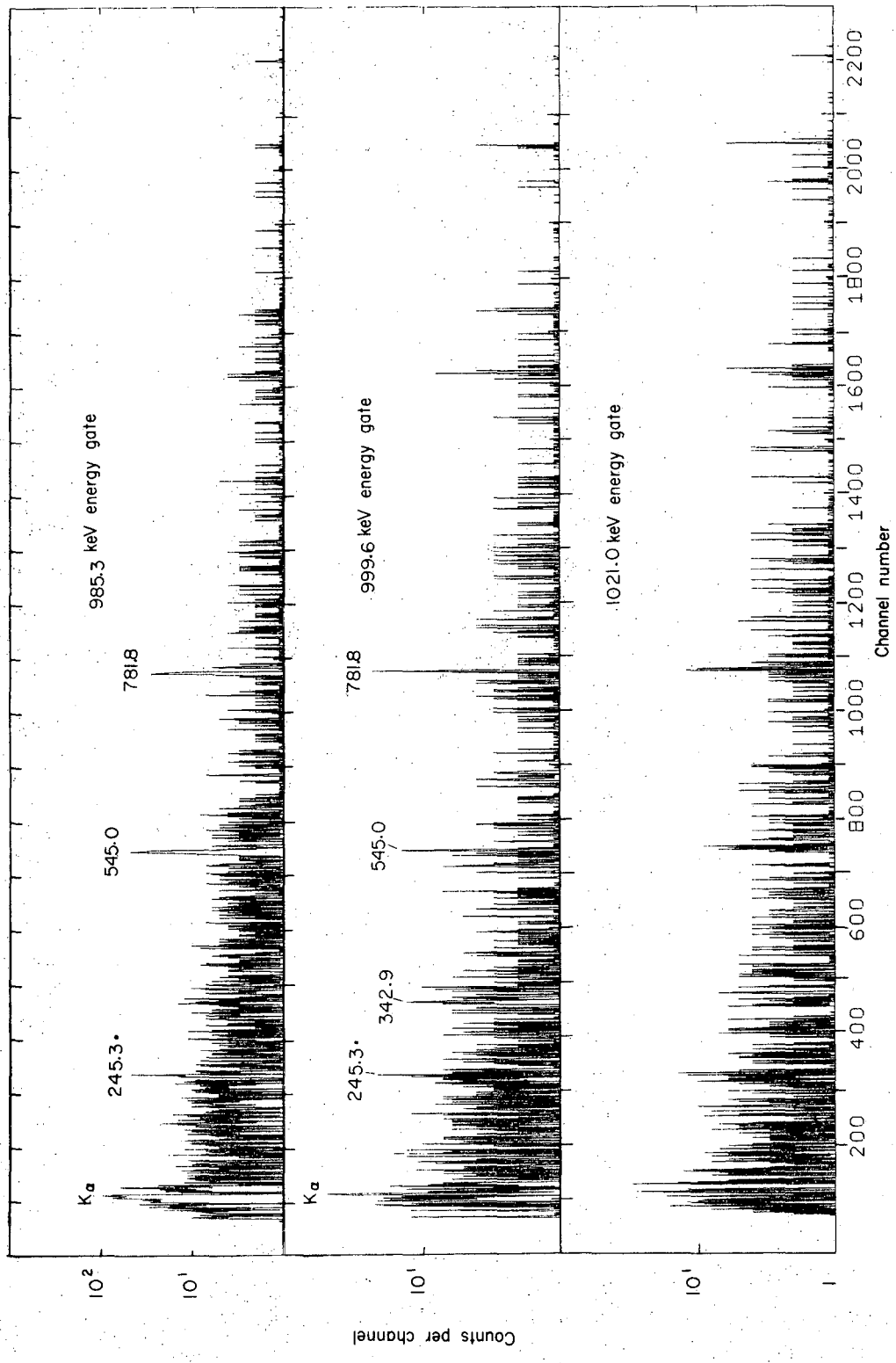

Fig. 66. Gamma-ray spectra in prompt coincidence with E_γ = 985.3 keV (top), E_γ = 999.6 keV (middle) and E_γ = 1021.0 keV (bottom).

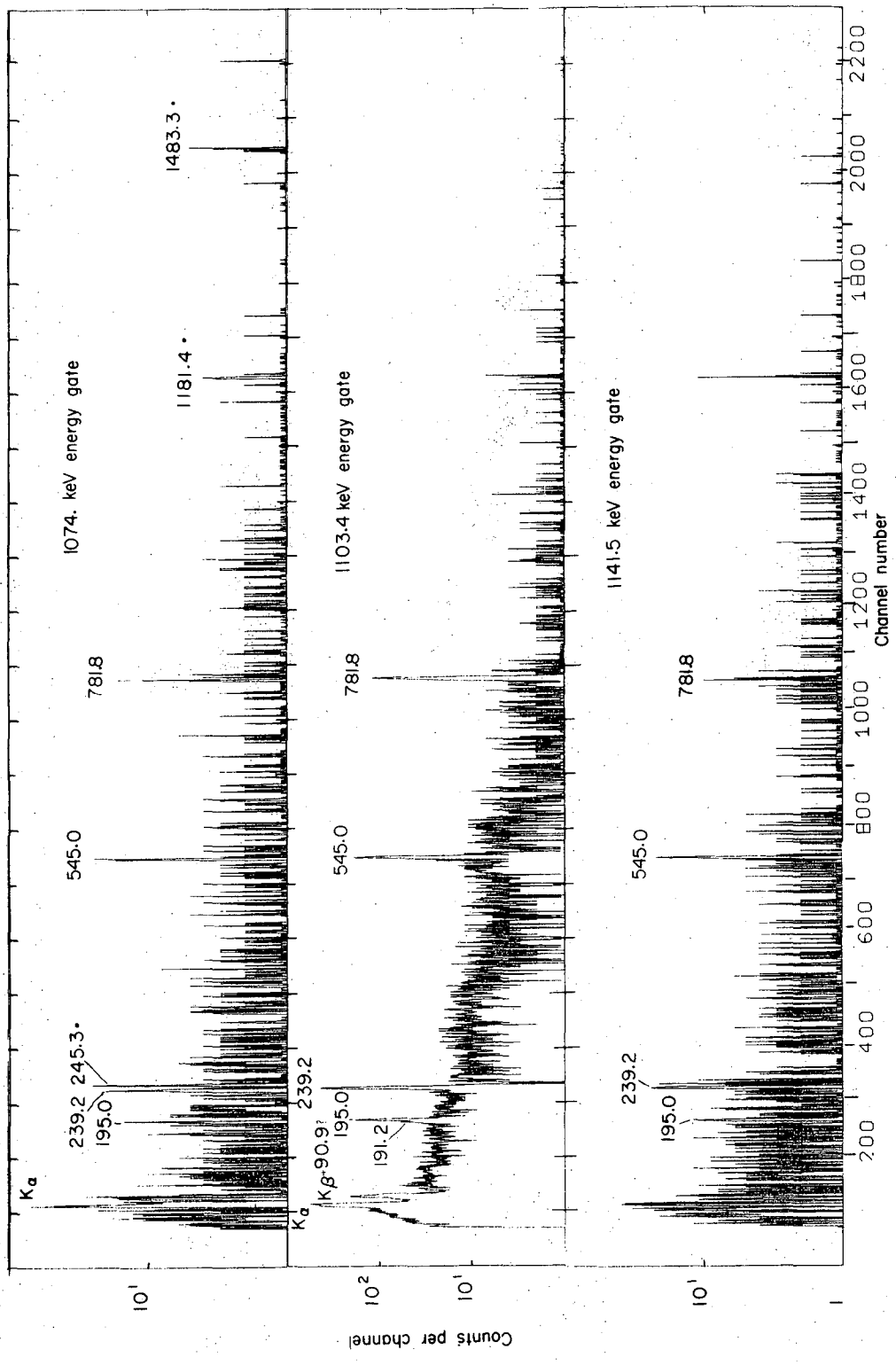

Fig. 67. Gamma-ray spectra in prompt coincidence with E_γ = 1074. keV (top), E_γ = 1103.4 keV (middle) and E_γ = 1141.5 keV (bottom).

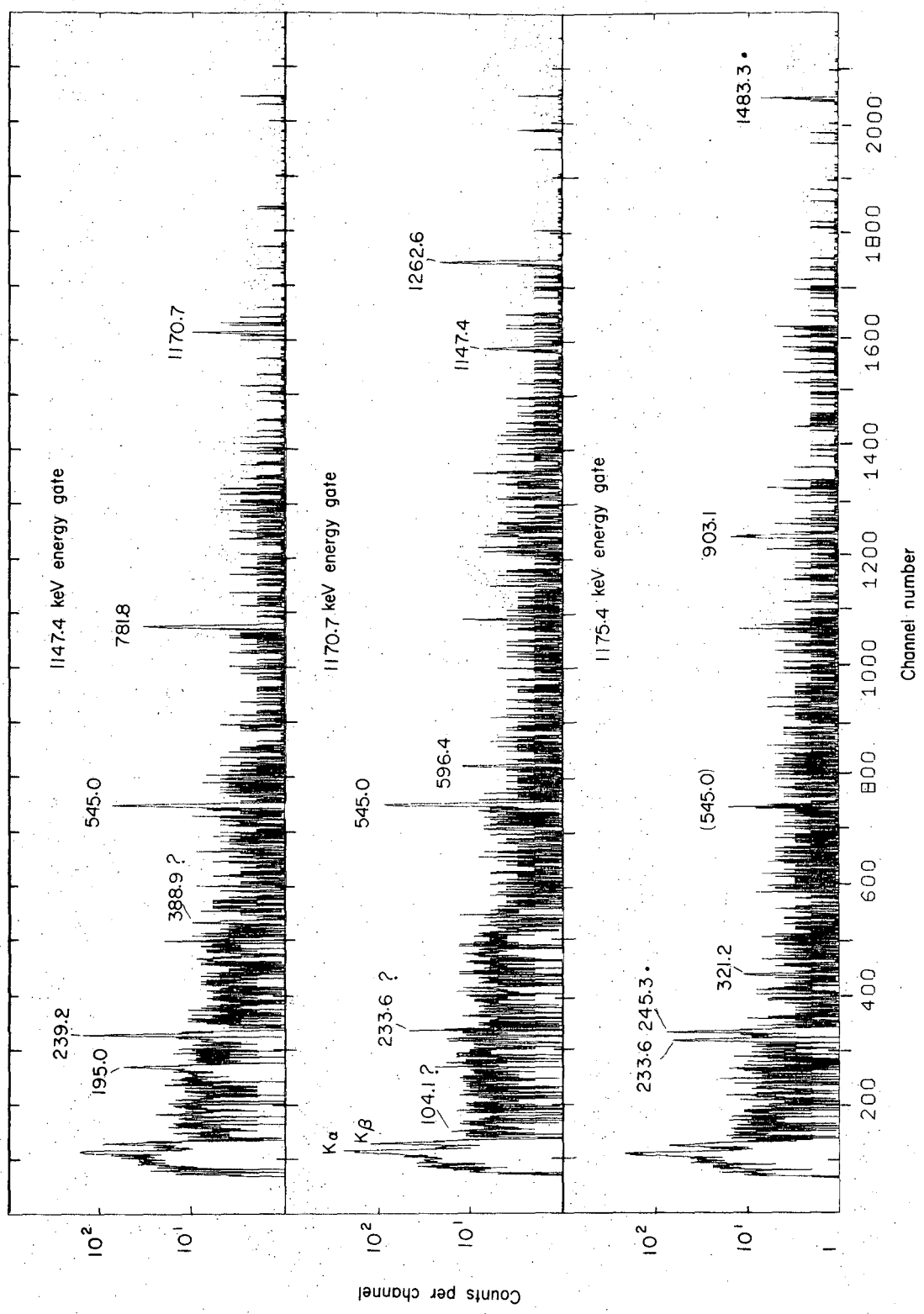

Fig. 68. Gamma-ray spectra in prompt coincidence with E_γ = 1147.4 keV (top), E_γ = 1170.7 keV (middle) and E_γ = 1175.4 keV (bottom).

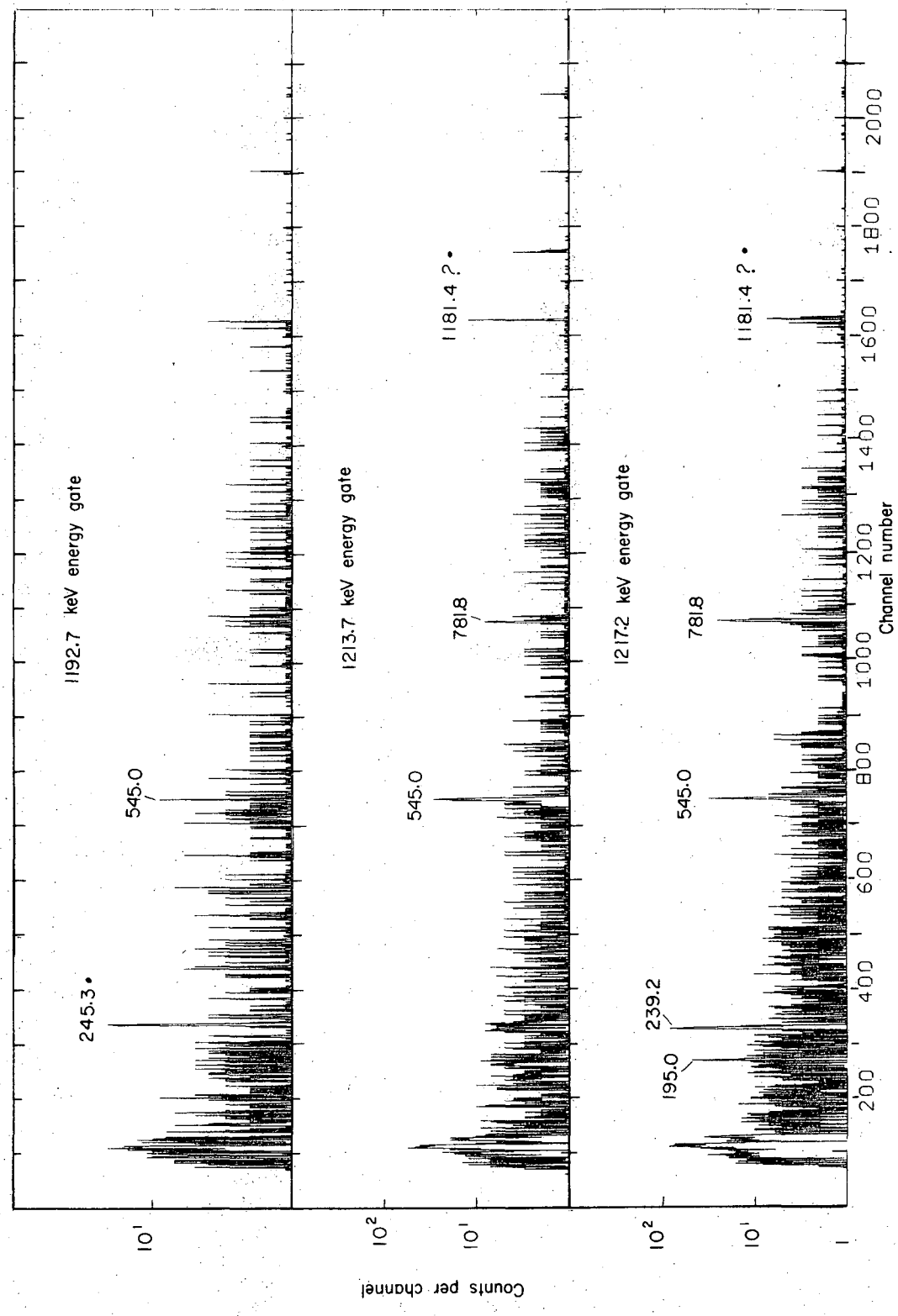

Fig. 69. Gamma-ray spectra in prompt coincidence with E_γ = 1192.7 keV (top), E_γ = 1213.7 keV (middle) and E_γ = 1217.2 keV (bottom).

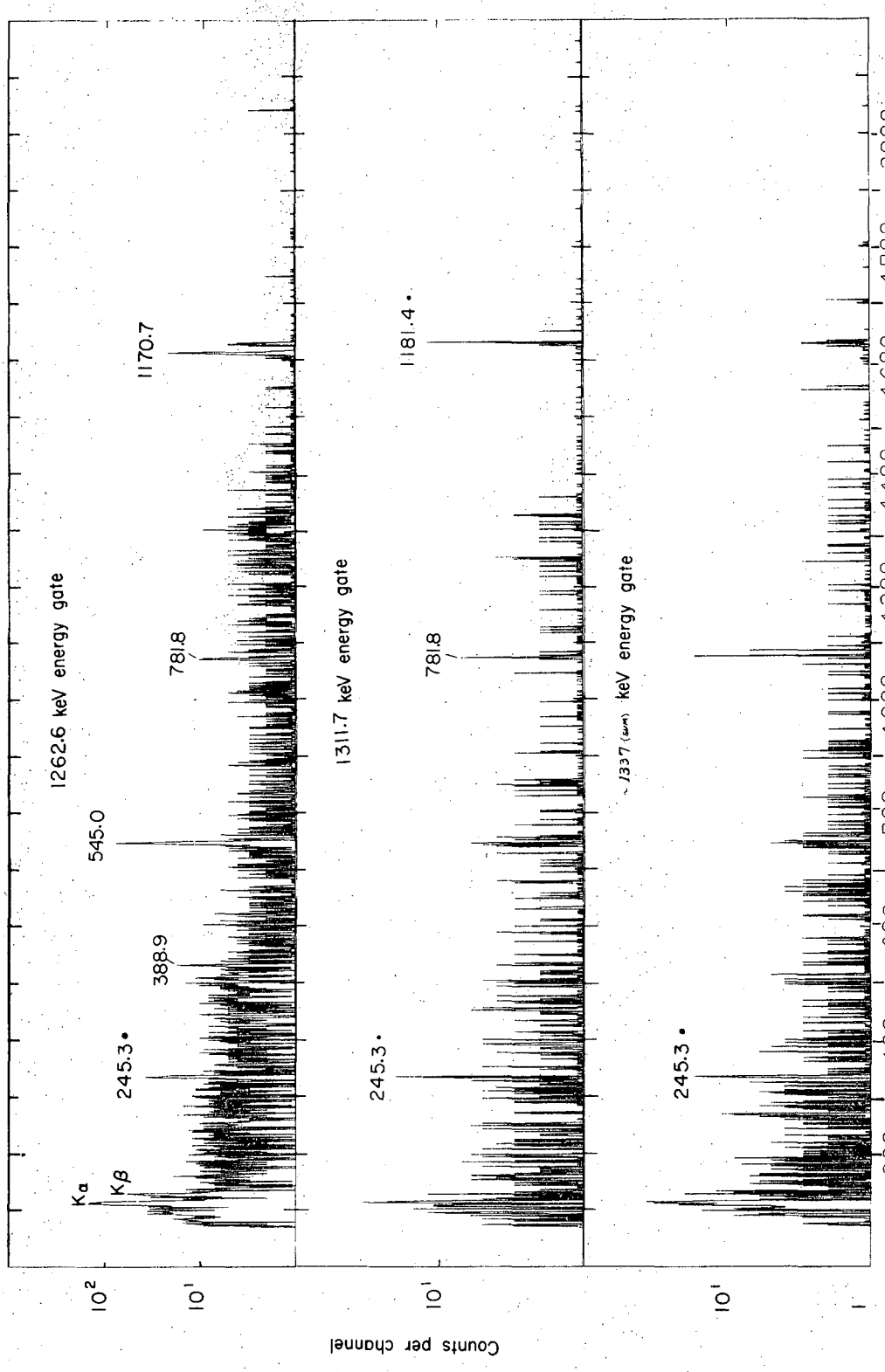

Fig. 70. Gamma-ray spectra in prompt coincidence with E_γ = 1262.6 keV (top), E_γ = 1311.7 keV (middle) and $E_\gamma \approx$ 1337 (sum) keV (bottom).

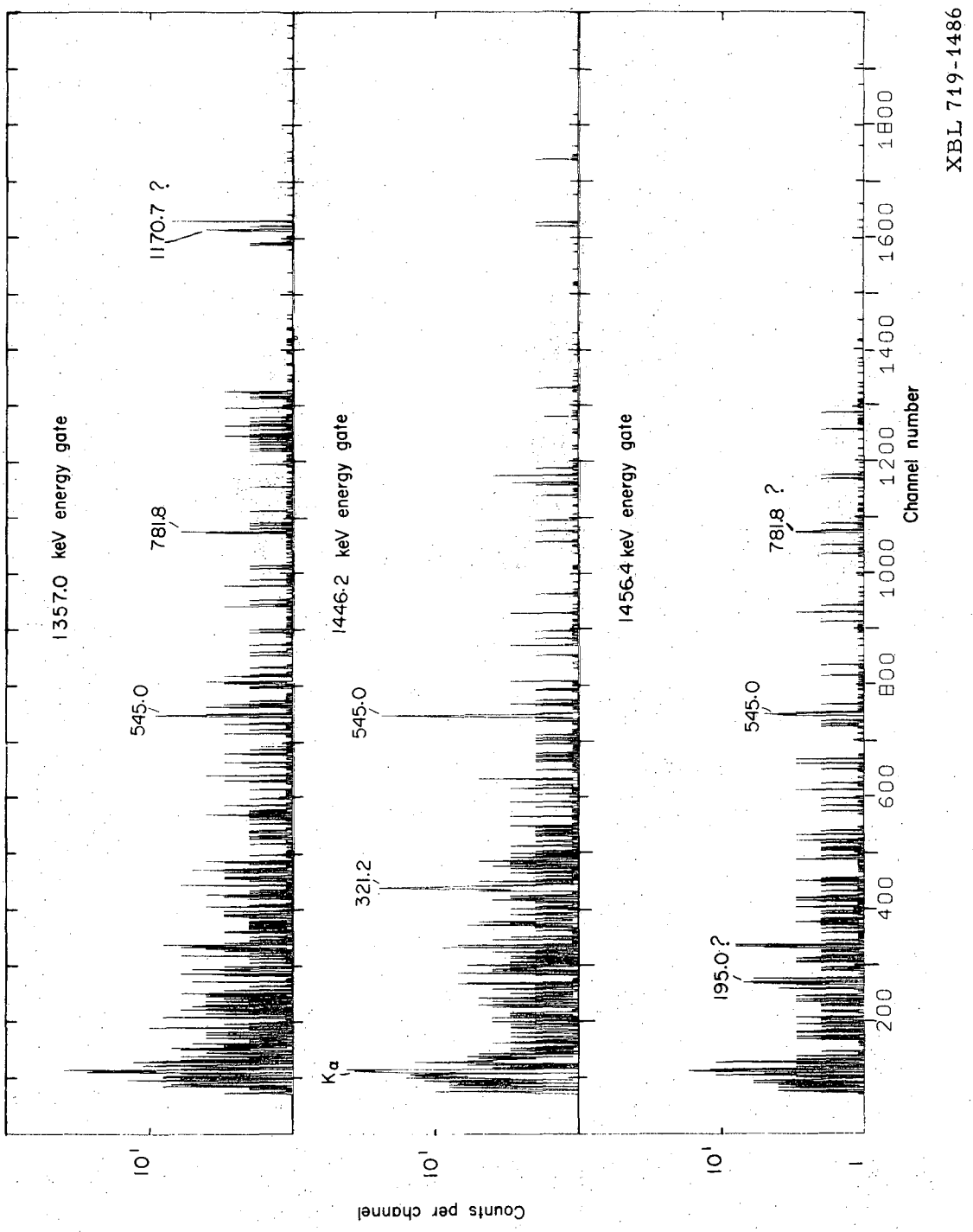

Fig. 71. Gamma-ray spectra in prompt coincidence with E_γ = 1357.0 keV (top), E_γ = 1446.2 keV (middle) and E_γ = 1456.4 keV (bottom).

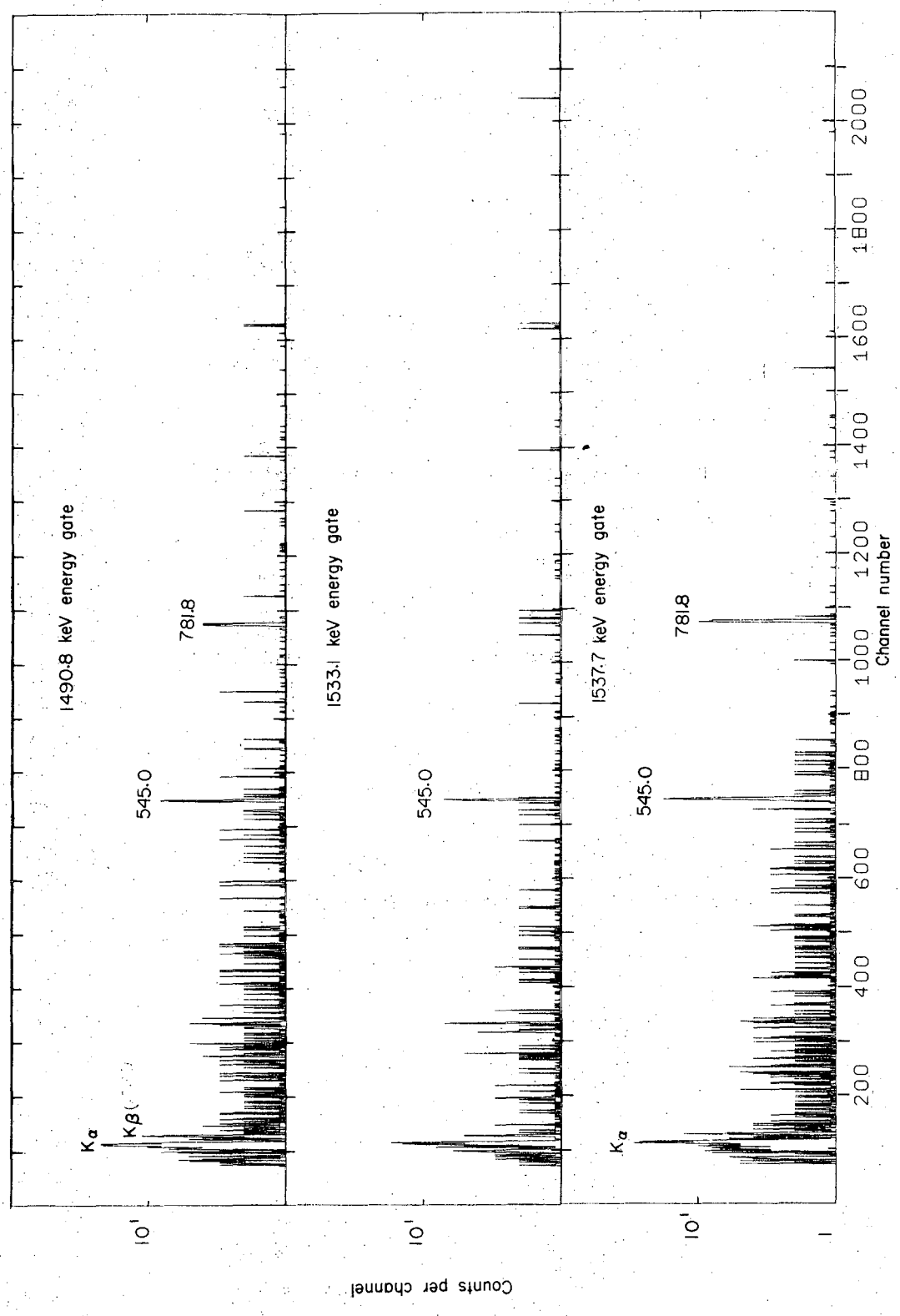

XBL 719-1493

Fig. 72. Gamma-ray spectra in prompt coincidence with E_γ = 1490.8 keV (top), E_γ = 1533.1 keV (middle) and E_γ = 1537.7 keV (bottom).

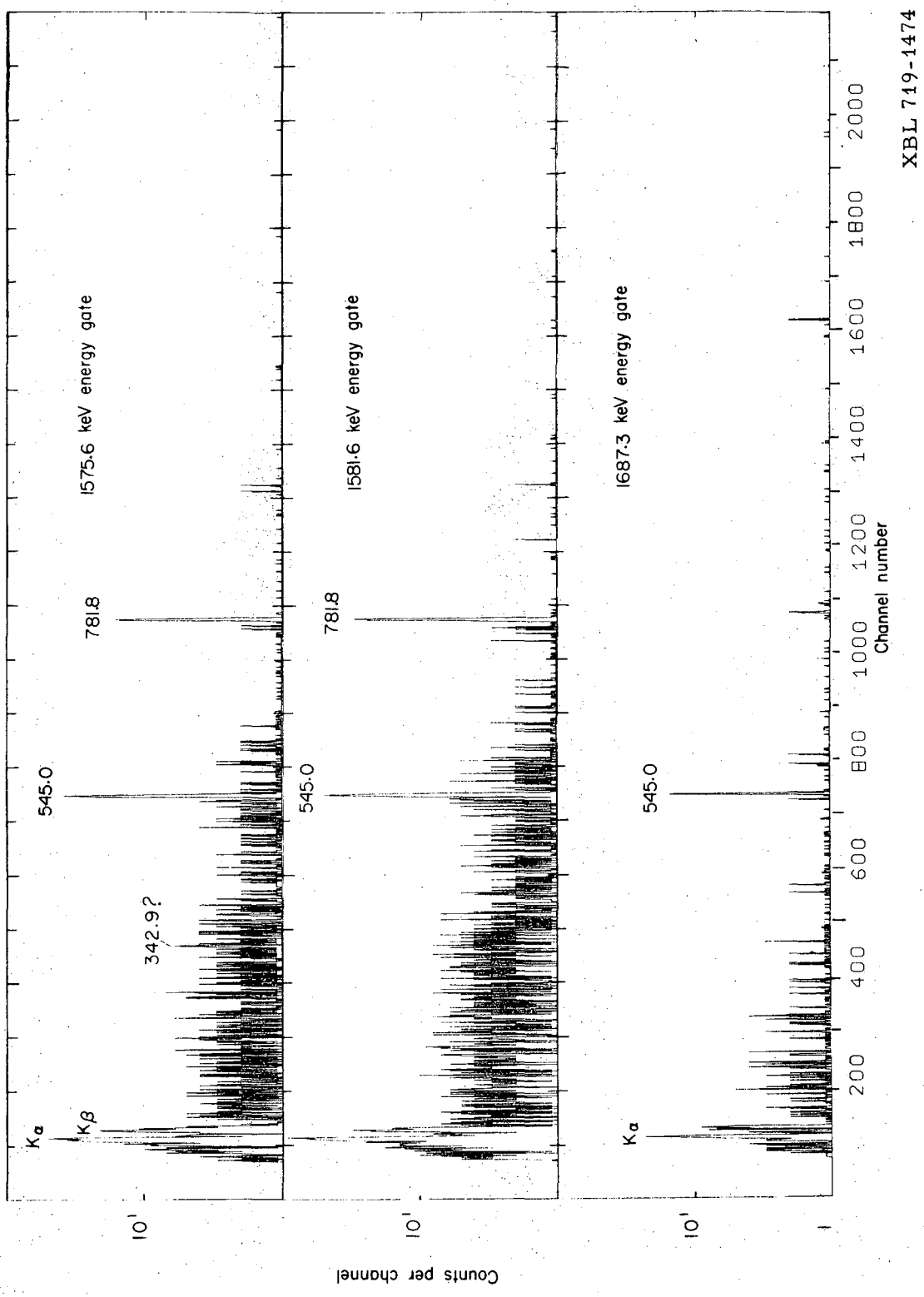

Fig. 73. Gamma-ray spectra in prompt coincidence with E_γ = 1575.6 keV (top), E_γ = 1581.6 keV (middle) and E_γ = 1687.3 keV (bottom).

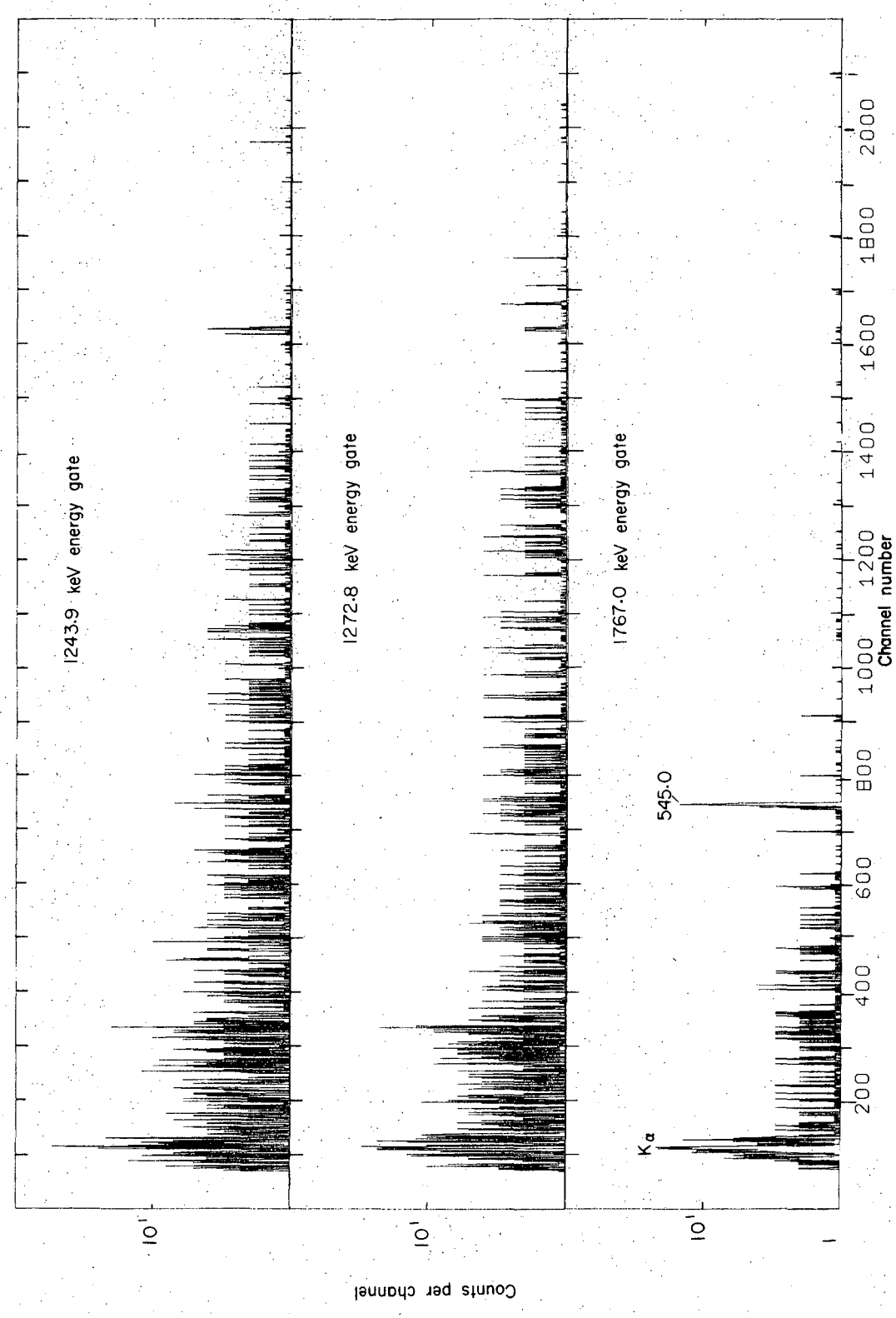

XBL 719-1488

Fig. 74. Gamma-ray spectra in prompt coincidence with E_γ = 1243.9 keV (top), E_γ = 1272.8 keV (middle) and E_γ = 1767.0 keV (bottom).

3. Internal Conversion Electron Spectra

Sources for electron measurements were prepared as described in section VC. Spectra of conversion electrons were obtained with a 5-mm × 0.785 cm^2 (active volume) Si(Li) detector operated at liquid nitrogen temperature coupled to the same data acquisition system and pulse electronics used in the gamma-ray singles measurements. This system gave a resolution of 1.2 keV (FWHM) for 100 keV electrons and 2.2 keV (FWHM) for the 1063 K-electrons from the decay of ^{207}Bi. The electron spectra were analyzed for energies and intensities with the computer code SAMPO[40,41]. The K-electron lines of the stronger transitions were used as internal energy calibration standards. The relative efficiency of the Si(Li) spectrometer was determined to ±8% over the energy range of 100-1500 keV and to ±12% over the range of 1200-1700 keV using the methods described in Appendix F.

The conversion electron spectra obtained for ^{209}At decay with a low intensity mass separated source are shown in figs. 75 and 76. Because of the relatively high compton background and complex spectra obtained with mixed ^{209}At and ^{210}At sources, the conversion coefficients of only the more intense (or highly converted) transitions could be determined. The conversion coefficients for many weaker transitions were determined with the mass separated ^{209}At source because of the reduced background. Other spectra obtained with mixed astatine isotopes were used to extract conversion coefficients of the stronger transitions where pulse summing of the x-rays and electrons caused interference in the spectrum of fig. 76. We have used these data along with the gamma-ray

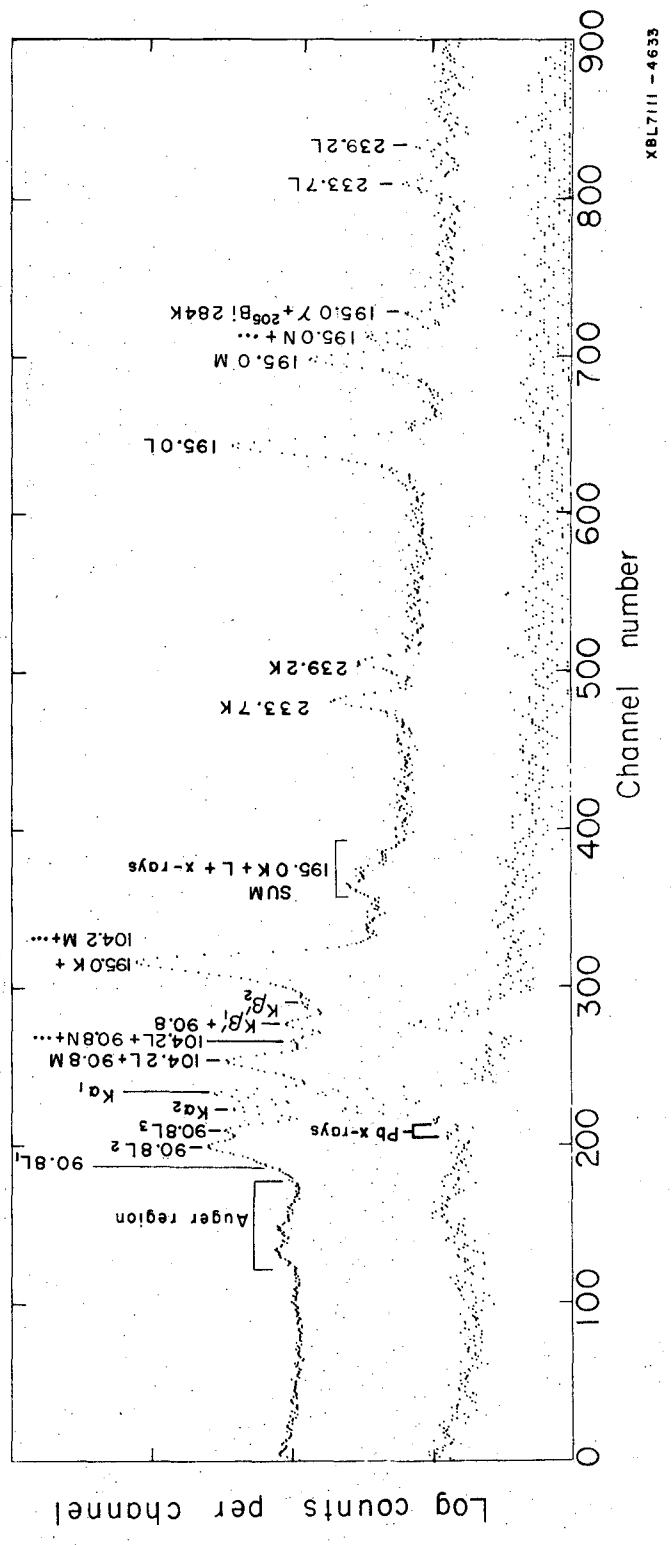

Fig. 75. Conversion-electron spectrum (top) and X-ray spectrum (bottom) of a (mass separated) ^{209}At source in the energy range of 16-240 keV taken with a Si(Li) spectrometer. The X-ray spectrum (bottom) was taken with telflon absorber covering the electron source.

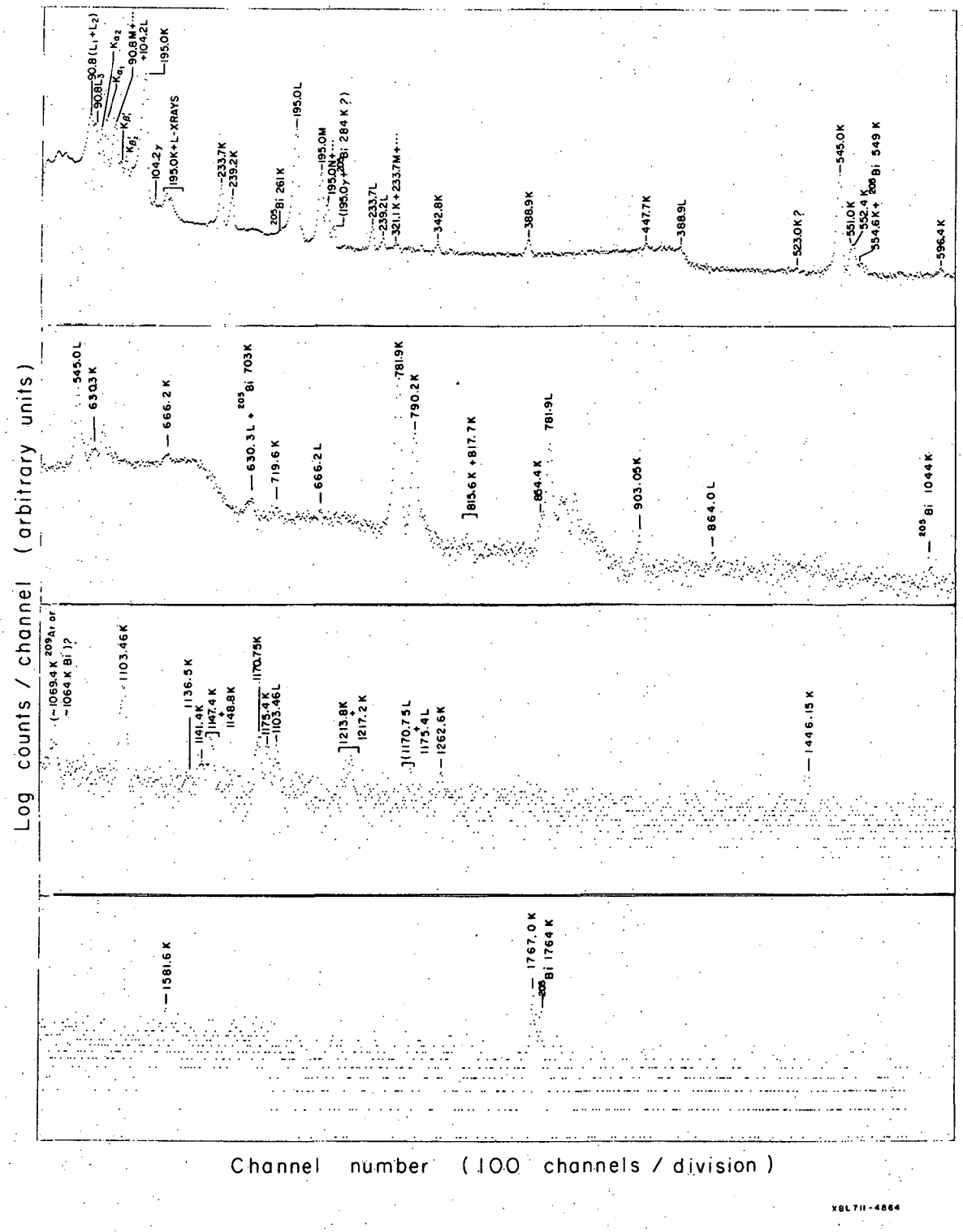

Fig. 76. Conversion-electron spectrum of a (mass separated) ^{209}At source in the energy range of 80-1800 keV.

intensities to determine the K, L and M conversion coefficients relative to that for the 545.0 keV ($5/2^- \rightarrow 1/2^-$) ground-state transition (assumed to be pure E2) and these are given in Table 19 along with the multipolarity assignments deduced by comparison with the theoretical values of Hager and Seltzer[42,43]. The theoretical K-conversion coefficients for the 1767.0 keV transition are those of Sliv and Band[82]. The K-conversion coefficients are also shown in fig. 77 with the theoretical curves constructed from the values of ref. [42]. We comment on two of our results.

90.8 keV transition: As mentioned in section VD1, no gamma-ray photon intensity was determined for this transition. However, our measured $(\alpha_{L_1} + \alpha_{L_2})/\alpha_{L_3}$ ratio determined this as an E2 transition. The measurement of the total L-electron intensity relative to the 545.0 keV K-electron intensity determined the 90.8 keV transition intensity as 19.8% thru use of the theoretical E2 conversion coefficient. This established our estimate of 1.69±0.12% for the 90.8 keV gamma-ray intensity.

195.0 keV transition: The mixing ratio M1 + 20% E2 for this transition was determined from the ratio of our measured K and M conversion coefficients. The experimental ratio was 193±21 and the theoretical ratio for M1 + 20% is $\alpha_K/\alpha_M = 193.5$.

Table 19. Experimental and theoretical internal conversion coefficients: ^{209}At.

Transition energy keV	Experimental[d] conversion coefficient (10^{-3})	Theoretical[c] conversion coefficient E1(10^{-3})	E2(10^{-3})	M1(10^{-3})	M2(10^{-3})	Assigned multipolarity
90.8	$(\alpha_{L_1} + \alpha_{L_2})/\alpha_{L_3} = 1.34$ (10)		1.304			E2
195.0	$\alpha_K = 1170$ (120)	70.9	178	1420	5910	
	$\alpha_L = 220$ (20)	13	256	250	1800	M1 + 20% E2
	$\alpha_M = 61$ (7)	3.06	67.4	58.9	456	
233.7	$\alpha_K = 760$ (50)	46	119	855	3230	
	$\alpha_L = 136$ (10)	8.22	120	151	910	M1
	($\alpha_M = 28$ (10))[a]	1.93	31.5	35.5	229	
239.2	$\alpha_K = 37$ (4)	43.5	113	801	2990	
	$\alpha_L = 5.0$ (10)	7.75	109	141	834	E1
321.1	($\alpha_K = 26$ (15))[a]	22	58	357	1150	(E1)[a]
342.8	$\alpha_K = 110$ (10)	19	30.1	299	935	M1 + E2
388.9	$\alpha_K = 190$ (20)	14.4	28.1	213	631	M1
447.7	$\alpha_K = 130$ (20)	10.7	21	146	410	M1
523.0	($\alpha_K = 320$ (80))[e]	7.73	20.4	96.6	257	(M2)[e]

(continued)

Table 19 (continued)

Transition energy keV	Experimental[d] conversion coefficient (10^{-3})	Theoretical[c] conversion coefficient E1(10^{-3})	E2(10^{-3})	M1(10^{-3})	M2(10^{-3})	Assigned multipolarity
545.0	$\alpha_K \equiv 18.7$[c]		18.7			pure E2
596.4	$\alpha_K = 31\ (5)$	5.94	15.6	68.4	175	M1 + E2
630.3	$\alpha_L = 13.5\ (40)$	0.859	3.83	10.2	31.1	M1
666.2	$\alpha_K = 13\ (2)$	4.79	12.6	51.2	128	E2
	$\alpha_L = 3.0\ (8)$	0.768	3.29	8.79	26.3	
719.6	$(\alpha_K = 130\ (40))$[e]	4.14	10.9	41.9	103	(M2)[e]
781.9	$\alpha_K = 9.1\ (7)$	3.54	9.26	33.8	81.4	E2
	$\alpha_L = 1.9\ (2)$	0.560	2.10	5.62	15.7	
790.1	$\alpha_K = 3.3\ (3)$	3.47	9.08	32.9	79	E1
	$\alpha_L = 0.50\ (7)$	0.549	2.04	5.46	15.2	
815.6	$(\alpha_K = 29\ (8))$[a]	3.27	8.55	30.3	72.3	(M1)[a]
817.7	$(\alpha_K = 16\ (8))$[a]	3.26	8.51	30.1	71.8	(M1 + E2)[a]

(continued)

Table 19 (continued)

Transition energy keV	Experimental[d] conversion coefficient (10^{-3})	Theoretical[c] conversion coefficient E1(10^{-3})	E2(10^{-3})	M1(10^{-3})	M2(10^{-3})	Assigned multipolarity
854.4	α_K = 26 (5)	3.00	7.84	26.9	63.7	M1
903.1	α_K = 3.3 (4)	2.71	7.07	23.3	54.8	E1
1103.5	α_K = 9.0 (9)	1.90	4.89	13.9	32.0	M1 + E2
	α_L = 1.6 (4)	0.294	0.954	2.36	6.03	
1136.5	α_K = 37 (12)	1.8	4.63	12.9	29.3	M2
1141.4	α_K = 19 (6)	1.79	4.59	12.8	28.9	M1
1170.7	α_K = 4.6 (6)	1.71	4.39	12.0	27.4	E2
	α_L = 0.94 (32)	0.264	0.838	2.03	5.12	
1175.4	α_K = 4.9 (8)	1.70	4.35	11.9	27.1	E2
1213.8	(α_K = 6.8 (20))[a]	1.61	4.11	10.9	25.0	(M1 + E2)[a]
1217.2	(α_K = 7.1 (20))[a]	1.60	4.09	10.9	24.8	(M1 + E2)[a]
1262.6	α_K = 1.8 (4)	1.50	3.82	9.89	22.5	E1

(continued)

Table 19 (continued)

Transition energy keV	Experimental[d] conversion coefficient (10^{-3})	Theoretical[c] conversion coefficient E1(10^{-3})	E2(10^{-3})	M1(10^{-3})	M2(10^{-3})	Assigned multipolarity
1446.1	α_K = 4.4 (10)	1.19	2.99	7.0	1.59	M1 + E2
1581.6	α_K = 0.87 (40)	1.03	2.55	5.57	12.7	E1
1767.0	α_K = 9.6 (20)	0.854	2.01[b]	3.96[b]	9.3[b]	M2

[a]This value was extracted from a complex (doublet) peak and is only suggestive due to poor resolution.

[b]This theoretical conversion coefficient was obtained by extrapolation from the tables of Sliv and Band[82].

[c]Theoretical values were obtained by computer interpolation[43]) from the tables of Hager and Seltzer[42]).

[d]The NPG method (see Appendix F), assuming the 545.0 keV transition ($5/2^- \rightarrow 1/2^-$) was pure E2, was used to extract these relative internal conversion coefficients.

[e]The assignment of this conversion coefficient is uncertain.

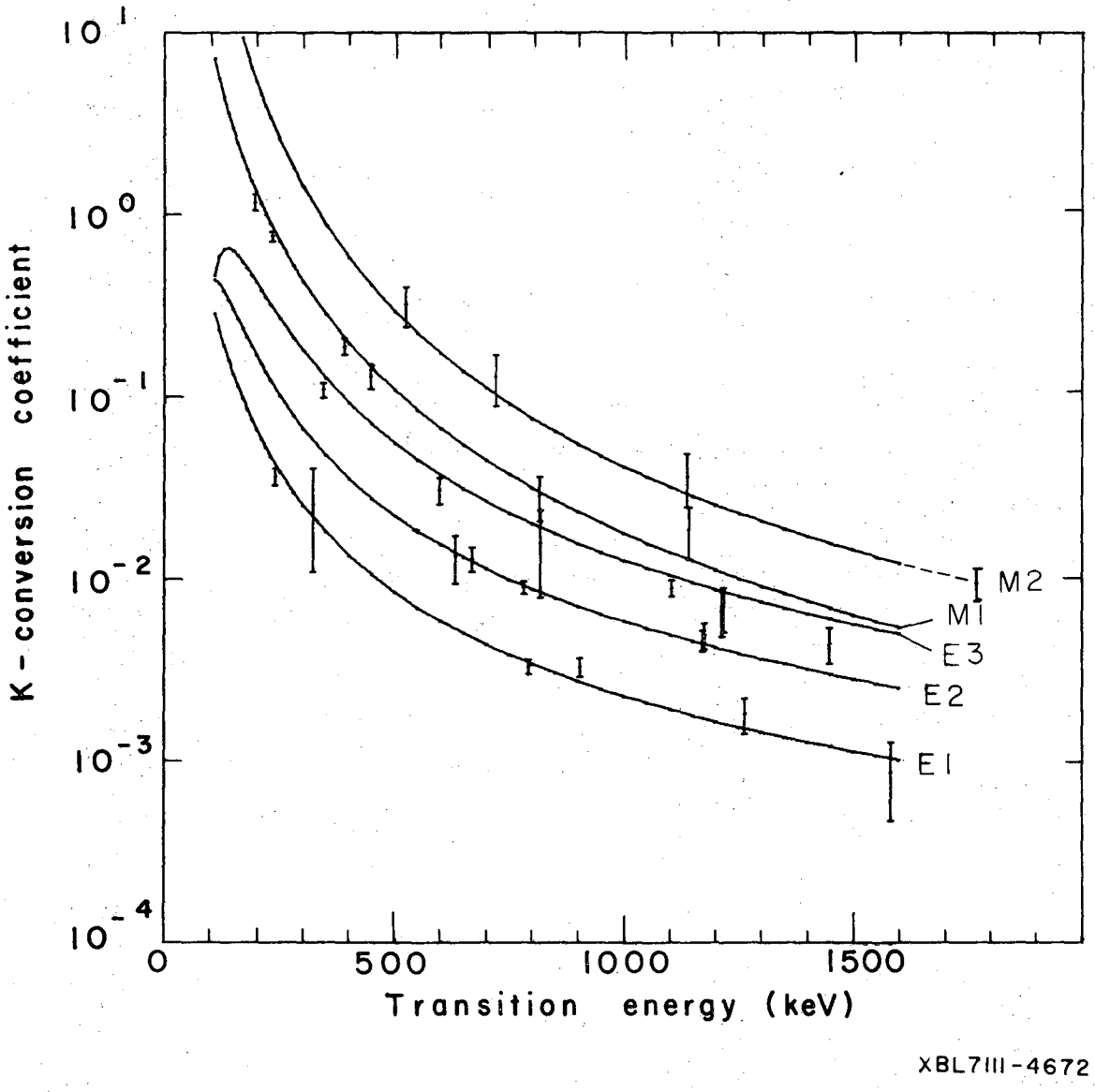

Fig. 77. Comparison of the experimental K-conversion coefficients of some ^{209}At transitions with the theoretical values of Hager and Seltzer[42]. Lines are theoretical values[42]) and points are experimental values measured relative to the 545.0 keV E2 transition. The values for M2 transitions were extrapolated (dotted line) to 1770 keV.

E. ^{209}At Decay Scheme

1. Introduction

Before discussing in detail the level scheme in the next sections, a brief qualitative description of the expected level structure of ^{209}Po is given. A schematic representation of the ^{209}Po ground state configuration is given in fig. 78 based on experimental[9]) single-particle states in the lead region. A series of states which are single neutron (particle or hole) in character are expected to be observed in this even-odd nucleus. Zero-order energy estimates of these states may be made from the even-odd nucleus ^{207}Pb. The addition of the 83rd and 84th protons in ^{209}Po is expected to alter the energy of the single-neutron states from those observed in ^{207}Pb. In particular the $3p^{-1}_{1/2}$, $2f^{-1}_{5/2}$, $3p^{-1}_{3/2}$, $1i^{-1}_{13/2}$, $2g^{1}_{9/2}$ and $1i^{1}_{11/2}$ neutron particle or hole states are observed at energies of 0, 570, 898, 1633, 2340, 2803 and 3581 keV in ^{207}Pb. Similar states are expected in the level structure of ^{209}Po.

The 83rd and 84th protons of ^{209}Po are also expected to produce a series of two-proton states similar to those observed in section IV for ^{210}Po to which the odd-neutron of ^{209}Po can couple to produce states that are of two proton-one neutron in character. If the couplings involved are weak, these states should occur at energies similar to those observed in ^{210}Po. For example the $p^{-1}_{1/2}$ neutron-hole can couple to the 2^+ two-proton state (at 1181.4 keV in ^{210}Po) to produce two states of spin 3/2 and 5/2 near 1181.4 keV. The configurations would be

$$[\pi(h^{2}_{9/2})_{2^+}\ \nu(p^{-1}_{1/2})_{1/2^-}]_{3/2^-,5/2^-}.$$

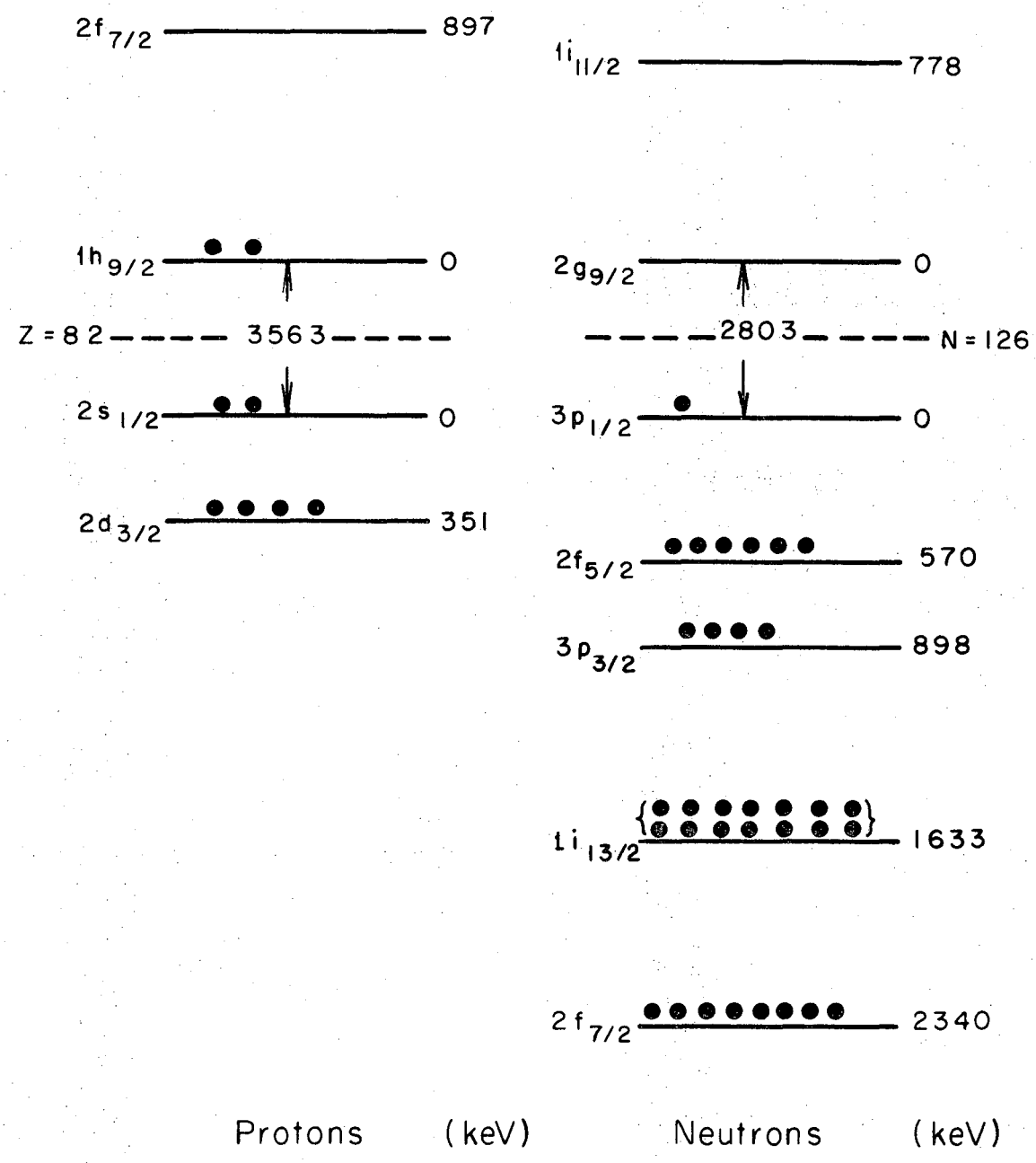

Fig. 78. Representation of the ^{209}Po ground-state and neighboring experimental[9]) single-particle states.

For energies $\gtrsim$ 2 MeV the level structure should become very complex since the number of possible configurations for the even-odd ^{209}Po nucleus becomes very large.

2. The Level Scheme

Coincidence measurements and the sum-difference relationships of our γ-ray energies have been used to construct the level scheme shown in fig. 79. Twenty excited states of ^{209}Po are proposed as populated in the decay of ^{209}At. Spin and parity assignments are based on previously reported data and our internal conversion electron measurements. Levels shown with broken lines are relative uncertain and should be taken as only tentatively identified. Several weak transitions observed with the mass separated source for which no coincidence relations were established, but which fit between known levels from energy sum-difference relations, are shown as broken lines indicating a tentative placement. The levels are discussed below in related groups.

a. Odd Parity Ground and First Excited States at 0.0 and 545.0 keV

The ground state spin has been measured as 1/2 by Vander Sluis and Griffin[72]) and it is reasonable to associate this state with a $p_{1/2}$ neutron in anology with ^{207}Pb. The configuration of the ground state of ^{209}Po would then be $[\pi(h^{2}_{9/2})_{0^+} \nu(p^{-1}_{1/2})]_{1/2^-}$.

The first excited state at 545.0 keV was assigned a spin and parity of $5/2^-$ by Yamazaki and Matthias[74]) from angular distribution measurements of gamma-rays from the ^{208}Pb(α,3n)^{209}Po reaction. The shell model predicts a low-lying $f_{5/2}$ neutron hole state and the experimental[9]) levels of ^{207}Pb show such a $\nu(f^{-1}_{5/2})$ state at 570 keV so

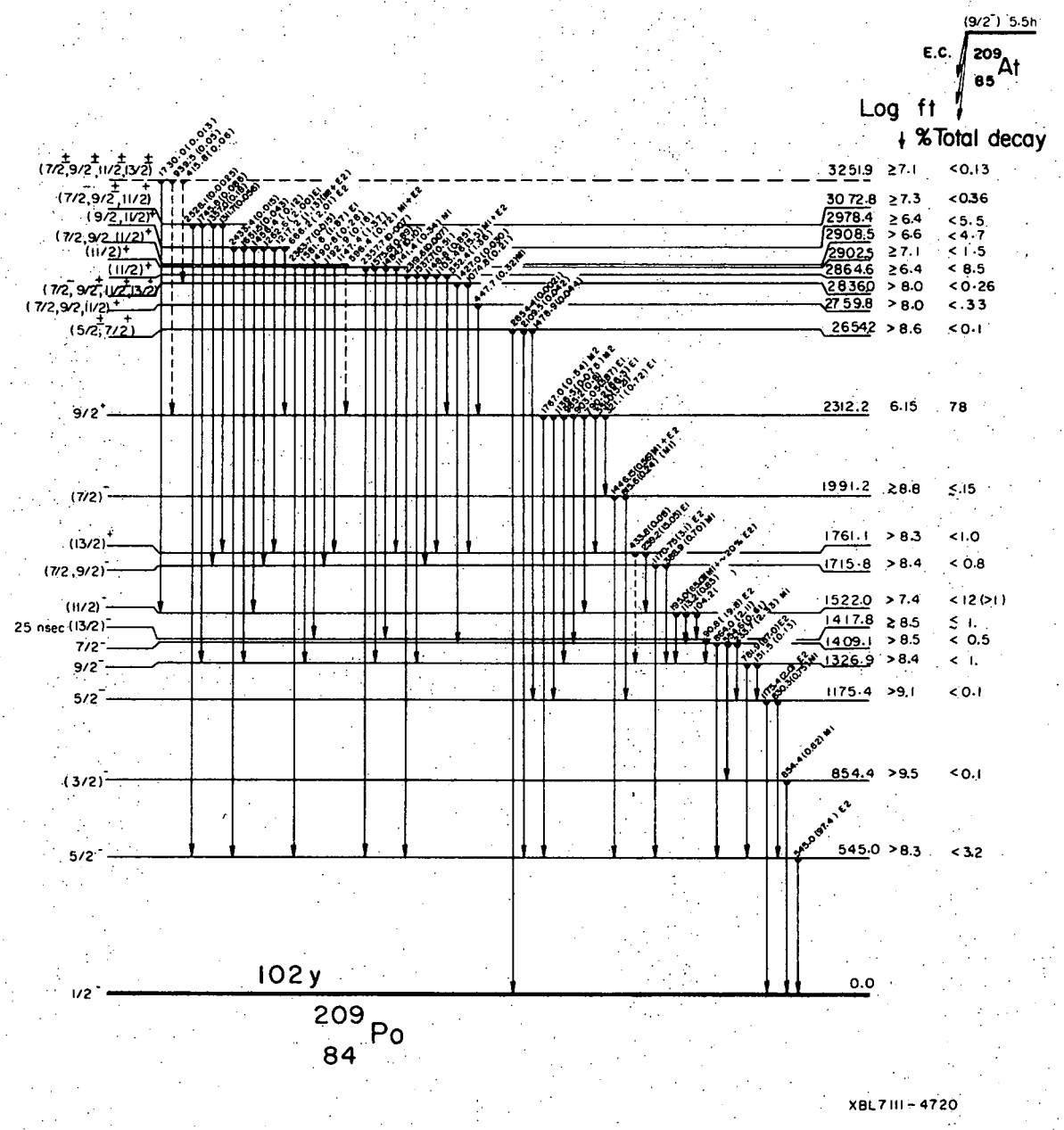

Fig. 79. Experimental decay scheme of ^{209}At. (Absolute transition intensities per electron-capture decay are shown on the level scheme.)

that the spin and parity assignment of $5/2^-$ for this level is reasonable. Our measured log ft ≥ 8.3 is consistent with this assignment as direct decay to this state would be a second forbidden transition.

We assume in the following discussion of the decay scheme that the ground state and first excited state are $1/2^-$ and $5/2^-$, respectively with a 545.0 keV E2 transition connecting them. The 545.0 keV E2 transition was used to measure relative conversion coefficients of other transitions (see Section VD3). Assignments of spin and parities to other levels were inferred directly by our relative conversion coefficients with these assumptions.

b. Even Parity Level at 2312.2 keV

This level receives about 78% of the electron capture decay. The weak 1767.0 and 1136.5 keV M2 transitions to the $5/2^-$ levels at 545.0 and 1175.4 keV establish the parity as even and limits the spin to 1/2 or 9/2. The spin 1/2 can be ruled out by the log ft value and by transitions from the 2312.2 keV level to other high-spin levels which then establish the spin as 9/2. We favor the assignment $9/2^+$ which can be associated with the probable dominant configuration $(\pi(h_{9/2}^2)_{0^+}\ \nu(g_{9/2}))_{9/2^+}$. The electron-capture decay would be of the first forbidden type $(\pi(h_{9/2}) \rightarrow \nu(g_{9/2}))$ and the low log ft is similar to other values for first-forbidden beta decays in the lead region[65].

c. Odd Parity Level at 854.4 keV

This level was established from the γ-γ coincidence data on the 854.4 and 554.6 keV cascade. Our coincidence measurements also showed that the 321.1 keV transition should not be placed between the 1409.1 and

854.4 keV levels. The M1 multipolarity of the 854.4 keV transition establishes the parity of the 854.4 keV level as odd and limits the spin to 1/2 or 3/2. The ordering of the transitions used to establish the level at 854.4 keV is due to an anology with the $\nu(p^{-1}_{3/2})$ state at 898 keV in ^{207}Pb. Our log ft $\geq$ 9.5 is consistent if this level had the dominant neutron-hole configuration $\nu(p^{-1}_{3/2})$. Also the 309.4 keV transition connecting this level to the $5/2^-$ level at 545.0 keV is missing as in ^{207}Pb. We favor the assignment $(3/2)^-$ for this level as due to the dominant configuration $(\pi(h^2_{9/2})_{0^+}\ \nu(p^{-1}_{3/2}))_{3/2^-}$.

d. Odd Parity Levels at 1175.4, 1326.9, 1409.1, 1417.8 and 1522.0 keV

The parity of the 1175.4 keV level is established as odd and the spin is limited to (3/2, 5/2) by the 1175.4 keV E2 and 630.3 keV M1 transitions to the $5/2^-$ states at 0.0 and 545.0 keV. The weak 1136.5 M2 transition from the $9/2^+$ level at 2312.2 keV then establishes the spin as 5/2.

Yamazaki and Matthias[74]) established the 1326.9 keV level as $9/2^-$. The 781.9 keV E2 transition to the $5/2^-$ level is consistent with their assignment.

The level at 1409.1 keV was established from γ-γ coincidence relations of the 903.05, 233.7, and 1175.4 keV transitions. The 903.05 keV E1 transition from the $9/2^+$ level at 2312.2 keV establishes the parity as odd and limits the spin to (7/2, 9/2, 11/2). The 233.7 keV M1 transition to the $5/2^-$ level at 1175.4 keV establishes the spin of the level as 7/2.

The 90.8 keV transition was determined as pure E2 from our measurement of the ratio $(\alpha_{L_1} + \alpha_{L_2})/\alpha_{L_3}$ in section VD3. This agrees with the E2 assignment made by Stoner[36]) and by Alpsten, Appleqvist and Astner[75]). The spin and parity of the level at 1417.8 keV can only be limited to $(5/2, 7/2, 9/2, 11/2, 13/2)^-$ on the basis of the 90.8 keV E2 transition since no other multipolarities of transitions involving this level were determined. However, if the 90.8 keV transition was pure E2 with no M1 component, the limits for the spin can be reduced to 5/2 or 13/2 . There are several arguments for favoring the high spin assignment of 13/2 . First, the strong intensity reported in the ^{208}Pb $(\alpha,3n)$ reaction studies by Bergström et al.[77]) for the 90.8 keV transition indicates population of this (high-spin) level. Second, the lack of transitions from this level to low-spin states below is another argument for the high-spin assignment. We favor the assignment of $(13/2)^-$ which requires the 90.8 keV transition to be pure E2.

The 1522.0 keV level is of odd parity because of the 790.2 keV E1 transition from the $9/2^+$ level at 2312.2 keV. The spin can only be limited to (7/2, 9/2, 11/2). The population of this level in $^{208}Pb(\alpha,3n)$ reaction studies[77]) and the lack of transitions to the $5/2^-$ levels are weak arguments for choosing the higher spin (11/2) which we favor.

e. Odd Parity Levels at 1715.8 and 1991.2 keV

These levels were established from coincidence data. The parity of the 1715.8 keV level is established as odd by the 1170.75 keV E2 transition. The spin can be limited to 7/2 or 9/2 by the 388.9 keV M1 transition to the $9/2^-$ level at 1326.9 keV.

The parity of the level at 1991.2 keV is established as odd by the 321.1 keV E1 transition. The 1446.15 keV M1 + E2 transition to the $5/2^-$ level at 545.0 keV and the 321.1 keV E1 transition from the $9/2^+$ level at 2312.2 keV limit the spin assignments to 7/2 or 9/2. Weak evidence that the 815.6 keV transition to the $5/2^-$ level at 545.0 keV is of M1 multipolarity favors the assignment $(7/2)^-$.

f. Even Parity Level at 1761.1 keV

The parity is established as even by the 239.2 keV E1 transition to the odd parity level at 1522.0 keV. The 239.2 keV transition was also observed in the in-beam work of Bergström et al.[77]) so that a high-spin assignment is likely. Our conversion data only limit the spin to (9/2, 11/2, 13/2). A shell model calculation[83]) predicts a low-lying even parity $13/2^+$ state at 1910 keV due to the dominant configuration $(\pi(h_{9/2})^2\ \nu(i_{13/2}))_{13/2^+}$. ^{207}Pb also has a low-lying $13/2^+$ state at 1633 keV due to the $i_{13/2}$ neutron-hole so that we favor the assignment $(13/2)^+$ for this level.

g. Even Parity Levels at 2759.8, 2864.6, 2902.5, 2908.5 and 2978.5 keV

The level at 2759.8 keV was established from our coincidence data. The measured M1 multipolarity for the 447.7 keV transition determines the parity as even and limits the spin to (7/2, 9/2, 11/2).

The parity of the levels at 2864.6 and 2902.5 keV is established as even by the 1103.46 keV M1 + E2 and 1141.4 keV M1 transitions to the even parity level at 1761.1 keV. The spin of the level at 2864.6 keV can be limited to (11/2, 13/2, 15/2) by the 1103.46 keV M1 + E2 transition to the $(13/2)^+$ level at 1761.1 keV. The low log ft of 6.4 for

decay to this level and the weak 2319.6 keV transition to the $5/2^-$ level at 545.0 keV make the assignment $(11/2)^+$ more likely. The 1141.4 keV M1 transition to the $(13/2)^+$ level at 1761.1 keV limit the assignment of the 2902.5 keV level to $(11/2, 13/2, 15/2)^+$. The weak 2357.7 keV transition to 545.0 keV $5/2^-$ level coupled with the relatively low log ft of 7.1 argue for the assignment $(11/2)^+$.

The 1581.6 keV E1 transition to the $9/2^-$ level at 1326.9 keV limit the spin and parity of the 2908.5 keV level to $(7/2, 9/2, 11/2)^+$ which is consistent with other transitions from this level and the log ft value of 6.6.

The parity of the level at 2978.4 keV is established as even by the 1262.6 keV E1 transition to the odd parity level at 1715.8 keV. The spin can be limited to (5/2, 7/2, 9/2, 11/2). The strength of the 1217.2 keV transition to the $(13/2)^+$ level at 1417.9 keV coupled with weak evidence of the 1217.2 keV multipolarity as M1 + E2 argue strongly for a $(9/2, 11/2)^+$ assignment. The log ft of 6.4 and other transitions from this level are consistent with these assignments.

h. Levels at 2654.2, 2836.0, 3072.8, and 3251.9 keV

The level at 2654.2 keV was placed from our energy sum-difference data for the three transitions of 2654.4, 2109.5, and 1478.9 keV. Allowing M2 and E3 transitions, tentative spin and parity assignments of $(5/2^\pm, 7/2^+)$ are suggested for this level.

The level at 2836.0 keV was established from the 1074.8 keV - 239.2 keV γ-γ coincidence relation. The spin and multipolarity remain undetermined but the probable assignments of $(7/2^-, 9/2^\pm, 11/2^\pm, 13/2^+)$ can

be made based on the gamma-ray branching to the $7/2^-$ and $(13/2)^+$ levels at 1326.9 and 1761.1 keV.

The level at 3072.8 keV was established from energy sum-difference relations. Transitions to the $5/2^-$ level at 545.0 keV and the $(13/2)^+$ level at 1761.1 keV coupled with the log ft of 7.3 argue weakly for tentative assignments of $(7/2^-, 9/2^\pm, 11/2^+)$ for this level.

A tentative level was placed at 3251.9 keV from energy sum-difference relations. The 939.5 and 415.8 keV transitions were observed with the mass separated source but not in mixed astatine sources indicating the weakness of the transitions involved. Our log ft $\geqslant$ 7.1 limit was set assuming that no feeding of this level occurred from higher-lying states. We can not make a definite spin or parity assignment for this level although $(7/2^\pm, 9/2^\pm, 11/2^\pm, 13/2^\pm)$ are likely estimates.

F. Electron-Capture Decay Rates (log ft values)

The ^{209}At electron-capture branching ratios to the various ^{209}Po levels were estimated in our work from the total transition intensity depopulating each level using our γ-ray intensity data corrected for internal conversion. For decay energies $\gtrsim$ 700 keV, the expanded version of the nomogram of Moszkowski[58,22]) was used and for decay energies of $\leqslant$ 700 keV the method discussed by Konopinski and Rose[59]) for allowed transitions was employed. This method is discussed in detail in Appendix B. The Q-value was taken for the electron-capture decay as[60]) Q_{EC} = 3485 ± 15 keV and the half-life was taken as 5.5 hours. The transition intensities were corrected for fractional decay by K-capture using the graphs in the ref. [22]).

G. ^{209}Po Level Structure in Comparison with Levels of ^{207}Pb and ^{210}Po

The low-lying states of ^{207}Pb are determined by the odd neutron and of ^{210}Po by the 83rd and 84th protons. It is of interest to compare the experimental and theoretical level structure of ^{209}Po with the experimental[9]) levels of ^{207}Pb and ^{210}Po. The comparison can be used to qualitatively describe the low-lying levels of ^{209}Po in terms of neutron (hole or particle) states and neutron states weakly coupled to the two-proton states. A shell model calculation for ^{209}Po by Baldridge, Freed and Gibbons[83]) using a semirealistic core polarization[84]) approach can serve as a guide in making the comparisons. They have calculated the level spectrum of ^{209}Po up to 1910 keV using a non-local Tabakin interaction plus pairing forces (P_0, P_2, and P_4) which simulate the core polarization.

To make the comparisons we discuss the ^{209}Po level structure in two sections using the experimental results and the theoretical calculation to group the states according to their dominant configuration.

1. Neutron-Hole and Neutron-Particle States

We have plotted in fig. 80 the experimentally[9]) observed states of ^{207}Pb due to the odd neutron and four of these states in ^{209}Po as calculated by Baldridge, Freed and Gibbons[83]). Also shown are five experimental states of ^{209}Po which we believe to correspond to states arising predominately from the odd neutron as in ^{207}Pb.

The correspondence for the first four levels is quite good and the $3p^{-1}_{1/2}$, $2f^{-1}_{5/2}$, $3p^{-1}_{3/2}$, and $1i^{-1}_{13/2}$ neutron-hole states in ^{209}Po are thus believed identified. The theoretical wavefunctions[83]) for the $3p^{-1}_{1/2}$,

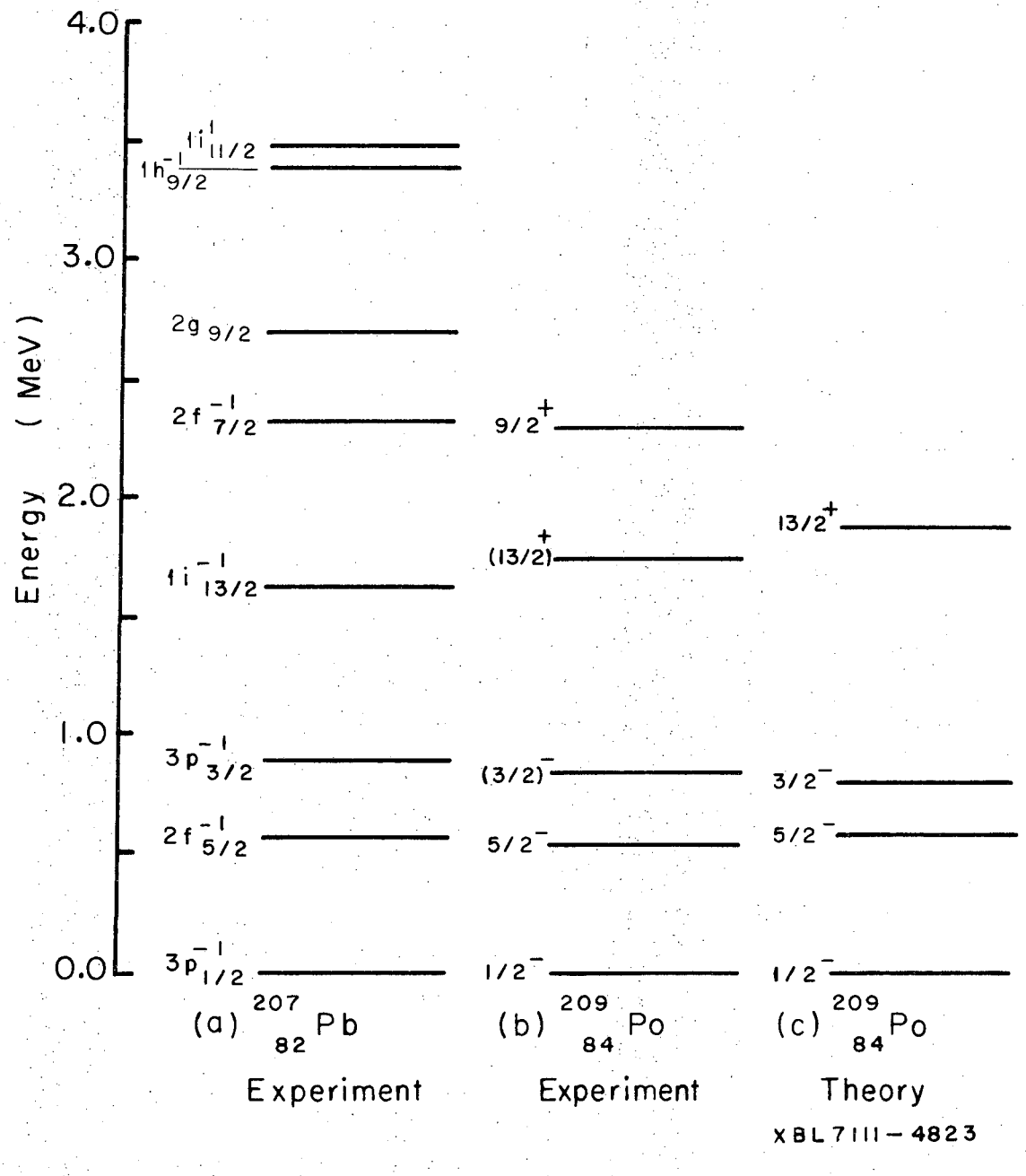

Fig. 80. Comparison of the experimental level structure of ^{209}Po (arising from the odd neutron) (b) with the experimental[9]) level scheme of ^{207}Pb (a) and with a shell model calculation[83]) (c).

$2f^{-1}_{5/2}$, and $1i^{-1}_{13/2}$ neutron states had amplitudes $a_i \geq 0.94$ for these neutron components. The $3p^{-1}_{3/2}$ state was not as pure (with a $p_{3/2}$ amplitude of only 0.863) because of configuration mixing with other near-by $3/2^-$ states arising from the coupling of the neutron-hole states with the two-proton states coupled to other than zero. The main contributor is the configuration $[\pi(h^2_{9/2})_{2^+} \nu(p^{-1}_{1/2})]_{3/2^-}$ at 1181 keV as discussed in section VG2. Our experimental log ft values involving these four levels are relatively high (≥ 8.3) and are consistent with these neutron-hole states assignments. The $9/2^+$ level was not calculated theoretically but we can argue for its identification as the dominant $2g_{9/2}$ neutron-particle state from our experimental observations. The ground state of ^{209}At presumably has the configuration $[\pi(h^3_{9/2})_{9/2^-} \nu(f^6_{5/2})_{0^+}]_{9/2^-}$ and in the electron-capture decay a $1h_{9/2}$ proton would undergo the transition to a neutron. Transitions from the odd-even (neutron) nucleus ^{209}At to the even-odd (neutron) nucleus ^{209}Po should favor population of single neutron states (or states with such large components) where the transition is not hindered. Transitions to the four neutron states previously discussed would be of the type $\pi(1h_{9/2}) \xrightarrow{EC} \nu(3p_{1/2})$, or $\nu(2f_{5/2})$, or $\nu(3p_{1/2})$, or $\nu(1i_{13/2})$. These transitions are hindered because of the relatively large $\Delta\ell$ or Δj changes involved and our values of log ft support this. The log ft for the $9/2^+$ level is low (log ft = 6.15) indicating an unhindered transition. It is reasonable to identify this level with spin and parity of $9/2^+$ as the dominant $2g_{9/2}$ neutron state where the transition $\pi(1h_{9/2}) \xrightarrow{EC} \nu(2g_{9/2})$ would be of the first-forbidden type and relatively unhindered. A

similar log ft value has been observed in the decay of ^{210}At to ^{210}Po and explained in section IV as due to the same transition. The $9/2^+$ level in ^{209}Po compared with the experimental $9/2^+$ level in ^{207}Pb is depressed about 500 keV in energy. This could be due in part to configuration mixing with other $9/2^+$ states in the approximate same energy region as discussed further in section V I.

In summary, we favor identifying the levels at 0.0, 545.0, 854.4, 1761.1 and 2312.2 keV as the $3p^{-1}_{1/2}$, $2f^{-1}_{5/2}$, $3p^{-1}_{3/2}$, $1i^{-1}_{13/2}$ and $2g^{1}_{9/2}$ neutron states, respectively.

2. Comparison with the Zero-Order Weak Coupling Model

We will use the experimental levels of ^{207}Pb and ^{210}Po to obtain zero-order estimates of the level energies for a series of odd parity states of ^{209}Po in the energy region $\leqslant$ 2 MeV. A model for states in ^{209}Po can be constructed by considering the couplings of neutron (hole or particle) states to the $(h_{9/2})^2$ two-proton configurations. For this model, we take the first three levels at 0, 570, and 898 keV in ^{207}Pb as the single neutron-hole states $3p^{-1}_{1/2}$, $2f^{-1}_{5/2}$, and $3p^{-1}_{3/2}$, respectively, and we consider the zero-order coupling of these states the 2^+, 4^+, 6^+ and 8^+ (two-proton) excited states of ^{210}Po at 1181, 1427, 1473, and 1557 keV, respectively. The resulting band structure is shown in column (b) of fig. 81. The residual interactions between the neutron-hole and the two-protons, if included, would remove the degeneracy of the coupled states. This zero-order model predicts nothing about the order of the states once the degeneracy is removed but the density of levels at 2 MeV is predicted to be very high.

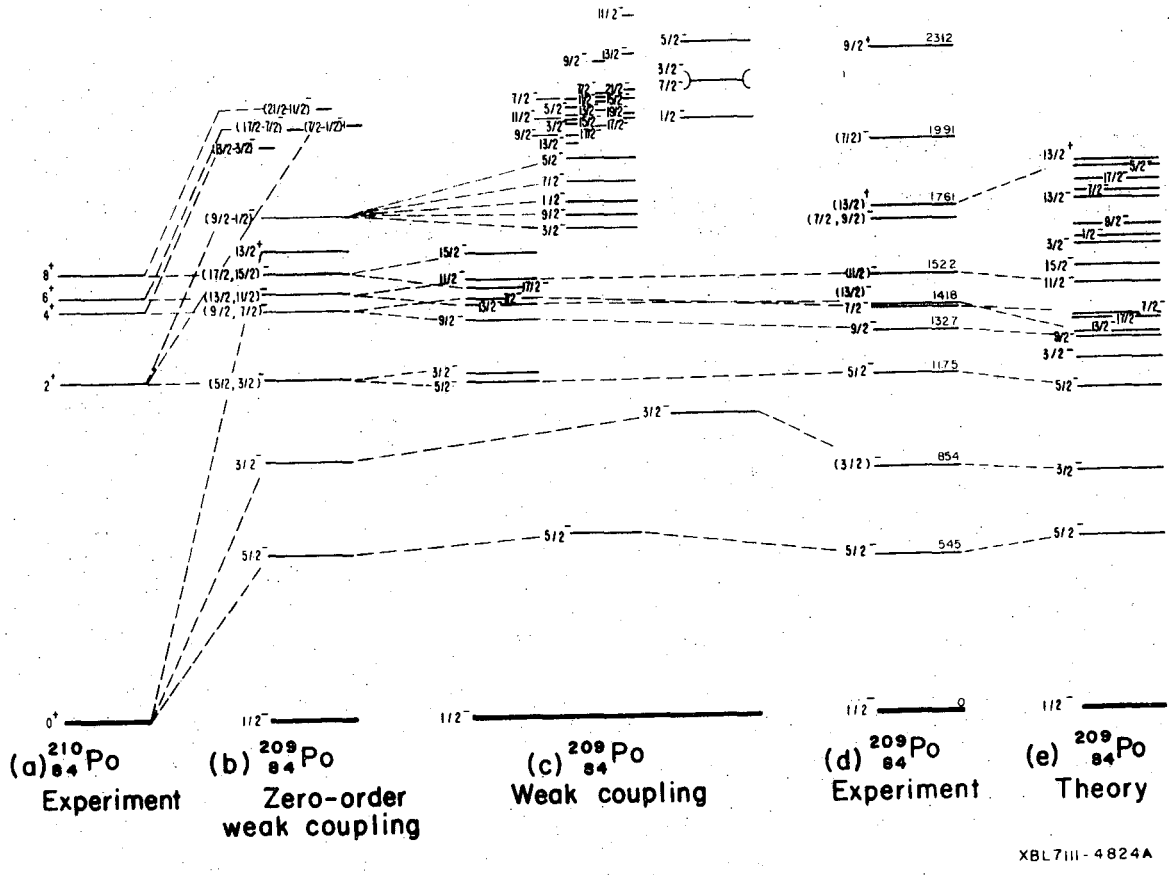

Fig. 81. Comparison of the level structure of ^{209}Po (d) below 2.3 MeV with:

(a) ^{210}Po experimental level structure.

(b) Zero-order weak coupling calculation.

(c) Weak-coupling calculation.

(e) Shell model calculation[83]).

The experimental levels of ^{210}Po are shown in column (a) of fig. 81. Shown in column (e) are the levels from the theoretical calculation of Baldridge, Freed and Gibbons[84]), and in column (d) our experimental levels of ^{209}Po in this energy region. This simple model is in very good qualitative agreement with the level structure of the available experimental data and the more complex theoretical calculation which included configuration mixing. It seems probable that the experimental levels of $5/2^-$, $9/2^-$, $7/2^-$, $(13/2)^-$, $(11/2)^-$ at 1175.4, 1326.9, 1409.1, 1417.8, and 1522.0 keV have the dominant configuration $\nu(p_{1/2}^{-1})$ coupled to the 2^+, 4^+, and 6^+ configurations of the 83rd and 84th protons, each in the $1h_{9/2}$ orbital. The level at 1715.8 keV assigned $(7/2, 9/2)^-$ may belong to the states arising from the $f_{5/2}^{-1}$ neutron-hole coupled to the 2^+ two-proton state. Finally the $(7/2)^-$ level at 1991.2 keV may be one of the $f_{5/2}^{-1}$ neutron-hole states coupled to the 4^+, 6^+, or 8^+ two-proton configurations; however, the possibility that this state may have a large amplitude of the single-hole configuration $\nu(2f_{7/2}^{-1})$ due to configuration mixing can not be excluded. In any event this level, and others occuring higher in energy, should be very highly mixed due to the many different configurations possible from such an odd A nucleus.

H. Comparison with the Weak Coupling Model

The description of the 11^- and 13^- states of ^{210}Po at approximately 4.3 MeV by Blomqvist et al.[33] in terms of weak particle-core coupling has met with limited success. Briefly, the two levels were treated as the weak coupling of the 8^+ two-proton configuration with the 3^- and 5^- ^{208}Pb core states. In section IID a formalism was extended to estimate level energies of ^{209}Po by including the coupling of the odd neutron with angular momentum $\vec{j}_n$ to the two-proton angular momenta ($\vec{j}_1$ and $\vec{j}_2$) coupled to an angular momentum $(j_1 j_2)J$. We assumed that the proton-proton interaction could be approximated from experimental data on the levels of ^{210}Po and the neutron hole-proton interaction from available experimental data on the levels of ^{208}Bi in the following way.

We defined the mass (or energy) of a state in ^{209}Po with angular momentum $\vec{I}$ as $M^I(^{209}\text{Po})$. (The mass of $M^I(^A\text{X})$ of excited states of angular momentum $\vec{I}$ of a nucleus ^{A}X includes the ground state mass plus the energy of the excited state.) Recoupling of two-proton angular momenta $\vec{j}_1$ and $\vec{j}_2$ in terms of Racah coefficients lead to the following expression to estimate the mass of ^{209}Po.

$$M^I(^{209}\text{Po}) = M^{(j_1 j_2)J}(^{210}\text{Po}) + M^{j_n}(^{207}\text{Pb}) - M^{0^+}(^{208}\text{Pb})$$

$$+ \sum_{J'} (2J+1)(2J'+1)\left|W(j_1 j_2\ I\ j_n;\ J\ J')\right|^2 \Delta M^{J'}_{j_1 j_n}$$

$$+ \sum_{J''} (2J+1)(2J''+1)\left|W(j_2 j_1\ I\ j_n;\ J\ J'')\right|^2 \Delta M^{J''}_{j_2 j_n} \qquad (105)$$

where

$$\vec{I} = \vec{J} + \vec{j}_n \quad , \quad \vec{J} = \vec{j}_1 + \vec{j}_2 \quad , \quad \text{and} \quad \vec{J}' = \vec{j}_1 + \vec{j}_n \qquad (106)$$

We have defined the term representing the neutron hole-proton interaction in terms of experimental masses of ^{208}Bi, ^{209}Bi, ^{208}Pb and ^{207}Pb as

$$\Delta M^{J'} = M^{(j_1 j_n)J'}(^{208}\text{Bi}) + M^{0^+}(^{208}\text{Pb}) - {}^{j_1}M(^{209}\text{Bi}) - {}^{j_n}M(^{207}\text{Pb}) \qquad (107)$$

For the evaluation of eq. (105), we used the tables of ground-state masses of Wapstra and Gove[73]), and the experimental level energies and spin assignments for ^{207}Pb, ^{208}Bi and ^{209}Bi recommended by Nuclear Data[9]). These values have been given in fig. 4 and Table 7 for ^{207}Pb and ^{209}Bi while Table 20 shows the values used for ^{208}Bi. The results of the calculation are shown in column (c) of fig. 81 and in Table 21. The agreement of this weak coupling calculation with the experimental results is quantitatively very good up to 1552 keV. The correct order of the $\nu(p_{1/2}^{-1})$ couplings to the 4^+ and 6^+ two-proton configurations is predicted. (Our previous zero-order calculation could not predict the ordering as the states were degenerate.) An apparent discrepancy of the first $3/2^-$ state in columns (c) and (d) seems to exist. However, the weak coupling calculation did not allow for any configuration mixing with the nearby ($\sim$ 150 keV) $(\pi(h_{9/2}^2)_{2^+}\ \nu(p_{1/2}^{-1}))_{3/2^-}$ state. Configuration mixing of the two $3/2^-$ states would lower the energy of the first $3/2^-$ state into better agreement with the experimental value. The effect of

Table 20. Spin, parity, and energy assignments[9]) used for ^{208}Bi states.

Spin and Parity J^{π}	Energy keV	Configuration
$(5)^+$	0.0	$\pi(1h_{9/2})\ \nu(3p_{1/2}^{-1})$
$(4)^+$	63.5	
$(6)^+$	510.3	
$(4)^+$	602.3	
$(5)^+$	629	$\pi(1h_{9/2})\ \nu(2f_{5/2}^{-1})$
$(3)^+$	634.4	
$(7)^+$	650.1	
$(2)^+$	925.6	
$(5)^+$	887	
$(4)^+$	960	$\pi(1h_{9/2})\ \nu(3p_{3/2}^{-1})$
$(3)^+$	1070	
$(6)^+$	1096	

Table 21. Energy levels of ^{209}Po calculated with the weak coupling model.

Spin and Parity J^{π}	Energy[a] keV	Spin and Parity J^{π}	Energy[a] keV
$(0^+\ 1/2^-)\ 1/2^-$	0	$(4^+\ 5/2^-)\ 3/2^-$	2068
$(0^+\ 5/2^-)\ 5/2^-$	633	$(4^+\ 5/2^-)\ 5/2^-$	2126
$(0^+\ 3/2^-)\ 3/2^-$	1052	$(4^+\ 5/2^-)\ 7/2^-$	2150
		$(4^+\ 5/2^-)\ 9/2^-$	2028
$(2^+\ 1/2^-)\ 5/2^-$	1169	$(4^+\ 5/2^-)\ 11/2^-$	2092
$(2^+\ 1/2^-)\ 3/2^-$	1200	$(4^+\ 5/2^-)\ 13/2^-$	1999
$(4^+\ 1/2^-)\ 9/2^-$	1385		
$(4^+\ 1/2^-)\ 7/2^-$	1458	$(6^+\ 5/2^-)\ 7/2^-$	2173
$(6^+\ 1/2^-)\ 13/2^-$	1435	$(6^+\ 5/2^-)\ 9/2^-$	2284
$(6^+\ 1/2^-)\ 11/2^-$	1518	$(6^+\ 5/2^-)\ 11/2^-$	2153
$(8^+\ 1/2^-)\ 17/2^-$	1496	$(6^+\ 5/2^-)\ 13/2^-$	2141
$(8^+\ 1/2^-)\ 15/2^-$	1614	$(6^+\ 5/2^-)\ 15/2^-$	2117
		$(6^+\ 5/2^-)\ 17/2^-$	2058
$(2^+\ 5/2^-)\ 1/2^-$	1794		
$(2^+\ 5/2^-)\ 3/2^-$	1692	$(8^+\ 5/2^-)\ 11/2^-$	2444
$(2^+\ 5/2^-)\ 5/2^-$	1946	$(8^+\ 5/2^-)\ 13/2^-$	2303
$(2^+\ 5/2^-)\ 7/2^-$	1866	$(8^+\ 5/2^-)\ 15/2^-$	2150
$(2^+\ 5/2^-)\ 9/2^-$	1744	$(8^+\ 5/2^-)\ 17/2^-$	2181
		$(8^+\ 5/2^-)\ 19/2^-$	2100
$(2^+\ 3/2^-)\ 1/2^-$	2088	$(8^+\ 5/2^-)\ 21/2^-$	2181
$(2^+\ 3/2^-)\ 3/2^-$	2204		
$(2^+\ 3/2^-)\ 5/2^-$	2341		
$(2^+\ 3/2^-)\ 7/2^-$	2203		

[a]The ground state mass of ^{209}Po was subtracted from all values calculated with Eq. (105) in order to give the ground state energy as 0.0 keV.

configuration mixing on the $3/2^-$ states, as well as others, can be observed from the theoretical[83]) level structure of column (e) which included mixing. Perhaps the good agreement of the remaining levels in column (c) with (d) is indicative of the purity of the states and is proof that the weak coupling model is a very good approximation for explaining the low-lying nuclear structure of this nucleus.

It should be noted that this weak coupling calculation depends strongly and rather sensitively on the level energies and spin assignments to other nuclei, namely, ^{208}Bi. Perhaps a further consistency of data in the lead region can be tested with this weak coupling approach as more detailed data becomes available for other nuclei, and hopefully the lower-lying states predicted for nuclei for which detailed spectroscopic information does not exist.

I. Final Remarks

With the present data not much can be said with certainty of the remaining levels in the energy region greater than 2.3 MeV. However, we note the rather low values of log ft to several of the even parity states at approximately 2.8-3.0 MeV which are fed directly in the decay. Applying the zero-order weak coupling model to ^{209}Po in this energy region, a high density of levels at 3 MeV was predicted. In particular, even parity states of spins 3/2-23/2, two each except for 3/2 and 23/2, are expected due to the configurations $(\pi(h_{9/2}\, i_{13/2})\nu(p_{1/2}^{-1}))_{J^+}$. (A comparison of the ^{210}Po configurations $\pi(h_{9/2}\, i_{13/2})_{J^-}$ discussed in section IV provided the energy estimate as 3 MeV.) Population by electron-capture of any "pure" state in ^{209}Po of the above configuration requires the transition $\pi(h_{9/2}) \xrightarrow{EC} \nu(p_{1/2})$ and should be relatively hindered because of the large change in orbital angular momentum ($\Delta\ell = 4$). However, configuration mixing of the two $9/2^+$ states with the configuration $(\pi(h_{9/2}^2)_{0^+}\, \nu(g_{9/2})_{9/2^+})_{9/2^+}$ would allow an unhindered decay through this admixed component. The transition would be via a first-forbidden decay of the type $\pi(1h_{9/2}) \xrightarrow{EC} \nu(2g_{9/2})$ which is also believed to be mainly responsible for decay to the $9/2^+$ level at 2312.2 keV.

Unhindered electron-capture decay could also populate states in the 3 MeV energy region with small components of the type $\pi(h_{9/2}^3\, s_{1/2}^{-1})\nu(p_{1/2}^{-1})$ due to <u>proton</u> excitations of the ^{208}Pb core. (States in ^{210}Po at 3.8 MeV of the configuration $\pi(h_{9/2}^3\, s_{1/2}^{-1})\nu(p_{1/2}^2)$ were believed responsible for the low values of log ft in the decay of ^{210}At

in section IV.) The $7/2^+$, $9/2^+$, $11/2^+$ states of ^{209}Po due to the configurations $\pi(h_{9/2}^{3}\, s_{1/2}^{-1})\nu(p_{1/2}^{-1})$ are predicted with a zero-order weak coupling model at an energy of ~ 3.8 MeV which is greater than the decay energy (3.5 MeV) of ^{209}Po. Such states would not be directly populated in the electron-capture decay and this might explain why no higher-lying levels of ^{209}Po were observed as directly fed with any appreciable strength in the decay. However, configuration mixing with lower-lying $7/2^+$, $9/2^+$, $11/2^+$ states would provide a second component to be populated in the decay via a first-forbidden transition of the type $\pi(3s_{1/2}) \xrightarrow{EC} \nu(3p_{1/2})$.

In summary the $3p_{1/2}^{-1}$, $2f_{5/2}^{-1}$, $3p_{3/2}^{-1}$, $1i_{13/2}^{-1}$ and $2g_{9/2}^{1}$ states in ^{209}Po arising from the odd-neutron have been identified. The effect of 83rd and 84th protons on these states, when compared to ^{207}Pb, was to depress the energy of the $2g_{9/2}$ neutron-particle state by 500 keV. This is probably due to configuration mixing with other $9/2^+$ states which occur in the same energy region. The energies of the $3p_{1/2}^{-1}$, $2f_{5/2}^{-1}$, and $1i_{13/2}^{-1}$ neutron-hole states were not altered appreciably from those observed in ^{207}Pb and these results were summarized in fig. 80. Odd parity states due to the weak coupling of the two-proton configurations $\pi(h_{9/2})^2$ with the $\nu(p_{1/2}^{-1})$ neutron-hole also have been identified. A weak coupling model was found to describe the ^{209}Po level structure for energies of less than 2 MeV with the exception of one serious discrepancy in the energy of the $\nu(p_{3/2}^{-1})$ neutron-hole state. This discrepancy between experiment and theory was removed in a detailed shell model calculation[83]) with configuration mixing which was not included in our

weak coupling calculation. The experimental, weak coupling model, and shell model level structure in the energy region of less than 2.3 MeV are summarized in fig. 81 where the agreement was found to be very good.

The absence in our study of a series of odd parity states of the configuration $\pi(h_{9/2}\ f_{7/2})\nu(p_{1/2}^{-1})$ (which a zero-order weak coupling model predicts at 2.4 MeV) does not alter our conclusions about the validity of weak coupling to describe the ^{209}Po level structure. Direct decay of ^{209}At to these "pure" states would be hindered in the same way as direct decay of ^{210}At to configurations in ^{210}Po of the type $\pi(h_{9/2}\ f_{7/2})\nu(p_{1/2}^{2})$ where values of log ft were observed to be ≥ 8 (see section IV). No odd parity states exist in the immediate energy region for configuration mixing which could allow an unhindered decay. Thus these states in ^{209}Po should be populated only by gamma decay of higher lying levels. The fact that 78% of the decay "bypasses" these states by populating the lower-lying $9/2^+$ level at 2.3 MeV could explain the absence of these levels in our decay scheme. The ^{208}Bi$(\alpha,t)^{209}$Po reaction, if possible, should populate such states and would help confirm or refute the weak coupling model at energies greater than 2.3 MeV, even though the density of levels expected is very high.

The study of ^{209}Po through the electron-capture decay of ^{209}At has revealed only a limited number of states. All of the states due to the $2f_{5/2}^{-1}$ and $3p_{3/2}^{-1}$ neutron-holes coupled to the configurations $\pi(h_{9/2}^{2})_{J^+}$ have not been observed. These and many other states not populated in the beta decay could be populated and studied by different reactions. In particular, further ^{208}Pb$(\alpha,3n)$ studies and possibly a high resolution

$^{208}Bi(\alpha,t)$ or $^{208}Bi(^{3}He,d)$ reaction study would be very informative. It is now known[85] that the $^{210}Po(p,d)^{209}Po$ has been investigated and the data are being analyzed. The results of this reaction study should be most interesting as the weak coupling model can be further tested. States of the configuration $[(\pi(h_{9/2})_{J^+} \nu(p_{1/2}^{-1})]_{J^-}$ should be populated very weakly, (only through small admixtures) compared to the neutron-hole states.

ACKNOWLEDGEMENTS

To the many people who generously contributed to the successful completion of this work I shall be forever indebted. I owe special thanks to:

My research director Professor S. G. Prussin for providing the thoughtful guidance and constant encouragement necessary in carrying out this study and for being a genuine person.

Dr. C. M. Lederer for many fruitful discussions and suggestions related to this work.

Dr. G. L. Struble for many stimulating discussions about the theoretical aspects of this work and for allowing use of his gamma-ray transition probability computer code.

Dr. J. M. Hollander for support without whom this work could not have been carried out.

The generosity of Dr. M. C. Michel and staff for providing the mass separated astatine sources is greatly appreciated.

I am greatly indebted to the many LBL electronics groups and especially to Dr. J. M. Jaklevic, Mr. W. L. Searles, and Mr. D. F. Malone for building and maintaining the Si(Li) electron detector system.

The staffs of the Vacuum Evaporation Shop and the 88-Inch Cyclotron for the preparation and bombardment of targets are acknowledged, especially Mrs. Ruth-Mary Larimer for the scheduling of several bombardments on rather short notice.

The excellent technical support of Mr. G. G. Young, Gerti Boltz, and the late Mr. George Driscoll was of the highest order.

I thank Drs. W. F. Lanford and R. Tickle for providing unpublished data and Drs. C. W. Ma and W. W. True for providing their theoretical wavefunctions.

My association with fellow colleagues Dr. A. A. Shihab-Eldin and Messrs. J. J. Bucher, M. D. Holtz, G. M. Moore, F. M. Nuh, and D. R. Slaughter has been both extremely enjoyable and profitable.

Finally I would like to express my sincere gratitude to my wife Kathy for her nine years of patience and understanding without which this work would not have been completed and for the typing of the original manuscript(s) of this thesis, and to my daughter Renee for her day-to-day smile, and to my grandparents and parents for their early guidance and continuing interest.

The financial support of the Atomic Energy Commission in the form of a Nuclear Science and Engineering Fellowship during my first three years at Berkeley is acknowledged.

This work was performed under the auspices of the U. S. Atomic Energy Commission.

REFERENCES

1. W. W. True and K. W. Ford, Phys. Rev. 109, 1675 (1958).
2. A. de Shalit and I. Talmi, Nuclear Shell Theory, Academic Press (1963) 158.
3. G. Eder, Nuclear Forces, translated by I. Kaplan, M.I.T. Press (London) 1968.
4. O. Haxel, J. H. D. Jensen, and H. E. Suess, Phys. Rev. 75, 1776 (1949); Z. Physik 128, 295 (1950).
5. M. G. Mayer, Phys. Rev. 74, 235 (1949).
6. M. G. Mayer, Phys. Rev. 75, 1969 (1949).
7. M. G. Mayer, Phys. Rev. 78, 16 (1950).
8. M. G. Mayer and J. H. D. Jensen, Elementary Theory of Nuclear Shell Theory, Wiley (New York) 1960.
9. Nuclear Data B5 (1971).
10. S. G. Nilsson, UCRL-18355 (1968) 13.
11. J. Blomqvist, B. Fant, K. Wikström, and I. Bergström, Phys. Scripta 3, 9 (1971).
12. G. L. Struble, private communication (Sept. 1971).
13. F. S. Goulding, UCRL-17559 (1967).
14. F. S. Goulding, D. A. Landis, and R. H. Pehl, UCRL-17560 (1967).
15. L. B. Robinson, F. Gin, and F. S. Goulding, UCRL-17419 (1967).
16. L. B. Robinson and J. D. Meng, UCRL-17220 (1967).
17. J. O. Radeloff, L. B. Robinson, and J. D. Meng, UCRL-18883 (1969).
18. F. M. Bernthal, UCRL-18651, Ph.D. Thesis (1969) unpublished.
19. L. J. Jardine, UCRL-20476 (1971).

20. L. J. Jardine, Nucl. Instr. Methods 96, 259 (1971).

21. J. M. Jaklevic, F. M. Bernthal, J. D. Radeloff, and D. A. Landis, Nucl. Instr. Methods 69, 109 (1969).

22. C. M. Lederer, J. M. Hollander, and I. Perlman, Table of Isotopes, Wiley (1967).

23. I. Bergström, B. Fant, A. Filevich, G. Lindén, K. G. Rensfelt, J. Sztarkier, and K. Wikström, Research Institute for Physics, Annual Report, Stockholm (1970) 96.

24. J. W. Mihelich, A. W. Schardt, and E. Segre', Phys. Rev. 95, 1508 (1954).

25. R. W. Hoff and J. M. Hollander, Phys. Rev. 109, 447 (1958).

26. F. Schima, E. G. Funk, Jr., and J. W. Mihelich, Phys. Rev. 132, 2650 (1963).

27. S. G. Prussin and J. M. Hollander, Nucl. Phys. A110, 176 (1968).

28. R. Tickle and J. Bardwick, Phys. Letters 36B, 32 (1971).

29. W. F. Lanford, U. of Rochester, private communication (March 1971, Sept. 1971).

30. I. Bergström, J. Blomqvist, B. Fant, and K. Wikström, Research Institute for Physics, Annual Report, Stockholm (1970) 80.

31. N. Newby, Jr. and E. J. Konopinski, Phys. Rev. 115, 434 (1959).

32. Y. E. Kim and J. O. Rasmussen, Nucl. Phys. 47, 184 (1963); Nucl. Phys. 61, 173 (1965).

33. C. W. Ma and W. W. True, private communication (Sept. 1971).

34. R. Hoff, UCRL-2325, Ph.D. Thesis (1953) unpublished.

35. N. A. Golovkov, Sh. Guetkh, B. S. Dzhelepov, Y. V. Norsev, V. A. Khalkin, and V. G. Chumin, Bulletin of the Academy of Sciences of the USSR 33, 1489 (1969).

36. A. W. Stoner, UCRL-3471, Ph.D. Thesis (1956) unpublished.

37. I. Bergström, B. Fant, and K. Wikström, Research Institute for Physics, Annual Report, Stockholm (1970) 78.

38. E. H. Appleman, UCRL-9025, Ph.D. Thesis (1960) unpublished.

39. E. H. Appleman, National Academy of Sciences, National Research Council Report #NAS-NS 3012 (1960).

40. J. R. Routti and S. G. Prussin, Nucl. Instr. Methods 72, 125 (1969).

41. J. R. Routti, UCRL-19452 (1969).

42. R. S. Hager and E. C. Seltzer, Nucl. Data A4, 1 (1968).

43. C. M. Lederer, UCRL-19980 (1971).

44. E. G. Funk, Jr., H. J. Prask, F. Schima, J. McNulty, and J. W. Mihelich, Phys. Rev. 129, 757 (1963).

45. T. Yamazaki and G. T. Ewan, Phys. Letters 24B, 278 (1967).

46. T. Yamazaki, Phys. Rev. C1, 290 (1970).

47. M. Ishihara, Y. Gono, K. Ishii, M. Sakai, and T. Yamazaki, Phys. Rev. Letters 21, 1814 (1968).

48. R. Tickle, private communication (Sept. 1971).

49. M. H. L. Pryce, Proc. of Phys. Society 65, 51 (1952).

50. D. E. Alburger and M. H. L. Pryce, Phys. Rev. 95, 1482 (1954).

51. J. Solf, W. R. Hering, J. P. Wurm, and E. Gross, Phys. Letters 28B, 413 (1969).

52. O. Hansen, O. Nathan, R. Chapman, and S. Hinds, Nucl. Phys. 127, 71 (1969).

53. M. B. Lewis, Nucl. Data Sheets B5 (1971).

54. E. Ellegaard, P. D. Barnes, E. R. Flynn, and C. J. Igo, Nucl. Phys. A162, 1 (1971).

55. I. Hamamoto, Nucl. Phys. A155, 362 (1970).

56. I. Hamamoto, private communication (May 1971).

57. B. R. Mottelson, Proc. Int. Conf. on Nuclear Structure, J. Sanada, ed., Tokyo (1967).

58. S. A. Moszkowski, Phys. Rev. 82, 35 (1951).

59. E. J. Konopinski and M. E. Rose, Alpha-, Beta-, and Gamma-Ray Spectroscopy, Vol. 2, K. Siegbahn, ed. (North-Holland, Amsterdam) (1965) 1357.

60. A. H. Wapstra and N. B. Gove (June 1970), Concepts of Nuclear Physics by B. L. Cohen (McGraw-Hill, New York) (1971), 418.

61. W. W. True, C. W. Ma, and W. T. Pinkston, Phys. Rev. C3, 2421 (1971).

62. E. A. McClatchie, C. Glashausser, and E. L. Hendrie, Phys. Rev. C1, 1828 (1970).

63. J. Bardwick and R. Tickle, Phys. Rev. 161, 1217 (1967).

64. J. Damgaard and A. Winther, Nucl. Phys. 54, 615 (1964).

65. J. Damgaard, R. Broglia, and C. Riedel, Nucl. Phys. A135, 310 (1969).

66. P. Bondorf, P. von Brentano, and P. Richard, Phys. Letters 27B, 5 (1968).

67. G. Astner, I. Bergström, J. Blomqvist, B. Fant, K. Wikström, Research Institute for Physics, Annual Report, Stockholm (1970) 69.

68. K. H. Maier, K. Nakai, J. R. Leigh, R. M. Diamond, and F. S. Stephens, UCRL-19593 (1970).

69. V. S. Shirley, Hyperfine Structure and Nuclear Radiations, E. Matthias and D. A. Shirley, eds. (North-Holland, Amsterdam) (1967) 905.

70. R. A. Meyer, private communication (Sept. 1971).

71. G. H. Fuller and V. W. Cohen, Nucl. Data Tables A5, 433 (1969).

72. K. L. Vander Sluis and P. M. Griffin, J. Opt. Soc. Am. 45, 1087 (1955).

73. G. W. Barton, A. Ghiorso, and I. Perlman, Phys. Rev. 82, 13 (1951).

74. T. Yamazaki and E. Matthias, Phys. Rev. 175, 1476 (1968).

75. M. Alpsten, A. Appleqvist, and G. Astner, Research Institute for Physics, Annual Report, Stockholm (1969) 53.

76. M. Alpsten and G. Astner, Research Institute for Physics, Annual Report, Stockholm (1969) 86.

77. I. Bergström, B. Fant, C. J. Herrlander, K. Wikström, and P. Thieberger, Research Institute for Physics, Annual Report, Stockholm (1969) 49.

78. W. J. Ramler, J. Wing, D. J. Henderson, and J. R. Huizenga, Phys. Rev. 114, 154 (1959).

79. E. L. Kelly and E. Segre', Phys. Rev. 75, 999 (1949).

80. W. A. Aron, B. G. Hoffman, and F. C. Williams, UCRL-121 (1960).

81. W. J. Treytl, E. K. Hyde, and T. Yamazaki, Nucl. Phys. A117, 481 (1968).

82. S. A. Sliv and I. M. Band, Coefficients of Internal Conversion of Gamma-Radiation (Academy of Sciences of the USSR, Moscow-Leningrad, Part 1 K-shell (1956).

83. W. Baldridge, N. Freed, and J. Gibbons, Phys. Letters 36B, 179 (1971).

84. N. Freed and W. Rhodes, Nucl. Phys. A126, 481 (1969); N. Freed and J. Gibbons, Nucl. Phys. A136, 423 (1969).

85. T. S. Bhatia, T. R. Canada, C. Ellegaard, J. Miller, E. Romberg, and P. D. Barnes, Bull. Am. Phys. Soc. 16, 1147 (1971).

86. T. R. Canada, private communication (Nov. 1971).

APPENDIX A

GAMMA-RAY TRANSITION PROBABILITIES

The transition probability for gamma-ray transitions within a nucleus has been formulated by several authors[1,2,3,4]. We shall outline the methods for calculation of M1 and E2 transition rates for the one and two proton models after a general formalism. E1, M2, and E3 transition rates will not be considered. The transition probability $T(E(t)LM;\ J_i \rightarrow J_f)$ (in units of $[\text{sec}]^{-1}$) for the emission of a given gamma radiation of multipole type E(t) (e.g. M1 or E2) carrying off orbital angular momentum L (with projection M) for a nucleus going from some initial excited state $\vec{J}_i$ to some final state $\vec{J}_f$ is given by

$$T(E(t)LM;\ J_i \rightarrow J_f) = \frac{8\pi(L+1)}{L[(2L+1)!!]^2}\ \frac{1}{\hbar}\left(\frac{E_\gamma(\text{MeV})}{197.3}\right)^{2L+1} B(E(t)LM;\ J_i \rightarrow J_f) \tag{1}$$

where $B(E(T)LM;\ J_i \rightarrow J_f)$, the <u>reduced</u> transition probability, is defined by

$$B(E(t)LM;\ J_i \rightarrow J_f) = \sum_{MM_f} |\ \langle J_f M_f | \hat{O}^L_M(E(t)) | J_i M_i \rangle\ |^2 \tag{2}$$

The Wigner-Eckart theorem[3] can be applied to eq. (2) to remove the M dependence. Using the (double-bar) reduced matrix element as defined in ref. [3], eq. (2) can be rewritten as the square of a reduced matrix element.

$$B(E(t)L;\ J_i \to J_f) = \sum_{MM_f} \begin{bmatrix} J_i & L & J_f \\ M_i & M & M_f \end{bmatrix}^2 \left| \langle J_f \| \hat{O}^L(E(t)) \| J_i \rangle \right|^2$$

$$= \frac{1}{2J_i + 1} \left| \langle J_f \| \hat{O}^L(E(t) \| J_i \rangle \right|^2 \qquad (3)$$

The multipole operator $\hat{O}^L_M(E(t))$ in eq. (3) has different forms for electric and magnetic transitions. It is assumed that it can be written as a sum of single particle operators involving the coordinates of each nucleon p, i.e.,

$$\hat{O}^L_M(E(t)) = \sum_p \hat{O}^L_M(E(t),p) \qquad (4)$$

summed over all p particles involved in the transition. The <u>magnetic</u> multipole operators $\hat{O}^L_M(Ml)$ have the general form[1])

$$\hat{O}^L_M(ML) = \frac{e\hbar}{2m_p c} \sum_p \left[g_s(p)\vec{s}_p + \frac{2g_\ell(p)}{L+1}\vec{\ell}_p \right] \cdot \vec{\nabla}\, r_p^L\, Y^L_M(\Omega_p)$$

$$= \frac{e\hbar}{2m_p c} \sum_p \left[\left(g_s(p) - \frac{2g_\ell(p)}{L+1} \right) \vec{s}_p + \frac{2g_\ell(p)}{L+1}\vec{J}_p \right] \cdot \vec{\nabla}\, r_p^L\, Y^L_M(\Omega_p) \qquad (5)$$

where $Y^L_M(\Omega_p)$ are spherical harmonics and r_p is the radial coordinate of the particle p which is assumed to have the orbital angular momentum $\vec{\ell}_p$ and spin $\vec{s}_p$ coupled to a total angular momentum $\vec{J}_p$. The factors g_ℓ and g_s are the g factors for the free-proton (or neutron). The second form

of eq. (5) was obtained from the relation $\vec{\ell}_p = \vec{J}_p - \vec{s}_p$. The M1 operators are rather complicated functions with different forms for the various M components. As an example the magnetic dipole operator has the form for the M = 0 component[2])

$$\hat{O}^1_0(M1) = \sqrt{3/4\pi}\ \frac{e\hbar}{2m_p c} \sum_p g_s(p)\ s_z + g_\ell(p)\ \ell_z \qquad (6)$$

However, to calculate the gamma-ray transition probabilities, reduced matrix elements of these operators are needed and the explicit forms for all components will not be considered further. The reduced matrix elements for the M1 and E2 operators will be defined later. (See eq. (10), eq. (11), eq. (23), Eq. (25), and eq. (26).)

The electric multipole operator has the form

$$\hat{O}^L_M(EL) = \sum_p e\ r_p^L\ Y^L_M(\Omega_p) \quad . \qquad (7)$$

The operator for E2 transitions has the form for the M components.

$$\hat{O}^2_M(E2) = \sum_p e\ r_p^2\ Y^2_M(\Omega_p) \qquad (8)$$

Having given the forms for the multipole operators, the transition probabilities of eq. (1) (in units of $[\text{sec}]^{-1}$) can be rewritten in terms of the evaluated constants, the transition energy E_γ, and reduced transition probabilities as[1])

$$T(E1) = 1.59 \cdot 10^{15} \cdot E_\gamma^3 \cdot B(E1)$$

$$T(E2) = 1.22 \cdot 10^{9} \cdot E_\gamma^5 \cdot B(E2)$$

$$T(E3) = 5.67 \cdot 10^{2} \cdot E_\gamma^7 \cdot B(E3)$$

$$T(E4) = 1.69 \cdot 10^{-4} \cdot E_\gamma^9 \cdot B(E4)$$

(9)

$$T(M1) = 1.76 \cdot 10^{13} \cdot E_\gamma^3 \cdot B(M1)$$

$$T(M2) = 1.35 \cdot 10^{7} \cdot E_\gamma^5 \cdot B(M2)$$

$$T(M3) = 6.28 \cdot 10^{0} \cdot E_\gamma^7 \cdot B(M3)$$

$$T(M4) = 1.87 \cdot 10^{-6} \cdot E_\gamma^9 \cdot B(M4)$$

The units of the quantities in eq. (9) are E_γ in (MeV), B(EL) in e^2 $[fm]^{2L}$, and B(ML) in $\left(\frac{e\hbar}{2m_p c}\right)^2$ $[fm]^{2(L-1)}$.

I. SINGLE-PARTICLE MODEL

This model applies to an odd A nucleus in which the odd nucleon is assumed to undergo the transition from a state of initial angular momentum $\vec{J}_i$ to a final state $\vec{J}_f$ as the nucleus emits a gamma-ray. In this model the angular momentum of the nucleus $\vec{J}$ is assumed to be the same as the angular momentum of the nucleon undergoing the transition. If the initial and final states of the nucleus involved in the transition are pure single-particle states, the expressions for the reduced transition

probabilities can be simplified to terms involving a Clebsch-Gordon coefficient and a matrix element of radial wavefunctions. For the special case of $\vec{J}_f = \vec{J}_i + \vec{L}$, the magnetic reduced transition probability of eq. (3) takes the form[1,3])

$$B_{s.p.}(ML;\ J_i \to J_f = L + J_i) = \left(\frac{e\hbar}{2m_p c}\right)^2 \left(g_s - \frac{2}{L+1} g_\ell\right)^2 L^2 \frac{(2L+1)}{4\pi}$$

$$\begin{bmatrix} J_i & L & J_f \\ \frac{1}{2} & 0 & \frac{1}{2} \end{bmatrix}^2 |\langle J_f | r^{L-1} | J_i \rangle|^2 \quad [\mathrm{fm}]^{2(L-1)} \qquad (10)$$

with the selection rule $\vec{\ell}_f = \vec{\ell}_i + \vec{L} - 1$. The Clebsch-Gordon coefficient $\begin{bmatrix} J_i & L & J_f \\ \frac{1}{2} & 0 & \frac{1}{2} \end{bmatrix}$ in eq. (10) has the phase convention of ref. [3]).

If the more general restriction $|\vec{J}_f - \vec{J}_i| \leq L$ for magnetic transitions is allowed, a more complex expression (but of the same form as eq. (10) results with the additional selection rule[3])) that $\vec{\ell}_i - \vec{\ell}_f + \vec{L} - 1$ must be even. The detailed expression of the reduced transition probability for this case is given in ref. [1]) and ref. [3]) (in full half-page glory!). The reduced transition probabiltiy for single-particle electric multipole transitions is

$$B_{s.p.}(EL;\ J_i \to J_f) = \frac{e^2}{4\pi} (2L+1) \begin{bmatrix} J_i & L & J_f \\ \frac{1}{2} & 0 & \frac{1}{2} \end{bmatrix}^2 |\langle J_f | r^L | J_i \rangle|^2 \quad [\mathrm{fm}]^{2L} \qquad (11)$$

with the selection rule that $\vec{\ell}_i + \vec{L} - \vec{\ell}_f$ must be even[3]).

The transition probabilities of eq. (9) may be calculated in terms of eq. (10) and eq. (11) once the radial matrix elements

$\langle J_f|r^L|J_i\rangle$ have been determined. The radial wavefunctions needed to compute the matrix elements may be obtained from various potentials. It should be noted that the calculations of the M1 transition rates is trivial as the matrix elements are unity. A partial list of computed matrix elements near closed shells is given in ref. [1]) for a Woods-Saxon potential. These allow evaluation of matrix elements for most E2 transitions. Hence M1 and E2 transitions probabilities for odd A nuclei may be calculated relatively simply within the framework of the single-particle model.

In order to standardize the comparison of transition rates for different nuclei, the Weisskopf single-particle estimates are often employed. These estimates involve some further approximations[2,4]) of eq. (10) and eq. (11) which remove the model dependence for the calculation of radial matrix elements. There are four additional basic assumptions made over the previous formalism. The radial wave function for both the initial and final states is assumed constant throughout the nucleus (for $r < R$) and to vanish outside (for $r > R$). This leads to the two approximations

$$\langle J_f|r^L|J_i\rangle = \frac{3R}{L+3} \qquad (12)$$

where the nuclear radius is taken as

$$R = 1.2\ A^{1/3}\ \text{[fm]} \quad . \qquad (13)$$

Third, the transition is assumed to go from an initial state $\vec{J}_i = \vec{L} + 1/2$

to a final $(1s_{1/2})$ state with $\vec{J}_f = 1/2$. This fixes the Clebsch-Gordon coefficients as unity. Finally for ML transitions the following approximation is made

$$L^2 \left(g_s - \frac{2g_\ell}{L+1} \right) = 10 \qquad (14)$$

These four approximations give the Weisskopf estimates[4]) for the reduced transition probabilities. Replacing the appropriate quantities in eq. (10) and eq. (11) we obtain

$$B_W(ML) = \frac{10}{\pi} (1.2)^{2(L-1)} A^{2(L-1)/3} \left(\frac{e\hbar}{2m_p c} \right)^2 [fm]^{2(L-1)} \qquad (15)$$

$$B_W(EL) = \frac{(1.2)^{2L}}{4\pi} \left(\frac{3}{L+3} \right)^3 A^{2L/3} e^2 [fm]^{2L}$$

The units of eq. (15) are referred to as Weisskopf units.

II. TWO-PROTON MODEL

This model calculates for even-even nuclei the gamma-ray transition probabilities between states which are composed of mixed configurations of two identical nucleons. Consider a pure state formed from two protons of angular momenta $\vec{j}_1 \equiv a$ and $\vec{j}_2 \equiv b$ coupled together to the angular momenta $\vec{J}$ (i.e. $\vec{a} + \vec{b} = \vec{J}$). The two-particle wavefunction $\psi \equiv |\alpha(ab)JM)$ for such a state must be properly antisymmetrized which is denoted by the curved ket $|\quad)$. Explicitly the pure two-particle wavefunction can be written as[3])

$$|\alpha ab;JM) = N_{ab}[\,|\alpha a(1)b(2);JM\rangle - (-)^{a+b-J}|\alpha b(1)a(2);JM\rangle\,] \qquad (16)$$

where the normalization factor is

$$N_{ab} = \frac{1}{\sqrt{2(1 + \delta_{ab})}} \tag{17}$$

We have used in eq. (16) the notation a(1) to represent the particle of angular momentum j_1 located at the radial position r_1. Any additional quantum numbers needed to specify the states are represented by α. Since states of the same J^π can configuration mix, the actual wavefunction of a state will be a linear combination of two-particle states of the same $(ab)J^\pi$. The wavefunction for an initial state (with $C_{ab}(\alpha_i)$ representing the amplitudes of various two-particle components) can be written in terms of two-particle antisymmetrized components as

$$|\alpha J_i M_i) = \sum_{(ab)} C_{ab}(\alpha_i) |\alpha ab;\ J_i M_i) \tag{18}$$

where the summation is only over allowed two-particle configurations <u>not</u> prohibited by the Pauli principle.

Consider the gamma transition between an initial state $|\alpha J_i M_i)$ and a final state $|\alpha' J_f M_f)$. Only angular momentum (coordinates or) quantum numbers can change in the emission of a gamma-ray. Two nucleons in the initial state with the spatial coordinates a(1) and b(2) will have the same spatial coordinates in the final state but may have different values of angular momenta c(1) and d(2). This allows single-particle transitions of the type a(1) → c(1) and/or b(2) → d(2). The reduced

matrix element of eq. (3) can be computed using the form of eq. (18) for the wavefunction of the initial and final states.

$$B(E(t)L;\ J_i \to J_f) = \frac{1}{2J_i + 1} \left| \sum_{(abcd)} C_{ab}(\alpha_i)\ C_{cd}(\alpha_f')(\alpha_f' J_f \| \hat{0}^L(E(t)) \| \alpha_i J_i) \right|^2$$

$$= \frac{1}{2J_i + 1} \left[\sum_{(abcd)} C_{ab}(\alpha_i)\ C_{cd}(\alpha_f')\ N_{ab} N_{cd} \left[\langle \alpha_f'\ c(1)d(2);\ J_f \| \hat{0}^L \| \alpha_i\ a(1)b(2);\ J_i \rangle \right.\right.$$

$$-(-)^{a+b-J_i} \langle \alpha_f'\ c(1)d(2);\ J_f \| \hat{0}^L \| \alpha_i\ b(1)a(2);\ J_i \rangle$$

$$-(-)^{c+d-J_f} \langle \alpha_f'\ d(1)c(2);\ J_f \| \hat{0}^L \| \alpha_i\ a(1)b(2);\ J_i \rangle$$

$$\left.\left. +(-)^{a+b-J_i+c+d-J_f} \langle \alpha_f'\ d(1)c(2);\ J_f \| \hat{0}^L \| \alpha_i\ b(1)a(2);\ J_i \rangle \right] \right]^2 \qquad (19)$$

Equation (19) can be simplified by recoupling the angular momenta of the two particles. The two-particle bra and ket vectors of the fourth term when recoupled have the following relationships:

$$|\alpha_f'\ d(1)c(2);\ J_f M_f\rangle = (-)^{d+c-J_f} |\alpha_f'\ c(2)d(1);\ J_f M_f\rangle$$

$$|\alpha_i\ b(1)a(2);\ J_i M_i\rangle = (-)^{b+a-J_i} |\alpha_i\ a(2)b(1);\ J_i M_i\rangle \qquad (20)$$

Replacing these forms in the vectors of the fourth term shows that the first term and fourth term are identical (because the double intergrations involved in the matrix elements are over dummy parameters

(i.e. $\vec{dr}_1\ \vec{dr}_2 = \vec{dr}_2\ \vec{dr}_1 = \vec{dx}_1\ \vec{dx}_2$ ...) and the phase factor vanishes). Hence the first and fourth terms maybe combined into a single term equal to twice the first. The same method may be used to combine the second and third terms. The result is that eq. (19) can be rewritten as the first two terms with an additional factor of two.

$$B(E(t)L;\ J_i \to J_f) = \frac{1}{2J_i + 1}\left[\sum_{\substack{(ab)\\(cd)}} C_{ab}(\alpha_i)\ C_{cd}(\alpha_f')2N_{ab}N_{cd}\right.$$

$$[\langle \alpha_f' c(1)d(2);\ J_f \| \hat{O}^L \| \alpha_i a(1)b(2);\ J_i \rangle$$

$$\left. -(-)^{a+b-J_i} \langle \alpha_f' c(1)d(2);\ J_f \| \hat{O}^L \| \alpha_i b(1)a(2);\ J_i \rangle\ ]\right]^2 \tag{21}$$

To evaluate the reduced two-particle matrix elements of eq. (21), we use the fact that $\hat{O}^L$ is a sum of (two) operators each involving only the spatial coordinates of r_1 (or (1)) and r_2 (or (2)). This allows eq. (21) to be rewritten in terms of two single-particle reduced matrix elements. We use the assumption that the <u>spatial</u> coordinates of a(1) and c(1) are the same but different than those of b(2) and d(2) (i.e. the allowed transitions are a(1) → c(1) and/or b(2) → d(2)). Consider only the first term of eq. (21). The two-particle reduced matrix element may be rewritten in terms of two single-particle reduced matrix elements[3,5]).

$$\langle \alpha_f' c(1)d(2);\ J_f \| \hat{O}^L(1) + \hat{O}^L(2) \| \alpha_i a(1)b(2);\ J_i \rangle$$

$$= \delta_{db}\ (-)^{a-c+J_f-J_i} \sqrt{(2J_f+1)(2J_i+1)}\ W(baJ_fL;\ J_ic)\ \langle \alpha_f' c(1) \| \hat{O}^L(1) \| \alpha_i a(1) \rangle$$

$$+ \delta_{ca} \sqrt{(2J_f+1)(2J_i+1)}\ W(abJ_fL;\ J_id)\ \langle \beta_f' d(2) \| \hat{O}^L(2) \| \beta_i b(2) \rangle \qquad (22)$$

The second term of eq. (21) may be evaluated by simply replacing a(1) with b(1) and b(2) with a(2) in eq. (22). We note that the form of eq. (22) requires that only <u>one</u> particle contribute to the transition. As an example, consider the transition $a(1) \to b(1)$ which is represented by the first term of eq. (22). The delta function δ_{db} requires that $b(2) = d(2)$, but if $a(1) \to b(1) \neq a(1)$ the 2nd term vanishes. This is why only one particle can be involved in the gamma-ray transition. All quantities necessary to evaluate eq. (21) have been defined in this model except for the single-particle reduced matrix elements of the multipole operators in eq. (22). The single-particle matrix elements have been defined in a paper by True and Ford[6]) for M1 and E2 transitions. Reduced matrix elements of the M1 operators are generally divided into two groups which are either diagonal or nondiagonal in the single-particle angular momentum. Explicitly, the diagonal <u>M1</u> single-particle reduced matrix elements are given by[5,6])

$$\langle (n_c \ell_c 1/2)c \| \hat{O}^1_M(M1) \| (n_a \ell_a 1/2)a \rangle = \frac{3}{4\pi} \sqrt{a(a+1)(2a+1)}\ g_a\ \frac{e\hbar}{2m_pc}\ \delta_{ac} \qquad (23)$$

where g_a is the g factor for the state $(\ell_a 1/2)j_a$. The value of g_a can be obtained from the relation for the magnetic moment $\vec{\mu}$ and the total angular momentum $\vec{j}_a$

$$g_{j_a} \equiv g_a = \frac{|\vec{\mu}|}{|\vec{j}_a|} \tag{24}$$

For calculations g_a is obtained from eq. (24) with the experimental value of the magnetic moment (in units of nucleon magnetons) which has been measured for many single-particles states. However, the Schmidt values are used if the appropriate moment has not been measured.

The off-diagonal M1 single-particle reduced matrix elements have the form[5,6]

$$\langle (n_c \ell_c 1/2)c \| \hat{O}^1_M(M1) \| (n_a \ell_a 1/2)a \rangle = (-)^{c-\ell_c-1/2} (g_\ell - g_s) \sqrt{\frac{3}{4\pi}} \frac{2\ell_c(\ell_c+1)}{2\ell_c+1} \frac{e\hbar}{2m_p c}$$

$$\delta_{\ell_c \ell_a} \delta_{n_a n_c} (1 - \delta_{ac}) \tag{25}$$

with the additional selection rule $|\vec{j}_a - \vec{j}_c| \leq 1$. The single-particle reduced matrix elements for the E2 operator are given in terms of a Clebsch-Gordon coefficient and radial matrix in a form similar to eq. (11)[5,6]

$$\langle (n_c \ell_c 1/2)c \| \hat{O}^2_M(E2) \| (n_a \ell_a 1/2)a \rangle = e \sqrt{(2c+1)\frac{5}{4\pi}} \begin{bmatrix} c & 2 & a \\ \frac{1}{2} & 0 & \frac{1}{2} \end{bmatrix}$$

$$|\langle c|r^2|a\rangle|^2 \frac{1}{2}[1 + (-)^{\ell_a+\ell_c}] \tag{26}$$

with the additional selection rule $|\vec{j}_a - \vec{j}_c| \leqslant 2$. All values necessary to evaluate the transition probability of eq. (1) or eq. (9) for M1 and E2 transitions have been defined within this two proton model. The modification of this treatment necessary for the odd-odd nuclei is straight forward.

REFERENCES

1. A. Bohr and B. Mottelson, Nuclear Structure, Vol. 1, W. A. Benjamin (1969) 380.

2. S. A. Moszkowski, Alpha-Beta, and Gamma-Ray Spectroscopy, ed. K. Siegbahn, Vol. 2 (1965) 863.

3. A. de Shalit and I. Talmi, Nuclear Shell Theory, Academic Press (1963) 158.

4. J. M. Blatt and V. F. Weisskopf, Theoretical Nuclear Physics, John Wiley and Sons, New York (1952).

5. G. L. Struble, private communication (Sept. 1971).

6. W. W. True and K. W. Ford, Phys. Rev. 109, 1675 (1958).

APPENDIX B

THEORETICAL LOG FT CALCULATIONS - ELECTRON-CAPTURE

I. INTRODUCTION

For β^-, β^+, or EC decay the nomogram method of Moszkowski[1]) or Verrall et al.[2]) is generally used for rapid calculations of log ft values once the experimental partial half-lives $(t_{1/2})^{part.}_{expt.}$ for the levels populated in the decay have been determined. These nomograms are also reproduced in an expanded version in the Table of Isotopes[3]). However, when the decay energy Q_d is less than about 300 keV (for $Z \sim 85$), the nomogram method fails to give the correct values of log ft due to the neglect of the electron binding energy BE(X) (of the daughter nucleus) in the expressions used in the original calculations for f. It has been noted[5]) that log ft values obtained from the nomograms for first-forbidden nonunique transitions ($\Delta^{\pm}J$ = 0, 1 yes) often show deviations of 30% from those calculated theoretically for β^+ decay (which were then corrected with the K/β^+ ratio to obtain the value of f for electron-capture). Presented below are a series of formulas which take into account the electron binding energy corrections. These formulas were used for calculation of the log ft values in this work. This method gives the same results (for Z = 85) as the nomogram method for $Q_d \geq 400$ keV and log ft values 0.1-0.8 units lower for $BE(K) < Q_d \leq 400$ keV.

II. METHOD

Reproduced here are two equations from volume 2 of Siegbahn[4]) (chapter 2) which allow the user to get from his text to the actual case

of doing a calculation. The formulation was written by Konopinski and Rose[4]) and the interested reader should consult the original article for details. From the text[4]) we have the following equations:

$$ft \equiv f \frac{\ell n\ 2}{\lambda^{\pm}} = f(t_{1/2})^{part.}_{expt.} = \ell n\ 2\ \frac{2\pi^3}{g^2}\ \xi^{-1} \qquad (1)\ \text{(p. 1341 eq. (21))}$$

and

$$\lambda_K = \left(\frac{g^2 q^2}{4\pi^2}\right) g_K^2(R)\ S_{0,1} \qquad (2)\ \text{(p. 1359 eq. (77A))}$$

The total allowed decay rate by <u>all</u> allowed modes (e.g. K, L, M, ... capture) is defined as $\lambda^{\pm}$, g^2 is the coupling constant, and $g_K(R)$ is the large radial wavefunction for the electron evaluated at the nuclear radius. The K-electron capture rate is given by λ_K and cq is the energy available for the neutrino.

$$cq = W_0 + mc^2 - BE(X) \qquad (3)$$

where the decay energy Q_d is defined as

$$Q_d = cq + BE(X) \equiv W_0 + mc^2 \qquad (4)$$

The units $c = \hbar = m = 1$ are used which implies

$$q = Q_d - BE(X) \qquad (5)$$

where the units of energy are in terms of electron rest mass (MeV).

We now assume that the approximation $S_0 \cong \xi$ for allowed transitions ($\Delta I = 0, 1$ no) holds for 1st-forbidden electron-capture decays (i.e. $S_{0,1} \cong \xi$). Substituting our approximation $S_{0,1} = \xi$, we can combine eqs. (1) and (2)

$$ft = \frac{\ell n\ 2\ 2\pi^3}{g^2\ \xi} = \frac{\ell n\ 2}{\lambda_K}\ \frac{\pi}{2}\ g_K^2(R)\ q^2 = t_{1/2}(K)\ \frac{\pi}{2}\ g_K^2(R)\ q^2 \qquad (6)$$

All three values in eq. (6) may be obtained with reference to fig. 1 and the following methods:

(a) $g_K(R)$ This is a dimensionless quantity obtained from fig. 1a for the Z (parent) of interest.

(b) q This can be evaluated from eq. (5) where the decay energy Q_d is obtained from the (Q-value) energy available for electron-capture decay Q_{EC} and the energy of the level $E_{\ell ev}$ to which the decay proceeds in the daughter (units of electron mass):

$$Q_d = Q_{EC} - E_{\ell ev} \qquad (7)$$

(c) $t_{1/2}(K)$ This is the <u>partial half-life</u> if all decay went by K-capture. This quantity is obtainable from the experimentally determined partial half-life $(t_{1/2})^{part.}_{expt.}$ thru use of fig. 1b and the ratio of total electron-capture EC (total) to K-electron capture EC(K) as follows:

$$t_{1/2}(K) = (t_{1/2})^{part.}_{expt.}\ \frac{EC(total)}{EC(K)} \qquad (8)$$

where the total to K-capture rate is defined as

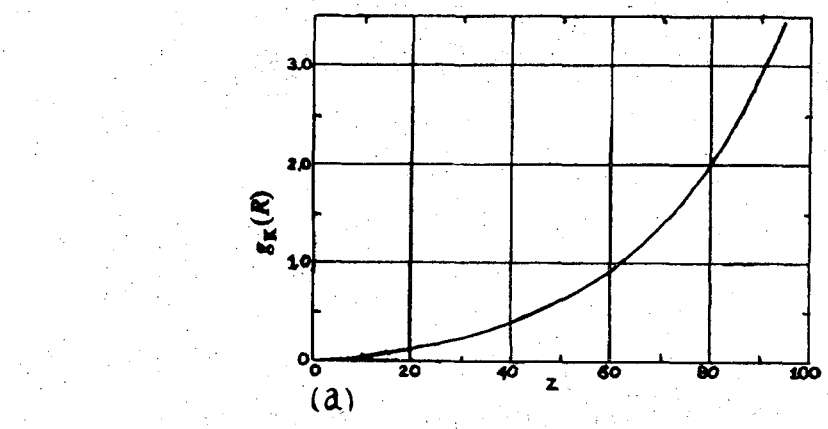

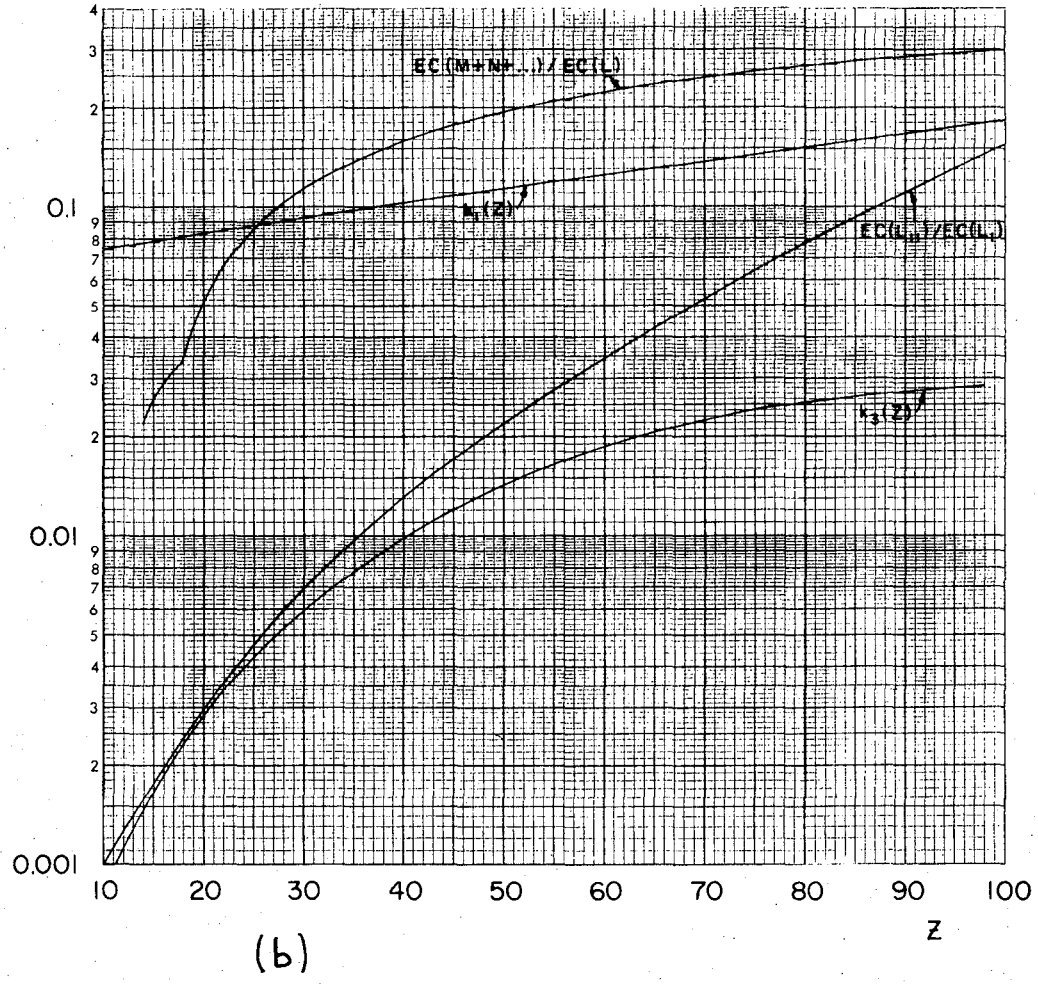

XBL 719-1475

Fig. 1. (a) Large radial wavefunction $g_K(R)$ for the 1s-electrons evaluated at the radius R [1]).

(b) Subshell ratios for electron capture[3]).

$$\frac{EC(\text{total})}{EC(K)} = \frac{EC(K) + EC(L_1 + L_{11} + L_{111}) + EC(M + N + \cdots)}{EC(K)} \qquad (9)$$

Using the approximation $EC(L_{111}) \cong 0$ (which is valid for allowed and approximately valid for first-forbidden nonunique transitions[3,5])), eq. (9) reduces to

$$\frac{EC(\text{total})}{EC(K)} \cong 1 + \left(\frac{EC(L_1)}{EC(K)}\right) \left(1 + \frac{EC(L_{11})}{EC(L_1)}\right) \left(1 + \frac{EC(M + N + \cdots)}{EC(L)}\right) \qquad (10)$$

For allowed and first-forbidden nonunique transitions[3])

$$\frac{EC(L_1)}{EC(K)} = k_1(Z) \left(\frac{Q_d - BE(L_1)}{Q_d - BE(K)}\right)^2 \qquad (11)$$

where $k_1(Z)$ is given by fig. 1b. The values for $\frac{EC(L_{11})}{EC(L_1)}$ and $\frac{EC(M + N + \cdots)}{EC(L)}$ may be read directly from fig. 1b also. Finally rewriting eq. (6) in terms of eqs. (5), (8), (10), and (11) we arrive at the final expression used in our log ft calculations

$$ft = (t_{1/2})^{\text{part.}}_{\text{expt.}} \left[1 + k_1(Z) \left[\frac{Q_d - BE(L_1)}{Q_d - BE(K)}\right]^2 \left[1 + \frac{EC(L_{11})}{EC(L_1)}\right] \left[1 + \frac{EC(M + N + \cdots)}{EC(L)}\right]\right]$$

$$\frac{\pi}{2} g_K^2(R)(Q_d - BE(K))^2 \qquad (12)$$

In summary, eq. (12) allows the calculation of log ft values for allowed or first-forbidden decays thru use of fig. 1 and eq. (7) once the

decay energy is known. (The binding energies of the electrons and the K/β^+ ratios are tabulated in ref. [3].)

REFERENCES

1. S. A. Moszkowski, Phys. Rev. 82, 35 (1951).

2. R. I. Verrall, J. C. Hardy, and R. E. Bell, Nucl. Instr. Methods 42, 258 (1966).

3. C. M. Lederer, J. M. Hollander, and I. Perlman, Table of Isotopes, Wiley, New York (1967) p. 576.

4. E. J. Konopinski and M. E. Rose, Alpha-, Beta-, and Gamma-Ray Spectroscopy, Vol. 2, ed. K. Siegbahn, North-Holland, Amsterdam (1965) p. 1327.

5. A. H. Wapstra, G. J. Nijgh, R. van LieShout, Nuclear Spectroscopy Tables, North-Holland, Amsterdam (1959) 60.

APPENDIX C

DATA ACQUISITION SYSTEM

ABSTRACT

The electronic systems used for β and γ-ray spectroscopy are described in the form of a user's manual. The assembly and testing of singles and coincidence logic circuits utilizing a PDP-7 computer is discussed.

I. INTRODUCTION

It is the purpose of this note to outline the types, and the use, of electronics and other hardware used in our laboratory at LBL in spectroscopy experiments in conjunction with a PDP-7 computer data acquisition system shown in fig. 1. This is intended to help ease the minds of future graduate students faster after their first introduction to the system and also serve as a guide in setting up the systems initially. The text is in the form of a user's manual, and if details are desired, one is referred to the available technical references[1,2,3,4,5] on which it is based. Singles and coincidence electronics and methods are discussed. The PDP-7 system has been well documented[4,5,6] and no attempt is made here to expand on it.

II. GAMMA-RAY "SINGLES"

The electronics used with the PDP-7 computer system to collect experimental data is discussed with reference to fig. 2.

A. Linear Amplifier (LRL model #11 × 5501-P1)

The amplifier[1]) will accept by switch control either positive or negative preamp pulses and it contains a pole-zero preamp compensation adjust screw. One sets the pole-zero compensation by bringing the output pulse overshoots or undershoots to the baseline with a scope set on a high gain. The final adjustment is best made with a long-time constant on the oscilloscope. The unit has two outputs (1) slow: which has been optimumaly filtered, gaussian-shaped, and pole-zero compensated for pulse height analysis (2) fast: which has only differential shaping so

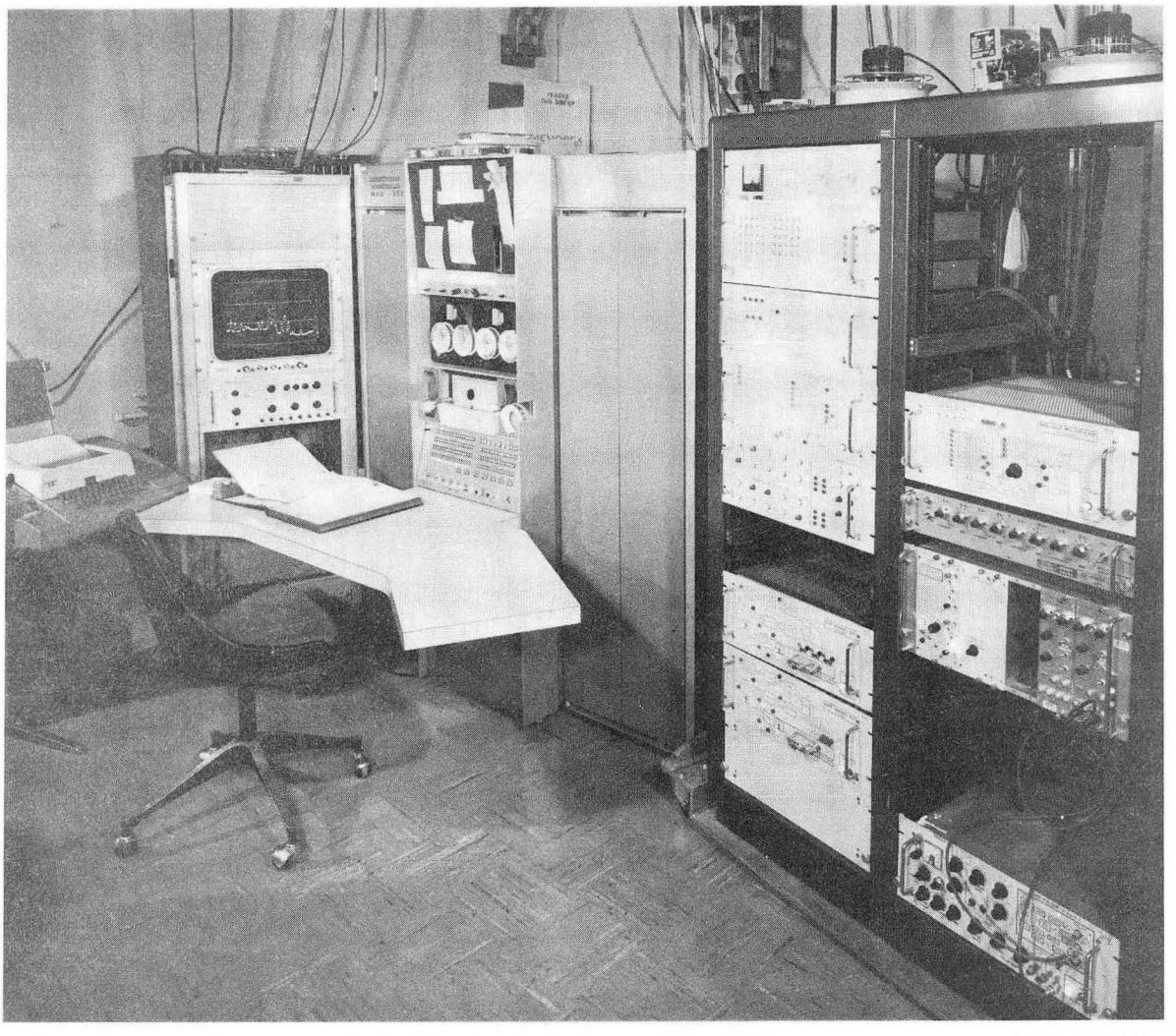

XBB 688-5165

Fig. 1. The PDP-7 data acquistion system[6]).

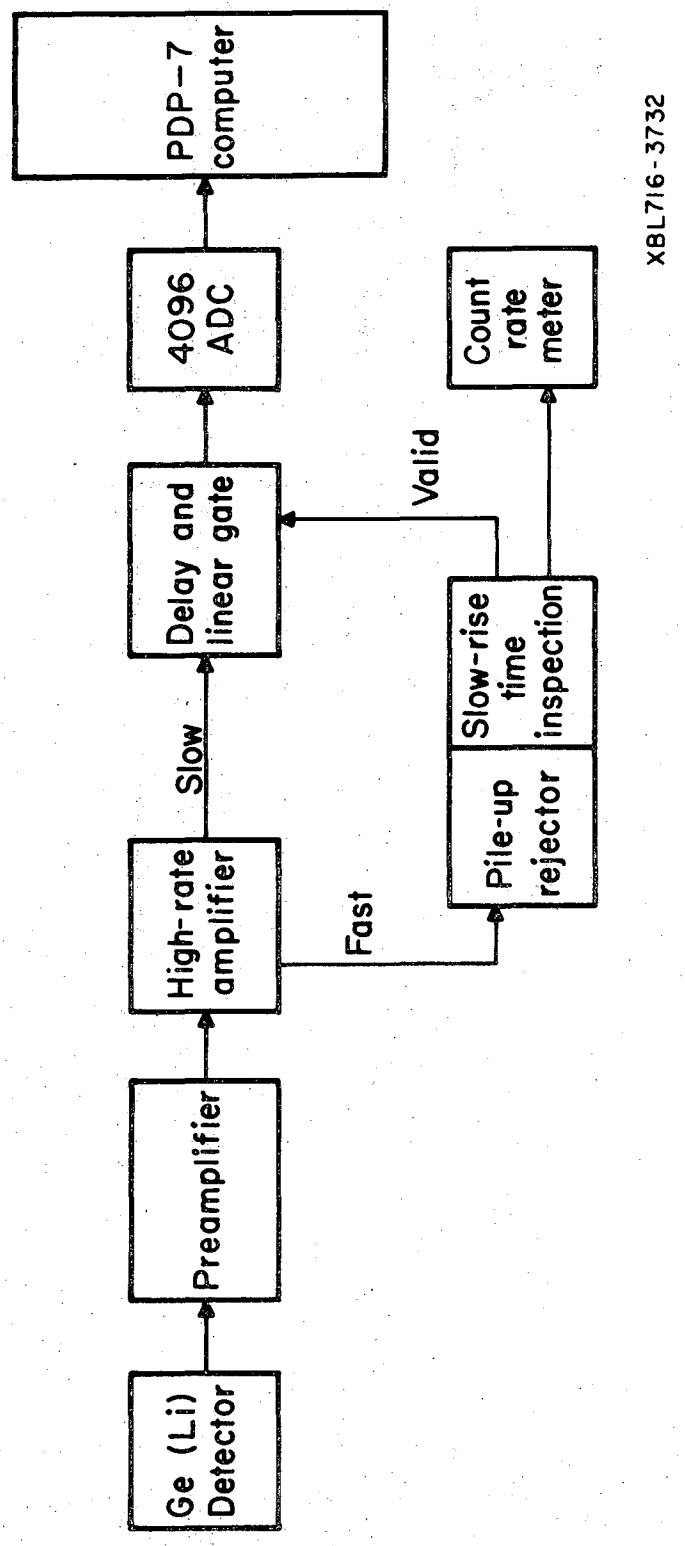

Fig. 2. Block diagram of gamma-ray "singles" spectra system.

that all optimum timing information is still contained in the signal. The input is internally terminated so that no terminator should be used.

B. Pile-up Rejector and Slow-Rise Time Inspect (LRL model #11 × 5551-P1)

The slow output signal from the amplifier, used for pulse height analysis, passes thru the linear gate to the analyzer only when the pile-up rejector produces a valid output pulse which opens the linear gate (fig. 2). The pile-up rejector[1]) has two functions: (1) rejection of pulses which occur too close in time (pile-up rejector); (2) rejection of "slow-rise" pulses, which result from slow, partial charge collection in the detector which occurs when a gamma-ray is absorbed just outside the active volume region. The pile-up rejector input is obtained from the fast output of the linear amplifier.

The pile-up circuit rejects a pulse preceeded by another within a variable (5-30 μsec, "inspect-time" knob) preset time (e.g. 25 μsec), or one which is followed by another within approximately 0.5 μsec. It has two adjustments; an input discriminator and a "inspect-time" setting. Set the discriminator just above the noise-level by triggering the scope on the discriminator output and observing the slow output of the linear amplifier. Set the "inspect-time" by setting the output (of the pin-jack) to approximately 25 μsec time duration.

The slow rise-time inspect may be switched in with a toggle switch and has three adjustments; an input discriminator (set it roughly to the same dial-setting as the input-discriminator on the pile-up inspect unit), a maximum rise-time adjustment, and dead-time setting. The maximum rise-time is adjusted in one of two ways: (1) with the

linear gate input gated by the valid output of the pile-up rejector, observe the output signal of the linear gate and decrease the maximum rise-time screw until the highest pulses (near saturation) disappear and then back the screw off one or two turns; (2) with the linear gate open but the delay in, observe the output while gating the scope on the dead-time pin-jack in the maximum rise-time section of the pile-up rejector (note: this pulse is negative). These pulses are the rejected pulses due to excessive rise-time. Decrease the maximum rise-time requirement screw until the highest pulses just start appearing with increasing intensity and then back off one or two turns. The dead-time adjustment for the slow rise-time inspect should normally be set at approximately 30 μsec.

When a pulse passes all tests imposed by the pile-up rejector unit, it emits a valid output logic pulse which opens the linear gate, allowing the energy signal (slow output of the amplifier) to pass. Finally if the external coincidence toggle switch on the pile-up rejector is engaged, an external signal, occuring at the same time as the valid output, is also required to produce a valid output to open the linear gate. The input signals to this unit should be terminated (125 Ω).

C. Linear Gate (LRL model #11 × 5510-P1)

In the trigger mode the linear gate[1]) takes two inputs. The gate trigger signal (e.g. from the pile-up rejector) drives the gate trigger which then allows input pulses (e.g. from the slow output from the amplifier) to pass. There is also a special baseline restorer circuit in the linear gate to insure that modulation of pulse-heights due

to baseline errors are minimized. The final output of this unit has a variable width "chopper" so that the width of the output pulse to the analyzer can be varied in order to avoid an excessive pulse duration. The width should be adjusted to obtain approximately symmetrical pulses. Also, care must be taken to match the voltage pedestal in this unit. Set the pedestal by removing the (slow) input signal and allowing only the valid output pulses of the pile-up rejector to enter the trigger. Trigger the scope off the discriminator output (pile-up rejector) while looking at the linear gate output on a high gain setting. Adjust the pedestal screw until the DC levels are matched. The unit also has the option of mixing multiple inputs and a fixed delay (1.5 μsec) switch that can be engaged. Thus this unit can also be used as a signal mixer and/or a linear delay box, whether or not used in the trigger mode. The delay is normally in when the unit is used with the pile-up rejector. Again all inputs to this unit should be terminated.

D. ADC (LRL model #11 × 4680)

The analogue-to-digital converter (ADC) used in all experiments was of the high speed successive binary approximation type and is described in detail in ref. [2]) and was interfaced to the PDP-7 [4,5]).

E. Conclusion

Hopefully, study of fig. 2 and the sections on the electronic components will allow the "singles" experiment to be set up easily. Figure 3 is a more detailed schematic drawing of the electronic components described above and is taken from ref. [1]).

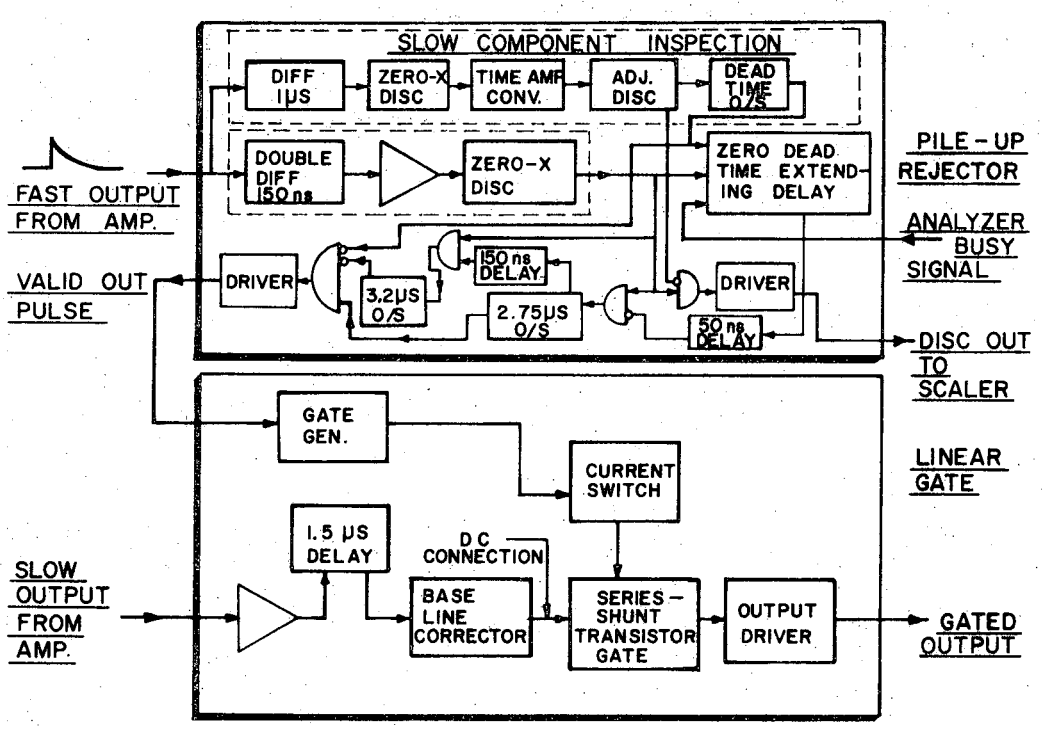

XBL 675-1474

Fig. 3(a). Block diagram of the pile-up rejector and linear delay gate[1]).

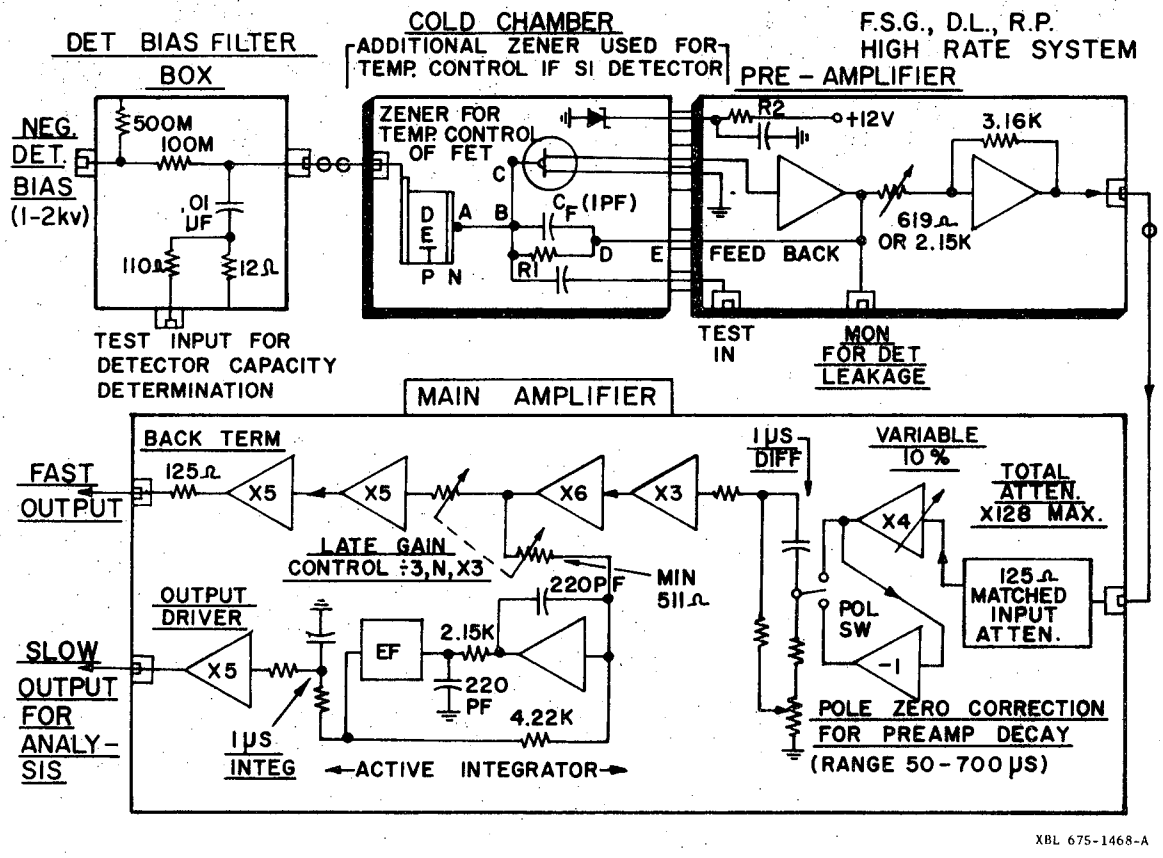

Fig. 3(b). Block diagram of the high-rate linear amplification system[1]).

III. COINCIDENCE (MULTIPARAMETER) DATA SYSTEM

A. Coincidence Logic Circuit

If one knows how to set the energy part of the coincidence circuit in fig. 4 (see gamma-ray "singles" section for the amplifier, pile-up rejector, and linear gate), only the methods of setting the timing part of the circuit remain. With reference to fig. 4, the following procedures based on experience are outlined:

(A) Set the gains of two of the four linear amplifiers to cover the range of pulse heights of interest. These will be used to extract the timing information, with the leading edge method, by taking their fast outputs. (In principle, pulse saturation should not matter since leading edge timing is used after the x10 amplifier.) Only two linear amplifiers are necessary but four make it unnecessary to readjust the timing circuit (except for the energy-walk compensator) when the energy range is changed.

(B) With no inputs* to the x10 amplifiers, set the x10 amplifier DC level (output) slightly negative (or zero) so that the fast discriminator level can be adjusted just above the noise level. These x10 amplifiers take negative signals and a pulse inverter (e.g. EG & G model #IT100) must be used to connect the fast output of linear amplifier to the x10 amplifier. An impedence matcher (125 Ω → 50 Ω) is also used and no termination is needed on 50 Ω inputs to the x10 amplifier.

---

*All fast circuits are 50 Ω and slow ones 125 Ω. All unused fast outputs on the discriminators and TAC, as well as the negative signal output of the TAC, must be terminated.

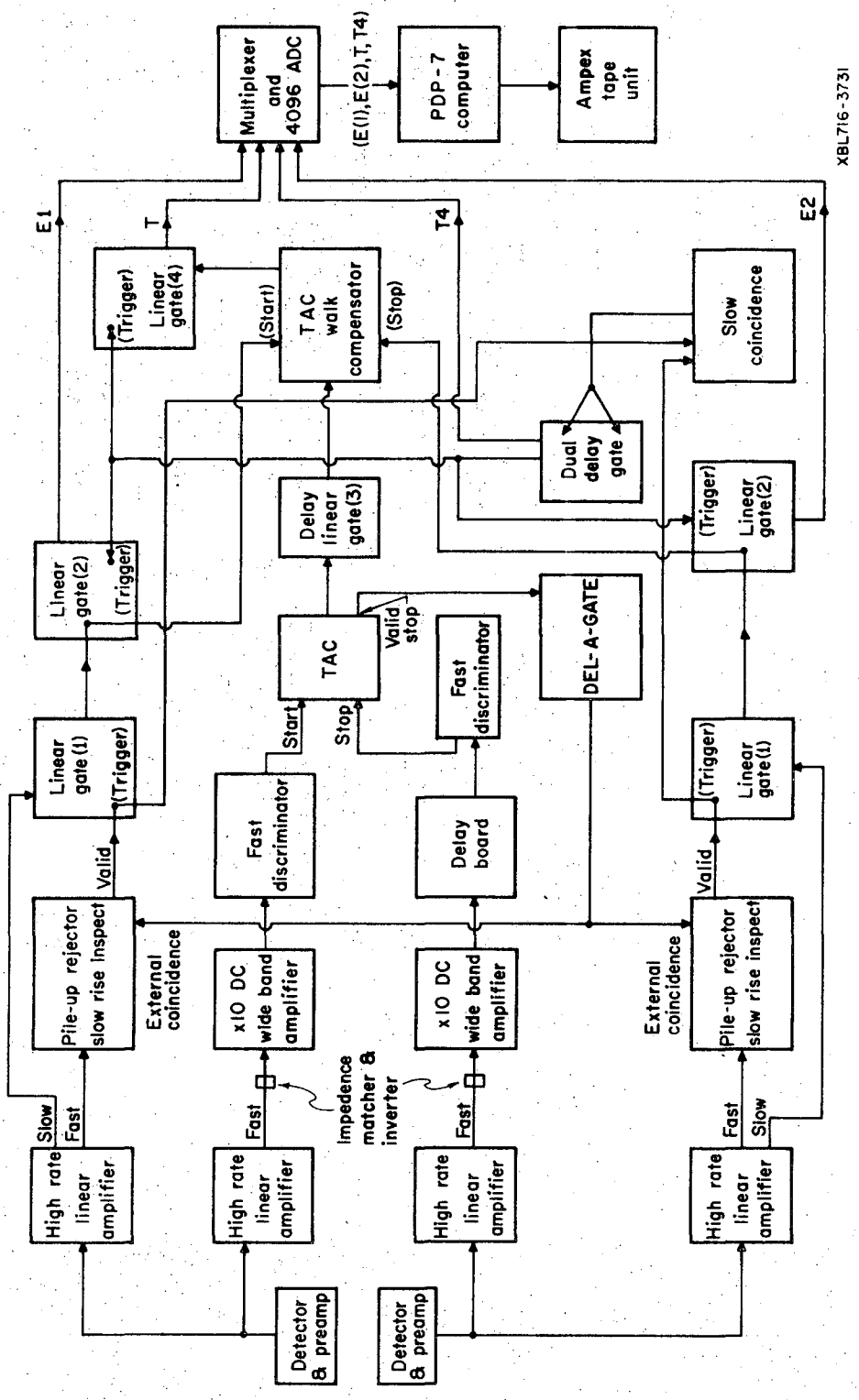

Fig. 4. Block diagram of the γ-γ coincidence system.

(C) With the output of the x10 amplifier connected to the fast discriminator DC input (negative signal), the gated switch "on", and the attenuated switch = 1, set the fast discriminator level (10 turn pot) just above the noise level so that the slow rising pulses (low energy) are detected with a minimum of "walk". Set the discriminator level by triggering the scope on the slow output of the fast discriminator while looking at the slow output of the linear amplifier. The discriminator level is very sensitive to the DC level setting on the x10 amplifier so if the fast discriminator cannot be set low enough (i.e., down to the noise level before "zeroing-out" the pot), set the DC level more negative. The idea is to have some leeway for adjusting the discriminator pot for any slight noise or DC level variations during the course of an experiment. Put the delay board (e.g. 80 nsec) before the fast discriminator to avoid any possible attenuation of the signal that may cause a failure in driving the STOP signal on the time-to-amplitude converter (TAC). The present output of the fast discriminator is "just" enough to drive the EG and G TAC which requires input signals $\geqslant$ 200 mvolts.

(D) Run the fast discriminators outputs to the START-STOP inputs of the TAC. The TAC START-STOP inputs are internally terminated. Check the system constructed so far by looking for the output signal of the START-STOP posts of the TAC with a source present (e.g. ^{22}Na with 180° detector geometry).

(E) Connect the valid STOP output of the TAC (negative signal) to a BNC del-a-gate (negative input). Take the positive del-a-gate output

and run to both pile-up rejectors (external coincidence input) and set the external coincidence switch "on" on both pile-up rejectors. Vary the del-a-gate settings so as to make the signal time-coincident with the valid output signals of the pile-up rejectors. This external coincidence will reduce the valid outputs of the pile-up rejectors to those pulses that are coincident in both (1) and (2) and have produced a valid TAC signal. ((1) and (2) refer to detectors START = (1) and STOP = (2) .) Note however that it is still possible for one pile-up rejector to not produce a valid output (due to pulse pile-up on one side) so that a further coincidence test of valid outputs of the pile-up rejectors still must be made. To do this final test connect the output signal from the pile-up rejectors to the slow coincidence unit. (This can be done by connecting the valid output to the rear "trigger" input on the linear gate (1) and then connecting the front "trigger" input (now producing an output) to the slow coincidence input. Terminate only once and at the slow coincidence input.)

(F) From the linear gates (1), run the outputs to the rear inputs of the linear gates (2) and do not terminate. From the front of the same linear gate input posts, take the signals (gamma-ray energy pulses) and run them to the START and STOP posts of the TAC walk compensator (terminated). (By splitting the signal in this manner, the two coincident (gamma) signals are available for energy analysis and for the logrithmic TAC walk compensator inputs.) We shall require a further coincidence on the linear gates (2).

(G) Connect the output of the TAC to a linear (delay) gate (3) input (no trigger mode) in order to delay the TAC signal (if needed) which probably occurs before the energy signals at the output of the gates (1). Connect the output of this gate to the energy-walk compensator "TAC" signal input. In the end, the TAC signal ≡ T and the two energy signals ≡ E(1) and E(2) must be coincident in time.

(H) Connect the TAC walk compensator output to the linear gate (4) input. This signal, when gated, has the final coincidence logic, and also selects the "clean" portion of the time signal (by varying the delays and width of the "chopper") which contains the TAC and compensation signals mixed together. The output of this gate ≡ T should occur at the same time as the energy signals at the outputs of gates (2), and be of approximately the same width (see fig. a).

(I) Connect the slow coincidence output of section (E) to a dual delay gate unit. (This coincidence output occurs only for events for which neither γ-ray was pile-up rejected.) Split the slow coincident output and use as the inputs to both delay gates so that two variable delay signals are now available. Adjust both delay signals to make the signals time coincident with E(1) and E(2) (at the input of the linear gates (2)). A coincidence on (T, E(1), E(2)) can be required by taking one of these delay gate signals to the trigger input of the linear gates (2) and (3). The second delay gate signal should occur at the same time as the first and is used as a valid coincidence signal which starts the computer processing the four coincident parameters (E(1), E(2), T, T4) and is fourth parameter (dummy ≡ T4) input to the analyzer.

(J) The four output pulses (E(1), E(2), T, T4) of fig. 4 sent to the PDP-7 should occur at the same time and look crudely like those shown in fig. a.

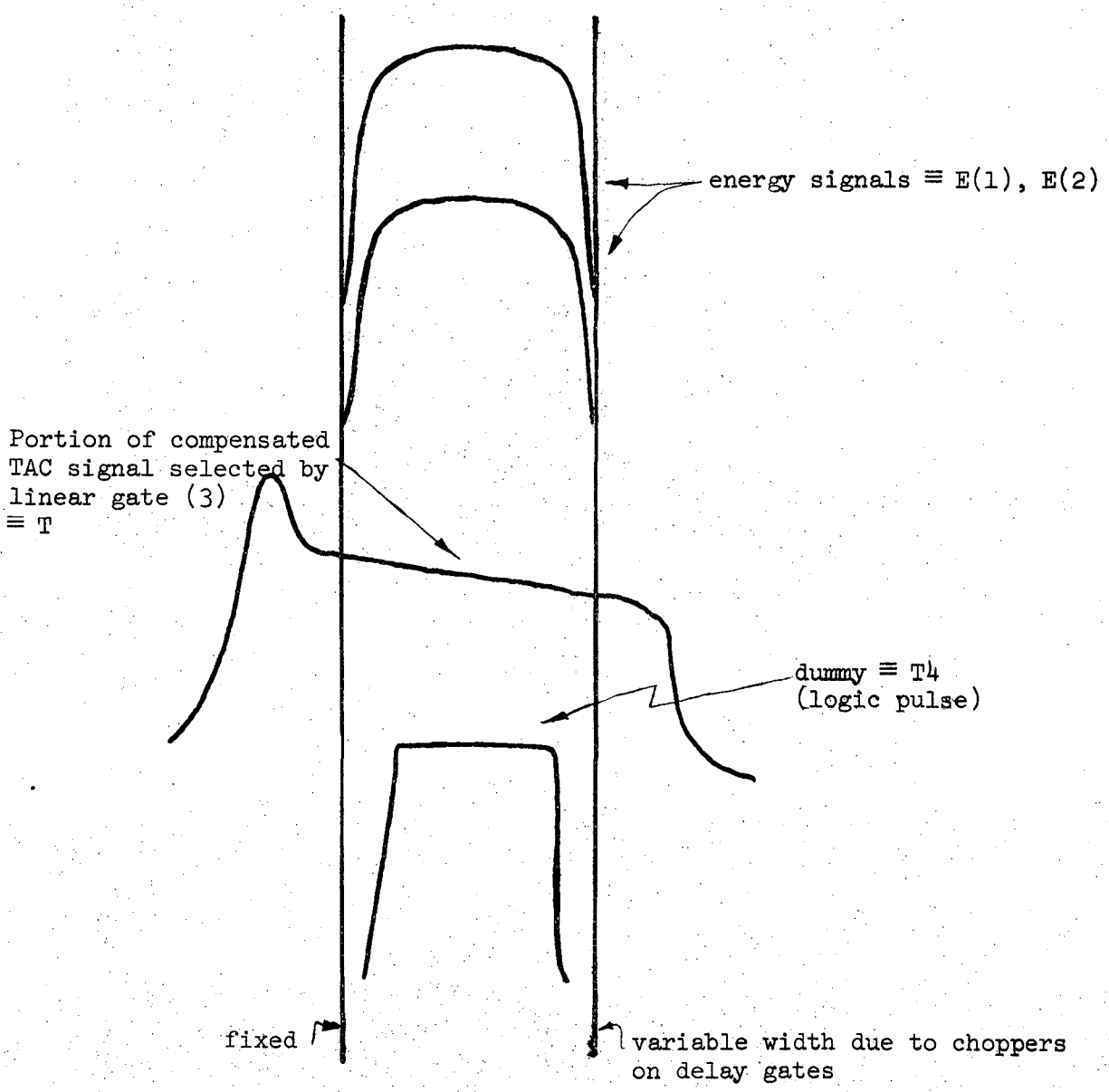

Fig. a

B. Conclusions

The final signals (T, E(1), E(2), T4) must all start at the same time on the scope. These are the four coincident inputs to the PDP-7 computer and the multiplexer unit for the multiparameter data (coincidence) experiment.

Some patient juggling of the delays is usually necessary in order to make the required coincidences. This is done most effectively by adjusting the stretchers on the TAC, TAC walk compensator, and the dual delay gates (timing and widths) to match the relatively fixed time of the energy signals.

The details on the use and the need for the TAC walk compensation unit were discussed by Jaklevic et al.[3]).

A list of the model numbers for the equipment used for the coincidence circuit of fig. 4 not described in the "singles" section follows:

Double x10 D.C. Amplifiers (LRL model #18 × 1281-P2)

100 MHz fast Discriminator (LRL model #18 × 1201-P4)

TAC (EG & G model Th 200 A/N)

TAC Energy Walk compensator (LRL model #11 × 6891-P1)

BNC Del-a-gate (BNC model #CT-1A

Dual Delay Gate (LRL model #11 × 6361-P1)

Slow Coincidence Box (LRL model #11 × 5591-P1)

The coincidence system (resolving time) can be optimized by placing a ^{22}Na source between two 180° detectors to utilize the 511-511

keV gamma-ray prompt coincidence. The timing spectrum is then optimized by adjusting the TAC walk compensation unit until the spectrum is made as symmetrical as possible and the width (FWHM) and the tailing (due to different pulse rise-times) is the smallest possible for the detectors being used.

IV. ANALOGUE MULTIPLEXER UNIT AND PDP-7 COMPUTER

The PDP-7 peripheral hardware[6]) used is shown in fig. 5. The multiplexer (LRL model #11 × 4440-P1) accepts the four coincident input signals (T, E(1), E(2), T4) and stretches them individually in time so that one 4096 ADC can analyze all four signals. Analysis is started by receipt of a valid coincidence input (T4). The total time to process all four pulses is approximately 200 μsec and is constant for each event due to the successive binary approximation ADC unit[2]). These four processed parameters (E(1), E(2), T, T4) then go to the buffer storage area of the 18 bit PDP-7. When the storage buffer (512 words) is full, the data is written by an Ampex tape unit (model #C208), 3 words per coincident event, (512 words equal one record) on an IBM magnetic tape. The IBM tapes are 2400' in length and can hold approximately by 20.5 million characters each. They require 2-6 hours to fill depending on the input rate of coincident events. The data is thus written, 170 coincident events at a time, for later sorting and analysis on the CDC 6600. The time left over between processing coincident events is used to generate a 6144 channel display of the data being collected. The following is a representation of the area and parameters displayed by the PDP-7 during the experiment.

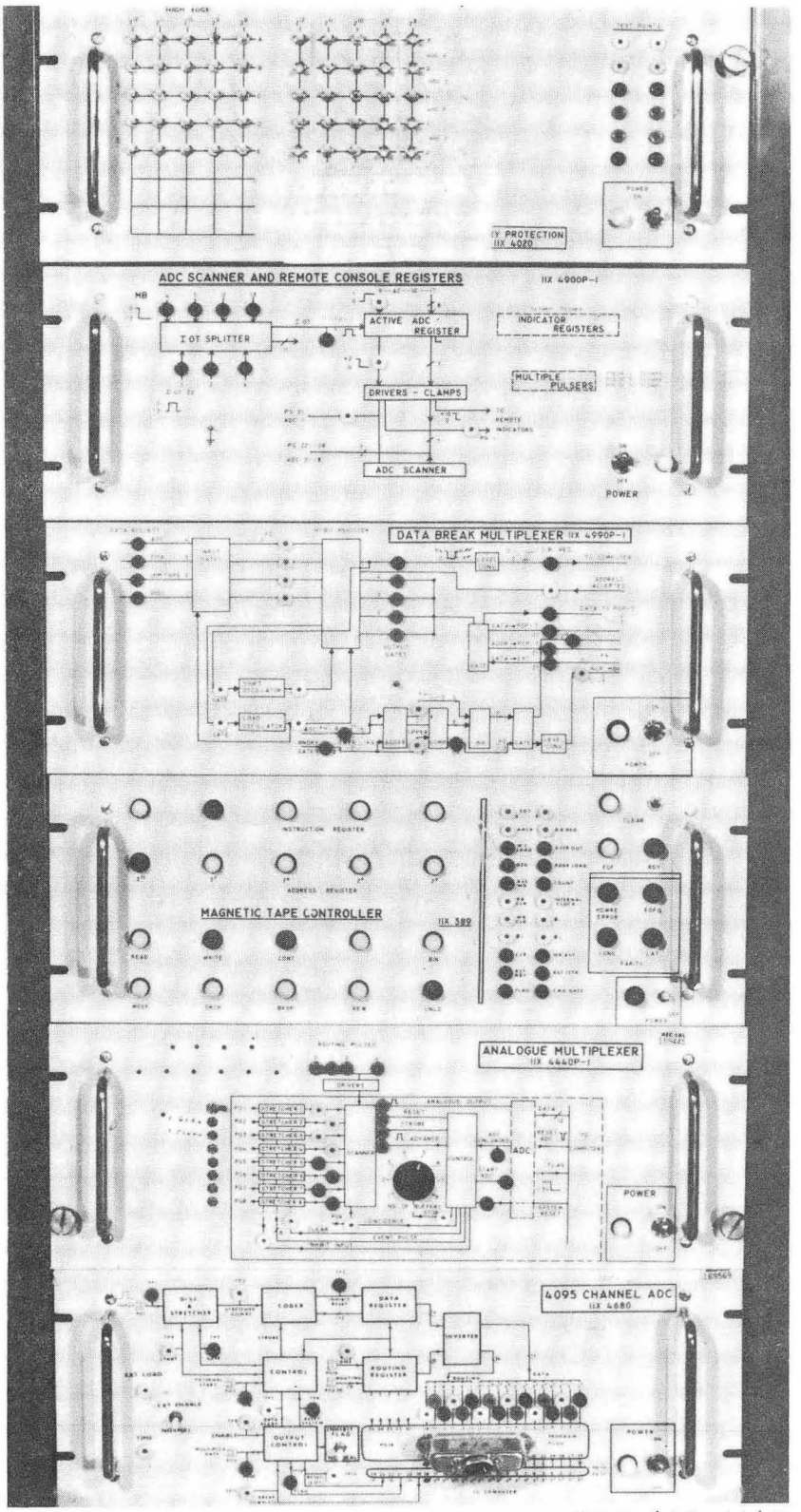

XBB 688-5165

Fig. 5. The PDP-7 peripheral hardware used in acquiring multiparameter coincidence data[6]).

Detector ①	Detector ②	T	T4	Buffer	Window 1	Window 2	Window 3
$(1024)^a$	$(1024)^a$	$[(256)^a$	$(256)^a$	$(512)^a]$	$(1024)^a$	$(1024)^a$	$(1024)^a$
$A0^b$	$A1^b$		$A2^b$ $Z0^b$		$A3^b$ $Z1^b$	$Z2^b$	$Z3^b$

[a]Number of Channels [b]Display Switches

NOTES:

Detectors ① and ② refer to the full 4096 channel spectra compressed to a display of 1024 channels for the START and STOP detectors, respectively.

T is the time distribution of the (gamma-gamma) coincidences.

T4 is the dummy parameter.

Buffer: it looks like snow--don't panic!

Windows are events coincident in Detector ② with 3 gates (2 display markers for each gate) set on the spectrum of Detector ① (e.g. pick three peaks in the first (1024) display group (A0) and then coincident events between selected windows are displayed as three (1024) groups (Z1, Z2, Z3).

One can refer to the PDP-7 users manuals[4,5] for more detailed operation of the computer and multiparameter programs. MULTIS is the program used for sorting of data tapes and MULTID R is the program for the acquisition of multiparameter data on the PDP-7.

REFERENCES

1. F. S. Goulding, D. A. Landis, and R. H. Pehl, University of California, Lawrence Radiation Laboratory Report UCRL-17560 (1967). Submitted to Gatlinburg Conference on Semi-Conductor Detectors and Associated Circuits (May 1967).

2. L. B. Robinson, F. Gin, and F. S. Goulding, University of California, Lawrence Radiation Laboratory Report UCRL-17419 (1968). Submitted to Nuclear Instruments and Methods.

3. J. M. Jaklevic, F. M. Bernthal, J. O. Radeloff, and D. A. Landis, Nucl. Instr. Methods 69, 109 (1969).

4. L. B. Robinson and J. D. Meng, University of California, Lawrence Radiation Laboratory Report UCRL-17220 (1967) unpublished.

5. J. O. Radeloff, L. B. Robinson, and J. D. Meng, University of California, Lawrence Radiation Laboratory Report UCRL-18883 (1969) unpublished.

6. F. M. Bernthal, (Ph.D. Thesis), University of California, Lawrence Radiation Laboratory Report UCRL-18651 (1969) unpublished.

APPENDIX D

GAMMA-RAY CALIBRATION STANDARDS*

ABSTRACT

A collection of γ-ray energies and intensities is given that are suitable for use in the calibration of high resolution γ-ray spectrometers. The energy range included in this tabulation is 25 keV < E_γ < 3452 keV. Adopted values are given for gamma-ray energies based on weighted averages of the uncertainties reported in the literature. Relative γ-ray intensities are also given for ^{133}Ba, ^{182}Ta and ^{56}Co. No attempt was made to establish weighted averages for the intensity values.

*This appendix appeared as a Lawrence Radiation Laboratory Report UCRL-20476 (April 1971).

I. INTRODUCTION

With the development of high resolution Ge(Li) detectors coupled with highly stablized linear electronics and computer photopeak analysis of data, it has become possible to measure gamma-ray energies to a precision of better than 0.1 keV. However, to do this, it is necessary to have available a large number of standards with energies known to better than tens of eV. Marion[1]) compiled a list of such standards in 1968, but since that time there have been improvements in the measurements of standards, and their number has increased substantially. Because the newer information is scattered in the literature, it is the purpose of this report to collect and tabulate those measurements and references for standards that are routinely being used in our nuclear spectroscopy research. In the recent literature, the most extensive work has been that of Gunnink et al.[2,13]).

Gamma-ray energies are listed by source in Table 1. The original data are shown along with the reference. The "adopted values" that are given represent weighted averages (weighted inversely as the square of the author's stated uncertainties). The errors given are the larger of the σ values as defined below. E_i and σ_i are the author's stated energy and error, respectively.

$$\sigma^2 = \frac{1}{\sum_i 1/\sigma_i^2} \qquad \sigma^2 = \frac{1}{n-1} \sum_{i=1}^{n} (E_m - E_i)^2 \qquad E_m = \frac{\sum_i E_i/\sigma_i^2}{\sum_i 1/\sigma_i^2}$$

Marion's[1]) values, which are also tabulated, often represent weighted

averages of several measurements. In these cases the original measurements reported by ref. [1]) were used in obtaining the new weighted set of adopted values.

Table 2 lists gamma-ray energy and intensity measurements for ^{133}Ba, ^{182}Ta, and ^{56}Co. No attempt was made to establish a weighted set of intensity values. The energy values of Gunnink et al.[2]) are used for ^{56}Co while weighted sets are given for ^{133}Ba and ^{182}Ta.

The ^{182}Ta low energy (84-265 keV) γ-ray intensity measurements[18]) were made using a calibrated 10-cm^3 Ge(Li) detector. Details of these measurements are to be published later. (See Appendix E.)

Table 1. Gamma-ray energies used as calibration standards listed by source.

Isotope	Half-Life	γ-Ray Energy keV	Refs.	Adopted
^{241}Am	432.9 ± 0.8y	26.348 ± 0.010	1	
		26.345 ± 0.010	12	26.3465 ± 0.007
		59.543 ± 0.015	1	
		59.536 ± 0.010	13	59.538 ± 0.008
^{170}Tm	120d	84.2572 ± 0.0026	11	
		84.257 ± 0.003	12	84.257 ± 0.002
^{109}Cd	453d	88.034 ± 0.010	13	
		88.035 ± 0.006	9	
		88.036 ± 0.008	11	88.035 ± 0.004
^{57}Co	271.6 ± 0.5d	122.046 ± 0.020	13	
		122.061 ± 0.010	9	
		122.04 ± 0.02	14	122.055 ± 0.013
		136.465 ± 0.020	13	
		136.471 ± 0.010	9	
		136.47 ± 0.02	14	136.470 ± 0.008

(continued)

Table 1. (continued)

Isotope	Half-Life	γ-Ray Energy keV	Refs.	Adopted
^{203}Hg	46.8 ± 0.2d	279.191 ± 0.008	1	
		279.179 ± 0.010	13	279.186 ± 0.009
^{113}Sn	115.2 ± 0.8d	391.688 ± 0.010	9	
		391.71 ± 0.02	23	391.692 ± 0.018
^{198}Au	2.7d	411.795 ± 0.009	1	
		411.792 ± 0.008[c]	13	411.795 ± 0.009
^{137}Cs	30.5 ± 0.3y	661.635 ± 0.076	1	
		661.615 ± 0.030	2	661.618 ± 0.028
^{54}Mn	312.6 ± 0.3d	834.81 ± 0.03	1	
		834.84 ± 0.05[c]	2	834.81 ± 0.03
^{88}Y	107.4 ± 0.8d	898.04 ± 0.04	1	
		898.023 ± 0.065	13	
		898.010 ± 0.030	10	898.021 ± 0.023
		1836.13 ± 0.040	1	
		1836.127 ± 0.050	2	
		1836.030 ± 0.030[b,c]	10	1836.129 ± .031

(continued)

Table 1. (continued)

Isotope	Half-Life	γ-Ray Energy keV	Refs.	Adopted
^{60}Co	5.28 ± 0.01y	1173.23 ± 0.04	1	
		1173.231 ± 0.030	13	1173.231 ± 0.024
		1332.49 ± 0.04	1	
		1332.505 ± 0.025	2	1332.501 ± 0.021
^{22}Na	2.602 ± 0.005y	511.006 ± 0.002[c]	1	
		511.0041 ± 0.0016	15	511.0041 ± 0.0016
		1274.55 ± 0.04	1	
		1274.550 ± 0.040[c]	13	1274.55 ± 0.04
^{24}Na	15h	1368.526 ± 0.044	1	1368.526 ± 0.044
		1731.91 ± 0.12[c]	1	
		1732.130 ± 0.060[a]	2	1732.130 ± 0.060
		2753.92 ± 0.12	1	
		2754.142 ± 0.060	2	2754.098 ± 0.183

(continued)

Table 1. (continued)

Isotope	Half-Life	γ-Ray Energy keV	Refs.	Adopted
^{40}K	$1.26 \cdot 10^9$y	1460.75 ± 0.06	1	
		1460.9 ± 0.3	16	
		1460.95 ± 0.07	23	1460.836 ± 0.11
		1460.75 ± .06[c]	18	
^{207}Bi	30y	569.653 ± 0.020	10	
		569.62 ± 0.06	1	569.650 ± 0.030
		1063.63 ± 0.030	10	
		1063.44 ± 0.090	1	(1063.611 ± 0.172)
		1769.71 ± 0.13[c]	1	
		1770.22 ± 0.040[c]	10	
		1770.06 ± 0.07	7	1770.06 ± 0.07
^{192}Ir	74.2d	295.938 ± 0.009	1	
		295.938 ± 0.010	2	295.938 ± 0.007
		308.429 ± 0.010	1	
		308.440 ± 0.010	2	308.435 ± 0.008
		316.486 ± 0.010	1	
		316.490 ± 0.010	2	316.488 ± 0.007

(continued)

Table 1. (continued)

Isotope	Half-Life	γ-Ray Energy keV	Refs.	Adopted
^{192}Ir (continued)		468.053 ± 0.014	1	
		468.060 ± 0.010	2	468.058 ± 0.008
		588.557 ± 0.017	1	588.557 ± 0.017
		604.385 ± 0.017	1	
		604.378 ± 0.020	2	604.382 ± 0.013
		612.435 ± 0.017	1	
		612.430 ± 0.020	2	612.433 ± 0.013
^{110m}Ag	253d	446.77 ± 0.04	5	
		446.790 ± 0.020	10	446.786 ± 0.020
		620.22 ± 0.03	5	
		620.310 ± 0.020	10	620.282 ± 0.068
		657.71 ± 0.03	5	
		657.720 ± 0.020	10	
		657.75 ± 0.04	14	657.722 ± 0.022

(continued)

Table 1. (continued)

Isotope	Half-Life	γ-Ray Energy keV	Refs.	Adopted
^{110m}Ag (continued)		677.55 ± 0.03	5	
		677.580 ± 0.020	10	
		677.58 ± 0.05	14	677.572 ± 0.017
		686.80 ± 0.03	5	
		686.950 ± 0.030	10	
		686.95 ± 0.05	14	686.886 ± .088
		706.68 ± 0.04	5	
		706.650 ± 0.020	10	
		706.63 ± 0.06	14	706.654 ± 0.025
		744.19 ± 0.04	5	
		744.260 ± 0.030	10	
		744.23 ± 0.07	14	744.234 ± 0.036
		763.88 ± 0.04	5	
		763.920 ± 0.030	10	
		763.93 ± 0.07	14	763.908 ± 0.027

(continued)

Table 1. (continued)

Isotope	Half-Life	γ-Ray Energy keV	Refs.	Adopted
^{110m}Ag (continued)		818.00 ± 0.04	5	
		817.995 ± 0.030	10	
		817.95 ± 0.08	14	817.993 ± 0.031
		884.67 ± 0.04	5	
		884.650 ± 0.030	10	
		884.68 ± 0.04	6	
		884.69 ± 0.05	14	884.667 ± 0.019
		937.48 ± 0.04	5	
		937.450 ± 0.030	10	
		937.48 ± 0.04	6	
		937.54 ± 0.07	14	937.472 ± 0.042
		1384.22 ± 0.04	5	
		1384.240 ± 0.040	10	
		1384.26 ± 0.05	6	1384.237 ± 0.025
		1475.73 ± 0.04	5	
		1475.710 ± 0.040	10	
		1475.76 ± 0.07	6	1475.726 ± 0.027

(continued)

Table 1. (continued)

Isotope	Half-Life	γ-Ray Energy keV	Refs.	Adopted
^{110m}Ag (continued)		1504.9 ± 0.08	5	
		1504.945 ± 0.040	10	
		1505.01 ± 0.07	6	1504.951 ± 0.055
		1562.22 ± 0.06	5	
		1562.255 ± 0.050	10	
		1562.35 ± 0.08	6	1562.261 ± 0.069
^{108m}Ag	127 ± 7y	434.0 ± 0.10	5	
		433.94 ± 0.06	14	433.956 ± 0.051
		614.37 ± 0.10	5	
		722.95 ± 0.08	5	
		722.87 ± 0.06	14	722.899 ± 0.059
^{228}Th	1.910y[d]	39.85 ± 0.01	1(^{212}Bi)	
		238.624 ± 0.009	1(^{212}Pb)	
		510.723 ± 0.020	1(^{208}Tl)	

(continued)

Table 1. (continued)

Isotope	Half-Life	γ-Ray Energy keV	Refs.	Adopted
^{228}Th (continued)		583.139 ± 0.023	1(^{208}Tl)	
		727.1 ± 0.1	1(^{212}Bi)	
		727.08 ± 0.07		727.09 ± 0.06
		785.37 ± 0.08	7(^{212}Bi)	
		763.13 ± 0.08	7(^{208}Tl)	
		860.37 ± 0.08	7(^{208}Tl)	
		893.43 ± 0.09	7(^{212}Bi)	
		1078.62 ± 0.10	7(^{212}Bi)	
		1592.696 ± 0.050[a]	2(^{208}Tl)	
		1620.50 ± 0.10	7(^{212}Bi)	
		2614.47 ± 0.10	1(^{208}Tl)	
		2614.708 ± 0.050	2	2614.66 ± 0.20

(continued)

Table 1. (continued)

[a] Since these values are for double-escape pair peaks, care, as warned by Gunnink et al.[2]), should be employed if using them.

[b] The calibration is from the double-escape peak. See ref. [10]).

[c] This is not included in the adopted value given.

[d] ^{228}Th energies listed are from daughters in ^{228}Th decay chain.

Table 2. Gamma-ray energies and intensities used as calibration standards listed by source

Isotope	Half-Life	γ-Ray Energy keV	Refs.	Adopted	γ-Ray Intensity Relative	Refs.
^{133}Ba	7.2y	53.18 ± 0.04	1		3.78 ± 0.09	19
		53.17 ± 0.01	8	53.171 ± 0.010	3.81 ± .10	8
		79.60 ± 0.05	1			
		79.63 ± 0.03	8		4.50 ± .40	8
		80.997 ± 0.006	1			
		80.99 ± 0.01	8		55.3 ± 3.0[c]	8
		80.998 ± 0.008	9			
		160.66 ± 0.06	1		1.21 ± 0.05	19
		160.63 ± 0.02	8	160.633 ± 0.027	1.12 ± 0.05	8
		223.37 ± 0.23[e]	1		0.803 ± 0.042	19
		223.12 ± 0.01	8	223.12 ± 0.01	0.78 ± 0.04	8
		276.46 ± 0.2[e]	1		11.61 ± 0.17	19
		276.45 ± 0.02	8		11.6 ± 0.2	8
		276.397 ± 0.012	9	276.411 ± 0.041		

(continued)

Table 2. (continued)

Isotope	Half-Life	γ-Ray Energy keV	Refs.	Adopted	γ-Ray Intensity Relative	Refs.
^{133}Ba (continued)		303.08 ± 0.2[e]	1		29.75 ± 0.29	19
		302.93 ± 0.03	8		29.6 ± 0.3	8
		302.851 ± .015	9	302.867 ± 0.065		
		356.27 ± 0.14[e]	1		100.	19
		356.09 ± 0.04	8		100.	8
		356.005 ± 0.017	9	356.018 ± 0.073		
		384.10 ± 0.18[e]	1		14.18 ± 0.26	19
		383.83 ± 0.03	8		14.1 ± 0.3	8
		383.851 ± 0.020	9	383.845 ± 0.017		
^{182}Ta	115d	84.257 ± 0.003	12		7.6 ± 0.4	18
		84.678 ± 0.003	17			
		100.106 ± 0.003	12		40.2 ± 1.0	18
		100.104 ± 0.002	3[d]	100.105 ± 0.002		
		152.435 ± 0.003	3[d]		20.5 ± 0.51	18
		156.387 ± 0.003	3[d]		7.63 ± 0.19	18
		179.393 ± 0.004	3[d]		8.81 ± 0.22	18
		198.358 ± 0.008	17		4.15 ± 0.11	18

(continued)

Table 2. (continued)

Isotope	Half-Life	γ-Ray Energy keV	Refs.	Adopted	γ-Ray Intensity Relative	Refs.
^{182}Ta (continued)		222.109 ± 0.005	3[d]		21.30 ± 0.56	18
		229.322 ± 0.008	3[d]		10.27 ± 0.27	18
		264.072 ± 0.009	3[d]		10.10 ± 0.26	18
		891.982 ± 0.015	4		0.15 ± 0.02	4
		927.995 ± 0.015	4		1.79 ± 0.09	4
		959.730 ± 0.015	4		1.02 ± 0.06	4
		1001.694 ± 0.015	4		5.98 ± 0.3	4
		1044.409 ± 0.015	4		0.69 ± 0.08	4
		1113.398 ± 0.052	4		1.13 ± 0.10	4
		1121.298 ± 0.013	4		100.	4,18
		1121.28 ± 0.12	3			
		1121.31 ± 0.04	6	1121.299 ± 0.016		
		1157.311 ± 0.013	4		1.84 ± 0.35	4
		1158.080 ± 0.015	4		0.99 ± 0.28	4
		1189.046 ± 0.013	4		47.4 ± 0.7	4
		1189.03 ± 0.2	3			
		1189.06 ± 0.04	6	1189.047 ± 0.015		

(continued)

Table 2. (continued)

Isotope	Half-Life	γ-Ray Energy keV	Refs.	Adopted	γ-Ray Intensity Relative	Refs.
^{182}Ta (continued)		1221.399 ± 0.013	4		79.3 ± 1.2	4
		1221.42 ± 0.10	3			
		1221.42 ± 0.04	6	1221.401 ± 0.019		
		1231.010 ± 0.013	4		33.4 ± 0.5	4
		1257.412 ± 0.013	4		4.33 ± 0.07	4
		1273.725 ± 0.013	4		1.90 ± 0.04	4
		1289.147 ± 0.013	4		4.05 ± 0.07	4
		1342.714 ± 0.051	4		0.75 ± 0.02	4
		1373.825 ± 0.013	4		0.66 ± 0.02	4
		1387.396 ± 0.013	4		0.217 ± 0.01	4
		1410.100 ± 0.100	4		0.117 ± 0.008	4
		1453.115 ± 0.013	4		0.123 ± 0.010	4
^{56}Co	77d	846.79 ± 0.030	20		100.	20
		846.782 ± 0.060	2		100.	22
		846.76 ± 0.05	1		100.	1
		846.741 ± 0.025	21	846.782 ± 0.060[b]	100.	21
		1037.91 ± 0.030	20		14.302 ± .170	20
		1037.851 ± 0.060	2		13.08 ± 0.35	22
		1037.97 ± 0.07	1		13.02 ± 0.35	1
		1037.84 ± 0.05	21	1037.851 ± 0.060[b]	12.9 ± 0.5	21

(continued)

Table 2. (continued)

Isotope	Half-Life	γ-Ray Energy keV	Refs.	Adopted	γ-Ray Intensity Relative	Refs.
^{56}Co (continued)		1175.13 ± 0.050	20		2.302 ± 0.025	20
		1175.085 ± 0.070	2		1.73 ± 0.13	22
		1175.026 ± 0.13	1		1.86 ± 0.23	1
		1175.1 ± 0.1	21	1175.085 ± 0.070[b]	2.26 ± 0.23	21
		1238.30 ± 0.020	20		67.638 ± 0.680	20
		1238.290 ± 0.040	2		68.3 ± 1.4	22
		1238.34 ± 0.09	1		69.35 ± 1.47	1
		1238.28 ± 0.06	21	1238.290 ± 0.040[b]	67.8 ± 1.5	21
		1360.22 ± 0.030	20		4.340 ± 0.045	20
		1360.219 ± 0.040	2		4.15 ± 0.12	22
		1360.35 ± 0.090	1		4.38 ± 0.16	1
		1360.26 ± 0.04	21	1360.219 ± .040[b]	4.16 ± 0.21	21
		1771.41 ± 0.030	20		15.778 ± 0.160	20
		1771.33 ± 0.06	2		14.95 ± 0.40	22
		1771.57 ± 0.10	1		15.30 ± 0.53	1
		1771.38 ± 0.15	21	1771.33 ± 0.06[b]	16.5 ± 0.8	21
		2015.36 ± 0.030	20		3.095 ± 0.031	20
		2015.33 ± 0.07	2		2.78 ± 0.14	22

(continued)

Table 2. (continued)

Isotope	Half-Life	γ-Ray Energy keV	Refs.	Adopted	γ-Ray Intensity Relative	Refs.
^{56}Co (continued)		2015.49 ± 0.20	1		2.93 ± 0.16	1
		2015.24 ± 0.12	21	2015.33 ± 0.07[b]	2.99 ± 0.20	21
		2034.92 ± 0.030	20		7.952 ± 0.080	20
		2034.90 ± 0.06	2		7.56 ± 0.21	22
		2035.03 ± 0.12	1		7.33 ± 0.30	1
		2034.82 ± 0.10	21	2034.90 ± 0.06[b]	8.2 ± 0.6	21
		2598.58 ± 0.030	20		16.851 ± 0.170	20
		2598.52 ± 0.05	2		16.55 ± 0.44	22
		2598.80 ± 0.12	1		16.77 ± 0.57	1
		2598.53 ± 0.06	21	2598.52 ± 0.05[b]	18.0 ± 0.9	21
		3202.30 ± 0.080	20		3.030 ± 0.030	20
		3202.18 ± 0.07	2		3.03 ± 0.14	22
		3202.25 ± 0.19	1		3.15 ± 0.16	1
		3202.1 ± 0.2	21	3202.18 ± 0.07[b]	3.2 ± 0.35	21
		3253.62 ± 0.040	20		7.392 ± 0.074	20
		3253.61 ± 0.06	2		7.35 ± 0.21	22
		3253.82 ± 0.15	1		7.70 ± 0.34	1
		3253.5 ± 0.2	21	3253.61 ± 0.06[b]	7.7 ± 0.9	21

(continued)

Table 2. (continued)

Isotope	Half-Life	γ-Ray Energy keV	Refs.	Adopted	γ-Ray Intensity Relative	Refs.
^{56}Co (continued)		3273.26 ± 0.08	20		1.756 ± 0.018	20
		3273.16 ± 0.07	2		1.72 ± 0.13	22
		3273.38 ± 0.18	1		1.55 ± 0.11	1
		3273.08 ± 0.10	21	3273.16 ± 0.07[b]	1.71 ± 0.25	21
		3451.56 ± 0.20	20		0.875 ± 0.009	20
		3451.29 ± 0.10	2		0.85 ± 0.07	22
		3452.18 ± 0.22	1		0.88 ± 0.10	1
		3451.5 ± 0.3	21	3451.29 ± 0.1[b]	0.93 ± 0.20	21
		1576.561 ± 0.050[a]	2			
		2180.17 ± 0.07[a]	2			
		2231.60 ± 0.06[a]	2			
		2251.15 ± 0.07[a]	2			
		2429.28 ± 0.10[a]	2			

[a]Since these values are for double-escape pair peaks, care, as warned by Gunnink et al.[2]), should be employed if using them.

[b]This not a weighted value, but that of ref. [2]).

[c]This is an adopted value from previous works. See ref. [8]) for details.

[d]These energy values are averaged results of refs. [17,24]) as calculated in ref. [3]).

[e]This not included in the adopted value given.

REFERENCES

1. J. B. Marion, Nucl. Data A4, 301 (1968).
2. R. Gunnink, R. A. Meyer, J. B. Niday, and R. P. Anderson, Nucl. Instr. Methods 65, 26 (1968).
3. C. M. Lederer, J. M. Hollander, and I. Perlman, Table of Isotopes, John Wiley and Sons, New York (1967), 6th edition.
4. D. H. White and R. E. Birkett, Nucl. Phys. A136, 657 (1969).
5. S. M. Brahmavar, J. H. Hamilton, A. V. Ramayya, E. F. Zganjar, and C. E. Bemis, Jr., Nucl. Phys. A125, 217 (1969).
6. R. Doebler, Nuclear Chemistry Annual Report (1969), Michigan State University, 175.
7. S. M. Brahmavar and J. H. Hamilton, Nucl. Instr. Methods 69, 353 (1969).
8. W. G. Winn and D. G. Sarantites, Phys. Rev. C 1, 215 (1970).
9. R. C. Greenwood, R. G. Helmer, and R. J. Gehrke, Nucl. Instr. Methods 77, 141 (1970).
10. J. Kern, Nucl. Instr. Methods 79, 233 (1970).
11. D. E. Raeside, Nucl. Instr. Methods 87, 7 (1970).
12. G. C. Nelson and B. G. Saunders, Nucl. Instr. Methods 84, 90 (1970).
13. R. Gunnink, J. B. Niday, R. P. Anderson, and R. A. Meyer, UCID-15439 (1969).
14. C. M. Lederer, unpublished results (1968).
15. B. N. Taylor, W. H. Parker, and D. N. Langenberg, Rev. Mod. Phys. 41, 375 (1969).

16. Y. Yoshizawa, T. Morii, T. Kotoh, and H. Gotoh, J. Nucl. Sci. & Tech. 5, 432 (1968).

17. U. Gruber, R. Koch, B. P. Maier, O. W. B. Schult, Z. Naturforsch. 20a, 929 (1965).

18. L. J. Jardine, unpublished results (1970).

19. Y. Gurfinkel and A. Notea, Nucl. Instr. Methods 57, 173 (1967).

20. D. Camp, Nucl. Phys. (to be published, 1971).

21. R. J. Gehrke, J. E. Cline, and R. L. Heath, Nucl. Instr. Methods 91, 349 (1971).

22. G. Aubin, J. Barrette, and S. Monaro, Nucl. Instr. Methods 76, 93 (1969).

23. J. F. W. Jansen, B. J. Meijer, and P. Koldewijn, Radiochim. Acta 13, 171 (1970).

24. E. J. Seppi, H. Henrikson, F. Boehm, and J. W. M. Dumond, Nucl. Instr. Methods 16, 17 (1962).

APPENDIX E

RELATIVE INTENSITY CALIBRATION OF A Ge(Li) GAMMA-RAY SPECTROMETER*

ABSTRACT

Portions of the gamma-ray spectra of ^{182}Ta and ^{180m}Hf have been remeasured with a Ge(Li) spectrometer system to determine accurate relative intensities. For ^{182}Ta the eleven strongest transitions in the energy range of 100-1300 keV were measured. The relative gamma-ray branching ratio $I_\gamma(443)/I_\gamma(501)$ in ^{180m}Hf was remeasured to be 5.70 ± 0.15. The intensity values derived from these measurements are recommended for use with an IAEA standard intensity set in the calibration of relative photopeak efficiencies for Ge(Li) detectors. An overall accuracy of ±4% for the relative intensity calibration over the energy range of 100-1300 keV can be expected and ±3% for the 500-2800 keV energy range.

---

*This appendix appeared as a Lawrence Radiation Laboratory Report UCRL-20435 (May 1971) and in Nucl. Instr. Methods 96, 259 (1971).

I. INTRODUCTION

The development of energy calibration standards for Ge(Li) detectors has advanced to a state where many standards in the energy range of 60-2800 keV are determined with errors of less than 0.1 keV. However, the absolute or relative gamma-ray intensities of these standards are often uncertain by as much as 5%. In a few exceptional cases relative intensity determinations have been performed with errors of less than 2% by careful consideration of gamma-ray cascades corrected for internal conversion[10]). The criteria of either simple cascades with no cross-over transitions or highly accurate decay schemes place a severe restriction on both the availability and on the use of absolute transition intensities for intensity calibrations. However, relative transition intensities for complex decay schemes can be determined accurately, and these data are generally more easily applied.

It is the purpose of this paper to suggest ^{182}Ta and ^{180m}Hf as isotopes spanning the energy range of 100-1300 keV to supplement the IAEA[1]) or similar standard intensity source sets for relative photopeak efficiency determinations of Ge(Li) detectors. Relative intensity measurements have been performed on ^{182}Ta in the energy range of 100-1300 keV and are compared with others[3,4,23]). The absolute gamma-ray intensities for ^{180m}Hf are presented and compared with values reported in the literature[10,30,33]) based upon the remeasured $I_\gamma(443)/I_\gamma(501)$ gamma-ray branching ratio. Relative intensity values for isotopes are included in the tables in order to collect the best sets of data necessary to calibrate Ge(Li) detectors over the energy range of 100-2800 keV to ±4%.

II. EXPERIMENTAL

The 115.1d ^{182}Ta was produced in the Berkeley Research Reactor by irradiation of 1.0 and 0.5 mil foils of natural Ta (99.9877% ^{181}Ta)[2]) which has a large thermal neutron cross-section of 21 barns. The small 0.07 barn cross-section to produce the 16.5 m ^{182m}Ta did not interfer after a short decay period following irradiation. The intensities of the eleven strongest gamma-rays were measured on a calibrated 10-cm^3 Ge(Li) detector. This detector had been calibrated with two sets of absolute intensity sources obtained from the IAEA. ^{180m}Hf was also used to define the efficiency curve in the critical 100-335 keV region. The accuracy of the photopeak efficiency determination was checked by measuring several radioisotopes whose relative intensities are known[10,11]) to 2%. These measured intensities agreed to within 3% with those in Kane and Mariscotti[10]) and Donnelly et al.[11]). The efficiency curve for the 10-cm^3 detector obtained in this way is shown in fig. 1. The detector resolution ranged from 1.4 keV at 122 keV to 2.3 keV at 1332.5 keV. The areas of photopeaks were determined using two separate computer codes, SAMPO[6]) and SPECT[7]), which use gaussian functions with exponential tails to approximate the experimental photopeak shapes. Photopeak areas from the codes agreed to within 1% in the selected peaks. Measurements of photopeak intensities were made for each of the two ^{182}Ta foils which were corrected for attenuation[45]) due to source thickness, and these were verified with an isotopically separated ("mass free") source. The results are given in Table 1 and are compared to other results[4,5,24]).

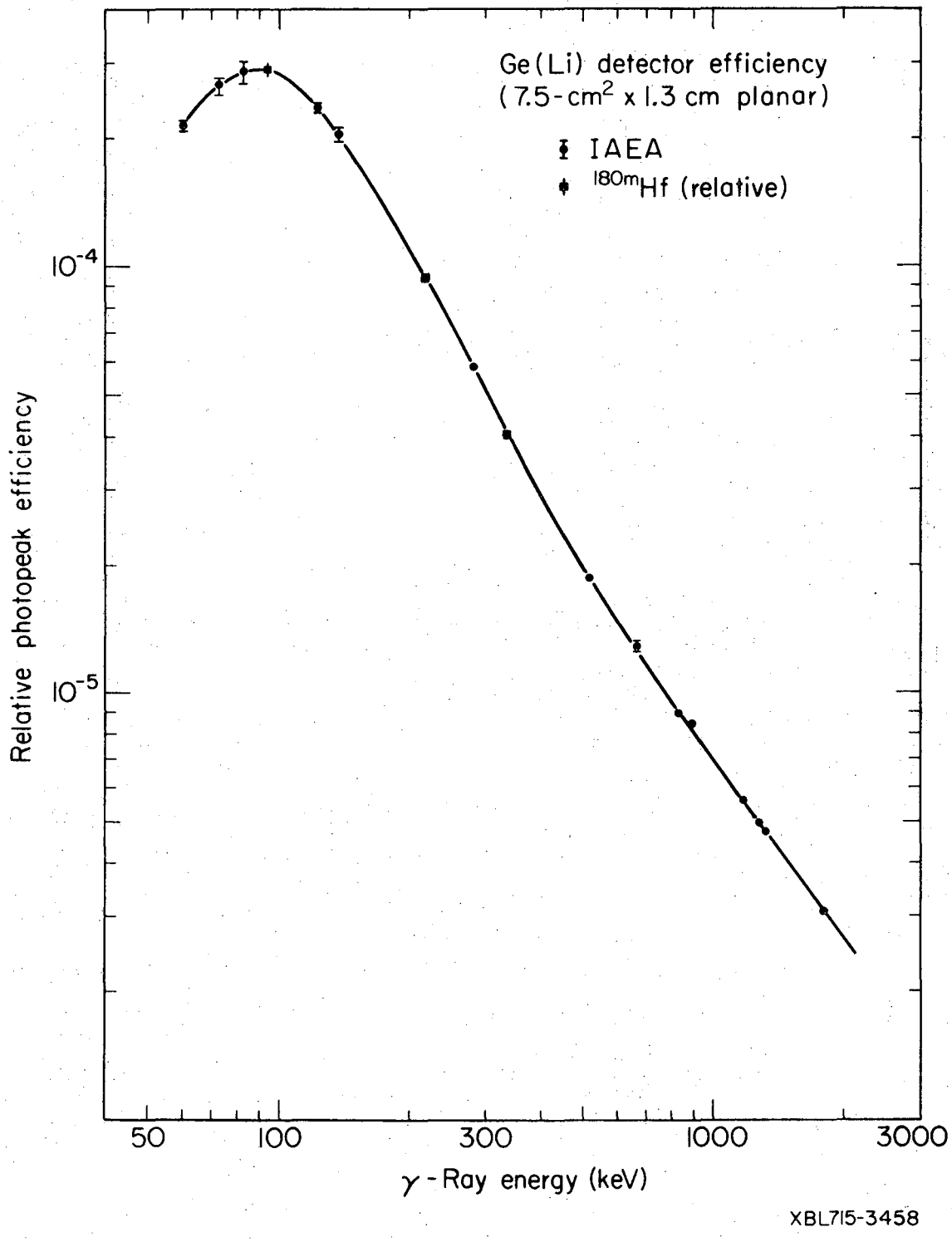

Fig. 1. The relative photopeak efficiency curve for the 10-cm^3 Ge(Li) detector as a function of gamma-ray energy.

Table 1. Energies and Relative Intensities of ^{182}Ta in Energy Range 100-1300 keV

E_γ[a]	Edwards et al.[4] I_γ[b]	White et al.[5] I_γ[c]	Sapyta et al.[23] I_γ[c]	Present Work I_γ[c]
100.104±0.002	40.2		40.7±4.1	40.2±1.0
152.435±0.003	20.5±0.8	21.3±1.0	19.5±2.0	20.5±0.5
156.387±0.003	8.04±0.4	8.07±0.4	7.5±0.75	7.6±0.2
179.393±0.004	9.2±0.4	9.57±0.5	8.7±0.9	8.8±0.3
222.109±0.005	22.5±0.9	22.6±1.2	21.2±2.1	21.3±0.55
229.322±0.005	11.1±0.5	10.9±0.5	10.5±1.1	10.3±0.3
264.072±0.009	10.8±0.5	10.6±0.4	10.3±1.0	10.1±0.3
E_γ[d]				
1121.298±.013		100.	100.	100.
1189.046±.013		47.4±0.7	46.3±3.2	46.5±0.7
1221.399±.013		79.3±1.2	77.3±5.4	77.3±1.2
1231.010±.013		33.4±0.5	32.7±2.3	32.8±0.5

[a] Energies listed in keV are those reported by Edwards et al.[4].

[b] Intensities[4] are renormalized to the 100 keV transition of present work.

[c] Intensities are normalized to 1121 keV transition.

[d] The energies listed in keV are those reported by White and Birkett[3].

The measured ^{182}Ta relative intensities should be accurate to 3% over the energy range of 100-1300 keV. Previously, Edwards et al.[4]) quoted errors of 4-5% over the energy range of 100-264 keV. White et al.[5]) measured the relative intensities of ^{182}Ta gamma-rays in the energy range of 152-1300 keV with errors of 4-5%. Over the smaller energy range of 1000-1300 keV, errors quoted were in the range, 1.5-2%.

^{180m}Hf was produced by reactor irradiation of the separated isotope ^{179}Hf. ^{180m}Hf is very convenient[10,11]) in the energy region between 93-501 keV where calibration points for efficiency curves are sparse. The decay scheme[31,33]) of ^{180m}Hf (fig. 2) allows absolute gamma-ray intensities to be derived by correcting for internal conversion if the $I_\gamma(443)/I_\gamma(501)$ gamma-ray intensity branching is accurately known. With reference to fig. 2 and the ^{180m}Hf decay scheme the following equations apply.

$$I_t(93) = I_t(215) = I_t(332) = I_t(443) + I_t(501) \qquad (1)$$

and

$$I_t(443) + I_t(501) = (1 + \alpha(443))I_\gamma(443) + (1 + \alpha(501))I_\gamma(501) \qquad (2)$$

I_t and I_γ are the transition and gamma-ray intensities, respectively; α is the total internal conversion coefficient. The $I_\gamma(443)/I_\gamma(501)$ relative gamma-ray branch was measured to be 5.70 ± 0.15 on the above detector in agreement with ref. [31]). The mixing ratio of 3.5% M2 and 96.5% E3 reported by Bodenstedt et al.[34]) for the 500.7 keV transition was used in calculating absolute gamma-ray intensities from the transition intensities

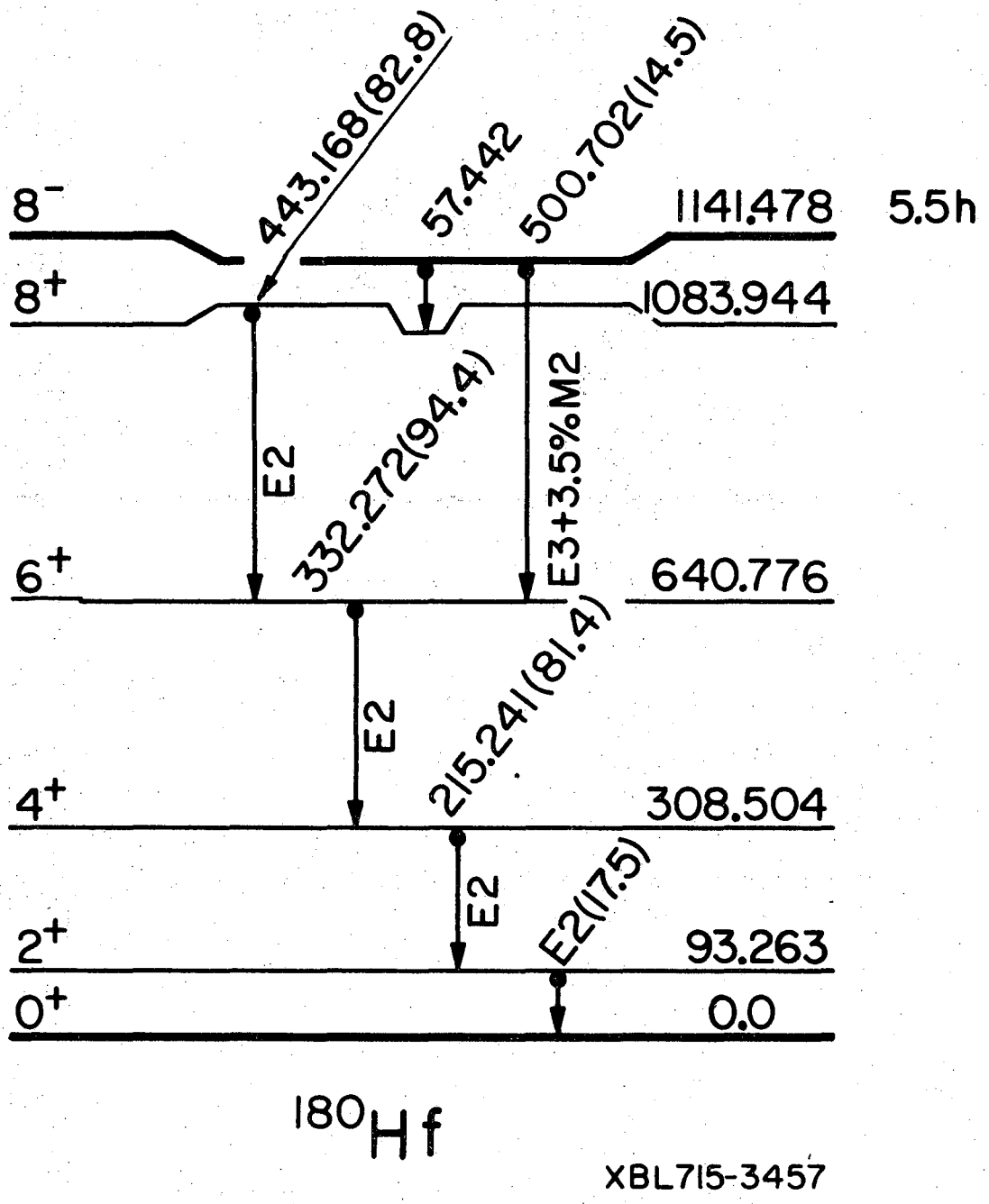

Fig. 2. The ^{180m}Hf decay scheme used in the photopeak efficiency determination. The energies (keV) are based on the measurements of Gujrathi and D'Auria[30]). The absolute gamma-ray intensities expressed in per cent from this study are shown in parenthesis.

of eq. (1). The other transitions are of E2 multipolarity. Theoretical conversion coefficients used were those of Hager and Seltzer[35]). The calculated absolute gamma-ray intensity results obtained from eq. (1) are shown in Table 2 with other results[10,30,33]). Included are the 93.3 and 500.7 keV transitions not given by ref. [10]). The calculated 14.5 ± 0.4% gamma-ray intensity for the 500.7 keV transition is in agreement with the values ~ 15% given by Gvozdev et al.[37]) and 14.8 ± 0.8% of Goldhaber and McKeown[31]) and Paul et al.[32]).

Table 3 shows the absolute gamma-ray intensity values used for the IAEA calibrated set and ^{24}Na. The intensity values are those recommended by the IAEA. They are given to collect the necessary intensity values, along with ^{182}Ta and ^{180m}Hf, into one paper to be used for the efficiency calibration of Ge(Li) spectrometer systems. ^{24}Na is also listed since it is useful for extending the curve to higher energies.

III. CONCLUSIONS

The ^{182}Ta intensities determined in this work were used to derive the relative photopeak efficiency curve of a 40-cm^3 coaxial detector together with ^{180m}Hf, ^{24}Na, and the IAEA calibrated set for which the results are shown in fig. 3. A third detector has been recently calibrated[9]) at this laboratory using this method and showed similar results. These isotopes and intensity values, when combined with the IAEA intensity sources and ^{24}Na, should determine the relative photopeak efficiency of Ge(Li) spectrometers to ±4% over the energy range of 100-500 keV and ±3% over the energy range of 500-2800 keV.

Table 2. Gamma Energies and Absolute Gamma-ray Intensities of ^{180m}Hf in the Range of 57-501 keV

E_γ [a]	I_γ [a]	I_γ [b]	I_γ [c]	I_γ [d]
57.442	47.5±3.4		48.6±0.86	
93.263	18.40±0.16		16.7±0.33	17.47±0.17
215.241	81.1±2.4	81.4	83.4±2.3	81.4±0.8
332.272	94.4±4.0	94.4±0.8	94.4±4.0	94.4±0.9
443.168	84.8	83.0±1.2	81.9±4.3	82.8±1.5
500.702	15.7±1.3		17.05±5.2[e]	14.5±0.4

[a] Gujrathi and D'Auria[30]) results with stated energy errors of ±0.015 keV. The measured gamma intensities were renormalized to 332 keV.

[b] Kane and Mariscotti[10]) renormalized results.

[c] Edwards and Boehm[33]) results using a bent crystal gamma spectrometer.

[d] Present work where ~ 1% error was arbitrarily assigned for the 93, 215, and 332 keV transitions due to uncertainity in the theoretical E2 conversion coefficients.

[e] This was deduced from feeding and not measured directly (ref. [33]).

Table 3. Energies and Intensities of the IAEA Standards and ^{24}Na

Isotope	Half-Life[b]	E_γ[a]	I_γ[b]
^{241}Am	432.9±0.8y [38,39]	59.538±0.008	35.9±0.6 [12,13,14,15]
^{57}Co	271.6±0.5d [40]	122.055±0.013	85.0±1.7 [8,16,27,28]
		136.47±0.008	10.65±0.4 [8]
		136.47±0.008	11.4±1.3 [16,27,28]
^{203}Hg	46.8±0.2d [40,41]	72.873±0.001	9.7±0.5 [17,18]
		82.5±0.2	2.8±0.2
		279.186±0.009	81.55±0.15
^{22}Na	2.602±0.005y [40]	511.0041±0.0016	181.1±0.2 [19,20]
		1274.55±0.04	99.95±0.02
^{137}Cs	29.90±0.05y [42]	32.1±0.1	5.7±0.2 [12,21]
		36.5±0.1	1.3±0.1
		661.618±0.028	85.1±0.4
^{54}Mn	312.6±0.3d [15,19,43]	834.81±0.03	100.0 [22]
^{60}Co	5.275±0.005y [41,42,44]	1173.231±0.024	99.87±0.05 [23]
		1332.501±0.021	99.999±0.001

(continued)

Table 3. (continued)

Isotope	Half-Life[b]	E_γ[a]	I_γ[b]
^{88}Y	107.4±0.8d [40,43])	898.021±0.023	91.4±0.7 [24,25,26])
		1836.129±0.031	99.4±0.1
^{24}Na	15.00±0.02h	1368.526±0.044	100.0
		2754.098±0.183	100.0

[a]Energy values are adopted values from Jardine[36]).

[b]Absolute intensity and half-life values recommended by Nuclear Data and the IAEA[1]).

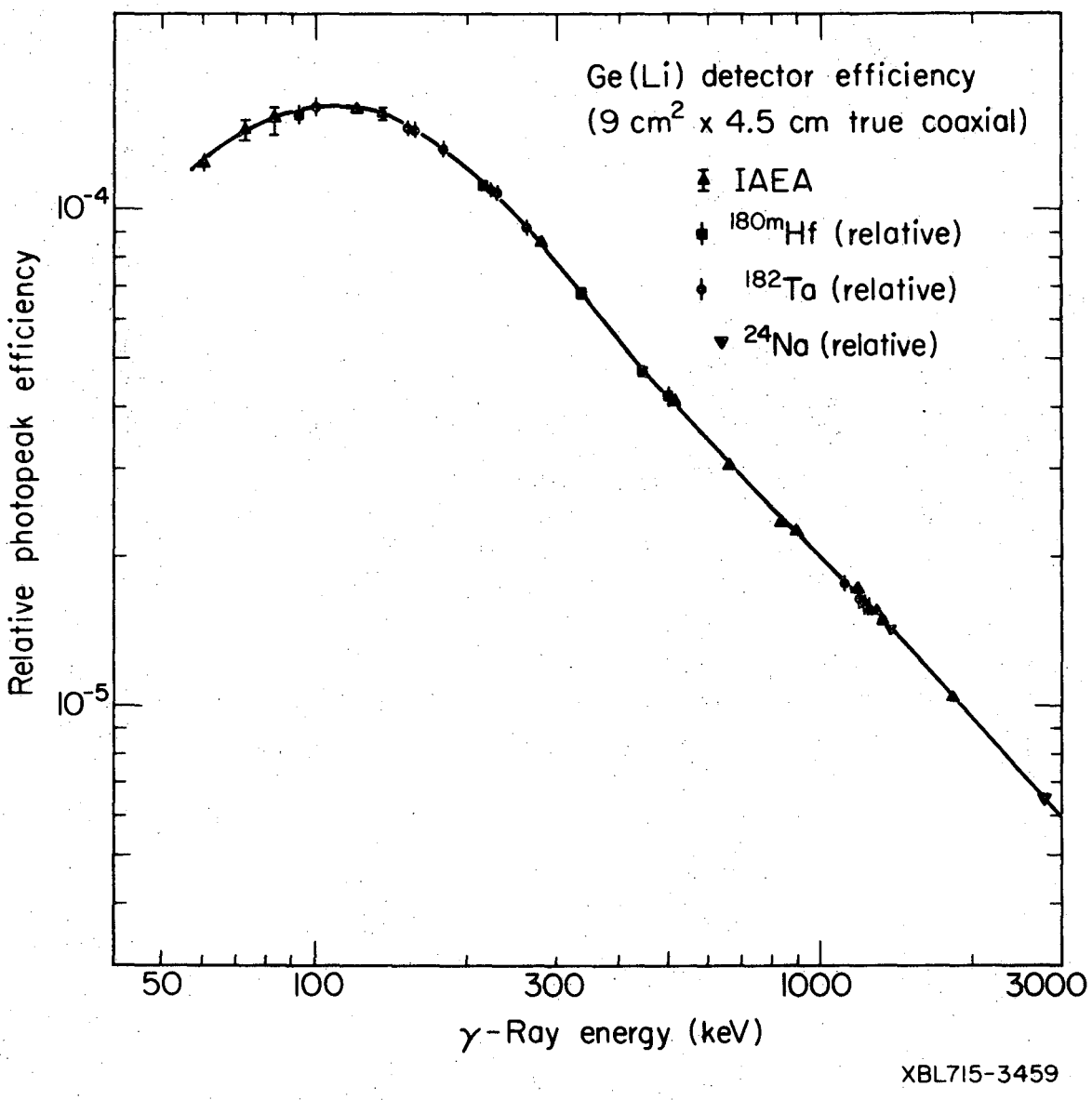

Fig. 3. The relative photopeak efficiency curve for a 40-cm^3 true coaxial Ge(Li) detector as a function of energy obtained using the isotopes and intensities reported in the study.

REFERENCES

1. International Atomic Energy Agency, Vienna (Set of calibrated to $\leq 1\%$ intensity sources listed in Table 3).
2. F. A. White, T. L. Collins, and F. M. Burke, Phys. Rev. 97, 566 (1955).
3. D. H. White and R. E. Birkett, Nucl. Phys. A136, 657 (1969).
4. W. F. Edwards, F. Boehm, J. Rogers, and E. J. Seppi, Nucl. Phys. A63, 97 (1965).
5. D. H. White, R. E. Birkett, and T. Thomson, Nucl. Instr. Methods 77, 261 (1970).
6. J. T. Routti and S. G. Prussin, Nucl. Instr. Methods 72, 125 (1969).
7. C. M. Lederer, University of California, Lawrence Radiation Laboratory Report No. UCRL-18948, unpublished (1969).
8. L. J. Jardine, unpublished results (1970).
9. L. J. Jardine and E. Temple, unpublished results (1970).
10. W. R. Kane and M. A. Mariscotti, Nucl. Instr. Methods 56, 189 (1967).
11. D. P. Donnelly, H. W. Baer, J. J. Reidy, and M. L. Wiedenbeck, Nucl. Instr. Methods 57, 219 (1967).
12. T. Yamazaki and J. M. Hollander, Nucl. Phys. 84, 505 (1966).
13. L. B. Magnusson, Phys. Rev. 107, 161 (1957).
14. W. Bambynek, European Atomic Energy Community Report No. EUR 2632d (1965).
15. A. Peghaire, Nucl. Instr. Methods 75, 66 (1969).
16. G. D. Spouse and S. S. Hanna, Nucl. Phys. 74, 177 (1965).
17. W. L. Croft, B. G. Pettersson, and J. H. Hamilton, Nucl. Phys. 48, 267 (1963).

18. R. W. Fink, R. C. Jopson, H. Mark, and C. D. Swift, Rev. Mod. Phys. 38, 513 (1966).

19. C. M. Lederer, J. M. Hollander, and I. Perlman, Table of Isotopes, Wiley, New York (1967).

20. E. Vatai, D. Varga, and J. Uchrin, Nucl. Phys. A116, 637 (1968).

21. H. H. Hansen, G. Lowenthal, A. Spernol, W. van der Eijk, and R. Vaninbroukx, Z. Physik 218, 25 (1969).

22. J. H. Hamilton, S. R. Amtey, B. van Nooijen, A. V. Ramayya, and J. J. Pinajian, Phys. Letters 19, 682 (1966).

23. S. Raman, Z. Physik 228, 387 (1969).

24. J. I. Rhode, O. E. Johnson, and W. G. Smith, Phys. Rev. 129, 815 (1963).

25. N. H. Lazar, E. Eichler, and G. D. O'Kelley, Phys. Rev. 101, 727 (1956).

26. M. Sakai, T. Yamazaki, and J. M. Hollander, Nucl. Phys. 84, 302 (1966).

27. D. C. Hall and R. G. Albridge, Nucl. Phys. A91, 495 (1967).

28. W. Rubinson and K. P. Gopinathan, Phys. Rev. 170, 969 (1968).

29. J. J. Sapyta, E. G. Funk, and J. W. Mihelich, Nucl. Phys. 139, 161 (1969).

30. S. C. Gujrathi and J. M. D'Auria, Nucl. Phys. A161, 410 (1971).

31. G. Scharff-Goldhaber and M. McKeown, Phys. Rev. 158, 1105 (1967).

32. H. Paul, M. McKeown, and G. Scharff-Goldhaber, Phys. Rev. 158, 1112 (1967).

33. W. F. Edwards and F. Boehm, Phys. Rev. 121, 1499 (1961).

34. E. Bodenstedt, H. J. Körner, E. Gerdau, J. Radeloff, C. Günther, and G. Strube, Z. Physik 165, 57 (1961).

35. R. S. Hager and E. C. Seltzer, Nucl. Data A4, 1 (1968).

36. L. J. Jardine, University of California, Lawrence Radiation Laboratory Report No. UCRL-20476, unpublished (1971).

37. V. S. Gvozdev, L. I. Rusinov, Yu. I. Filimonov, and Yu. L. Knazov, Nucl. Phys. 6, 561 (1958).

38. F. L. Oetting and S. R. Gunn, J. Inorg. Nucl. Chem. 29, 2659 (1967).

39. R. E. Stone and E. K. Hulet, J. Inorg. Nucl. Chem. 30, 2003 (1968).

40. S. C. Anspach, L. M. Cavallo, S. B. Garfinkel, J. M. R. Hutchinson, and C. N. Smith, Natl. Bureau Stds. Misc. Publ. Report No. 260-9 (1965).

41. F. Lagourine, Y. LeGallic, and J. Legrand, Int. J. Appl. Rad. Isotopes 19, 475 (1968).

42. K. F. Walz and H. W. Weiss, Z. f. Naturforschung 25a, 921 (1970).

43. E. I. Wyatt, S. A. Reynolds, T. H. Handley, W. S. Lyon, and H. A. Parker, Nucl. Sci. Engr. 11, 74 (1961).

44. J. S. Merritt and J. G. V. Taylor, Atomic Energy of Canada, Ltd. Report No. AECL-3333, 32 (1969).

45. Kai Seigbahn, Alpha-, Beta-, and Gamma-Ray Spectroscopy, Volume 1, North-Holland Publishing Co., Amsterdam (1965) p. 827.

APPENDIX F

RELATIVE DETECTION EFFICIENCY CALIBRATION OF A Si(Li) ELECTRON SPECTROMETER

ABSTRACT

The method used to determine the relative efficiency calibration of a 5 mm × 0.785-cm^2 (active volume) Si(Li) electron spectrometer to ±8% over the energy range of 100-1700 keV is discussed.

I. INTRODUCTION

Si(Li) spectrometers can not compete with the best magnetic spectrometers for resolution, but their speed of data acquisition coupled with a much higher collection efficiency for conversion electrons has proven useful for making conversion electron measurements. A Si(Li) spectrometer has been constructed[16]), calibrated, and used for measuring relative internal-conversion coefficients.

It is the purpose of this paper to suggest isotopes and methods for determining the relative electron detection efficiency of a Si(Li) spectrometer to ±8% over the energy range of 100 to 1700 keV. We have used the Normalized Peak-to-Gamma-Peak[1]) (NPG) method for measurement of relative internal conversion coefficients. For the NPG method, the electron and gamma-ray intensities of a source are measured relative to a transition with a known conversion coefficient. This transition is then used to normalize the electron and gamma-ray intensities for use in determining other relative conversion coefficients.

The isotopes employed had simple decay schemes or well determined multipole mixing so that appreciable errors due to mixing were minimized. The primary isotopes we have used for calibration are ^{180m}Hf and ^{207}Bi. Three E1 transitions of ^{210}At in the energy range of 1436-1600 keV are recommended as possible calibration standards of future Si(Li) spectrometers. Conversion electrons from the electron-capture decay of ^{210}At have been measured with this calibrated spectrometer and the results are given as an example.

II. DESCRIPTION OF APPARATUS

Figure 1 shows a photograph of the Si(Li) spectrometer and a schematic of the Si(Li) cryostat region is shown in fig. 2. An unusual feature of this apparatus is that the cold finger-detector assembly is mounted on a movable tract with the distance between the source and detector variable from 1-195 mm. This is accomplished thru the use of a collapsable bellows to maintain the vacuum chamber and the movement is controlled thru the use of an electric motorized machine lathe tract. The movable detector feature allows the geometry to be changed which can be useful as short-lived isotopes decay.

The chamber can be separated into two parts by a large gate valve with the detector and associated electronics on one side of the valve under vacuum and the source chamber on the other side. Sources can be changed by means of a screw-held cap ("o" ring seal) without releasing the vacuum in the detector region which would take hours to warm and then cool back down if the gate valve were absent.

The detector was a 5 mm deep × 0.785 cm^2 Si(Li) crystal (made by the semiconductor group at this laboratory) and was mounted at the end of a liquid N_2 cold-finger and was maintained at ~ 77°K during operation. The FET was also in contact with the cold finger and the preamplifier[2]) was of conventional design made at this laboratory.

The output pulses from the preamplifier were fed to the same conventional high-rate electronics[3]) as being used with our Ge(Li) spectrometer systems. A PDP-7 system[4,5]) and a 4096-channel successive binary approximation analogue-to-digital converter ADC[6]) were used for memory storage and pulse-height analysis.

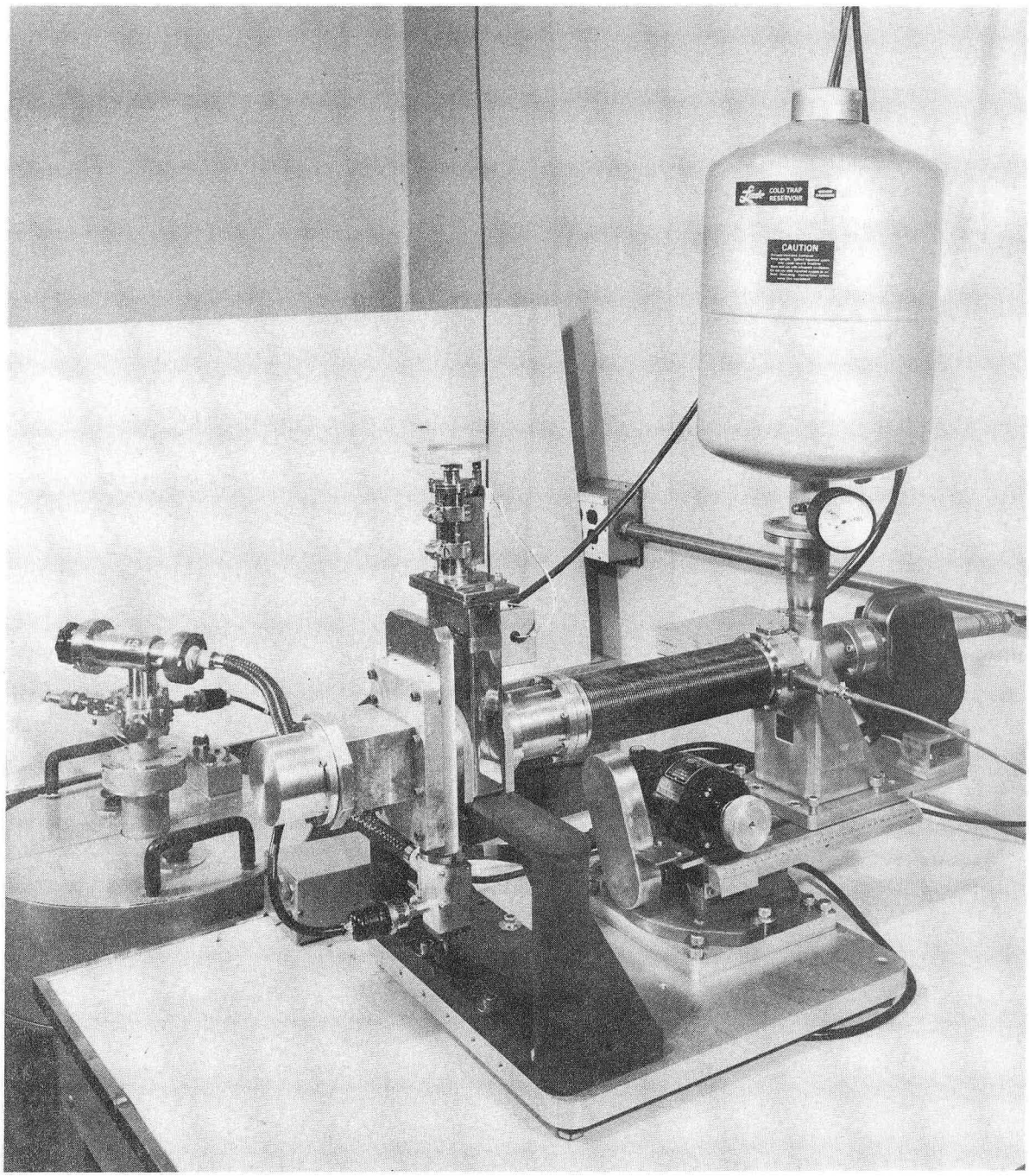

XBB 719-4244

Fig. 1. The Si(Li) electron spectrometer.

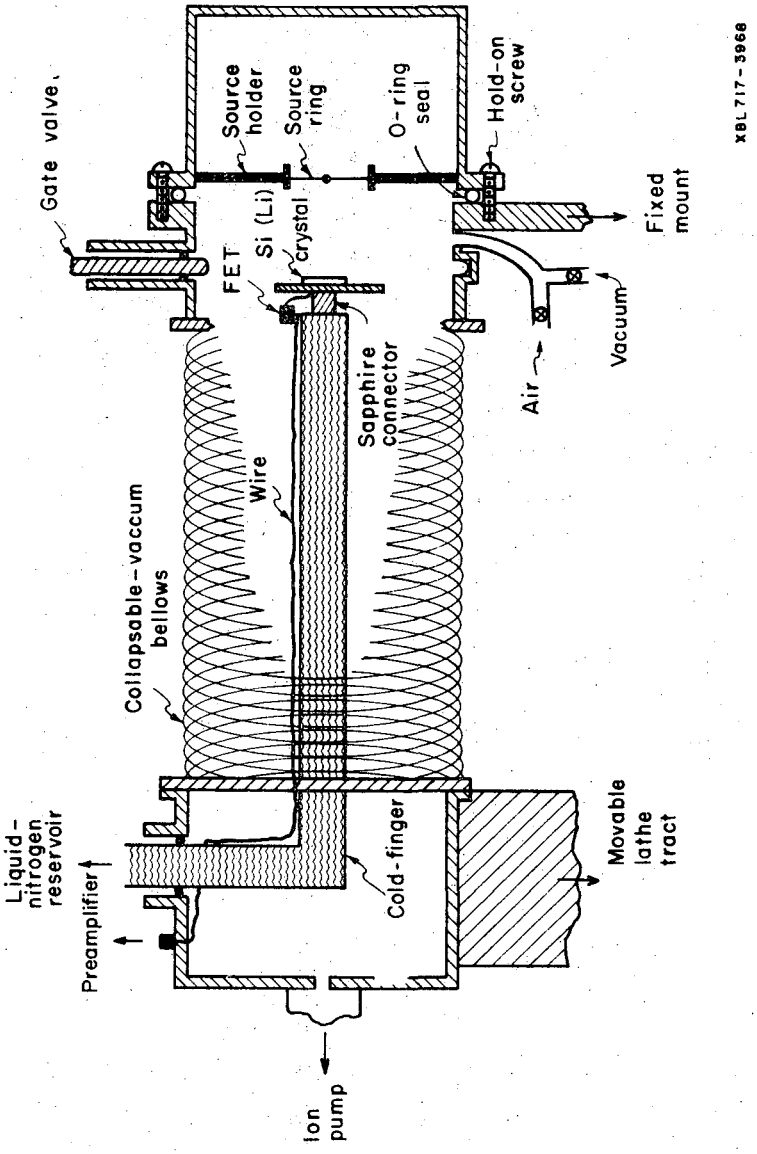

Fig. 2. Schematic diagram of the Si(Li) electron spectrometer source chamber.

The resolution of the system was measured with several isotopes. The resolution was approximately 1.2 keV (FWHM) for 100 keV electrons and 2.4 keV (FWHM) for the 1063 K-electrons of ^{207}Bi. A resolution vs. energy curve is shown in fig. 3 with the best resolution found at -1450 volts bias. The system resolution was somewhat reduced due to boiling liquid N_2 in the long cold finger which produced bad microphonics.

The Si(Li) crystal had an approximate 500-800 Å gold-coating for electrical contact which also allowed the crystal surface to be cleaned off gently with a soft Q-tip and ETOH when the surface became coated with oil or source materials. Ocassionally an apparent surface coating was indirectly observed by an increasing tail of electron peaks with the ^{207}Bi source. Cleaning removed the tailing and restored the resolution. To minimize vapor or material condensation on the low temperature Si(Li) surface, no mechanical pumps were used on the system. A cryosorption pump developed at this laboratory[7]), utilizing 15 lbs. of molecular sieve at liquid N_2 temperature, was used as the only chamber roughing pump. When the pressure was below $\sim 10^{-5}$-10^{-6} Torr, an 8-liter ion-pump was used to reduce and maintain the vacuum. A total pumping time of approximately 5 minutes was normally required to attain the $\sim 2 \cdot 10^{-8}$ Torr of the ion-pump with most sources.

III. SOURCE PREPARATION

The ^{207}Bi electron source used was obtained from a previous study[8]). ^{180m}Hf was produced by a four-hour neutron irradiation of 4 mg powder of $^{179}HfO_2$ in the Berkeley Research Reactor. The ^{179}Hf was an enriched isotope from Oak Ridge and the irradiation was in a sealed quartz

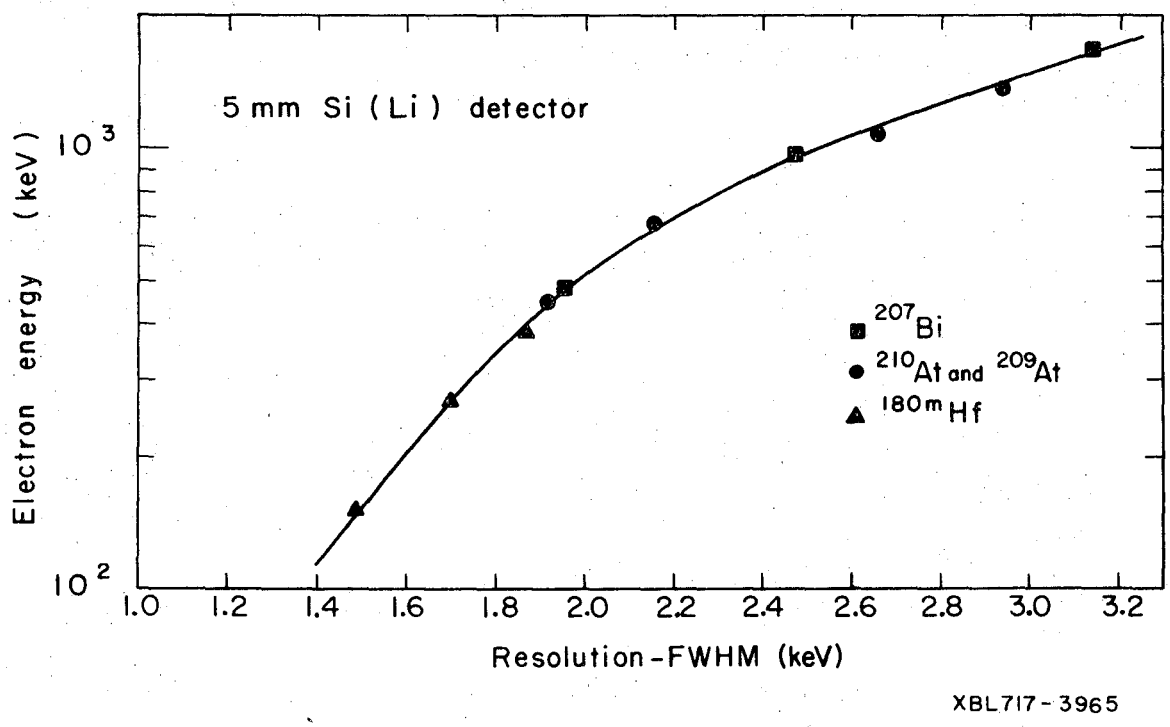

Fig. 3. Resolution of the Si(Li) spectrometer for electrons. Points are experimental.

tube. After irradiation the HfO_2 was dissolved in 50-50 solution of 48% HF and conc. HNO_3 and the excess HF and HNO_3 were destroyed by twice taking to dryness with conc. HCl to make the halfium chloride. Heating in a water bath with an air jet blowing speeded dissolution and evaporation to dryness. The final residue was dissolved in 3M HCl.

Electron sources were made by flash evaporation of the HCl solution from a tungstun boat onto a coliminated aluminum mylar film ($\sim$ 1 mg/cm^2) which was located 5.5 cm distance above the boat. The aluminum mylar had been stretched wrinkle-free on source ring mounts designed for the Si(Li) spectrometer. Sources with no visible mass were made using this technique and the total time to prepare such a source was about one hour.

^{210}At electron sources were described in another paper[13]) and in section IV of this thesis.

IV. METHOD

The electron efficiency ε for the Si(Li) system can be determined relative to one known standard transition using the NPG method[1]) and the following equation.

$$\varepsilon = \frac{A_{ce_x} \; I_{\gamma_{st}} \; \alpha_{st}}{I_{\gamma_x} \; A_{ce_{st}} \; \alpha_x} \qquad (1)$$

A_{ce} is the area of the conversion electrons in a peak in a spectrum, not corrected for detector efficiency.

I_γ is the area (intensity) under the corresponding gamma-ray photopeak corrected for the Ge(Li) detector efficiency.

α is either an accurately determined experimental or a theoretical conversion coefficient.

st refers to a standard or well-known transition in the source to which the NPG method is applied.

x refers to the transition being measured relative to the standard.

The NPG method relies on an accurate knowledge of the conversion coefficients and gamma-ray intensities, and if known, ε can then be measured relative to a standard transition in the source using eq. (1).

The values of I_γ and the theoretical values of Hager and Seltzer[11]) for α used for the ^{207}Bi and ^{180m}Hf isotopes are shown in Table 1. The gamma-ray intensity values of ^{207}Bi were determined by a remeasurement on two separate Ge(Li) detectors which had been calibrated with a IAEA standard intensity set[14]), and the values in Table 1 represent the average of those measurements. The intensity values of ^{180m}Hf have been recently compiled[14]) based on a remeasurement of the $I_\gamma(443)/I_\gamma(501)$ relative gamma-ray branch described in Appendix E.

Figure 4 shows an electron spectrum of ^{180m}Hf collected over a three-hour period. The efficiency calibration was made by normalizing the ^{207}Bi results to the 569 keV E2 transition and the ^{180m}Hf results to the 215 keV E2 transition. The resulting electron intensities are shown in Table 2. All photopeak areas were determined with the computer codes SAMPO[9]) and SPECT[10]). Summed areas for the L-conversion lines were used for the areas. To minimize detector edge effects and insure the same solid-angle, both sources were counted at the same (50 mm) distance.

Table 1. The theoretical conversion coefficients and gamma-ray intensities used in this study for ^{180m}Hf and ^{207}Bi.

Isotope	E_γ keV	Type	α_K	α_L	α_M	α_{Total}	I_t %	I_γ %
^{180m}Hf	93.3	E2	1.10	2.73	0.679	4.72	100.	17.47 ± 0.17
	215.2	E2	0.137	0.0684	0.0167	0.227	100.	81.5 ± 0.8
	332.3	E2	0.042	0.0129	0.00309	0.0590	100.	94.4 ± 0.9
	443.2	E2	0.0201	0.00489	0.00115	0.0265	85.2	82.8 ± 1.5
	500.7	.965 E3 + .035 M2	0.04097	0.0157	—	—	14.8	14.5 ± 0.4
^{207}Bi	569.65	E2	0.016	0.00445	—	—	—	100.
	1063.6	M4	0.097	0.0245	—	—	—	75.5 ± 2.2
	1770.	.993 M1 + .007 E2	0.00334[a]	0.000585[a]	—	—	—	6.9 ± .2

[a]These values are from the tables of Sliv and Band[15]). α_L was obtained by extrapolation of the ratio α_K/α_L.

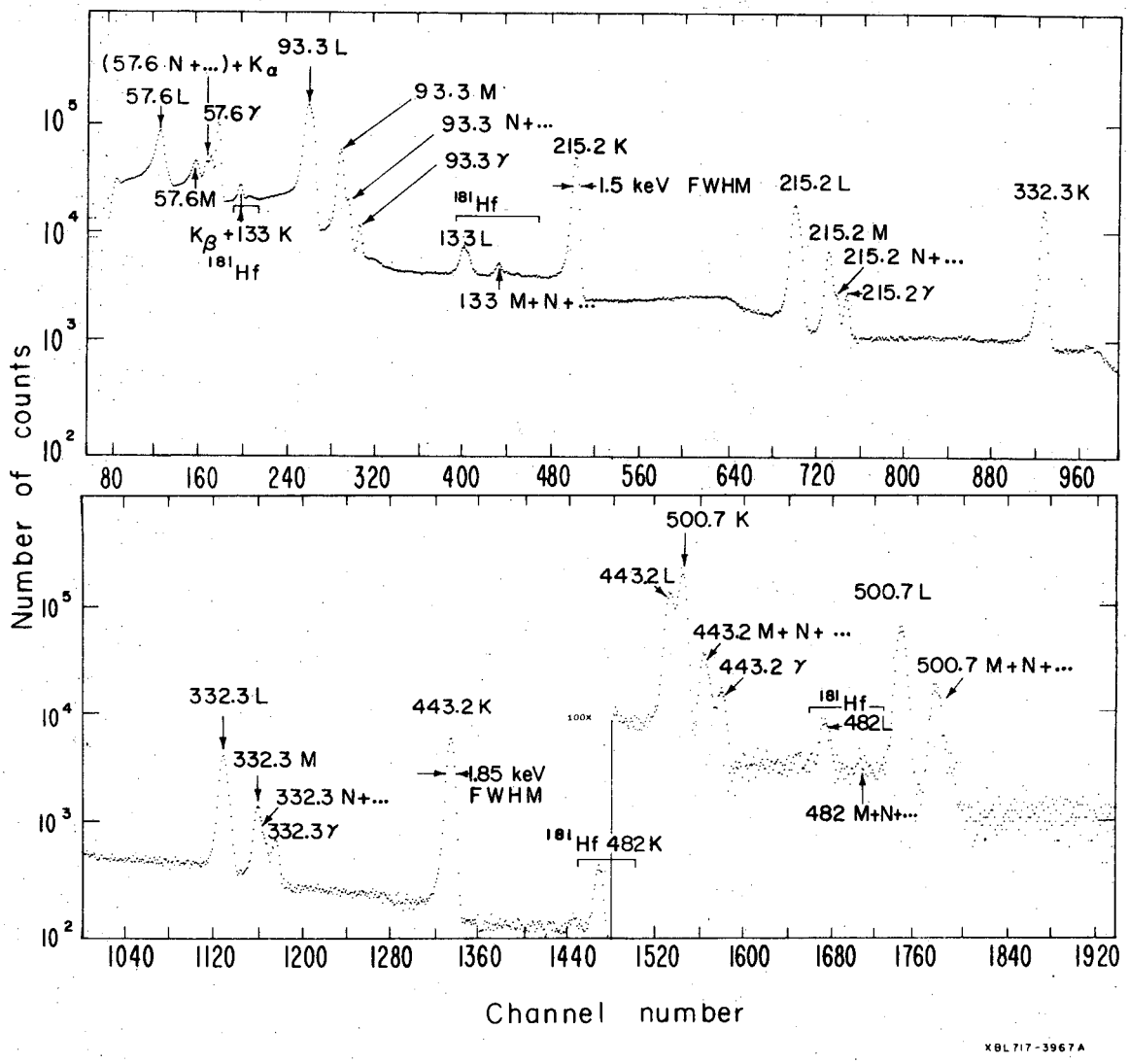

Fig. 4. Conversion electron spectrum of ^{180m}Hf decay.

Table 2. The measured and theoretical electron intensities and the relative electron efficiency for ^{180m}Hf and ^{207}Bi on the 5 mm Si(Li) detector.

Isotope	E_γ keV	Line Type	$I_{e^-}^{expt}$ [b] %	I_e^{Theory} %	Relative Efficiency %
^{180m}Hf	93.3	K	96.7 (5%)	172.2	56.2 ± 6.0
		L	409.3 (1.8%)	427.4	95.8 ± 2.1
	215.2	K	100. (1%)	100.	100.0 ± 1.5
		L	50.43 (1.8%)	49.92	101.0 ± 2.1
	332.5	K	36.05 (1%)	35.52	101.5 ± 1.5
		L	10.97 (4.2%)	10.91	100.6 ± 4.1
	443.2	K	15.16 (1%)	14.87	102.0 ± 1.5
		L		3.62	99.8 ± 2.1 [a]
	500.7	K		5.32	
		L	2.03 (10%)	2.04	101.3 ± 11.
^{207}Bi	569.65	K	22.35 (1%)	21.86	100.5 ± 2.0
		L	6.225 (2%)	6.08	100.5 ± 3.0
	1063.6	K	100.0 (1%)	100.0	100.0 ± 2.0
		L	25.5 (2%)	25.25	101.0 ± 3.0
	1770.	K	0.27 (2%)	0.314	86.8 ± 3.2
		L	0.044 (4%)	0.0552	79.8 ± 3.9

[a] The 443.2 L and 500.7 K-lines were not resolved and their areas were summed to calculate the efficiency.

[b] The fit error is given in the parenthesis in %.

Normalization and extrapolation of the ^{207}Bi and ^{180m}Hf sets of data (using eq. (1)) overlap enough to produce the relative efficiency curve shown in fig. 5 over the range of 100-1000 keV to ±8%. A gap exists in the energy region 1000-1680 keV for which few, if any, transitions with accurately known conversion coefficients are presently known to the author besides four transitions from decay of ^{210}At so that included in the efficiency curve are four points due to ^{210}At. The 1181.4 keV transition was assumed pure E2 for the NPG method and the 1436, 1483, and 1599 keV transitions as pure E1 transitions in further establishing the relative efficiency curve of fig. 5. The results of these measurements are shown in Table 3. These points fill the gap between the 1063 and 1770 keV transitions from the decay of ^{207}Bi and probably establish the relative efficiency curve to ±8% over the larger energy range of 100-1700 keV.

V. APPLICATION

For an example of the usefulness of Si(Li) spectrometer systems for the rapid determination of relative internal conversion coefficients, the results of K-conversion coefficient measurements of the 8.3 hr ^{210}At decay are summarized. Using the NPG method on the basis of the 1181 keV E2 transition in the ^{210}At decay[13]), 30 K-conversion coefficients were determined. The results for the measurements of ^{210}At are shown in fig. 8 together with the theoretical values of Hager and Seltzer[11]). The details of the ^{210}At measurements and decay scheme are the subject of section IV of this thesis. In the decay, three strong E1 transitions with the energy of 1436, 1483, and 1599 keV exist and might be useful for future

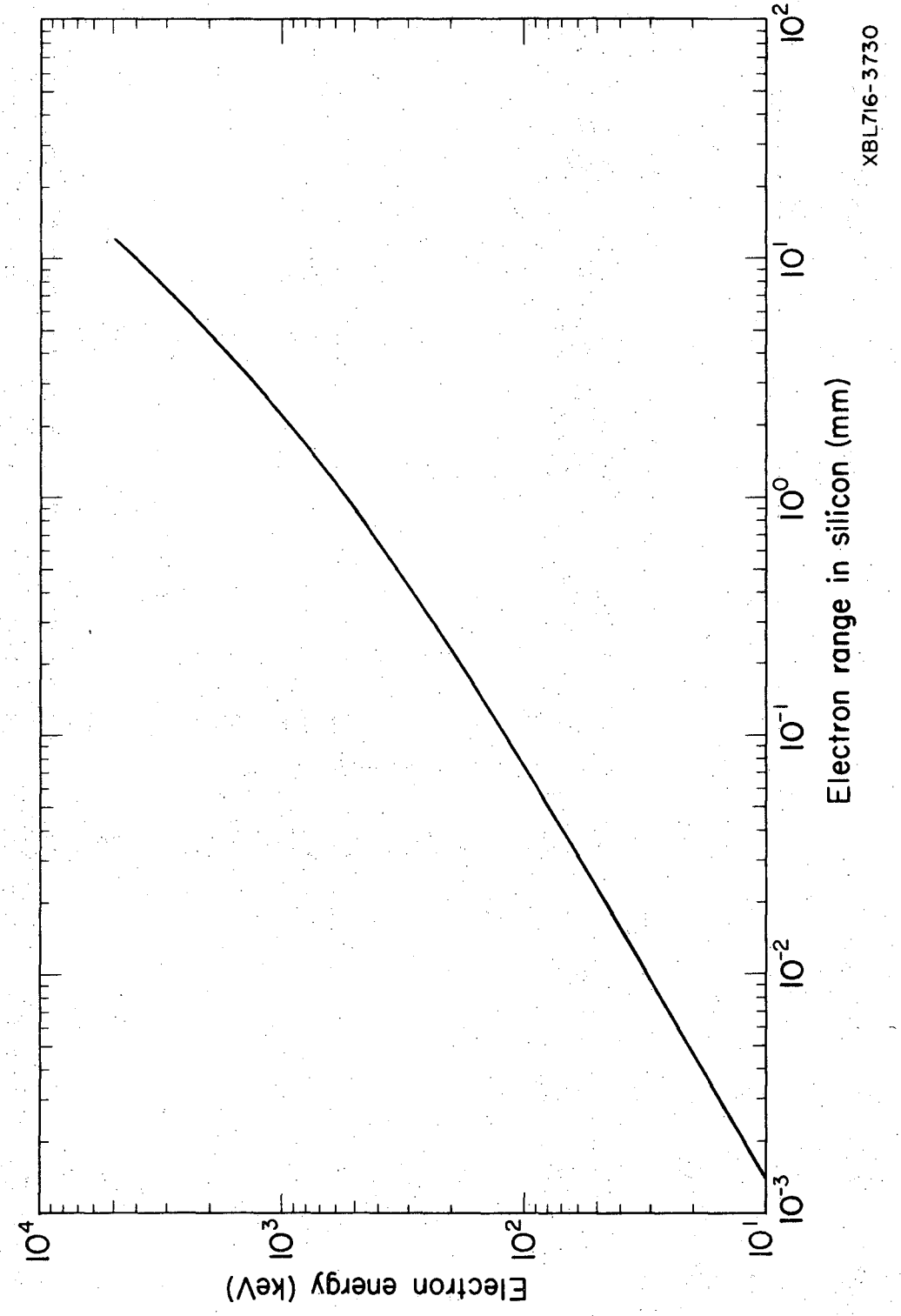

Fig. 5. Range[12]) of electrons in silicon.

Table 3. The experimental gamma-ray intensities, electron conversion coefficients, and in addition the theoretical conversion coefficients for ^{210}At. The 5-mm Si(Li) detector (K-line) efficiency is also given.

Isotope	E_γ keV	Type	I_γ %	$\alpha_{K(10^{-4})}$	$\alpha_{L(10^{-4})}$	$\alpha^{expt}_{K(10^{-4})}$	$\alpha^{expt}_{L(10^{-4})}$	K-line Efficiency %
^{210}At	1181.4	E2	100.	43.1	8.21		8.0±0.7	100.
	1436.7	E1	29.2±1.3	12.1	1.84	11.3±1.0	1.79±0.20	93.3±10.
	1483.3	E1	46.8±2.0	11.4	1.74	10.6±1.0	1.66±0.20	93.4±10.
	1599.5	E1	13.5±0.6	10.1	——	9.3±1.0	——	92.2±11.

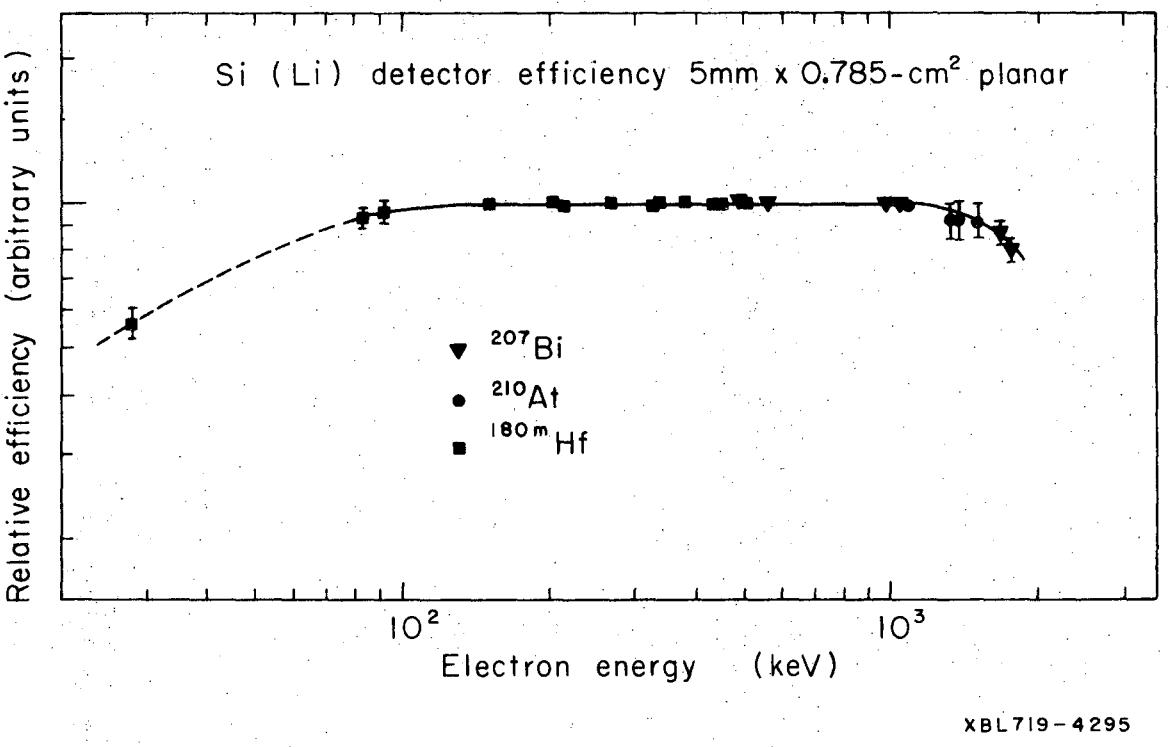

Fig. 6. Relative electron detector efficiency using the isotopes and methods reported.

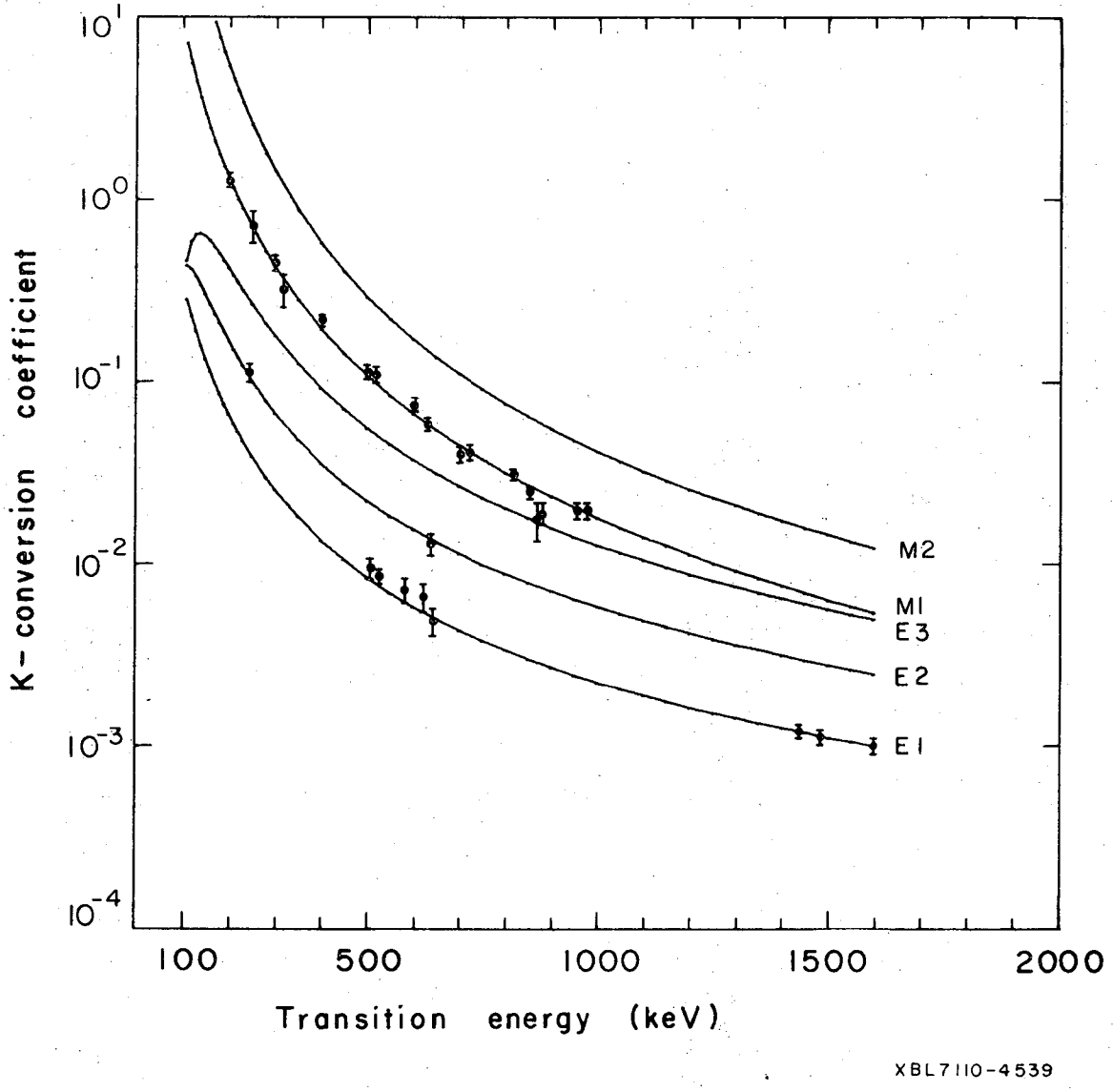

Fig. 7. Comparison of the experimental K-conversion coefficients from the decay of $^{210}_{85}$At with the theoretical values of Hager and Seltzer[11]).

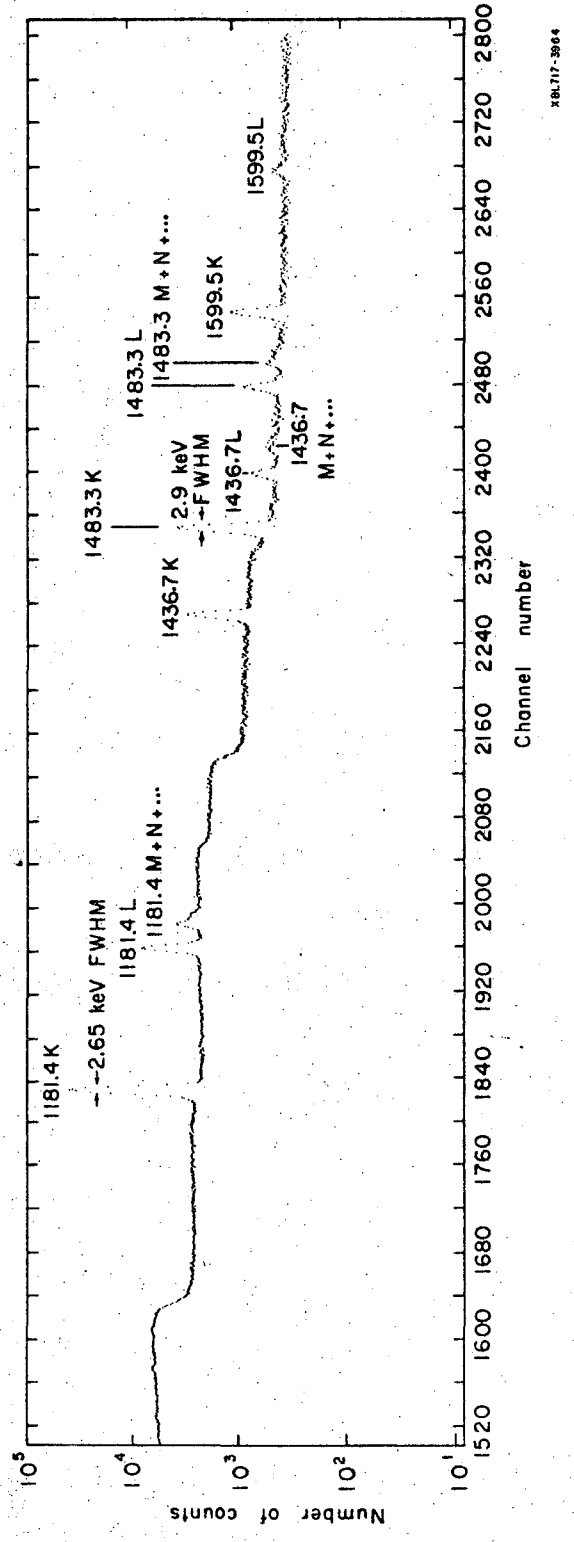

Fig. 8. High-energy conversion electron spectrum of ^{210}At decay in the energy range 1-1.6 MeV.

calibrations of Si(Li) spectrometers as previously discussed. The I_γ and theoretical α_K for those ^{210}At transitions are reported in Table 3. Figure 9 shows a portion of the ^{210}At conversion electrons covering the 1000-1500 keV energy region.

VI. CONCLUSIONS

The relative efficiency was found to be constant over the energy range of 100-1000 keV to ±8% and this might be expected, ignoring edge effects, because the mean range[12]) as shown in fig. 6 of electrons in 5 mm Si is approximately 2100 keV. The probable cause for the apparent decrease of efficiencey before the theoretical range in the detector is probably due to straggling and detector edge effects.

One might design future crystals with a larger surface area and/or introduce colimination of the source to reduce edge effects because of the short range of electrons.

REFERENCES

1. J. H. Hamilton, A. V. Ramayya, B. van Nooijen, R. G. Albridge, E. F. Zganjar, S. C. Pancholi, J. M. Hollander, V. S. Shirley, and C. M. Lederer, Nucl. Data A1, 521 (1966).
2. F. S. Goulding, UCRL-17559, unpublished (1967).
3. F. S. Goulding, D. A. Landis, and R. H. Pehl, UCRL-17560, unpublished (1967).
4. L. B. Robinson and J. D. Meng, UCRL-17220 (1967).
5. J. O. Radeloff, L. B. Robinson, and J. D. Meng, UCRL-18883 (1969).
6. L. B. Robinson, F. Gin, and F. S. Goulding, UCRL-17419 (1968).
7. R. Hintz and R. Parsons, UCRL-17299 (1966) 353.
8. W. J. Treytl, E. K. Hyde, and T. Yamazaki, Nucl. Phys. A117, 481 (1968).
9. J. Routti and S. G. Prussin, Nucl. Instr. Methods 72, 125 (1969).
10. C. M. Lederer, UCRL-18948, unpublished (1969).
11. R. S. Hager and E. C. Seltzer, Nucl. Data A4, 1 (1968).
12. M. J. Berger and S. M. Seltzer, NASA·Sp 3012.
13. L. J. Jardine and S. G. Prussin, LBL-278 (1971) submitted to Nucl. Phys.
14. L. J. Jardine, Nucl. Instr. Methods 96, 259 (1971).
15. L. A. Sliv and I. M. Band, "Coefficients of Internal Conversion of Gamma Radiation", Academy of Sciences of the USSR, Moscow-Leningrad, Part I, K-Shell (1956), Part II, L-Shell (1958).
16. J. M. Jaklevic, W. L. Searles, and D. F. Malone, LBL.

APPENDIX G

GAMMA-RAY TRANSITION RATES BETWEEN THE EVEN PARITY LEVELS OF ^{210}Po

The calculations of T(λ) discussed in section IVJ were repeated using Schmidt values of the magnetic moment to obtain values of g_j for all proton orbitals. In the recalculations all parameters except g_j were kept the same as in section IVJ so that only values of T(M1) changed while the values of T(E2) remained unchanged. These new results are shown in Table 1. To determine the effect of changing the value of g_j on the absolute T(M1) rates, these results can be compared with Table 11 of section IVJ. The comparison shows that a small change in g_j changes substancially (by three orders of magnitude in one case) some values of T(M1). It should be noted that g_j enters the calculations only when diagonal single-particle matrix elements are involved while g_ℓ and g_s enter off-diagonal matrix elements. (Equations (23) and (24) of Appendix A show this point rather explicitly.) An inconsistency in the previous calculations of section IVJ may exist because of the use of an effective (or experimental) value for g_j in diagonal terms, instead of that obtained from the Schmidt values which uses free space values of g_ℓ and g_s, and free space values of g_ℓ and g_s for off-diagonal terms. If an effective g_j is used, perhaps some effective g_ℓ and g_s should also be used. However, present data prevent the determination of any effective values of g_ℓ and g_s for the orbitals involved. Thus a more consistent set of g_j for use in transition probability calculations may be those obtained from the free space values of g_ℓ and g_s (the Schmidt values). However, since the Schmidt values do not predict the experimentally observed magnetic moments, a paradox seems to exist at the present for the choice of the parameters g_j, g_ℓ, and g_s.

Table 1. Calculated Transition Probabilities for M1 and E2 transitions for the $\pi(h_{9/2}\, f_{7/2})$ and $\pi(h_{9/2})^2$ configurations using the wave functions of Ma and True (MT),[1] Kim and Rasmussen (KR),[2] and Newby and Konopinski (NK).[3] The single-particle estimates[4] are also tabulated in addition to the observed gamma-ray intensities. The Schmidt values were used for all magnetic moments of ^{210}Po.

Transition Energy (keV)	Transition Angular Momentum[c] $J_i \to J_f$	Experimental Gamma-Ray Intensity (%)	T(λ)(sec^{-1}) Theoretical MT T(M1)10^{-8}	MT T(E2)10^{-8}	KR T(M1)10^{-8}	KR T(E2)10^{-8}	NK T(M1)10^{-8}	NK T(E2)10^{-8}	Single Particle T(λ) 10^{-8}
881.1	$7_1 \to 8_1$	0.22(2)	2668.7	51.0	822.2	60.1	---	---	$1.92\ 10^5$(M1)
250.5	$7_1 \to 8_2$	0.21(4)	1652.0	0.053	1671.5	0.0443	---	---	4400(M1)
964.9	$7_1 \to 6_1$	0.16(4)	585.0	36.9	643.4	33.3	1416.0	28.8	$2.51\cdot10^5$(M1)
112.2	$7_1 \to 6_2$	≈ .029[a]	182.9	$1.58\cdot10^{-6}$	248.4	$7.86\cdot10^{-5}$	246.7	$2.53\cdot10^{-4}$	140(M1)
929.9	$5_1 \to 6_1$	0.76(3)	2631.0	4.7	939.1	3.01	2066.9	1.80	$2.25\cdot10^5$(M1)
77.2	$5_1 \to 6_2$	≈ .026[a]	126.7	$2.63\cdot10^{-5}$	131.7	$2.04\cdot10^{-5}$	130.7	$3.14\cdot10^{-5}$	129(M1)
976.5	$5_1 \to 4_1$	0.81(4)	516.7	66.9	750.7	66.2	1306.6	88.0	$2.60\cdot10^5$(M1)
630.9	$8_2 \to 8_1$	0.31(2)	5966.4	21.5	1909.2	16.3	---	---	70300(M1)
714.4	$8_2 \to 6_1$	(<.04)[b]	0	$1.59\cdot10^{-7}$	0	0.0475	---	---	$1.02\cdot10^5$(E2)
769.2	$6_2 \to 8_1$	(<.05)[b]	0	1.05	0	33.2	---	---	538(E2)
852.7	$6_2 \to 6_1$	1.39(5)	2782.3	109.	869.8	65.5	1971.4	37.6	$1.73\cdot10^5$(M1)
899.3	$6_2 \to 4_1$	(<.2)[b]	0	26.5	0	6.08	0	17.1	1170(E2)
1201.2	$4_2 \to 2_1$	0.16(2)	0	433	0	98.0	0	161	4990(E2)
92.1	$4_2 \to 2_2$	(~.001)[a]	0	0.025	0	.022	0	.021	
955.8	$4_2 \to 4_1$	1.81(6)	3246.4	158	234.8	50.3	426.8	35.4	87300(M1)
909.2	$4_2 \to 6_1$	0.09(3)	0	46.1	0	107	0	126	1240(E2)
2290.0	$2_2 \to 0_1$	0.012(3)	0	17300	0	4400	0	6612	$1.26\cdot10^5$(E2)
1108.6	$2_2 \to 2_1$	---	4940.1	231	11.1	1.44	11.4	2.57	$3.74\cdot10^5$(M1)
863.3	$2_2 \to 4_1$	---	0	75.7	0	78.0	0	99.7	957(E2)

[a] Estimated from the conversion electron line intensities in the spectrographic plates obtained by Hoff and Hollander.[5]

[b] Estimated from preliminary data taken with a compton suppressed Ge(Li) spectrometer (Ref. 6).

[c] J_i and J_f refer to the spins of the initial and final states respectively. The subscripts 1 and 2 refer to the first and second levels (increasing energy) of a given spin.

To further compare these results with our experimental data, we recomputed the mixing ratios δ^2 and the gamma-ray branching ratios. These results are shown in Tables 2 and 3 and can be compared with Tables 12 and 13 of section IVJ. The values in Table 2 of δ^2 obtained from using the Schmidt values to obtain g_j were generally reduced by an order of magnitude over the previous results. The gamma-ray branching ratios were not nearly as sensitive to these changes in g_j and remained relatively unchanged. As in section IVJ, a choice of a better set of wavefunctions can not be made. More experimental data is needed in order to draw any definite conclusions about these present sets of calculations.

Table 2. E2-M1 Mixing Ratios[d] $(\delta^2)^a$ for ^{210}Po.

Angular[c] Momentum $J_i \rightarrow J_f$	Transition Energy (keV)	δ^2 (experimental)[b]	Theory MT	KR	NK
$7_1 \rightarrow 8_2$	250.5	<0.32	0.00003	0.000026	—
$8_2 \rightarrow 8_1$	630.9	<0.19	0.0036	0.00855	—
$6_2 \rightarrow 6_1$	852.7	$0.19^{+0.16}_{-0.14}$	0.0394	0.075	0.019
$7_1 \rightarrow 8_1$	881.7	$0.58^{+0.47}_{-0.29}$	0.019	0.073	—
$5_1 \rightarrow 6_1$	929.9	<0.32	0.0018	0.032	0.0087
$4_2 \rightarrow 4_1$	955.8	<0.29	0.0486	0.214	0.083
$5_1 \rightarrow 4_1$	976.5	<0.19	0.129	0.088	0.067

[a] The mixing ratio δ^2 is defined as $\delta^2 = \frac{|< \|E2\| >|^2}{|< \|M1\| >|^2} \equiv \frac{T(E2)}{T(M1)}$.

[b] The experimental δ^2 were obtained from comparison of our K-conversion coefficients with the theoretical values of Hager and Seltzer[7]).

[c] J_i and J_f refer to the spins of the initial and final states respectively. The subscripts 1 and 2 refer to the first and second levels (increasing energy) of a given spin.

[d] The value of g_j obtained from the Schmidt value of the magnetic moment was used for all orbitals in these calculations.

Table 3. Gamma-ray branching ratios[d] for some transitions in ^{210}Po.

Transitions Energy (keV)	Ratios[a] γ_1/γ_2 (Experiment)[b]	Theory MT	Theory KR	Theory NK
881.1/964.9	$1.38^{+.62}_{-.38}$	4.37	1.30	–
881.1/250.5	$1.04^{+.37}_{-.24}$	1.65	0.53	–
881.1/112.2	(≈ 6.75)[c]	14.9	3.55	–
929.9/976.5	$0.94^{+.09}_{-.08}$	4.5	1.15	1.48
929.9/77.2	(≈ 28.7)[c]	20.8	7.16	15.8
955.8/909.2	$20.1^{+11.2}_{-5.5}$	73.7	2.66	3.67
955.8/1201.2	$11.3^{+1.0}_{-2.2}$	7.86	2.91	2.87

[a] The γ-ray branching ratios are defined as $\gamma_1/\gamma_2 \equiv (T(M1) + T(E2))_1/(T(M1) + T(E2))_2$ from Table 1.

[b] The experimental ratios were obtained from our gamma-ray intensity data.

[c] Intensity was estimated from the conversion electron line intensities in the spectrographic plates obtained by Hoff and Hollander[5]).

[d] The value of g_j obtained from the Schmidt value for the magnetic moment was used for all orbitals in these calculations.

REFERENCES

1. C. W. Ma and W. W. True, private communication (Sept. 1971).

2. Y. E. Kim and J. O. Rasmussen, Nucl. Phys. 47, 184 (1963); Nucl. Phys. 61, 173 (1965).

3. N. Newby, Jr. and E. J. Konopinski, Phys. Rev. 115, 434 (1959).

4. C. M. Lederer, J. M. Hollander, and I. Perlman, Table of Isotopes, Wiley (1967).

5. R. W. Hoff and J. M. Hollander, Phys. Rev. 132, 2650 (1963).

6. R. A. Meyer, private communication (Sept. 1971).

7. R. S. Hager and E. C. Seltzer, Nucl. Data A4, 1 (1968).

TECHNICAL INFORMATION DIVISION
LAWRENCE BERKELEY LABORATORY
UNIVERSITY OF CALIFORNIA
BERKELEY, CALIFORNIA 94720